Analyses of

Adhesion Topography and Fluctuations

in Bio-Membranes by

Advanced Optical Microscopy

Doctoral Thesis

Submitted in partial fulfillment of the
requirements for the degree of

Doctor rerum naturalium (Dr. rer. nat.)

to the
Mathematisch-Naturwissenschaftlichen Fakultät der
Rheinischen Friedrich-Wilhelms-Universität Bonn
and the
Faculté des Sciences de la
Université de la Méditerranée - Aix Marseille II
by

Cornelia Monzel
from Bonn

Bonn, September 2011

Angefertigt mit Genehmigung der
Mathematisch-Naturwissenschaftlichen Fakultät der
Rheinischen Friedrich-Wilhelms-Universität Bonn

1. Referee: Prof. Dr. Rudolf Merkel
2. Referee: Dr. Kheya Sengupta
3. Referee: Prof. Ulrich Kubitscheck
4. Referee: Dr. Pierre Sens
Day of disputation: 20.04.2012

Für meine großartigen Eltern

Danksagung

Vielen Dank meinem Doktorvater Prof. Rudolf Merkel für die Auswahl dieses spannenden Themas und die optimale Ausstattung mit der dieses bearbeitet werden konnte, für die intensiven Diskussionsrunden in Ihrem Büro, die Möglichkeit zu jeder Zeit bei Ihnen 'anzuklopfen' und vor allem für Ihre vermittelte Begeisterung für die interdisziplinäre Forschung.

I thank my supervisor Kheya Sengupta, for the great support during my time in as well as far from Marseille. Thank you for your scientific advice, your encouragement, your endurance in validating the co-tutelle and last but not least: The numerous hours we shared discussing in your office and at lunch.

Vielen Dank ferner...

...Ana Smith, for the telephone sessions and your support in "building the bridge" between experiment and theory.

...Prof. Udo Seifert, für das Interesse an meiner Arbeit und Ratschläge.

...Daniel Schmidt, für die exakte Analyse meiner Daten, die spannenden Diskussionen in Stuttgart und die gute Zusammenarbeit.

...Susanne Fenz, für die Einführung in das Feld der biomimetischen Systeme, die guten Diskussionen und die schöne gemeinsame Zeit im Büro.

...Norbert Kirchgessner, Sebastian Houben, Ronald Springer und Georg Dreissen für die Ratschläge zu matlab und die große Hilfsbereitschaft inbesondere bei Fitproblemen.

...Bernd Hoffmann und Margret Giesen für die Kritik und kompetenten Ratschläge bei, respektive, biologischen Fragen und der Datenanalyse.

...Agnes Csiszár für die Beratung in Lipid- und Vesikelfragen, für die Aufnahme in das 'Fusionsprojekt', die unterhaltsame Zeit im Chemielabor und das Korrekturlesen.

...David Kirchenbüchler und Christian Kleusch für die gute Zusammenarbeit im Punkte FCS und die lustige Gesellschaft. Außerdem danke ich David und Thorsten Jonas für die tolle Versorgung mit Kaffee und

Abstract

Die Zellmembran bildet nicht nur eine mechanische Barriere, die Zellinneres und -äußeres voneinander trennt, sie ist auch eine aktive Organelle welche in vielen lebenswichtigen Funktionen involviert ist. Zu diesen zählen der osmotische Druckausgleich, Unterstützung der Endo/Exo-zytose, Regulierung der Zellform und die Vermittlung der Zelladhäsion. Die Zellmembran ist weich und leicht verformbar und kann daher aktiven Deformationen oder sogar thermischen Fluktuationen ausgesetzt sein. Die vorliegende Arbeit zielt auf ein quantitatives Verständnis von Fluktuationen einer Modellzellmembran ab, welche entweder adhäriert oder frei ist.

Das hier betrachtete Modellsystem bestand aus einschaligen Riesenvesikeln (GUVs). Die Adhäsion wurde durch die spezifische Ligand-Rezeptor-Wechselwirkung des Biotin-Neutravidin Komplexes vermittelt. Speziell strukturiert adhärente Substrate wurden entwickelt, auf denen Rezeptoren in Form von Linien und Gitterstrukturen angeordnet waren. Zwei lichtmikroskopische Methoden wurden verwendet um die Membran zu untersuchen (i) Zwei-Wellenlängen Reflektions-Interferenz-Kontrast Mikroskopie (DW-RICM), welches den Membran-Substrat Abstand mit einer Genauigkeit von einigen Nanometern und bis zu einem Abstand von einem Mikrometer, mit einer zeitlichen Auflösung von 50 ms messen kann. Hierbei wurden signifikante Fortschritte in der Automatisierung und Analyse von DW-RICM Daten erzielt. (ii) Fluktuations-Korrelations-Spektroskopie (FluCS), welche Membranfluktuationen mit einer räumlich und zeitlichen Auflösung von, respektive, 20 nm und 10 μs messen kann. Basierend auf der Fluoreszenz-Korrelations-Spektroskopie, misst FluCS mit der Korrelationsfunktion den Abfall des Fluoreszenzsignals. Jedoch wird in FluCS der Abfall durch Membranfluktuationen anstatt von Diffusion erzeugt. Dies ist eine neuartige Methode, die in dieser Arbeit entwickelt wurde.

Messungen mit DW-RICM zeigten, das GUVs auf strukturiert adhärenten Substraten Regionen gebundener und fluktuierender Membran in Übereinstimmung mit der zugrundeliegenden Struktur aufweisen. Innerhalb

von Fluktuationsbereichen bildete sich die Membran als abgeflachter Hügel aus, wobei die Membran-Substrat Höhe in einem Plateau bei $79 \pm 9\ nm$ lag. In diesem Plateaubereich wurden Fluktuationsamplituden von 12 ± 2 nm gemessen. Veränderung von Form (Gitter bzw. Linien) und Größe (Gitter mit 3.5 und 7 μm Gitterkonstanten) beeinflussten weder die Höhe, noch die Amplitude im Plateaubereich signifikant. Theoretische Analysen der Membranform und Fluktuationen (Kollaboration mit Daniel Schmidt, Universität Stuttgart/Prof. Udo Seifert, Universität Stuttgart/Prof. Ana Smith, Universität Erlangen-Nürnberg) erlaubten eine Bestimmung von Membranspannung ($3.7 \pm 0.7\ \mu J/m^2$) und Steifigkeit des unspezifischen Wechselwirkungspotentials (äquivalent zur zweiten Ableitung am Minimum; $2.3 \pm 0.2 \cdot 10^8\ J/m^4$). Fourieranalysen zeigten, dass sich bevorzugt Moden von 2 μm Wellenlänge ausbildeten. Die Plateauhöhe konnte durch Veränderung der effektiven Membranspannung zwischen 0 und 538 nm verändert werden. Dies wurde durch Veränderung des osmotischen Gradienten zwischen GUV Innen- und Außenseite erzielt. Die entsprechenden Fluktuationsamplituden variierten zwischen 'nicht detektierbar' und einem Maximum von 16 nm.

FluCS erlaubt Fluktuationsmessungen sowohl in großem Abstand, als auch in der Nähe vom Substrat. Messungen der Membranspannung mit FluCS für nicht strukturiert adhärierte Vesikel ergaben in großer Entfernung zum Substrat $0.4 \pm 0.2\ \mu J/m^2$. Vesikel, die nur sehr schwach an strukturierte Substrate adhärierten, wiesen Membranspannungen von $0.5 \pm 0.4\ \mu J/m^2$ auf. Im Vergleich zu RICM Messungen, wo Vesikel vergleichsweise stärker an die Substrate adhärierten, erlaubte FluCS eine Quantifizierung der Adhäsion im Grenzfall von weichen, schwach adhärierenden Vesikeln. Die Steifheit der unspezifischen Wechselwirkung für den Fall freier Vesikel ergab $7 \pm 3 \cdot 10^5\ J/m^4$. Die Analyse des Korrelationsabfalls von FluCS lieferte Informationen zur Dämpfung, die wir als effektive Viskosität mit einem Wert von $1.3 \pm 0.1 \cdot 10^{-3}\ kg/(m \cdot s)$ interpretierten. Dies wurde sowohl für frei als auch adhärierende Vesikel gemessen. In Substratnähe wurde zudem eine höhere Dämpfung detektiert.

Fluktuationen in Membranen von lebenden Zellen (HEK und Makropha-

gen) wurden mit FluCS gemessen. Eine neuartige Liposomen-Fusionsmethode wurde im Institut entwickelt um die Zellmembran mit fluoreszenten Molekülen zu sättigen (entwickelt in unserem Institut von Dr. Agnes Csiszár); dies ist eine entscheidende Voraussetzung für FluCS. Fluktuationsamplituden oberhalb der Auflösungsgrenze konnten detektiert werden. Der Abfall der Korrelation erschien qualitativ anders zu sein, als der, der für Vesikel gemessen wurde und variierte von Zelle zu Zelle. Wir vermuten, dass diese Veränderung von einer aktiven und gerichteten Zellbewegung herrührt. An Verbesserungen von FluCS in Datenakquisition und Verarbeitung, insbesondere mit Hinblick auf die Anwendbarkeit für Nicht-Gleichgewichtssysteme wie Zellen, wird derzeit gearbeitet.

Résumé

La membrane cellulaire, qui non seulement sépare de façon mécanique l'intérieur de la cellule de l'environnement externe, mais est aussi une organelle active impliquée dans de nombreuses fonctions vitales comme l'équilibre de la pression osmotique, l'assistance de l'endo/exo-cytose, la régulation de la forme de la cellule et une médiatrice de l'adhésion cellulaire. La membrane de la cellule est molle et facilement déformable et peut en conséquence être soumise à des déformations actives voire même à des fluctuations thermiques. Le présent travail a pour objet une compréhension quantitative des fluctuations d'une membrane cellulaire-modèle adhérente ou libre.

Le système-modèle ici observé consiste en une vésicule géante unilamellaire (GUV). L'adhésion est réalisée par l'interaction spécifique du ligand-récepteur de la biotine-neutravidine. Des substrats adhérents spécialement structurés sur lesquels sont disposés des récepteurs en forme de lignes ou de grilles ont été mis au point. Deux techniques de microscopie optique ont été utilisées pour examiner la membrane (i) la RICM (reflection interference contrast microcopy) réalisée avec double longueur d'onde (DW-RICM) mesure la distance membrane-substrat avec une précision de quelques nanomètres et jusqu'à une distance de quelques micromètres, avec une résolution temporelle de 50 *ms*. Des progrès significatifs dans l'automatisation et l'affinement de l'analyse des données de la DW-RICM ont été réalisés .(ii) La spectroscopie de fluctuation-corrélation (fluctuation correlation spectroscopy : FluCS), une méthode entièrement nouvelle qui a été mise au point au cours de ce travail de thèse. Basée sur la spectroscopie de corrélation de fluorescence, la FluCS mesure la décroissance de la fonction de corrélation en fluorescence due aux fluctuations de la membrane et non à la diffusion des fluorophores. La FluCS peut mesurer les fluctuations de la membrane avec des résolutions spatiale et temporelle de respectivement 20 *nm* et de 10 *μs*.

Les mesures avec la DW-RICM ont révélé que les GUV sur substrats adhérents structurés présentent des régions de la membrane reliées et fluc-

tuantes en accord avec la structure sous-jacente. Dans la zone de fluctuation la membrane se présente comme un monticule aplati. La hauteur de la membrane au niveau du plateau est égale à 79 ± 9 nm et les amplitudes de fluctuation à 12 ± 2 nm. Une variation de forme (grilles ou lignes) ou de grosseur (grille de 3.5 ou 7 μm) n'a d'influence significative ni sur la hauteur ni sur l'amplitude dans la zone-plateau. Des analyses théoriques sur la forme de la membrane et des fluctuations (collaboration avec Daniel Schmidt, Universität Stuttgart/Prof. Udo Sifert, Universität Stuttgart/ Prof. Ana Smith, Universität Erlangen-Nürnberg) ont permis de déterminer la tension de la membrane (3.7 ± 0.7 J/m^2) et la rigidité du potentiel interactif non spécifique (équivalent à la dérivée double au minimum ; $2.3 \pm 0.2 \cdot 10^8$ J/m^4). Les analyses de Fourier ont montré que se développent de préférence des modes de 2 μm de longueur d'onde. La hauteur du plateau a pu être modifiée de 0 à 538 nm par un changement de la tension effective de la membrane obtenu en modifiant le gradient osmotique entre l'intérieur et l'extérieur de la GUV. Les amplitudes des fluctuations correspondantes varient de "non détectable" à un maximum de 16 nm.

La FluCS permet des mesures de fluctuation aussi bien à grande distance qu'à proximité du substrat. Les mesures de tension de la membrane à grande distance sur des substrats adhérents non structurés varient entre 0.4 ± 0.2 $\mu J/m^2$. Des vésicules adhérant très faiblement au substrat structuré indiquent des tensions de membrane de 0.5 ± 0.4 $\mu J/m^2$. Comparées aux mesures de RICM dans lesquelles les vésicules adhèrent relativement plus fort au substrat, la FluCS donne une limite de quantification de l'adhésion de vésicules molles et faiblement adhérées. La rigidité de l'interaction non spécifique dans le cas de vésicules libres donne $7 \pm 3 \cdot 10^5$ J/m^4. L'analyse avec la FluCS des décroissances de corrélation donne des informations sur la dissipation visqueuse avec une valeur de $1.3 \pm 0.1 \cdot 10^{-3}$ $kg/(m \cdot s)$. Ceci a été mesuré autant pour des vésicules libres que pour des vésicules adhérées. En outre on a détecté une dissipation plus marquée à proximité du substrat.

Des fluctuations dans les membranes des cellules vivantes (HEK et ma-

crophages) sont mesurées avec la FluCS. Une nouvelle méthode de fusion de liposomes a été mise au point pour rendre la membrane de la cellule saturée avec des molécules fluorescentes (réalisé dans notre institut par Dr. Agnes Csiszár) ; c'est une condition déterminante pour la FluCS. Des fluctuations d'amplitude au-delà de la limite de résolution sont détectées. L'affaiblissement de la corrélation est apparu qualitativement différent de celui mesuré pour les vésicules et varie de cellule à cellule. Nous proposons l'hypothèse que cette modification est due à un mouvement de la cellule actif et directionnel. Nous donnons des pistes pour de futurs développements de la FluCS pour l'acquisition et le traitement de données, en particulier dans le but de son application à des systèmes hors-équilibres comme les cellules.

x

Abstract

The cell membrane not only mechanically separates the interior of the cell from the exterior environment but is also an active organelle involved in a host of functions like maintaining osmotic balance, aiding in endo/exocytosis, regulating cell shape and mediating cell adhesion. The cell membrane is soft and easily deformable and hence may be subject to active deformations or even thermal fluctuations. The present work aims at a quantitative understanding of fluctuations of model cell membranes which are either adhered or free.

The model system consisted of giant unilamellar vesicles (GUVs). Adhesion was effected via specific ligand-receptor interaction of biotin-neutravidin. Special structured adhesive substrates were developed where the receptors were presented in the form of grids or lines. Two light microscopic techniques were employed to probe the membrane (i) Dual-Wavelength Reflection Interference Contrast Microscopy (DW-RICM), which measures membrane-substrate distances with an accuracy of few nanometer and up to a range of one micrometer, with temporal resolution of about 50 ms. Here, significant progress in automating and refining the analysis of DW-RICM data was made. (ii) Fluctuation Correlation Spectroscopy (FluCS), which is an entirely novel method developed during this thesis and measures membrane fluctuations with spatial and temporal resolution of 20 *nm* and 10 *μs*, respectively. It is based on the set up of Fluorescence Correlation Spectroscopy, and like FCS measures the decay of the correlation in fluorescence signal, but in FluCS the decay is due to membrane fluctuations rather than diffusion.

DW-RICM measurements revealed that GUVs on the structured adhesive substrates exhibit regions of bound and fluctuating membrane, in accordance with the underlying pattern. In the fluctuating zone, the membrane presented itself as a flat-topped hill with the membrane-substrate distance saturated in a plateau of 79 ± 9 *nm*. In this plateau, the fluctuation amplitude was found to be 12 ± 2 *nm*. Variation of the shape (grid verses lines) or size (grids of 3.5 or 7 *μm* lattice constant) influenced neither the height

nor the fluctuation amplitude in the plateau. Theoretical analysis (collaboration with Daniel Schmidt, Universität Stuttgart/Prof. Udo Seifert, Universität Stuttgart/Prof. Ana Smith, Universität Erlangen-Nürnberg) of the membrane shape and fluctuations permitted us to infer the membrane tension ($3.7 \pm 0.7 \mu J/m^2$) and the stiffness of the unspecific interaction potential (equivalent to the double derivative at minimum ; $2.3 \pm 0.2 \cdot 10^8 J/m^4$). Fourier analysis revealed that modes of preferentially 2 μm wavelength developed. The plateau height could be tuned from 0 to 538 nm by changing the effective membrane tension via a change in the osmotic gradient between the inside and outside of the GUV. Corresponding fluctuation amplitude ranges from non-detectable to a maximum of 16 nm.

FluCS can probe fluctuation far away as well as near a substrate. Using FluCS, the tension far from the substrate was measured to be 0.4 ± 0.2 $\mu J/m^2$ in non-adhered vesicles, and $0.5 \pm 0.4 \mu J/m^2$ in vesicles very weakly adhering to structured substrates. Compared with RICM measurements, where the vesicles studied adhered relatively more strongly and exhibited higher tension and smaller amplitudes, FluCS allowed for quantification of adhesion in the limit of soft, weakly adhering vesicles. The stiffness of the unspecific interaction potential was measured to be $7 \pm 3 \cdot 10^5 J/m^4$ for the case of free vesicles. Analysis of the decay of correlation with FluCS can also give information about damping which we interpreted as an effective viscosity amounting to $1.3 \pm 0.1 \cdot 10^{-3} kg/(m \cdot s)$ in both free and adhered vesicles. As expected, close to the substrate, damping was even higher.

Fluctuations in membranes of living cells (HEK and macrophages) was probed with FluCS. A novel liposome-fusion method was developed to over-saturate the cell membrane with fluorescent dye molecules (developed in our institute by Dr. Agnes Csiszár) ; a prerequisite for FluCS. Fluctuation amplitudes above the resolution limit were detected. The decay in correlation was found to be different from those measured for vesicles and varied from cell to cell. We believe that this variation arises due to active and directed cell motion. We present some possible future advancement of FluCS including better acquisition and treatment of data in particular for application to out of equilibrium systems like cells.

Contents

Chapter 1

General Introduction

Self-organization of molecules into structures of specific function is an essential prerequisite to life. The lipid bilayer is a prominent example, as living organisms, e.g. eucariotic cells, only exist due to a lipid barrier forming the cellular limit. This plasma membrane allows separates cytoplasm from cell exterior and encloses all cytosolic proteins, ions and metabolites necessary for cellular proliferation [1]. Lipid membranes also surround organelles within the cell, thereby allowing for functional organization through compartmentalization [1].

All biological membranes share the same building blocks, comprising lipid molecules and proteins [2]. However, depending on the particular function, membranes vary in composition. This composition is highly dynamic and subject to molecular exchange and reorganization. For example, molecules of varying size and chemical structure cause different diffusion processes within the membrane, which creates lateral inhomogeneities. Also many of them play an important role in maintaining the metabolism and to generate response. Active and passive response are important in processes of cell communication, cell recognition and finally the formation of higher structures, such as tissue and organs. All of these involve a complex interplay of chemical reactions and physical interactions. The perfection with which cells control and distinguish between the

individual processes is fascinating.

The Plasma Membrane

Among the biological membranes composing the cell, the plasma membrane is of primary interest for the present work. Many of the lipids and proteins therein are glycosilated and form a layer of polysaccharides, called glycocalyx, at the outer cell surface. From the inside, the membrane is often stabilized by an actin rich cytoskeleton. In 1972 Singer and
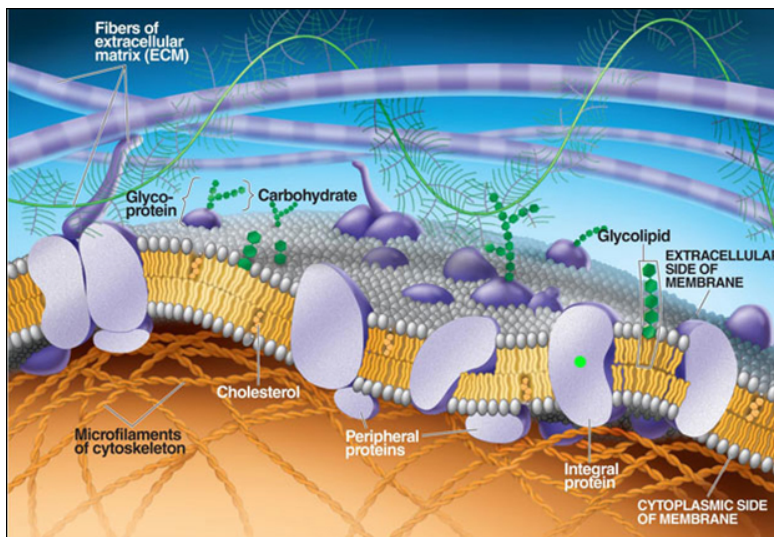
Figure 1.1: Fluid mosaic model of a cell membrane taken from [1].

Nicholson introduced the fluid mosaic model of the plasma membrane (an illustration of the fluid mosaic model is given in figure 1.1). This model describes the lipid bilayer as a two dimensional passive fluid with active molecules embedded therein [3].

However, the current view considers lipids as functional units rather than passive solutes. Lipids have been found to form small clusters of similar composition. Several studies on epithelial cells revealed the existence of these so called nanodomains [4, 5]. Yet, the process of their formation is unclear and actively as well as passively driven processes are believed to contribute. Indication for an influence of the latter was given by ba-

sic research on model systems consisting of ternary lipid mixtures. Here, temperature changes resulted in different lipid conformation and diffusion behaviour which eventually led to complex phase separation [6,7].

Cell Adhesion

In animals, plasma membranes are typically not free but confined by other surrounding membranes, adhere to other membranes and are attached to elastic networks such as the cytoskeleton or the extracellular matrix. Cell adhesion is the decisive factor for the formation of large cellular structures, as it establishes highly specific cell-cell linkages. In fact, adhesion relies on a complex interplay between numerous specific and unspecific forces. Specificity is provided for by topologically and chemically complementary molecules, which are expressed along opposing interfaces and form protein bonds by the so called lock and key principle [8,9]. In addition, initial molecular recognition triggers further selectivity by the formation of bonds at certain molecular sides. As these bonds may result in distinct shape changes which arise upon molecular interaction and enhance fidelity of molecular recognition, the term 'induced fit' introduced [10]. However, other interactions have also high influence on the adhesion process. These interactions are in part the well known classical interactions between pure lipid membranes [11]: The van-der-Waals (vdW) attractive interaction, which acts between dipoles, the hydration repulsion, which arises from water molecules between lipid bilayers, or the Helfrich entropic repulsion, which originate from out of plane fluctuations of the membrane [12]. These, so called generic interactions are an important part in understanding the physics of cell adhesion. For example, from the sensitive interplay of attractive and repulsive interactions, inhomogeneous adhesion areas between cells arise. Domains of weak adhesion, which are poor in receptor ligand pairs coexist with domains rich in adhesion molecules.

Numerous studies demonstrated how physical properties of the cell or the environment, and necessarily any interaction between the two, affect adhesion. E.g. extensive studies over the last decades were undertaken

to understand the implications of mechanical substrate variation on cell adhesion [13, 14]. Other observations focused on the cell glycocalyx and its steric repulsion which is hypothesized to negatively regulate adhesive phenomena [15]. Moreover, it was conjectured that membrane fluctuations counteract adhesion, since the necessary freezing of fluctuations is entropically unfavourable. A remarkable example of a living organism exhibiting pronounced fluctuations are erythrocytes. They feature an extremely soft membrane with an elastic modulus of $\sim 45\, k_B T$ and fluctuation amplitudes of ~ 100 nm [16, 17]. As red blood cells need to adapt to the wide range of capillary sizes in blood vessels, flexibility is in fact an essential property. It has often been conjectured that fluctuation generated forces impede the adhesion of these cells to the vessel surface [18].

Model Membranes

Model systems are a means to study physical properties of the cell membrane within an environment of reduced complexity. The lipid bilayer forming the cell membrane exhibits a variety of unique properties like fluidity, elasticity and fluctuation phenomena, which have been studied comprehensively by means of model systems. These are artificial membranes consisting of only few types of lipid molecules and sometimes proteins. Thus, they feature reduced complexity and high control over properties in comparison to cells. Model membranes commonly used in research consist of either lipid bilayers supported by a solid substrate, freestanding bilayers or closed lipid shells.

The relevant model membranes in this work are solid supported lipid bilayers (SLBs) and lipid vesicles. SLBs are insoluble films consisting of two oppositely arranged lipid sheets deposited on a solid. They feature high stability and are often used to study the nature and packing of lipid molecules. Lipid vesicles are hollow lipid capsules commonly used for studying membrane phase behavior and membrane processes such as membrane fusion, molecular recognition, cell adhesion and membrane trafficking. Therefore, they are produced from the key elements of cellular surfaces : Lipids, which form a closed lipid bilayer, ligand molecules, which

mediate specific adhesion, as well as lipopolymeres, which model the gly-cocalyx and serve as repellant factor. Depending on the particular application, vesicles of different size and lamellarity (the number of bilayers comprising the lipid shell) are produced. Here, one distinguishes between small ($< 0.1\ \mu m$ in diameter), large (up to $\sim 1\ \mu m$ in diameter) and giant ($10 - 100\ \mu m$ in diameter) vesicles.

Equilibrium shape and thermal fluctuations of giant unilamellar vesicles (GUVs) have been addressed in theory and experiment for various model systems [19–21]. In addition, numerous mechanical properties of free and homogeneously adhered membranes, such as membrane tension, bending rigidity and fluctuation, bilayer compressibility and intermonolayer friction, as well as lipid mobility and adhesion strength, have been derived [22–27]. For example, the importance of membrane fluctuations in the context of adhesion was highlighted with the result that model membranes under tension adhere to each other due to the suppression of the fluctuation induced force [28]. Investigations on adhesion dynamics also gave insight into molecular mobility changes during adhesion [29, 30]. And finally, discrete tethering of membranes to a substrate was subject to several theoretical studies [31, 32]. However, experiments and theories were often restricted to scenarios with homogeneously constituted substrates and free molecular diffusion in one or both adhesion interfaces. The role of membrane fluctuations and their modifications upon adhesion to a substrate and, in particular, to an inhomogeneous receptor distributions is yet barely understood. Here, some aspects have been considered in theory, while experimental confirmation is still missing. Moreover, while static membrane properties were subject to many studies, the understanding of the dynamics of membrane fluctuations such as hydrodynamic damping has not reached the same stage.

Thesis Outline

This thesis reports results on the influence of different adhesion conditions on membrane shape and fluctuations. Artificial test cells in the form of giant unilamellar vesicles (GUVs) served as models, where not only the

composition, but also the membrane tension was changed. The GUVs either simply sedimented on a substrate or adhered to selectively functionalized substrates. While the first system allowed to study mere effects of the substrate vicinity the latter mimicked adhesion to a surface with inhomogeneous receptor distribution. Precisely, for adhesion studies, highly controllable pattern of receptors were transferred to a substrate, which functioned as immobilized and spatially limited binding sites. Ligands in the vesicle membrane were free to diffuse until binding. The adhered equilibrium state was then characterized. Membrane components were kept constant[1] and the adhesion geometry was altered systematically. Moreover, osmotic pressure changes generated vesicles exhibiting strong and weak fluctuations. These were quantified near the substrate and a new method was developed which allowed for their quantification also far away from the substrate. In contrast to living cells all processes monitored here occurred without any active regulation, so that explicitly the physical laws governing structured adhesion could be studied.

Advanced light microscopic techniques were used to image membrane adhesion to patterned sites as well as to systematically quantify adhesion relevant membrane properties. More precisely, analysis of adhesion structures relied on microinterferometric recordings, as this versatile technique allowed to measure vertical distances close to the substrate with high precision. From upgrading the standard set-up and considering an advanced theoretical relation an unambiguous height determination was obtained. Dynamics of lipids near as well as far away from the substrate were comparatively studied by fluorescence microscopy techniques, fluorescence recovery after photobleaching (FRAP) and fluorescence correlation spectroscopy (FCS). Finally, the development of a novel variant of FCS allowed to quantify membrane fluctuations and properties at different vesicle positions.

Following this approach, understanding of the influence of receptor pattern on membrane properties and adhesion structures were obtained. In

---

[1]Sometimes a fluorescent molecule had to be added to the usual membrane composition, as for some microscopy techniques a fluorescent tracer molecule was needed.

addition, new perception of membrane - substrate interaction arose from subsequent recordings of membrane fluctuations near as well as far away from a substrate.

Finally, the FCS variant was used to measure membrane fluctuations of living cells. This verified the applicability of the method to measure fluctuations of different nature than model membrane fluctuations.

Chapter 2

Materials and Methods

In this chapter, an overview of the materials and methods employed for model system preparation, imaging as well as analysis is given. The model system used in this study, its components and preparation are described in detail. In the imaging section first the microscope equipment is described and second a brief overview of standard microscopy techniques is given. Finally, the two main techniques used for model system analysis, Fluorescence Correlation Spectroscopy and Reflection Interference Contrast Microscopy, are outlined in more detail including specialized applications for membrane topography reconstruction or diffusion constant determination. Advantages and disadvantages of each technique are discussed.

2.1   Materials

2.1.1   Buffers and Solutions

Phosphate buffered saline (PBS) served as standard buffer for all vesicle experiments and was prepared from 140 mM NaCl (Sigma, Saint Louis, MO, USA), 3 mM KCl (Sigma), 10 mM Na$_2$HPO$_4$ (Merck KGaA, Darmstadt, Germany) and 2 mM KH$_2$PO$_4$ (Merck) in ultrapure water, provided for by a water purification system (Millipore, San Francisco, CA, USA). The pH was adjusted to 7.2 . The osmolarity was checked with an osmometer (Osmomat 030, Gonotec GmbH, Berlin, Germany) prior to each

experiment and set to 300 $mOsm/l$, if not stated otherwise. PBS was kept at 4 °C and renewed every month.

For vesicle preparation 0.7 g of sucrose (Sigma) was dissolved in ultrapure water and the osmolarity adjusted to 230 $mOsm/l$ with an osmometer. Sucrose solution was stored at -20 °C and thawed to room temperature prior to each experiment.

2.1.2   Lipids

Figure 2.1 shows structural formulas of all lipids forming the model membranes. Lipids A-D, dissolved in chloroform, were purchased from Avanti Polar Lipids (Alabaster, AL, USA) and used without further purification. Lipids E-F were purchased from Invitrogen (Eugene, OR, USA) as lyophilized powder and dissolved in chloroform (Merck KGaA).

All lipid stock solutions were stored in glass containers at -20 °C and renewed at least every 6 months.

2.1.3   Proteins

Bovine serum albumin (BSA) was purchased as lyophilized powder (Sigma), kept at 4 °C and dissolved in ultrapure water shortly before usage. Biotinylated bovine serum albumin (BSA-biotin) was purchased from the same source and treated identically.

Neutravidin (NAV) as well as its fluorescent conjugate neutravidin- tetramethylrhodamine (NAV-TMR) were purchased from Invitrogen and reconstituted in PBS. Due to its tendency to form protein aggregates, NAV and NAV-TMR solutions were ultracentrifugated at 137000 g at 4 °C for 1.5 hours. After centrifugations NAV solutions were stored in plastic containers at -20 °C no longer than 6 months and thawed as required.

The concentration of all protein solutions was checked with an UV-Vis spectrophotometer (NanoDrop 1000, Thermo Fisher Scientific, MA, USA).
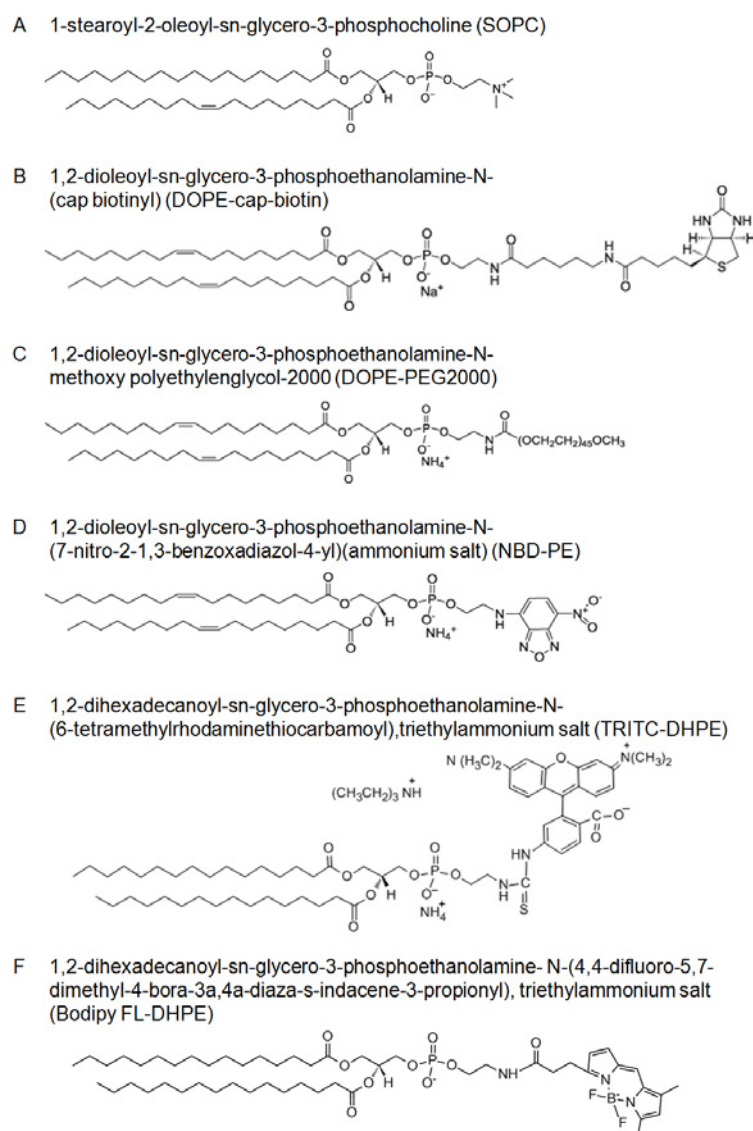
Figure 2.1: Structural formulas of lipids. Structural formulas E-F courtesy of A. Csiszár.

2.1.4   Fluorescent Material for FCS Validation

Fluorophores tetramethylrhodamine-5-(and-6)-isothiocyanate (TRITC), Alexa Fluor 488 (all: Invitrogen), Atto 488 and 550 (all: Atto-Tec, Siegen, Germany) were dissolved in PBS buffer to $10^{-8} - 10^{-6}$ M concentrations. These were tested for their photophysical suitability for FCS and were

used for several calibration purposes (see section A).

Fluorescently labeled antibodies Anti-Rabbit IgG - Alexa 488 (Invitrogen) and anti-mouse IgG - Atto 488, 550 and 633 (all: Sigma, Saint Louis, MO, USA) were treated identically. They were also tested for their photophysical properties (see A).

Multicolor fluorescent microspheres of 0.175 ± 0.005 μm size (PS-Speck Microscope Point Source Kit, Invitrogen, Eugene, OR, USA) served as subresolution objects for calibration of the point spread function.

2.1.5 Substrates and Observation Chamber

Silicon wafers with different pattern (kindly provided by Nico Hampe, ICS-7, Research Centre Jülich) and object slides (Menzel GmbH & Co. KG, Braunschweig, Germany) both silanized with trichloro(1H,1H,2H,2H-perfluorooctyl)silane (Sigma) were used for stamp fabrication. Stamps consisted of polyolefin plastomer (POP, kindly provided by Dr. Dirk Mayer, PGI-8/ICS-8, Research Centre Jülich) cut into pieces of $0.2 \times 1 \times 1$ cm^3 and were purged with 2-propanol and ultra-pure water. Polydimethylsiloxane (PDMS) produced from a mixture of base and curing agent (SYLGARD184, Dow Corning Co., MI, USA) in a 10:1 w/w ratio served as 'inkpad'.

The observation chamber (shown in figure 2.2) consisted of two steel
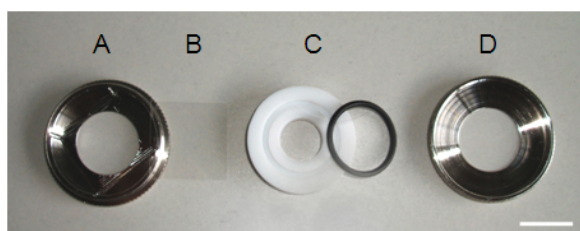
Figure 2.2: Components of the observation chamber. A: Lower metal ring with indentation for a coverslip, B: Thickness corrected coverslip, C: Teflon inset with perbunan o-rings, D: Upper metal ring. Scale bar: 2 *cm*.

rings, which were screwed together, a teflon inset with perbunan o-rings

to prevent water leakage and a coverslip [33]. The choice of teflon as working materials is most suitable in the present studies, as it is neither wetted by water nor by alkanes. A disturbing influence on measurements was therefore excluded. Thickness corrected glass coverslips (170 $\pm$ 10 μm thick, 24$\times$24 mm^2 area) were purchased from Assistent (Karl Hecht KG, Sondheim, Germany). A scale bar with 100 $\frac{lines}{mm}$ (Carl Zeiss MicroImaging GmbH, Göttingen, Germany) was used to calibrate the image pixel size. A chrome pattern on an electron beam mask of 2 μm lattice constant and dots of 0.5 μm diameter (kindly provided by Dr. van der Hart PGI-8/ICS-8, Research Centre Jülich) was employed to calculate the shift between two simultaneously recorded images.

2.2 Model Membranes and Substrates

Figure 2.3: Amphiphilic molecules self-assemble spontaneously to giant unilamellar vesicles.

Phospholipid molecules are the major components of biological membranes [2]. Each lipid consists of two apolar hydrocarbon chains and a head group containing one negatively charged phosphate group and possibly other polar groups. From this charge difference their amphiphilic character arises which drives the formation of supramolecular structures such as micelles or lipid bilayers when suspended in water or oil [34]. At sufficient hydration, structures of closed lipid shells arise and energetically unfavourable hydrophobic edges are shielded from the water interface, as depicted in figure 2.3. These so called vesicles are dominated in shape and dynamics by their elastic properties, which is perspicuous

13

considering that the vesicle diameter/width ratio is $\sim 10^4$ and bending rigidities are as low as several $k_B T$. These elastic properties are also the reason why free vesicles adopt macroscopic shapes of minimal bending energy and exhibit strong thermal fluctuations of up to several 100 nm in amplitude.

In the following, two preparation techniques are presented to generate the bilayer objects used in this work. Moreover, the fabrication of substrates particularly suitable for membrane fluctuation analysis is described and all components of the model system are introduced.

2.2.1 Model Membrane Preparation

2.2.1.1 Giant Unilamellar Vesicles (GUVs): Electroswelling Technique

Vesicles are popular biomimetic model systems, due to their numerous applications, their simple preparation as well as their limited and well defined number of constituents. For example, the properties of lipid molecules with their effect on microscopic as well as macroscopic scales have been studied extensively with vesicles [35], [24]. The phase behaviour of ternary lipid mixtures [36] or the individual function of polymers and proteins within the membrane are also interesting fields of research on their own [37], [38]. Finally, vesicles have become suitable model systems for cells and are of high interest in pharmacology for the use as drug delivery liposomes [39]. Several procedures exist to produce vesicles of preferred lamellarity and size. Depending on the desired vesicle type, a production procedure such as electroformation [40], extrusion [41], microfluidic jetting [42] or rehydration [43] is chosen.

In this thesis, giant unilamellar vesicles (GUVs) were studied, as their size of several μm and their single outer membrane are particularly suitable for light microscopic observations and quantitative studies. They served as biomimetic models for cells adhering to patterned receptor sites and were used as well-defined test objects to prove a measurement principle for thermal fluctuation analysis.

14

GUVs with an average diameter of 40 μm were produced via the elec-
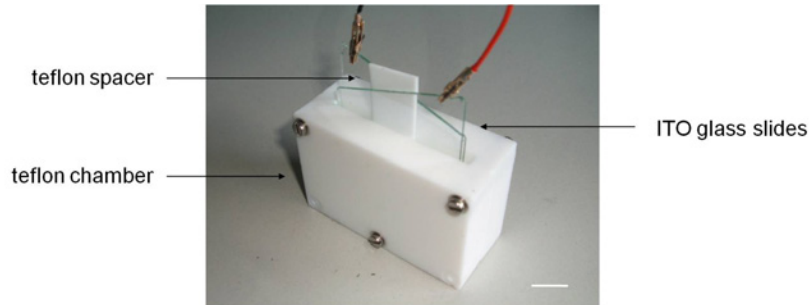
Figure 2.4: Electroswelling chamber and main components for GUV preparation. Scale bar: 1 cm.

troswelling technique [40]. 20 μl of a 2 mg/ml lipid mixture dissolved in chloroform were deposited on indium tin oxide (ITO) coated glass slides (4×4×0.5 cm^3, pgo, Iserlohn, Germany) by means of a Hamilton syringe (Hamilton Co., Bonaduz, Switzerland). Glass slides were put in vacuum over night, in order to ensure complete chloroform evaporation. Afterwards slides were transferred to a teflon chamber filled with 230 $mOsm/l$ sucrose solution. An AC voltage of ∼1.7 V at 10 Hz was applied to the slides, which were separated by a teflon spacer (width = 1 mm). Figure 2.4 shows the chamber and its main components. This way, a large number of unilamellar vesicles formed after 1.5 h. Vesicles were kept at 4 °C, but used no longer than two days.

For the experiment approximately 20 μl of vesicle solution was added to the observation chamber filled with 1 ml PBS of ≥250 $mOsm/l$. The osmotic gradient between vesicle in- and exterior led to hyperosmotic conditions resulting in water flux out of the vesicle. Consequently, vesicles became floppy i.e. they exhibited a large excess area, a property that had been shown to facilitate adhesion of vesicles as well as cells [44], [45]. Subsequently, the chamber was covered with a glass slide and vesicles were given at least 30 min to equilibrate before imaging. All preparation and measurements were conducted at room temperature.

Teflon swelling chamber, ITO glass slides and teflon spacer were cleaned

15

with the following detergent treatment: All material was put in 2 % Hellmanex solution (Hellma, Müllheim, Germany) and ultrasonicated for 15 min. After flushing thoroughly with ultrapure water another two cycles (2×15 min.) of ultrasonicating the material in water and flushing with ultrapure water followed.

2.2.1.2 Solid Supported Lipid Bilayers (SLBs): Langmuir-Blodgett Langmuir-Schäfer Technique

Solid supported lipid bilayers (SLBs) are another important model system, as they are of well-defined planar geometry and highly controllable lipid composition. In the past this model system already allowed for determination of lipid and bilayer properties (size, bending rigidity, intermolecular friction) [46], [27], studies on lipid phase transition [47] and gave insight into the prerequisites of lipid raft formation [48]. One technique for SLB preparation is vesicle fusion [49]. Here, small vesicles ($\sim \mu m$) are produced according to one of the formerly mentioned techniques (see section 2.2.1.1) and exposed to a hydrophilic glass slide. As vesicles burst upon contact with the glass, they form a bilayer of identical lipid composition in each leaflet.

In this thesis, SLBs were employed to study diffusion and to calibrate the confocal volume size (see sectionA). For their preparation a different technique, the Langmuir-Blodgett Langmuir-Schäfer Technique [50], was applied. In comparison to vesicle fusion, this technique has the advantage of producing a bilayer of higher homogeneity and less defects. Also it allows for the production of asymmetric SLBs as described in the following.

 SLBs were prepared in a two steps process whereby in each step a lipid monolayer was produced using a film balance (Nima, Coventry, UK). The film balance consists of a teflon trough filled with ultra-pure water, a teflon barrier, a pressure sensor and a motorized dipper element (see figure 2.5). In the first step a cleaned glass substrate was hold and positioned under water with the motorized dipper. Subsequently, a drop of lipid mix dissolved in chloroform was spread on the water surface and it was waited

16
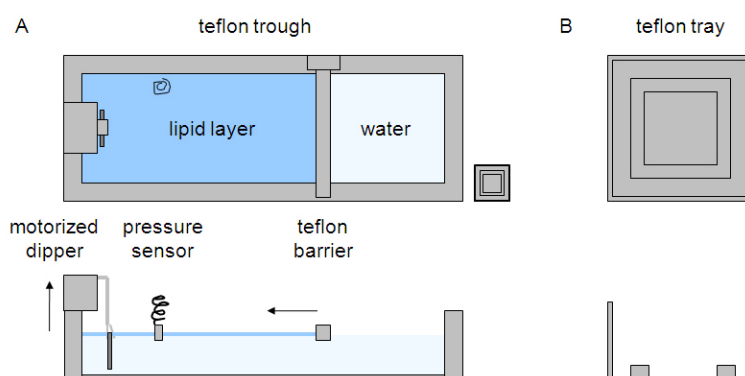
Figure 2.5: Top (upper row) and side view (lower row) of film balance and teflon tray. A: Main components of the film balance are sketched. A small teflon tray is shown to indicate correct proportions. B: The teflon tray contains a frame onto which the substrate is pressed during the second fabrication step.
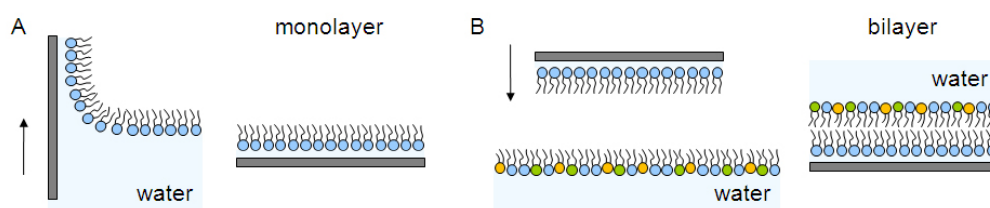
Figure 2.6: Langmuir-Blodgett Langmuir-Schäfer Technique. A: Lipid monolayer adsorbs to a hydrophilic glass substrate drawn out of the water. A thin water film remains at the glass-lipid interface. B: Monolayer coated substrate is pressed through a second monolayer. The assembled bilayer is kept under water. Modified sketch courtesy taken from [33].

for complete chloroform evaporation. Thereby lipids oriented at the air-water interface according to their amphiphilic nature. The teflon barrier was moved 50 mm/min to compress the lipid monolayer up to 25 mN/m, a surface pressure, chosen to ensure lipid mobility. As the substrate was drawn out of the water in perpendicular direction to the water surface and at a speed of 10 mm/min, the lipid monolayer adsorbed to the substrate (see figure 2.6). During this process the teflon barrier posi-

tion was adjusted as to maintain constant surface pressure over the whole substrate area. Between glass and monolayer a film of ~1 *nm* water remained [51], [27], which was necessary to ensure unconstrained diffusion of lipids within the bilayer formed thereafter. The monolayer coated substrate was stored in a teflon holder in an air environment until deposition of the second layer. Subsequently, the teflon trough of the film balance was cleaned by $10\times$ exchange of ultra-pure water and a teflon tray of a size just larger than the substrate was put under water (see figure 2.5). This tray was used for later transfer of the completed substrate from the trough to the observation chamber while keeping it under water. Any contact with air would lead to a destruction of the bilayer configuration. As before, a lipid mixture was spread on the water interface and the surface pressure was adjusted. The monolayer coated substrate was then pressed through the lipid-water interface thereby transferring the second monolayer. The teflon tray below the lipid-water interface features a square frame inset onto which the substrate was pressed to ensure minimal bilayer damage. Care was then taken to transfer the coated side of the substrate to the observation chamber, preventing any contact with air. The chamber was assembled under water and its filling volume exchanged for PBS buffer. SLBs were immediately used for experiments.

2.2.2 Substrate Preparation

2.2.2.1 Patterned Substrates

Micropatterned substrates are powerful tools to investigate mechanisms of adhesion and structure formation. High control over pattern size and shape already led to several studies on cell interaction, morphology and function [52]. Yet, substrates of controlled nm spacing evolved just within the last decade wherefore there is high potential for further application. Patterned substrates were mainly used to investigate the adhered vesicle lower site, i.e. the adhesion state, fluctuations within patterns or diffusivity of lipids. Patterned substrates were fabricated applying a soft lithographic technique called microcontact printing. The details of the tech-
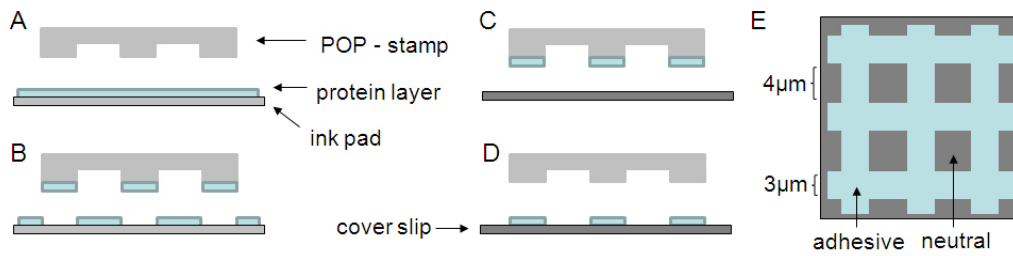
Figure 2.7: Microcontact printing technique. A: POP-stamp is pressed on an adsorbed protein layer. B-D: POP-stamp is lifted and the coated stamp side pressed to a coverslip with alike settings. E: The transferred protein layer marks posterior adhesive sites, while intermediate regions remain neutral with respect to adhesion. Patterns of 3 μm wide adhesive areas and $4\times4\ \mu m^2$ neutral squares were used most often.

nique can be found in [53]. Briefly, stamps consisting of POP (see section 2.1.5), were produced via hot embossing a desired structure from a silicon wafer into the plastomer. In addition, a layer from a mixture of silicone rubber and curing agent was spincoated on cleaned coverslips. This layer was cured at 150 °C for 1 h to form PDMS (see section 2.1.5 for mixing ratios). After cooling, it was incubated with a 0.1 mg/ml BSA-Biotin and BSA (1:1 ratio) solution in water over night to produce an 'inkpad' of adsorbed protein for microcontact printing. Inkpads were gently flushed with ultrapure water to remove surplus protein and dried with argon (gas purity 99.9995%). The POP stamp was pressed on the dried protein layer for 7 min using a Fineplacer (Finetech, Berlin, Germany) with a contact pressure of 5 $\times10^4$ Pa. The stamp was lifted manually from the inkpad and pressed on a cleaned coverslip using the same settings. This way, a grid or line structure of protein and ligands was transferred on the glass. Figure 2.7 summarizes the decisive steps of this technique.

For the experiment, microcontact printed coverslips were transferred to the measuring chamber, which was then filled with PBS and the following functionalization steps were employed: The space on the substrate free of protein was passivated once with 5 mg/ml BSA in buffer for 15 min. Sub-

sequently 0.1 mg/ml NAV-TMR in PBS buffer was incubated for 30 min to ensure complete binding to biotin ligands on the substrate. Finally, the BSA passivation step was repeated once more. In between each step, the chamber was washed $10\times$ with PBS to remove excess protein. In the following, PBS served as outer medium for the vesicle adhesion experiment. For this work three different pattern were investigated. The first pattern, henceforth referred to as small grid structure, exhibited a lattice constant of 3.5 μm, with squares 2×2 μm^2 in size and a grid of 1.5 μm width. The second pattern, henceforth called large grid structure, was of double size and used most often. Its pattern of 4×4 μm^2 squares and 3 μm wide grid is depicted in figure 2.7. The third pattern was a line pattern of lattice constant 6 μm, with 2.5 μm neutral and 3.5 μm wide adhesive areas. This is henceforth called line structure.

2.2.2.2 Homogeneous Substrates

Homogeneous substrates were prepared placing a cleaned coverslip in the measuring chamber and incubating it with a 1 mg/ml BSA solution in PBS buffer. After 15 min. the chamber was washed $10\times$ with PBS to remove excess protein and used immediately.

These substrates were used to investigate the vesicle top site, i.e. free membrane fluctuations and diffusivity of lipids.

2.2.3   The Model System

Most sampled studied in this thesis were GUVs adhered to patterned receptor sites. This structured adhesion served on the one hand as model system for cell adhesion to a limited number of receptors and on the other hand, it allowed for an in depth analysis of membrane fluctuations near a substrate. The adhesion to distinct sites on the substrate was realized by controlled positioning of receptors via microcontact printing. The specific interaction of a receptor-ligand complex mediated the adhesion. This way, effects of the presence of the substrate as well as effects of distinct receptor distribution on membrane properties were studied. Figure 2.8 shows a
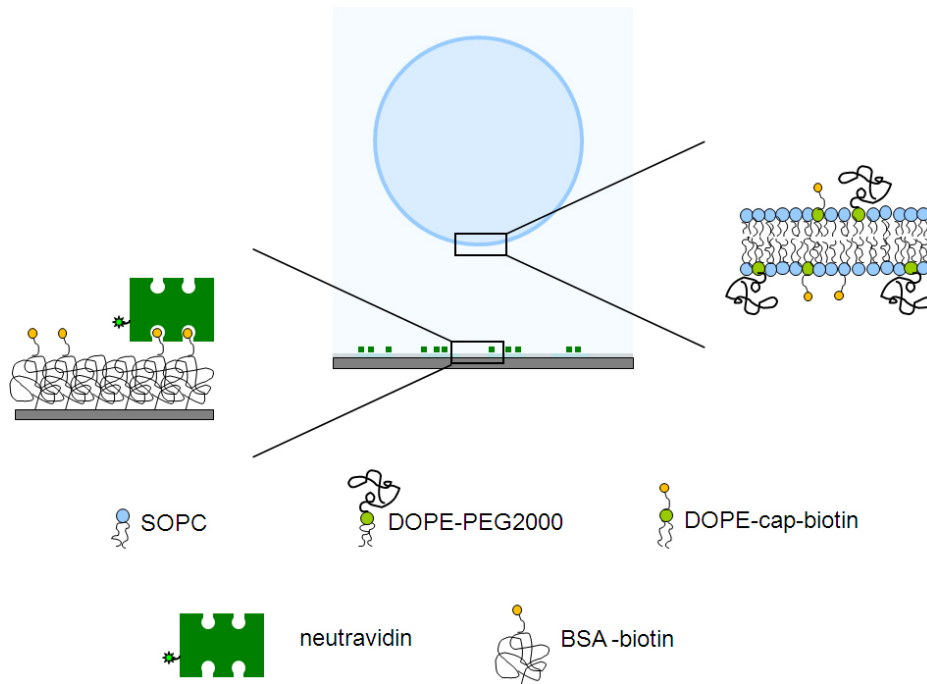
Figure 2.8: Sketch of the model system used most often in this study. GUVs consisted of phospholipids SOPC and DOPE (see text for details). DOPE lipids had either a polyethylene glycol polymer or biotin attached to their head group. A sucrose solution within the vesicle and PBS buffer outside of the vesicle provided the density gradient for vesicle sedimentation. The glass substrate was functionalized with proteins neutravidin and BSA as well as biotin coupled BSA.

sketch of the model system and components used mostly in this study. For optimal results, as it was developed during my diploma thesis [53], [54], the model system was designed as follows:

GUVs consisted mainly of the matrix lipid SOPC (see section 2.1.2). This uncharged phospholipid is particularly suitable when unspecific interaction needs to be avoided. Moreover, it exhibits a low phase transition temperature of $6.5\,°C$ [35] allowing for measurements in the fluid-crystalline phase at room temperature.

Incorporation of 2 mol%[1] PEG-DOPE was advantageous for two reasons. First of all, it ensured suppression of unspecific interaction during adhesion, as GUVs without PEG were prone to stick to the substrate [55]. With a PEG polymer chain covalently attached to the ethanolamine group of DOPE, the steric repulsion ensured sufficient space between membrane and substrate to prevent this effect. Second, PEG lipids are often used to mimic the glycocalix of real cells, where polysaccharides are linked to glycoproteins or glycolipids in the cell plasma membrane [1]. A size of the hydrated polymer chain was estimated from de Gennes' theory [56], who proposed a mushroom like configuration for polymers at low grafting densities. For this case, the thickness of the polymer layer is estimated from the Flory radius $R_F = \alpha N^{3/5}$ [57], where α is the length of the size of the monomer and N the number of entities. For a PEG chains of 2 kDa molecular weight N corresponds to the number of ethylene oxide repeats, 45 in this case. Hence, with a monomer size of $\alpha = 3.5$ Å [57] the PEG layer exhibits a thickness of 34.4 Å.

The biotinylated lipid DOPE-cap-biotin was necessary to mediate the specific adhesion between membrane and substrate. Here, biotin served as ligand while NAV served as receptor. Binding to NAV was facilitated by a short linker ($HOOC - (CH_2)_5 - NH_2$) between biotin and lipid [58], which ensured higher mobility, as shown for a similar linker structure [59].

Specific adhesion was realized by the interaction of biotin and neutravidin (NAV). The complex formed by their interaction is already well studied, particularly due to its numerous applications in diagnostics [60]. This knowledge is advantageous for the present studies.

NAV is a tetramer of size $56 \times 50 \times 40$ Å^3 which exhibits two binding pockets for biotin in a distance of 20 Å on each side [61]. It is a functional analogue of avidin and produced from avidin via chemical removal of the carbohydrate. While functional motifs are conserved in this process [62], the molecular weight changes from 67 to 60 kDa and its isoelectric point is reduced to 6.3. This effect makes NAV very suitable for biomembrane adhesion studies as it is almost uncharged at neutral pH and so unspecific

---

[1] All given percentages are molar fractions and refer to the number of matrix lipids.

interactions are reduced.

Biotin, also called vitamin H or B_7, binds in its natural state to one of the NAV pockets via ten hydrogen bonds and a superimposed hydrophobic effect [63]. Together, these interactions amount to a dissociation constant of 10^{-15} *M*, which marks the strongest specific interaction known [63]. However, due to the coupling of biotin to DOPE or BSA, it is speculative whether all ten bonds establish or whether only six interactions at the upper biotin ring (see structure formula 2.1.2) play a role. However, long time measurements (≥ 3 h), which were undertaken during my diploma thesis, showed that vesicle adhesion states were unchanged after the vesicle reached its equilibrium state. For the purpose of this work, biotin - NAV binding is considered irreversible. Moreover, biotin has a molecular size of 30 Å and so is comparable to the PEG size. This is advantageous, as the presence of PEG molecules led to some retardation in the adhesion process and thus gave the system more time to equilibrate. Conversely, biotin is just large enough such that a major hindrance of adhesion by the polymer can be excluded.

Substrates were fabricated and functionalized as described in 2.2.2.1.

2.2.4   Variants of the Model System

The lipid mix introduced in section 2.2.3 was sometimes extended by a fluorophore coupled lipid in order to monitor diffusion or fluctuation processes with FRAP or FCS.

For quantification of the fluidity of GUVs with FRAP, 2 mol% of NBD fluorescent labeled lipids were incorporated in the vesicle membrane. For quantification of fluidity and fluctuation processes of GUVs with FCS, TRITC - DHPE was incorporated in concentrations between 0.001 mol% and 1 mol%. In one case also Bodipy Fl DHPE in 1 mol% concentration was used. There is advice against the application of higher TRITC concentrations as rhodamine-to-rhodamine interactions results in self-quenching of fluorescence [64].

In all cases the fluorescent label was located at the hydrophilic head group

(see structure formulas in section 2.1.2).

2.3 Microoptical Measurements

Vesicles were investigated by means of light microscopic techniques. These are the most suitable tools for characterization of these objects, as first of all their size of typically some 40 μm is imaged with high precision. Second, in-vitro observation in an aqueous environment and under well defined experimental conditions is possible. Finally, the diversity of light properties such as wavelength, amplitude, phase or polarization can be utilized in several ways to image specific properties of the object.

In the following, techniques are presented, which were used to measure size, diffusion and fluctuation properties.

2.3.1 Microscope Set-up

Images were acquired either with an inverted microscope (Axiovert 200, Carl Zeiss) or a confocal laser scanning microscope (LSM 710, Carl Zeiss). In the former, depending on the application a metal halide lamp (X-Cite, Exfo, Quebec, Canada) or a halogen lamp (HAL 100 W, Osram GmbH, Munich, Germany) served as light source. While light of the metal halide lamp was coupled into the microscopic light path via fibre optics and used in epi-illumination mode, light from the halogen lamp was used in transmission mode. The microscope was equipped with two objectives. Either the 63× EC Plan-Neofluar Antiflex oil immersion objective with a numerical aperture (NA) of 1.25 was used or the 40× Plan-Apochromat oil immersion objective of NA 1.40 (both: Carl Zeiss). Unless stated otherwise, two images at two different illumination wavelengths were acquired. Therefore, the microscope was equipped with a mounting device to which two identical CCD cameras (sensicam qe, PCO, Kehlheim, Germany). For simultaneous acquisition of both images the CCD cameras worked in hardware trigger mode and were controlled by the software OpenBox (version 1.77, Informationssysteme Schilling, Munich, Germany).

The confocal laser scanning microscope (CLSM) consisted of a motorized inverted microscope base (Axio Observer Z.1, Carl Zeiss) and was equipped with a 25 mW argon-ion (Ar^+), a 1.2 mW helium-neon (HeNe) laser and a 5 mW HeNe laser, providing the excitation lines $\lambda = 458/488/514$ nm, 543 nm and 633 nm, respectively. Selection and attenuation of a specific laser line was achieved through an acousto-optic tunable filter (AOTF) which allowed intensity reduction by a factor 10^4. For minimal chromatic abberation in the visible range, a C-Apochromat $40\times$ water immersion objective of NA 1.2 (Zeiss) was used. Images were detected with photomultiplier tubes, while two avalanche photodiodes (APDs, Perkin Elmer, Waltham, MA, USA) served as single-photon count detectors for correlation analysis (see section 2.3.3). Image and data acquisition were controlled by the software ZEN (version 2008, Carl Zeiss).

Specifications on image and data acquisitions, e.g. filters, pixel resolution and recording times, are given separately for each technique (see e.g. 2.3.3.4 and 2.3.4.6).

2.3.2 Standard Microscopy Techniques

2.3.2.1 Phase Contrast Microscopy

Phase contrast microscopy was developed in the 1930s by the Dutch physicist Frits Zernike who was awarded the Nobel Prize in 1953 for this invention [65]. This technique exploits phase shifts the illumination light encounters upon interaction with objects of different refractive index.

In general, as light interacts with a medium, rays get diffracted according to the medium' s properties and result in a damped amplitude as well as a shifted phase. Thin biological membranes, however, absorb only a small amount of light such that mere amplitude changes which are imaged with simple bright field microscopy would not yield enough contrast [66]. Since neither the eye nor a camera can discern phase differences, a mechanism for transforming phase changes into amplitude changes had to be found.

In phase contrast microcopy, this is realized via an annular aperture and a phase plate, which are placed in the light path at the back focal planes
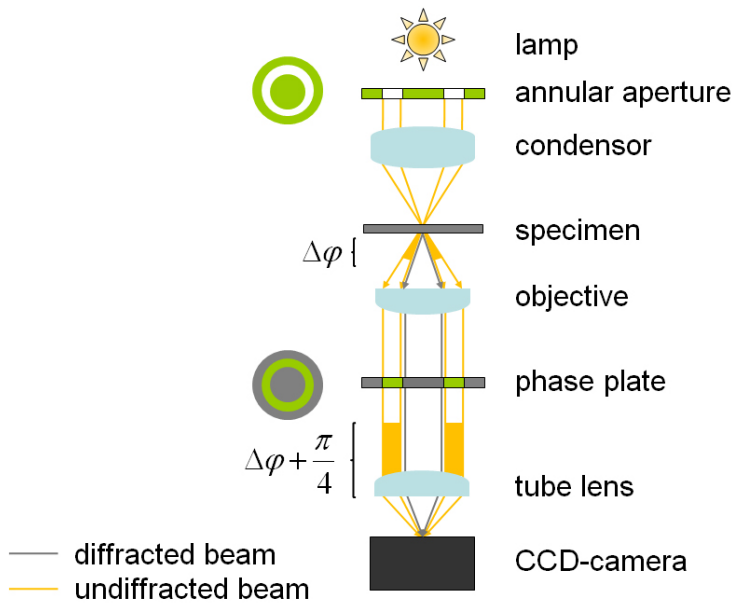
Figure 2.9: Light path in a phase contrast microscope. A small amount of light interacts with the specimen and is phase shifted by $\Delta\phi$. The phase plate causes further phase shift of the diffracted light by $\frac{\pi}{4}$. The mainly undiffracted light passes the plate only in a circular region and is therefore damped in its amplitude. Both ray types interfere depending on the total phase difference and yield a positive or negative contrast image. Sketch taken from [53].

of condensor and objective, respectively (see figure 2.9). Light emerging from a lamp passes the annular aperture resulting in a ring of light which is focused on the specimen by the condensor. There small amount of light interacts with the object and gets diffracted. This fraction encounters a phase shift $\Delta\phi$ while most of the light passes the specimen without interacting. The phase plate positioned behind the objective has two important features: On one hand the intense non-diffracted light can pass the plate only in a defined circular region where intensities are strongly reduced. On the other hand, the phase of the diffracted light gets shifted by a factor $\pi/4$ with respect to the non-diffracted light. In the following, constructive or destructive interference occurs depending on the total phase shift

$\phi = \Delta\phi + \pi/4$ between the diffracted and non-diffracted light and causes a positive or negative contrast in the image.

Besides the advantage of being able to image transparent objects without additional labeling, phase contrast microscopy generates high contrast without the need to change the illumination aperture.

In this work, phase contrast microscopy was used to visualize the strength of membrane fluctuations, to check for unwanted budding effects as well as to measure vesicle radii.

2.3.2.2 Introduction to Fluorescence
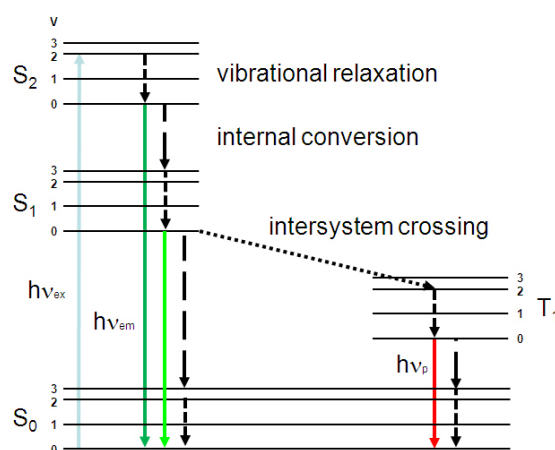
Figure 2.10: Jablonski diagram illustrating the processes involved in fluorophore excitation [67]. Full lines: Transitions between electronic energy level via absorption or creation of a photon. Dashed lines: Non-radiative transitions such as vibrational relaxation or internal conversion. Dotted line: Singlet-tripled intersystem crossing. S_i: Electronic singlet state, T_i: Electronic triplet state, $h\nu_{ex}$: Fluorophore absorption, $h\nu_{em}$: Fluorescence emission, $h\nu_p$: Phosphorescence emission.

Fluorescence is the result of a three-stage process which occurs in certain photoactive molecules called fluorophores or fluorochromes. In the first stage, a suitable quantum of light energy $h\nu_{ex}$ is absorbed by the fluorophore exciting the molecule from the state of lowest electronic en-

ergy, i.e. the singlet state S_0, to a higher vibrational level of an excited electronic singlet state S_i, $i \in \mathbb{N}_{>0}$(see figure 2.10). The higher vibronic states are unstable and occupied only for a few picoseconds before the fluorophore relaxes to the lowest sub-state of a singlet state S_i. In this second stage, energy is dissipated through the non-radiative processes of vibrational relaxation and internal conversion. As vibrational relaxation occurs only within the sub-state of one an electronic state, internal conversion describes the transition between neighbouring electronic states. The final stage marks the transition of the fluorophore to the lowest electronic energy level. This occurs by one of the following competing pathways: Depending on the quantum efficiency of the excited state a photon of energy $h\nu_{em}$, corresponding to the energy gap between the lowest vibrational state of S_1 and one of the vibrational states of S_0, is emitted. This process is called fluorescence and occurs within nanoseconds after excitation. In addition, energy may be dissipated again via internal conversion. Also, another radiationless relaxation process is possible, called intersystem crossing. In contrast to the formerly mentioned transitions between energy states S_i of the same spin, intersystem crossing to the first tripled state T_1 reverses the spin of the electron and therefore occurs rarely. Further relaxation from T_1 via non-radiative processes or emission of a photon of low energy, called phosphorescence, requires another spin flip. Therefore, the lifetime of this state is comparatively long and phosphorescence is detected at much longer time scales than fluorescence, usually within the range of a few milliseconds.

From the radiationless transitions two important consequences for fluorescence imaging arise: First, the absorbed energy of the fluorescent molecule is partially dissipated. The emitted fluorescent light is therefore red-shifted in its wavelength by typically 20-50 nm with respect to absorption. This photon energy difference $h\nu_{ex} - h\nu_{em}$ is called Stokes' shift [68] and allows for high fluorescence signal detection against a low background, since the light used for excitation can be separated from the fluorescence light. Secondly, a depopulation of S_1 occurs via various competing pathways (e.g. fluorescence, intersystem crossing), which is characteristic of the flu-

orophore and which have to be taken into account for measurements [69]. A measure of the suitability of a fluorophore for imaging is given by the fluorescence quantum yield ϕ, which is the ratio of fluorescence photons emitted to the total number of absorbed photons. In other words, it states the probability by which an excited molecule relaxes via emission of a photon. Ideally it has a value close to 1. Another characteristic parameter is the extinction coefficient ϵ, which denotes the radiation absorption efficiency of a dye. As the dye is suspended in solution of concentration c and within an illuminated sample volume of thickness d, ϵ is calculated via Lambert - Beer's law:

$$-lg\left(\frac{I}{I_0}\right) = \epsilon \cdot c \cdot d \quad ,$$

where I_0 is the initial intensity and I the detected intensity after absorbance of light from the molecule. Typical values range from 10.000 - 250.000 1/(M cm) and in general this value is also chosen as high as possible.

2.3.2.3 Fluorescence Microscopy

In 1904 August Köhler, the inventor of Köhler illumination, was the first to observe a luminescence phenomenon in the microscope. Together with Henry Siedentopf he developed the first fluorescence microscope which was presented four years later in Jena, Germany. Since then, several improvements followed including the development of a high variety of fluorophors as well as the use of epi-illumination[2]. With its simple principle and wide range of applications in cell biology, physical chemistry, geology and medicine [70], fluorescence microscopy has become a powerful tool in science. An image of a fluorescent object can be realized as follows with a standard light microscope: A filter set consisting of an excitation filter, a beam splitter and an emission filter is chosen in such a way, that the

---

[2]Here, illumination and detection light share the same optical path (see figure 2.11), such that the mostly non-interacting illumination light propagates away from the objective beneath the sample and so barely enters the detection path.
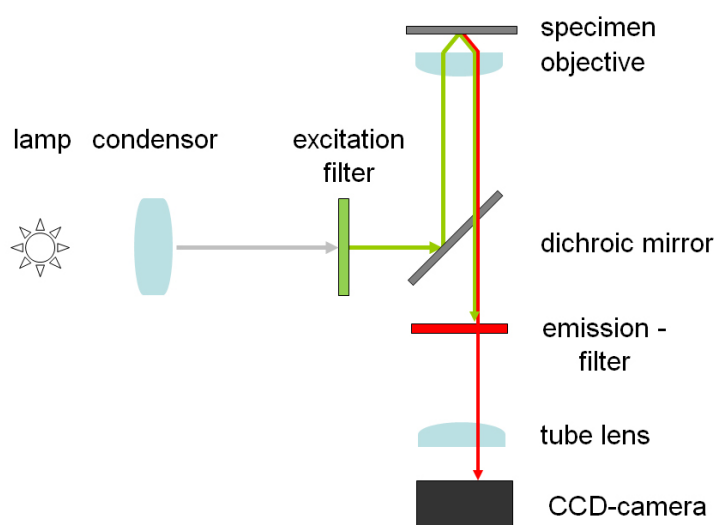
Figure 2.11: Schematic light path in an epi-fluorescence microscope. An excitation filter selects a specific wavelength to illuminate the specimen. The fluorophore therein is excited and subsequently emits fluorescence light. This light is red-shifted with respect to excitation. Thus, the two fractions can be separated by means of a beam splitter and an emission filter. Only fluorescent light is detected. Sketch taken from [53].

excitation light is separated from the emitted fluorescent light (see sketch in 2.11). Precisely, in order to achieve optimal excitation, one or a specific band of wavelengths from the spectrum of a light source are chosen, which are as close to the absorption maximum of the fluorophore as possible. This is achieved with the appropriate excitation filter. Subsequently, the light is directed onto the sample with a beam splitter and focused through an objective. After excitation of the fluorophore in the specimen, the red-shifted fluorescent light is collected by the same objective and passes a beam splitter as well as the emission filter, both transparent for this band of wavelength. Any scattered illumination light is blocked due to its shorter wavelength.

In this work epi-fluorescence microscopy was used to check the quality of patterned substrates and to visibly judge the amount of fluorescent labeling of vesicles and SLBs.

2.3.2.4 Confocal Laser Scanning Microscopy
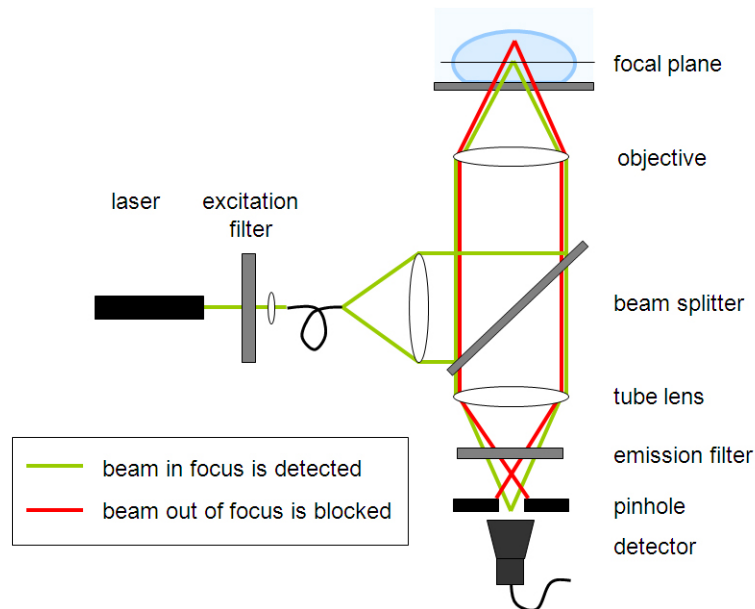
Figure 2.12: Light path in a confocal microscope. With the objective light is focused to a diffraction limited spot in the sample. Only light originating from the focal plane in the sample is detected. A pinhole in the back focal plane of the tube lens blocks all light coming from other planes. Thus, a specific layer in the sample is selected.

The confocal scanning microscope was developed by Minsky in 1961 [71] and further improved by the use of a scanning laser beam as illumination source by Brakenhoff in 1979 [72]. Due to its several advantages over conventional wide-field microscopy and in combination with fluorescence microscopy, it has become an ubiquitious tool in natural sciences as well as medical research [70] as outlined below. The key idea to the confocal approach is the insertion of a pinhole in the back focal plane of the tube lense which blocks any light coming from above and below the focal plane in the sample (see figure 2.12). This way not only the depth of focus is decreased but also a highly improved signal to noise ratio is achieved. In an epi-illumination microscopic set-up one or several distinct

wavelengths of the excitation laser beam are selected by a filter and subsequently pass the fiber optics. After reflection at a beam splitter (BS), the beam is focused by the objective, yielding a small focal volume at the side of the specimen. The light is recollected by the same objective, passes the BS and an emission filter before it reaches the pinhole. Depending on the width of the pinhole opening, light coming from a thin (small pinhole) or a thick sectional plane (wide pinhole) around the focus is allowed to pass. Subsequently, it is collected by a photon detection device, such as a PMT or APD. From the point like illumination full images are obtained via scanning mirrors which are capable of positioning the focus in lateral as well as axial dimension within the sample. Therefore, images are formed recording subsequent pixels and an acquisition of lateral image sections can be used to reconstruct 3D-images.

A confocal laser scanning microscope was used in this work to perform measurements of fluorescence correlation spectroscopy (FCS) and fluorescence recovery after photobleaching (FRAP) as well as to image SLBs, vesicles and cells in reflection, fluorescence and brightfield mode.

2.3.2.5   Fluorescence Recovery After Photobleaching (FRAP)

FRAP was first introduced by Peters et al. in 1974 [73] and Axelrod et al. in 1976 [74] and is primarily used to study lateral diffusion of molecules in membranes as well as to determine the amount of immobile components. A simple FRAP experiment is conducted as follows (see figure 2.13): A small region of interest of a planar fluorescent object is irradiated with high laser intensity for a short period of time. As a consequence the fluorescent molecules within the region are photobleached[3]. From the surrounding unbleached molecules diffuse into this region, repopulating the formerly bleached sites while bleached molecules diffuse out. This process is recorded at minimal laser power as a recovery of the fluorescence signal. The kinetics of the recovery as well as the saturation value of the

---

[3]In order to ensure sufficient bleaching, the chosen fluorophore should be of not too high stability.

32
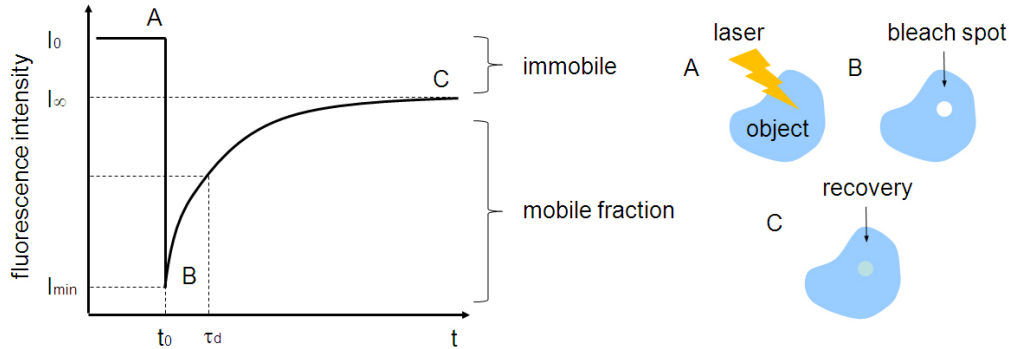
Figure 2.13: Fluorescence Recovery After Photobleaching. A: Laser bleaches a region of interest B: Fluorescence intensity in this region is minimal as most of the molecules are bleached C: Diffusion of unbleached molecules in the region results in fluorescence recovery.

recovered intensity depend on, respectively, the molecular diffusion coefficient D and the mobile fraction M_f of the species under study. The diffusion coefficient is a measure of the area a molecule probes within a certain time through a random walk[4]. It is calculated from the two-dimensional diffusion equation described by Axelrod et al. [74] yielding

$$D = \frac{\omega^2}{4\tau_d} \quad ,$$

where ω is the radius of the bleached area and τ_d the diffusion time of the molecule. The mobile fraction M_f is the amount of molecules, which were not hindered in their movement and therefore could be replaced by unbleached molecules. It is calculated from the fluorescence intensity ratio of final measured intensity I_∞ to initial measured intensity I_0 corrected by the amount of fluorescence which remained in the region after bleaching, I_{min}:

$$M_f = \frac{I_\infty - I_{min}}{I_0 - I_{min}} \quad .$$

---

[4]The random walk indicates a thermally driven molecular movement which excludes processes of active transport or external flow.

For a circular bleach spot the characteristic diffusion time τ_d is determined from a fit of equation 2.1 to the measured fluorescence recovery kinetics $I(t \geq t_0)$ [75]:

$$I(t \geq t_0) = (I_{\text{inf}} - I_0) \, e^{-\frac{2\tau_d}{t}} \left\{ B_0 \left(\frac{2\tau_d}{t} \right) + B_1 \left(\frac{2\tau_d}{t} \right) \right\} + I_0 \qquad (2.1)$$

It has to be noted that within the scope of this theory FRAP is restricted to two-dimensional diffusion. As contributions to recovered intensity originate from above or below the chosen plane, the recovery curve is altered strongly leading to erroneous results. Moreover, during measurements, intensities need to be recorded simultaneously in a reference area. This is necessary in order to determine the amount of bleaching, which occurs while probing fluorescence recovery. The measured intensity $I_m(t)$ is corrected with data of the reference area $I_{ref}(t)$, according to:

$$I(t) = \frac{I_m(t)}{I_{ref}(t)} I_{ref}(0) \quad .$$

Corrected curves were subsequently used for fitting. However, due this small amount of bleaching, the choice of this reference area is crucial for determination of diffusion times τ_d. Finally the radius of the bleached area ω should be determined with high accuracy as the square of ω is used to derive the diffusion coefficient. Despite these drawbacks FRAP is a popular technique as it applies to a wide range of diffusion processes and as measurements are simple to conduct with the precise and fast settings provided by CLSM.

In this work, FRAP measurements were undertaken at the vesicle top as well as in the fluctuating and bound regions of the adhesion zone.
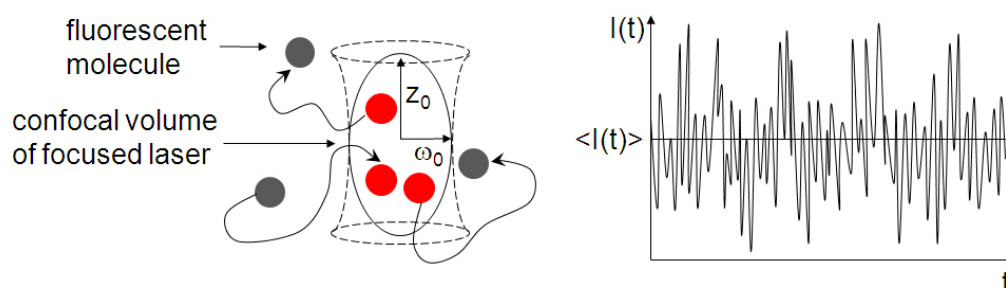
Figure 2.14: Principle of fluorescence correlation spectroscopy. Molecules entering the confocal volume are excited to fluorescence. Depending on the underlying diffusion process, molecules leave the confocal volume after a characteristic time (left). This process is reflected in intensity fluctuations, which are recorded for correlation analysis (right). For quantitative analysis the axial and radial waist radius, z_0 and ω_0, have to be known.

2.3.3 Fluorescence Correlation Spectroscopy (FCS)

2.3.3.1 Introduction

FCS was presented for the first time in 1972 by Elson, Magde and Webb as novel technique to measure molecular diffusion constants and chemical kinetics [76]. In the 90's renewed interest in this technique evolved from further improvements on the measurement technique, notably utilization of a CLSM and of the multiple tau algorithm for correlation analysis [77]. Nowadays, it is widely used to study photophysical properties of fluorophores [78], chemical reactions [79] as well as molecular concentration, orientation and diffusion processes in model systems and living cells [80], [81], [82]. In contrast to FRAP, where information on molecular dynamics are drawn from the way a system relaxes back to equilibrium after an external perturbation, FCS allows the study of dynamic processes under equilibrium conditions. Its principle is sketched in figure 2.14. It is based on recording intensity fluctuations which are caused by the number fluctuations of fluorescently labeled particles diffusing in and out of a very small observation volume ($\sim 10^{-15}$ l). The volume element is usu-

35

ally the focused laser beam of a confocal microscope, called the confocal volume, which remains stationary during measurement. Upon entering this volume element, particles excited to fluorescence emit photons, which are recorded by a highly sensitive photon-counting detector, e.g. an APD. These fluctuations vary characteristically with the number of molecules N in the observation volume as well as with the average time it takes them to move across the volume, which is called the diffusion time τ_d. While N can be converted into concentrations when the confocal volume size is known, τ_d is related to the diffusion coefficient D as it is for FRAP:

$$\tau_d = \frac{\omega_0^2}{4D} \quad . \tag{2.2}$$

With the appropriate theoretical model, N and D can be extracted from measurements. In a similar way, quantitative information is obtained on other processes exhibiting continuous fluctuations from equilibrium, such as fluorophore singlet-triplet dynamics or chemical reaction rates. Here the characteristic time scale is not the diffusion time , τ_d, but the triplet state life time or the time of reaction kinetics, respectively.

A major advantage of this technique is its high sensitivity, which is achieved from recording only a low number of molecules within a tiny spot. In addition, CLSM optics provide high spatial resolution and fast single-photon detection allows to probe processes with high temporal resolution in the $\sim \mu$s range. With respect to in vivo studies FCS is also advantageous as the low amount of fluorescent labeling results in reduced production of radicals in comparison to conventional fluorescence microscopy. However, for quantitative evaluation, the choice of fluorophore is crucial to the measurement, as artifacts may arise from saturation or bleaching and, in addition, appropriate derivatives are not always commercially available. Moreover, shape and size of the detection volume have to be known exactly as e.g. the square value of its size is used in correlation analysis. Since an intrinsic length scale is missing, one usually resolves this issue by referencing axial z_0 and radial waist radius ω_0 against a sample of known diffusion coefficient.

2.3.3.2 Autocorrelation Function

For correlation analysis of the recorded signal, intensity fluctuations are temporally autocorrelated. Here, the detected fluorescence intensity is multiplied with a time shifted replica of itself at different time shifts, so called lag times τ. Time averaging and normalization yield the autocorrelation function (ACF) of the fluorescence intensity signal, which is given by [83]:

$$G(\tau) = \frac{\langle \delta I(t)\delta I(t+\tau)\rangle}{\langle I(t)\rangle^2} \quad .$$

Here, $\langle ... \rangle$ denotes the average over time and $\delta I(t) = I(t) - \langle I(t)\rangle$ the intensity fluctuation around its mean. In other words, the ACF yields the probability to detect a signal at time $t + \tau$ when a signal was recorded at time t. Figure 2.15 shows a sketch of the ACF. In general, the ACF shape
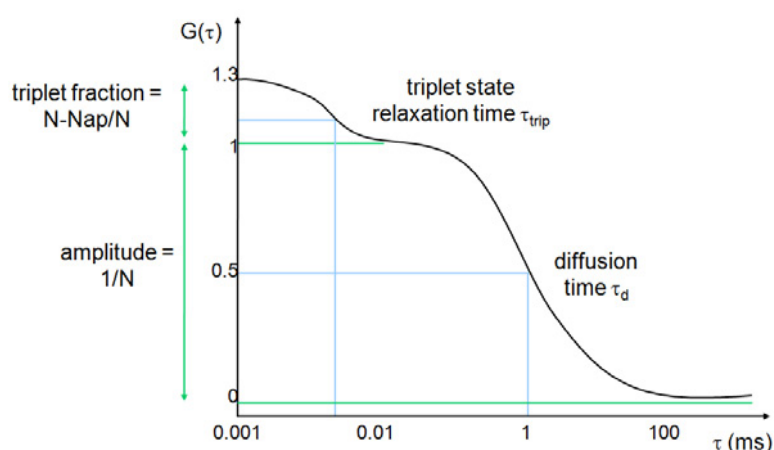
Figure 2.15: ACF sketch and properties. Fast triplet dynamics and slower diffusion dominate the ACF shape. Molecular numbers $N_{(ap)}$ and characteristic duration times $\tau_{d/trip}$ are calculated from the amplitude and exponential decay, respectively.

is dominated by an exponential decay extending over several time scales. The plateau region of this process at short timescales is called the amplitude of the ACF. Most often the observed process is diffusion and the value

at it's half amplitude marks the diffusion time τ_d of the molecule. The amplitude is $\propto 1/N$, with N being the average number of molecules in the observation volume. Interpretation of ACF graphs get more complicated as fast triplet dynamics have to be considered. Relaxation via the first excited triplet state shows up at short times as an additional shoulder of the ACF. Essentially this transition is forbidden by quantum mechanics and so the fluorophore needs a long time to relax to the ground state (see 2.3.2.3). During this time the fluorophore cannot contribute to fluorescence emission and the apparent number N_{ap} of molecules in the detection volume is smaller. Consequently, the intercept of the ACF rises and from measured apparent number N_{ap} and true average number of molecules N, the triplet fraction is calculated. Tripled relaxation typically occurs at $\sim \mu s$, such that diffusion and triplet processes separate. Triplet relaxation is also described by a simple exponential decay and relaxation times τ_{trip} are derived from the 1/e value of the triplet fraction amplitude.

Figure 2.16 gives an example of measured autocorrelation curves for different molecules and demonstrates the range of diffusion processes accessible with FCS. The fastest process probed is free diffusion of a fluorophore. In this graph it is rhodamine green, which has a molecular weight of 0.6 kDa and which exhibits a diffusion time of $\sim 10 \ \mu s$ in solution. Once a fluorophore is bound to a larger molecule, diffusion slows down and the decay of the autocorrelation function is shifted towards larger lag times τ. Here this is depicted in blue for Alexa 488 bound to the protein calmodulin, which exhibit a combined molecular weight of 17.3 kDa. A highly viscous environment, such as the cytosol of a HEK293 cell (dark blue curve), adds to the abating effect. Diffusion of molecules in the cellular membrane is one of the slowest processes detectable with FCS. Here diffusion times are on the order of several ms. An example of such a diffusing molecule is DiI with a molecular weight of only 0.9 kDa, which is anchored to the plasma membrane of HEK293 cell via its two aliphatic compounds. Due to this binding configuration and the densely packed environment, diffusion is strongly slowed (red curve).

The measured autocorrelograms exhibit the characteristic features intro-
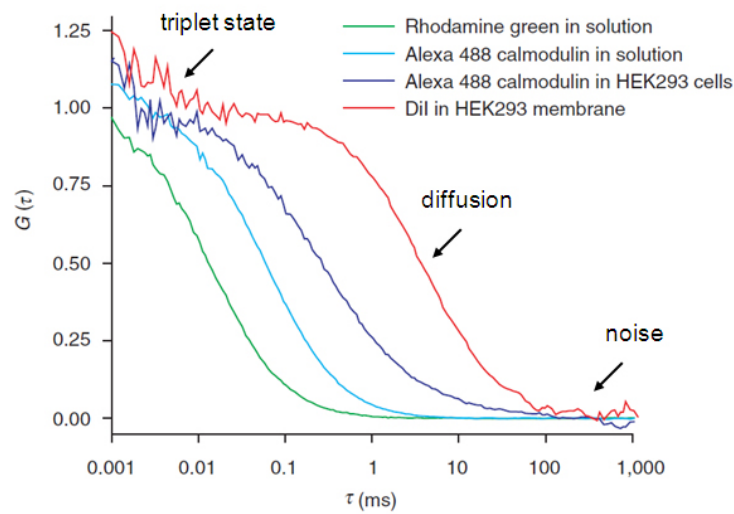
Figure 2.16: Measured autocorrelation curves for different diffusion processes: Fluorophore rhodamine green (green) in solution, the fluorophore-protein complex Alexa 488-calmodulin in solution (blue), the same fluorophore-protein complex in cytosol (dark blue) and fluorophore DiI anchored to cell plasma membrane (red). For comparison ACFs were normalized. Each curve is a mean of six measurements. Modified graph taken from [84].

duced before. Effects of dye transitions to the first excited triplet state show up at short times as additional shoulder followed by the spatial decay from diffusion. In addition, for long lag times τ, effects of noise become visible, as due to the finite measurement time, averages are taken only over a small number of intensity values.

These examples demonstrate how autocorrelation analysis is a successful mathematical tool to analyze stochastic signals. However, one has to be aware that this technique is highly sensitive to any systematic disturbance such as afterpulsing from APDs, laser intensity variation or vibrations of the microscope stage. Also, choosing the correct theoretical model for the observed process is of high importance, as results are impaired by any wrong assumption.

In the present study three and two-dimensional diffusion processes were

investigated. Subsequently, autocorrelograms were analyzed with the corresponding theoretical model. In order to avoid erroneous evaluation, a potential influence of the triplet fraction was accounted for. The theory for 3D Brownian diffusion of one molecular species yields the ACF [85]:

$$G(\tau) = \frac{1}{N} \frac{1}{1 + (\tau/\tau_d)} \frac{1}{\sqrt{1 + \left(\frac{\tau}{\tau_d}\right)\left(\frac{\omega_0}{z_0}\right)^2}}$$

where, as before, ω_0 and z_0 are the radial and axial $1/e^2$ waist of the confocal volume, respectively, τ_d is the characteristic diffusion time as given in equation 2.2 and N the average number of particles in the detection volume. When the molecule under study undergoes intersystem crossing to the triple state an additional factor has to be accounted for:

$$G(\tau) = \frac{1}{N} \frac{1 - T(1 - e^{\tau/\tau_{trip}})}{(1 - T)} \frac{1}{1 + \left(\frac{\tau}{\tau_d}\right)} \frac{1}{\sqrt{1 + \left(\frac{\omega_0}{z_0}\right)^2 \left(\frac{\tau}{\tau_d}\right)}} \quad , \qquad (2.3)$$

where T is the fraction of molecules in the triplet state and τ_{trip} the characteristic relaxation time. Similarly, on obtains for one component diffusion restricted to two dimensions and triplet dynamics:

$$G(\tau) = \frac{1}{N} \frac{1 - T(1 - e^{\tau/\tau_{trip}})}{(1 - T)} \frac{1}{1 + \left(\frac{\tau}{\tau_d}\right)} \qquad (2.4)$$

As in most of the present investigations lipid diffusion within a membrane was characterized, the last equation was the theoretical model primarily applied.

The desired physically relevant parameters, τ_d and N, were obtained via fitting the appropriate theoretical model to the measured autocorrelation curve. Fitting was done with a weighted Levenberg-Marquardt nonlinear-least squares routine. As the standard deviation for each point can not be calculated analytically, a method described by Wohland et al. [86] was used for their determination. This method is based on splitting up one

long measurement into a series of short measurements thus yielding for every delay time τ_i an average value and standard error $\sigma(\tau_i)$, which is a valid estimate of the real standard deviation:

$$\sigma(\tau_i) = \sqrt{\frac{1}{l(l-1)} \sum_{j=1}^{l} \left(\frac{G_j(\tau_i) - 1}{G_j(0) - 1} - \frac{1}{l} \sum_{j=1}^{l} \frac{G_j(\tau_i) - 1}{G_j(0) - 1} \right)^2} \quad .$$

Here, l is the number of short measurements, $G_j(\tau_i)$ corresponds to the value of the jth short autocorrelation function at delay time τ_i and $G_j(0)$ was determined from averaging over the first 5 data points of $G_j(\tau_i)$ at short delay times. In addition to each fitted autocorrelation curve absolute deviations of data and fit, so called residues, are given.

2.3.3.3 Z-scan FCS

The z-scan method is a novel tool to measure diffusion coefficients D and lateral beam waist ω_0 in planar systems without the need for extrinsic calibration. It was first introduced in 2003 by Benda et al. [87] and relies on recording FCS measurements in consecutive planes along the z-axis of an object. Assuming a Gaussian beam, the illuminated area is inherently changed with each position of the focus. This yields an axial dependence of the confocal radius ω, which can be expressed in terms of the lateral beam waist ω_0 and the distance from the confocal centre Δz [88], [89]:

$$\omega^2 = \omega_0^2 \left(1 + \frac{\lambda^2 \Delta z^2}{\pi^2 n^2 \omega_0^4} \right) \tag{2.5}$$

Here, λ is the wavelength of the excitation light and n the refractive index of the bulk medium. Similarly, an expression for the average number of particles N within the focus area is derived

$$N = N_0 \left(1 + \frac{\lambda^2 \Delta z^2}{\pi^2 n^2 \omega_0^4} \right) \quad , \tag{2.6}$$

41

where N_0 is the particle number at the beam radius minimum. For free diffusion with diffusion constant D, the z-dependence of the diffusion time τ_d is expressed in terms of equations 2.5 and 2.6:

$$\tau_d = \frac{\omega_0^2}{4D}\left(1 + \frac{\lambda^2 \Delta z^2}{\pi^2 n^2 \omega_0^4}\right) = \frac{\omega_0^2}{4D}\frac{N}{N_0} \quad . \tag{2.7}$$

Plotting particle number and measured diffusion times against the axial position, a parabolic distribution of points is obtained which can be fitted to yield values for D and ω_0. In comparison to conventional FCS, the z-scan approach allows for precise positioning of the object within the confocal volume and has shown to determine diffusion coefficients with 10 % precision, while usually an error of 20 % is anticipated [90].

In this thesis, z-scan FCS was applied to calibrate the confocal volume, to measured lipid diffusion constants in SLBs and GUVs as well as to study membrane spatial fluctuations (see e.g. section A or 6).

2.3.3.4   Data Acquisition

ACFs and images of the corresponding object were acquired with the confocal microscope described in section 2.3.1. Depending on the excitation spectrum of the fluorophore, the laser line closest to the wavelength of maximal excitation was chosen. This was either the $\lambda = 543$ nm line of the HeNe - laser or the $\lambda = 488$ nm line of the Ar^+ - laser. For FCS measure-

λ [nm]	AOTF [%]	laser intensity [%]	power [μW]
543	10	1 - 10	0.2 - 1.3
543	100	1 - 10	3.6 - 34.0
488	10	0.2 - 1 - 10	0.3 - 1.0 - 9.0
488	100	1	25.5

Table 2.1: Overview of typical laser intensity settings and measured excitation powers. The values are well below 0.1 mW, as recommended for FCS measurements [91]

ments, the incoming laser light was attenuated by an AOTF, which provided a damping between 0.1%-100%. For each AOTF setting, laser light

intensities were then chosen from an interval 0.2%-100%. Unless stated otherwise, the AOTF was set to 10% while percent laser intensities where chosen between 0.2%-10%. Table **??** gives an overview of the corresponding excitation powers for these settings, measured with and optical power meter (model 1916-C, Newport Spectra-Physics GmbH, Darmstadt, Germany) at the position of the sample.

A main beam splitter (488/543 nm, Zeiss) behind the AOTF was used to separate the illuminating light from the detected fluorescent light. Prior to detection with an APD the fluorescent light traversed another filter. For excitation with $\lambda = 543$ nm this was a $\lambda = 580$ nm long pass filter (Zeiss). For excitation with $\lambda = 488$ nm a band pass filter $\lambda = 505 - 530$ nm (Zeiss) was used.

Utilization of APDs as detectors is essential for FCS measurements, as their single-photon detection provides the high sensitivity needed. Moreover, the particular type used in this study featured particularly high quantum efficiency in the red spectral part and thus maintained its performance even at low fluorophore concentrations. A sampling frequency of 20 MHz in principle allowed to study processes occuring within 0.05 ns, while dark currents of 0.5 kHz were sufficiently low with respect to typically recorded signals of 10-100 kHz.

In addition, a water immersion objective was used, as a refractive index mismatch of a different immersion medium and buffer solution would impair the focal spot. Any broadening of the beam would then shift the ACF to higher diffusion times. The objective was equipped with a correction collar to adjust the working distance of 0.14 - 0.2 mm to the thickness of the glass substrate. Its correct position was checked shortly before measurement.

A correct positioning of an object in the centre of the confocal volume was facilitated by a cross-hair interface in the software. This was shifted and fixed at the site of the confocal volume prior to each measurement. In order to find the correct site, a homogeneous layer of fluorescently labeled antibodies, physisorbed to glass and dried, was imaged. For 3 s and with high intensity a hole was bleached in the layer at the site of the confocal

volume. At this point the cross-hair interface was fixed.

Finally, full fluorescence or reflection images were acquired in scanning mode at laser excitation intensities of 0.2%-5% for the Ar^+ laser and 1%-50% for the HeNe laser, with an AOTF set to 100%. For fluorescence images the main beam splitter was the same as for FCS measurements, while for reflection a beam splitter with 80% light transmission towards the probe and 20% transmission of reflected light from the sample (T80/R20, Zeiss) was used. Images were detected with photomultiplier tubes and recorded at a resolution of 1024×1024 pixels, a pixel dwell time of 3.15 μs and 8 bit colour depth.

For all FCS data and images, the pinhole was set to 1 Airy unit[5].

2.3.4 Microinterferometry

2.3.4.1 Introduction

Reflection interference contrast microscopy (RICM) is a microinterferometric technique, which allows the reconstruction of the three-dimensional shape of an object near a substrate.

Initially this technique was used to study thin film properties [92]. In 1958 Abercrombie and Ambrose [93] as well as Curtis in 1964 [94] were the first to apply this technique to cell adhesion studies. Nowadays, it is primarily used to study wetting phenomena [95], cell migration [96] as well as adhesion of cells and model membranes [97], [98], [99]. Its principle is based on recording an interference pattern, which forms from the reflection of polarized light at different interfaces within an object. Only when interfaces are sufficiently thin and close to the substrate, such interference pattern arises. The observed intensity variations correspond directly to height differences in the sample, such that an object's topography can be reconstructed.

RICM's remarkable strength is its axial resolution of 4 nm [100] as well as its simple microscopic set-up. On the other hand, the interference pat-

---

[5]The Airy unit refers to the central focused region of a diffraction pattern, which results from a uniformly-illuminated circular aperture

tern features a periodicity on height, such that determination of absolute object heights is not always well-defined. Therefore, analysis is often constrained to some 100 nm away from the substrate. During the last years, these drawbacks were partially overcome by the introduction of dual wavelength-RICM (DW-RICM) [101] as outlined below.

In the following, theoretical aspects of image formation and the way to quantitative analyses are described. Moreover, improved applicability of RICM from the introduction of DW-RICM and antiflex technique is demonstrated.

2.3.4.2 Theory of Image Formation
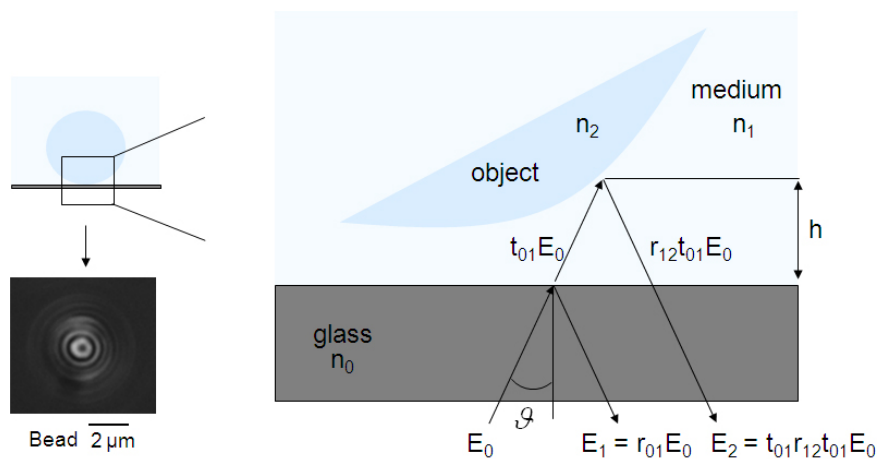
Figure 2.17: Principle of RICM image formation. As a bead hovers over a substrate, light is reflected at the glass - buffer and the buffer - bead interfaces. Reflected rays interfere constructively and destructively to Newton fringes. The height of the bead above the substrate is calculated from the reflected intensities, i.e. the electric field vectors E_i, $i \in \mathbb{N}$.

The RICM image is formed from the interference of rays, which were reflected at different thin optical layers in a sample. Figure 2.17 gives an example of a measured interferogram of a bead immersed in buffer and hovering on a substrate, which is illuminated from underneath. The circular fringes denote Newton rings, which form as the object curves away

from the glass substrate. Only light reflected from an area close to the substrate contributes to the interferogram, as here the prerequisite of interference, namely a fixed phase between the interfering rays, is met. Generally speaking, sufficient temporal and spatial coherence of the light source must be provided for, for interference to develop.

Temporal coherence describes the length of rays emerging from a light source, which can still interfere with themselves. If a light source is monochromatic, i.e. it features rays of single frequency, it has high temporal coherence. In reality this condition is not exactly fulfilled and phase differences between rays vary at some point. Therefore one speaks of wave trains which are emitted from the source and defines their average length as coherence length. For a metal halide lamp quasi-monochromatic light is achieved from the application of an interference filter. Its coherence length is approximately 200 μm and in general exceeds the measured object heights by far. Thus, temporal coherence is always given.

Spatial coherence describes the lateral separation of two points in the image plane which are still coherently illuminated. However, due to the finite extension of the light source full spatial coherence does not occur. Instead, the illumination zone exhibits different degrees of coherence. Theoretically this is solved by treating the light source as a collection of individual point sources and only light originating from the same source is able to interfere. For a circular homogeneous light source of illumination angle α the intensity distribution of the diffracted image corresponds to a first order Bessel function. Its amplitude is a measure of the mutual degree of coherence γ and given by the van Cittert-Zernike theorem [?]:

$$\gamma = \frac{2J_1(\nu)}{\nu} \sim \frac{\sin(\nu)}{\nu} \quad , \text{where} \quad \nu = kdn\sin(\alpha) \quad .$$

J_1 is the Bessel function of 1st kind, d the diameter of the illuminated area, n the refractive index of the sample medium and $k = \frac{2\pi}{\lambda}$ is the wavevector, given by the wavelength λ. With this measure an area of coherent illumination is defined by $d \leq \frac{0.16\lambda}{n\sin(\alpha)}$, while for any larger distance between illuminated points only partial coherence is achieved.

As these requirements are fulfilled, reflected rays interfere in a destructive or constructive manner, depending on the difference of their optical path length Δ. Image regions of highest intensity correspond to constructive interference, with $\Delta = 2\pi n, n \in \mathbb{N}$, while in dark regions, rays are eliminated due to a phase difference of $\Delta \sim \pi$. Thus, detected intensity variations correspond to height differences in the sample.

From the previously mentioned partial coherence another important consequence for the experiment arises: The size of light source can be determined with the aperture. As it is opened the illumination numerical aperture INA $= n \sin(\alpha)$ is increased and higher lateral resolution is achieved. On the other hand, the depth of focus is reduced $\propto 1/\alpha$ at the same time. Thus, from changing the aperture the lateral resolution is varied between typically 0.26 - 0.36 μm. With an INA of 0.54, a compromise between these opposing aspects was found.

An exact description of the arising interference pattern is given by Wiegand et al. [95]. Basically, intensities observed at point $\vec{r} = (x, y)$ in the image plane I(x,y) form from the sum of electric field vectors, $\vec{E}_i(\vec{r}, t)$, which were reflected in the sample at different layers i (see figure 2.17):

$$
\begin{aligned}
I(x, y) &= \langle \vec{E}^2(\vec{r}, t) \rangle_t \quad \text{where} & (2.8) \\
\vec{E}(\vec{r}, t) &= \sum_i \vec{E}(\vec{r}, t)_i = R\vec{E}_0(\vec{r}, t) \quad . & (2.9)
\end{aligned}
$$

Here, $\vec{E}(\vec{r}, t)$ is expressed in terms of the incident light E_0 and the reflection coefficient R is introduced, which represents the combined reflectivity of all interfering rays $\vec{E}(\vec{r}, t)_i$. This effective reflection coefficient is an important measure and calculated from the reflection r_{ij} and transmission coefficients $t_{ij} = \sqrt{1 - r_{ij}^2}$ as introduced by Fresnel. For a l layered system and with the assumption of perpendicular incident light R given by:

$$
R = r_{01} + \sum_{i=1}^{l} \left[\Pi_{m=1}^{i} (1 - r_{m-1,m}^2) \exp(-i2k\Delta_m) \right] r_{i,i+1} \quad , \tag{2.10}
$$

where

$$r_{ij}^{s} = \frac{n_j - n_i}{n_j + n_i} \quad \text{and} \quad r_{ij}^{p} = \frac{n_i - n_j}{n_i + n_j}$$

are the reflection coefficients for the linear polarization states p and s and $k = 2\pi/\lambda$ is the wavevector with λ the wavelength of light. Δ_m denotes the difference in optical path for a layer thickness d_m and a refractive index n_m: $\Delta_m = d_m n_m$.

From this simple theory interference patterns for height differences up to $\sim 100 \, \text{nm}$ are surprisingly well described. However, it considers only light entering the sample in normal direction to the plane of the substrate and reflections at planar objects. In addition, any divergence of the incident beam is neglected. Therefore, for higher INA settings and object heights, including curvature, a more advanced theory is considered.

2.3.4.3 Consideration of Interfaces and Finite Illumination Aperture
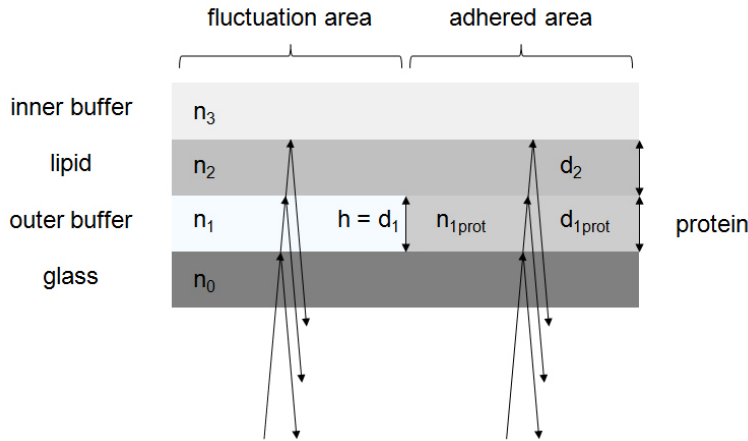
Figure 2.18: RICM image formation for reflections at three interfaces. For fluctuation and adhered membrane area different interfaces are taken into account. n_i, $i = 0 - 3$, denote refractive indices and d_i, $i = 1 - 2$, thicknesses of layers.

For the system in this thesis absolute object heights were determined from the theory of four layers. Precisely, either interfering rays from three

reflections within fluctuating membrane areas or from three reflections within the adhered part of the vesicle membrane were used for height reconstruction. In the first case, reflective interfaces were glass-buffer, buffer-membrane and membrane-sucrose interface. In the latter case, the same reflections occurred with the buffer layer substituted by the patterned and hydrated protein layer, as depicted in figure 2.18. The height profile h was calculated from the measured intensity distribution according to equation 2.8 - 2.10 with l=3:

$$
\begin{aligned}
I(h) \;=\; & \sum_{i=1}^{3} I_i + 2\sqrt{I_1 I_3}\,\cos(2k(n_1 h + n_2 d_2)) \\
& + 2\sqrt{I_1 I_2}\,\cos(2k n_1 h) + 2\sqrt{I_2 I_3}\,\cos(2k n_2 d_2)
\end{aligned}
\tag{2.11}
$$

Here, h is the height object above the substrate at point[6] $\vec{r} = (x, y)$, d is the thickness of the membrane, k is the wavevector and n_1 and n_2 are the refractive indices of buffer and membrane, respectively. I_i is the intensity of the reflected light at layer i, which depends on the refractive indices $n_0 - n_3$ and E_0, as seen from equations 2.10 and 2.9. Values for the parameters were: Membrane thickness d = 4 nm, refractive index of the glass substrate, $n_0 = 1.525$, of the BSA protein layer, $n_{1prot} = 1.386$ [102], and of the membrane, $n_2 = 1.486$ [103]. The remaining refractive indices of PBS buffer, $n_1 = 1.3346$, and sucrose solution, $n_3 = 1.3434$, were measured prior to each experiment with an Abbé refractometer (AR4D, Krüss, Hamburg, Germany).

In general, E_0 and hence the incident light intensity I_0 is unknown. To convert measured intensities into heights the theoretically expected intensity $I(h)$ is normalized with respect to the first reflection, I_1:

$$
I_{norm}(h) = \frac{I - I_1}{I_1} \quad , \text{where} \quad I_1 = r_{01}^2 I_0 \,.
\tag{2.12}
$$

Since I_1 is essentially the background intensity at the sites free of stamped protein, experimentally recorded images are normalized with this inten-

---

[6]For simplicity, xy-coordinates were suppressed.

sity as described in [53]. This way, all parameters of the system are known and height conversion is carried out in line with the following aspects: Equation 2.11 is derived from RICM theory for perpendicular incident light and can be rewritten using the sum S and difference D of the maximal and minimal intensity

$$I_{max} = \sum_{i=1}^{3} I_i + 2(\sqrt{I_1 I_3} + \sqrt{I_1 I_2} + \sqrt{I_2 I_3}) \quad , \tag{2.13}$$

$$I_{min} = \sum_{i=1}^{3} I_i - 2(\sqrt{I_1 I_3} + \sqrt{I_1 I_2} + \sqrt{I_2 I_3}) \tag{2.14}$$

$$\Rightarrow I(h) = \frac{1}{2}\left(S - D\cos\left\{2kn(h - h_0)\right\}\right) \quad . \tag{2.15}$$

An obvious feature of this simplified equation is the phase shift of the cosine, h_0. h_0 is characteristic of each system and appears upon consideration of reflections at ≥ 3 interfaces. A recent study demonstrated this effect [100] and indicated that consideration of all layers involved is necessary for exact absolute height measurements. The traditional analysis neglects reflections at the membrane-sucrose interface and thus underestimates heights by h_0.

Up to now, only perpendicular incident light has been considered and any incoherence from the divergence of the incident beam was not accounted for. As described before this effect leads to different degrees of coherence and so an advanced theory of partial coherence was developed which states that [104]:

$$I(h) = \frac{1}{2}\left(S - D\frac{\sin(\gamma)}{\gamma}\cos\left\{2kn\left[h\left(1 - \sin^2\left(\frac{\alpha}{2}\right)\right) - h_0\right]\right\}\right) \tag{2.16}$$

where $\gamma = \frac{\sin y}{y}e^{iy}$ with $y = 2kh\sin^2(\alpha/2)$ is the mutual coherence of the point spread function parallel to the optical axis. Other parameters are as before, k the wavevector, α the illumination aperture angle and n the refractive index of the medium. Depending on whether finite aperture effects were accounted for or not, either equation 2.16 or 2.15 was used.

Constants S, D and h_0 were determined from numerically fitting equation 2.15 to 2.12. Knowing the branch for conversion, heights were then easily determined.

In this thesis, for height reconstruction of objects at heights <100 nm the
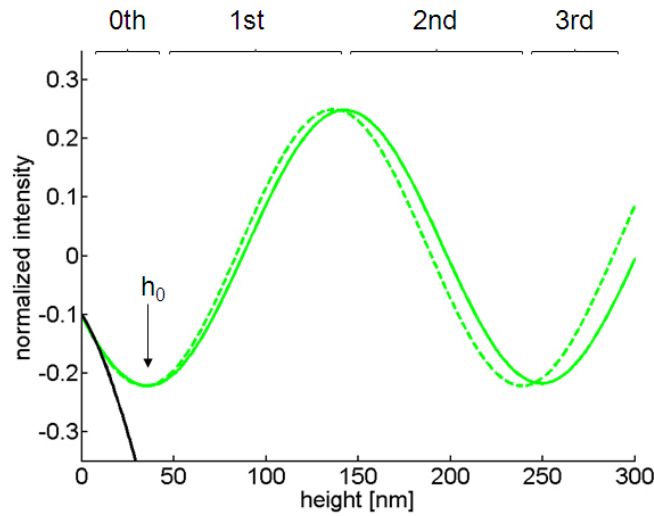
Figure 2.19: Normalized intensity for light reflected at three interfaces with (solid green line) and without finite INA (dashed green line) within fluctuation regions. The first minimum of the intensity curve is shifted by an offset h_0. The normalized intensity for reconstruction within adhered regions is shown at small heights < 30 nm (black). Branch numbers are indicated at the top.

simple theory was considered, while for experiments with more elevated heights the finite aperture theory was applied. Figure 2.19 shows the theoretical curves for three interface RICM, once neglecting and once accounting for numerical aperture effects. Note the shift by $h_0 = 35$ nm. Both curves in the 0th and 1st branch exhibit high agreement up to 3 nm at 100 nm height, which is just below RICM axial resolution and permits the application of the simple theory for low height objects.

2.3.4.4 Dual-Wavelength Reflection Interference Contrast Microscopy (DW-RICM)
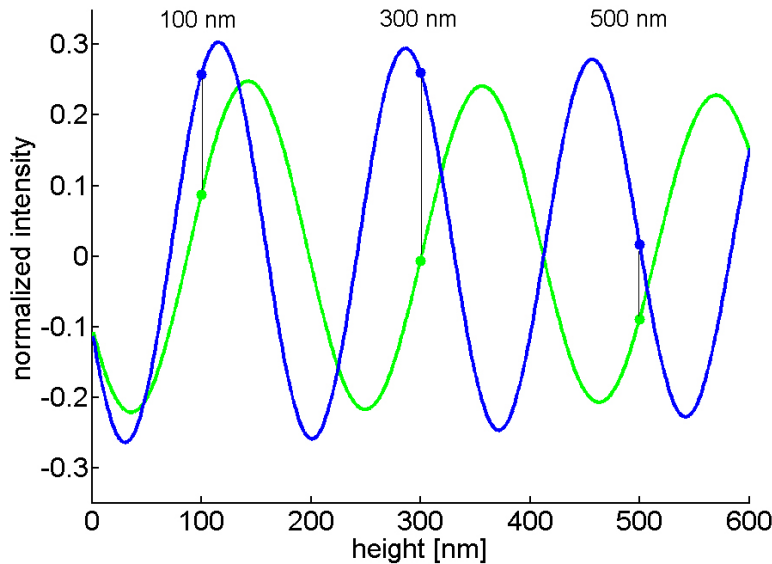
Figure 2.20: Normalized intensities of DW-RICM for $\lambda_b = 436$ *nm* (blue) and $\lambda_g = 546$ *nm* (green) with finite INA. From simultaneous recording of two intensities an unambiguous height can be assigned as indicated for 100 nm, 300 nm and 500 nm.

A serious limitation of RICM is the ambiguity in height determination, which arises from the cosine dependence of the intensity on height. Thus one intensity value can belong to multiple heights and high knowledge of the system is needed to choose the correct branch (see figure 2.19) for height reconstruction.

In order to overcome this limitation DW-RICM has been introduced [101]. Here, the object is illuminated simultaneously with a second wavelength and from the altered interference mechanism a different image is obtained. A simultaneous recording of two images then provides double intensity information which is used to assign one unambiguous height value, as depicted in figure 2.20. Depending on the different wavelengths chosen,

their common periodicity can be as high as $\sim 1\mu m$, such that absolute heights are measured unequivocally up to that distance. Moreover, as wavelengths are chosen to differ by several hundred nm, the enlarged phase difference between them facilitates a height assignment even further. However, often the choice of wavelengths is limited by the available lines in the spectrum of the light source, such that optimal conditions are not realized.

In this thesis, vesicle - substrate distances varied substantially within 1 μm, wherefore the application of DW-RICM proved to be a suitable tool for analyses. This technique was used to detect the structured adhesion area of the vesicle, to reconstruct membrane topography in the adhered and fluctuating regions for equilibrated vesicles as well as during dynamic changes. Moreover, membrane fluctuations were analyzed in its amplitudes an spectrum.

2.3.4.5 Antiflex Technique

RICM was drastically improved with the invention of the antiflex technique by Ploem in 1975 [105]. This technique exploits the polarized state of light in order to eliminate stray light. The resulting increase in contrast enables to image objects which reflect only a small amount of light, as it is the case for phospholipid membranes. Three optical elements, a polarizer, an analyzer and a $\lambda/4$ - plate are added to the light path of the microscope. The polarizer is placed in the beam path of the incident light and transmits only light of specific linear polarization. As the light is deflected onto the specimen, it passes the objective and subsequently the $\lambda/4$ - plate which changes the polarization from linear to circular. The electric field of the beam thus possesses a parallel and a perpendicular component with respect to the plane of incidence. As the light reaches the specimen and gets reflected at the transition of an optically dense to an optically thin medium, the parallel component of the electric field encouters a phase shift by π. On the other hand, as the light gets reflected at the optically dense medium, the perpendicular component is phase shifted by π [106].

Thus, all reflected light which traverses the $\lambda/4$-plate a second time exhibits a linear polarization which is perpendicular to the polarization of the incident beam. The analyzer is placed shortly before the detector and oriented to allow all light reflected by the object to pass the analyzer. This is detected, while almost all scattered light within the optics is blocked. As a result the image contrast is drastically enhanced.

2.3.4.6 Image Acquisition

Set-up and image acquisition were optimized during my diploma thesis [53]. As sketch of the light path is given in figure 2.21. Based on the settings reported therein experiments were conducted as follows:
DW-RICM images were acquired with the inverted microscope set-up described in section 2.3.1. From the spectrum of the metal halide lamp the two strongest intensity lines, $\lambda_g = 546\ nm$ and $\lambda_b = 436\ nm$, were selected with a dualband interference filter (436/10 nm 546/10 nm, AHF, Tübingen, Germany). For the application of the antiflex technique, the $63\times$ Plan-Neofluar Antiflex oil objective of NA 1.25 equipped with a $\lambda/4$ plate (Carl Zeiss) was used. Also, a filter cube consisting of crossed polarizers with a beam splitter in the centre (Carl Zeiss) was used. In order to detect the light of each spectral line by one CCD camera, another filter cube was positioned right before the cameras (beam splitter FT 460 nm, longpass filter LP 470 (Zeiss) and bandpass filter BP 436/10 nm (AHF)). The numerical aperture of illumination was set to 0.54. For vesicles in equilibrium, sequences of 2000 micrographs were recorded simultaneously for the two spectral lines. Each recorded frame had an exposure time of 51 ms. In addition, a phase contrast image of the vesicle as well as a fluorescence image of the underlying substrate were recorded at 100 ms.
To observe vesicles during changes of osmotic buffer conditions, approximately 200 frames were recorded prior to disturbance and recording was continued for some 1000 frames. Here the exposure time was set to 100 ms.
For posterior superposition of images, parallel camera orientation and
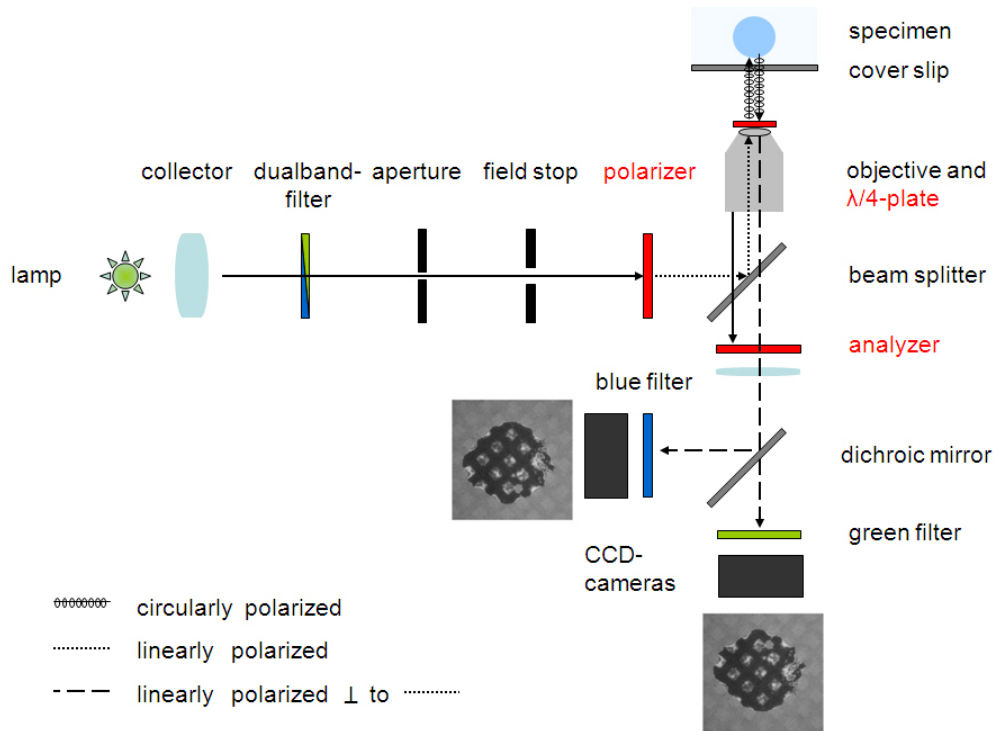
Figure 2.21: Light path in DW-RICM. Two spectral lines, $\lambda_g = 546$ nm and $\lambda_b = 436$ nm, are selected from a metal halide light source and linearly polarized. A $\lambda/4$ plate on top of the objective converts linearly to circularly polarized light and vice versa. As the circularly illumination light is reflected in the specimen, it encounters a phase shift by π. As a result the linear polarizations of reflected and initial light are perpendicular towards each other. Thus, the reflected light can be filtered and detected. A dichroic mirror before the CCD cameras, splits the beam into both spectral parts and two interferograms are recorded. Modified sketch taken from [33].

agreement in focus position were checked prior to each experiment by means of a chrome pattern on an electron beam mask (see section 2.1.5 for mask details). A yet remaining lateral shift between images was accounted for by a routine based on crosscorrelation leading to an error in superposition accuracy of ± 1.3 pixels [53].

Since quantitative information was drawn from the recorded intensity pat-

tern the camera was characterized in its linearity and shot noise. First, the linear intensity response of the camera was checked from recording a calibration curve of a well defined light standard. Therefore, a red light emitting diode (HLMP-4700, Hewlett Packard, Palo Alto, CA, USA) was triggered by a function generator (DS 345, Stanford Research Systems, Sunnyvale, CA, USA) in duty cycles of 0%-100% and the resulting intensity was recorded through an $20\times$ air objective. Evaluation of the recorded counts verified a linear camera response for intensities up to 2000 counts. Care was taken not to exceed this limit during experiments and the illumination intensity of the metal halide lamp was adjusted accordingly. Second, the cameras' shot noise dependence on the signals' intensity was determined. To this end, is was assumed that measured intensity fluctuations of the calibration standard follow Poisson statistics [107]:

$$stdI = \sqrt{\frac{1}{N-1}\sum_{i=1}^{N}(I_i - \langle I \rangle)^2} = p \cdot \sqrt{\langle I \rangle}$$

where p is the shot noise specific prefactor. Plotting the measured intensity fluctuations $stdI$ vs. $\sqrt{\langle I \rangle}$, the prefactor p = 0.698 was determined. Application of this relation to experimental data allowed for a calculation of shot noise. Evaluation of this calibration procedure was done by S. Fenz and is published elsewhere [108].

In addition, for quantitative analysis of images acquired with the $63\times$ EC Plan-Neofluar Antiflex objective, the square pixel size as well as the illumination numerical aperture (INA) were determined. For pixel sizes, images of a standard micrometer scale (Carl Zeiss) were recorded and analyzed. For INA, the microscope aperture was set to two well defined positions (outer site of the phase ring (PR) and closed) and the size of the illumination beam at the site of the specimen was recorded. Table **??** shows the results of these measurements.

pixel size [nm]	#	INA: outer PR/closed	#
100 ± 0.2	13	0.54/0.25	5 each

Table 2.2: Results of pixel size and INA determination for the inverted microscope set-up equipped with a $63\times$ EC Plan-Neofluar Antiflex objective. # denotes repeats in measurement and PR is the phase ring.

2.4 Data and Image Analysis

Images and Data were mostly analyzed using self-written routines in Matlab (version 3.0 (R2010b), The MathWorks, Inc. MA, USA) utilizing the image processing toolbox. Some FCS data was analyzed with OriginPro (version 8G, OriginLab Co., Northampton, MA, USA) and Microsoft Office Excel (2007, Microsoft Co., Redmond, WA, USA).

2.5 Conclusion

In this chapter details of the model system under study as well as the techniques used to probe it were presented. The model system was a giant unilamellar vesicle, produced by electro-swelling, which either rested on passivated substrates or adhered to specially prepared adhesive substrates. The substrates that were studied in detail exhibited receptors presented in the form of grid or line patterns, created by micro-contact printing. We focussed on membrane shape, membrane fluctuations and diffusion measurements. Standard optical microscopy techniques including phase contrast, confocal and FRAP microscopy was described. Principle and calibration of FCS, which was established in the laboratory in the course of this thesis was described. In later chapters I will describe how the conventional FCS set up was exploited to put in place the new technique of fluctuation correlation spectroscopy which measures small displacements of the membrane. Dual wave reflection interference contrast microscopy was described in detail as was the refinements achieved for

reliable measurement of the absolute membrane to substrate distance, the membrane shape close to the substrate and membrane fluctuations above the substrate.

Chapter 3

Constrained Membrane Fluctuations: Model System Characterization

This chapter first gives a short overview on the current understanding of adhesion to heterogeneously distributed receptors. Next, results on membrane adhesion topography, membrane fluctuation and lipid diffusion are presented. Differences arising from structured versus homogeneous adhesion are discussed.

3.1   Introduction

The adhesion of cells to each other or to the extracellular membrane involves the formation of complex adhesion structures. In the free membrane multiple constituents of the membrane with different mechanical and chemical properties naturally result in heterogeneous distributions of molecules, while any active cellular mechanism adds to this domain establishing effect. Upon adhesion, cluster of receptor-ligand bonds are observed, so called focal adhesions. In addition physico-chemical properties of the substrate proved to not only influence molecular adhesion structures on mesoscopic scales, but also induced microscopic changes.

These affected e.g. cell morphology in preferred orientation and dimension [109,110]. Other in vitro studies on cells demonstrated the influence of ligand concentration on adhesion dynamics and finally attained adhesion strengths [111]. Moreover, evidence on induced conformational changes as well as cell orientation along adhesion pattern was found [112]. At mesoscopic scales numerous diffusion studies revealed the state of molecular mobility at bound and unbound regions of the plasma membrane [113,114].

Yet, little is known on the physical effects governing adhesion to inhomogeneous structures. Due to the interplay of attractive and repulsive physical forces distinct differences on the final state of adhesion are anticipated, giving rise to a number of questions:

- Under what conditions are repulsive forces strong enough to prevent adhesion ?

- Does adhesion to specific structures alter membrane properties, like fluctuation and tension, in comparison to adhesion to homogeneous receptor distribution ?

- Are molecules confined to within distinct regions or is exchange still possible ?

- How does structure affect the response to external disturbances, such as osmotic shocks ?

In the present study these questions are addressed by means of giant unilamellar vesicles adhering to micropatterned substrates. These simplified biomimetic systems are most suitable for quantitative studies, however, no system of structured adhesion has been investigated so far. Only recently, with the advent of methods for controlled biomolecular micropatterning and the rising interest in biocompatible applications, more and more of the above questions are addressed. In contrast to the lack of biomimetic experiments, some theoretical studies already focused on discretely pinned membranes [31,32].

With the biomimetic model system described in section 2.2.3 this work aims to obtain an understanding of physical laws governing structured adhesion. While in this chapter, results on equilibrium membrane topography, fluctuation strength and lipid mobility are presented, effects of structure modification and external disturbances are addressed in the subsequent chapter.

3.2 Experimental Realization

The model system used in this study consisted of components described in section 2.2.3. The large grid structure of adhesive grid and neutral square regions (see section 2.2.2.1) was used as adhesive basis. For the observation of vesicle adhesion, GUVs and substrates were prepared according to the protocols of sections 2.2.1.1 and 2.2.2.1, respectively. For experiments on lipid diffusion first calibration measurements on SLBs were undertaken (see section 2.2.1.2 for preparation). Here, the lipid mix described in section 2.2.4 was used. Second, diffusion in structured adhered vesicles was examined. Therefore, GUVs contained a fluorophore coupled lipid, in addition to the regular lipid mixture (see section 2.2.4). In these cases, TMR coupled NAV was exchanged for plain NAV (see section 2.1.3) in order to avoid any cross talk in fluorescence detection. The chamber was filled with $300 \, \mathrm{mOsm/l}$ PBS and, after addition of $20 \, \mu l$ vesicle solution, covered with a glass slide. Vesicles filled with $230 \, \mathrm{mOsm/l}$ sucrose solution sedimented to the substrate and adhered immediately. After 30 min. recordings were started with settings described in section 2.3.4.6.

3.3 Results and Discussion

3.3.1 Membrane Equilibrium Shape and Fluctuations

3.3.1.1 Topography Analysis

After adhesion the vesicle exhibited bound and unbound membrane regions according to the underlying pattern. Towards the edge of the ad-
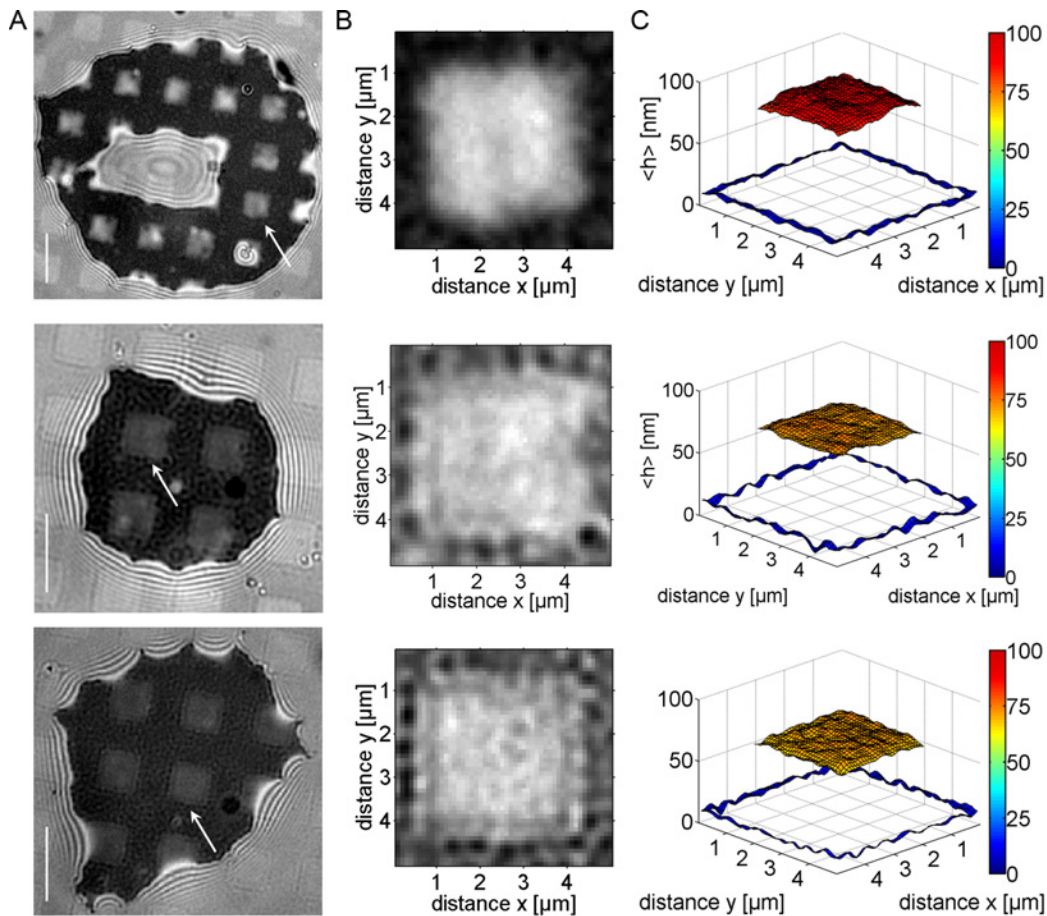
Figure 3.1: Reconstructed topography of structured adhered vesicles. A: RICM images of structured adhered vesicles. White arrows point to the fluctuation region depicted on the right. Scale bar 7 μm. B: Intensity images of square regions corresponding to arrow in A. C: Reconstructed height maps. Regions of steeply curved membrane were omitted from the analysis. This corresponds to the gap between the adhered edge and free membrane centre. The colorcode indicates average heights in nm. Note the scale difference between h and x, y axes.

hesion disc, 2-3 interference fringes were observable. In some cases, blisters of enclosed buffer within the adhesion zone were detected. These appeared as circular interference pattern, often spanning 1-3 lattice con-

stants and remained stable over the time of observation (see figure 3.1 for examples).

On the adhesive grid, the membrane was attached to the receptor at fixed average height of $\sim$ 19 nm. This value was deduced from AFM substrate analysis (undertaken in cooperation with S. Dieluweit, ICS-7, FZJ), which was reported in [53] and confirmed by DW - RICM height reconstruction (see figure 3.1).

Within square regions of the adhesion zone the membrane was free to fluctuate and exhibited variable intensity pattern. This observation demonstrated that repulsive interaction within the non-adhesive regions was strong enough to maintain spatial partitioning between membrane and substrate. As already presented in an earlier work of the author, height reconstruction of fluctuating regions revealed strong elevation of the membrane from the patterned edge towards the centre, where a plateau was reached [53].

For analyses, membrane topography was reconstructed with DW-RICM as described in section 2.3.4. Figure 3.1 gives typical examples of structured adhered vesicles and reconstructed topography of fluctuation areas. Between fluctuating and bound region, the membrane curves up strongly and RICM analysis is expected to fail in this region. To avoid errors introduced by this seven pixels around the fluctuation area were left out in reconstruction.

In the following, nine central points of each fluctuation area were considered and height values over time of each extracted (see figure 3.2). These were plotted in a histogram and fitted with a normal distribution to verify the applicability of Gaussian statistics. Heights were then averaged over time and, subsequently, the average of mean heights and standard deviations was calculated. An equilibrium height of $\langle h \rangle = 76 \pm_p 8 \ nm$[1] was determined averaging over 88 fluctuation areas. Long term studies of fluctuation areas over 30 - 60 min revealed no significant changes in height (see [53]). Moreover, the observed plateau together with the alike average

---

[1]To distinguish between standard deviation of the population and standard deviation of the mean, the symbols $\pm_p$ and $\pm_m$ are used, respectively.
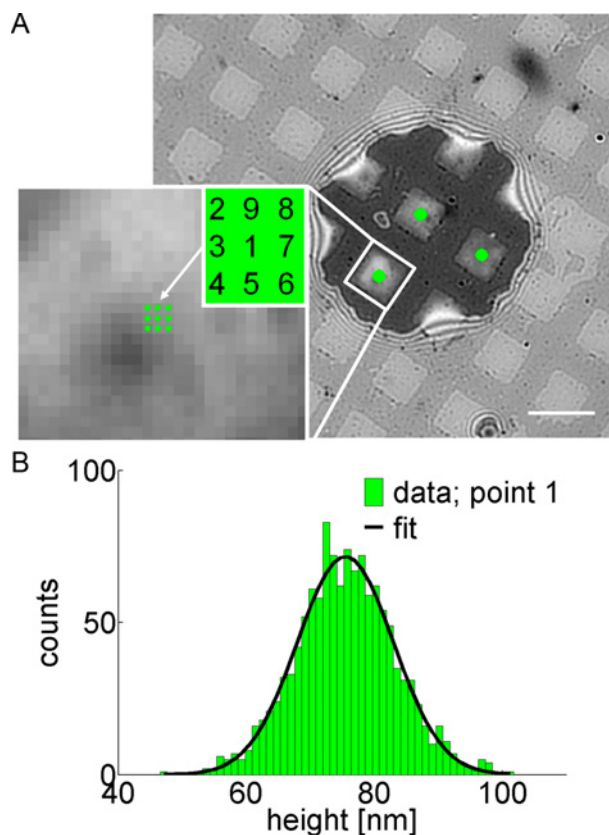
Figure 3.2: A: RICM image of structured adhered vesicle. The detail shows the position of nine central points, used for analysis. Scale bar: 7 μm. B: Histogram of measured heights over time in point 1 (green). A Gaussian was fitted to the data (black).

heights were interpreted as the position of the unspecific interaction potential minimum. This hypothesis was supported by further experimental analysis (see 3.3.2.2 and 4.2.1.2).

An upper limit for the equilibrium height and heights of similar value were found from RICM studies on free and weakly adhering vesicles: While Sengupta et al. [104] recorded vesicles hovering on a liquid cushion at $\sim 100 - 200$ nm above the substrate, Rädler et al. [115] determined an equilibrium height of ~ 40 nm for vesicles adhering to BSA covered MgF_2 substrates.

As a result, height analysis gives first evidence for weak vesicle adhesion
to patterned large grid substrates.

3.3.1.2 Fluctuation Analysis

To calculate mean square fluctuation amplitudes, first squared deviations
from the mean height were averaged over time $\langle \delta h^2 \rangle = \langle (h(t) - \langle h \rangle)^2 \rangle$ and
the average of nine central points was calculated. The average fluctuation
amplitude within the central area was $\sqrt{\langle \delta h^2 \rangle} = \sqrt{\langle (h - \langle h \rangle)^2 \rangle} = 12 \pm_p 2$
nm. This is in the range of values reported by Albersdörfer et al. [44] and
Bruinsma et al. [116], who observed vesicles in the process of adhesion.
Slightly smaller amplitudes were found by Rädler et al. [115].
Thus here fluctuations are of intermediate strength, between those of free
and strongly confined membranes, which confirms the previous finding
of weak adhesion to large grid patterned substrate (see section 3.3.1.1).
Further analysis of measured amplitudes plotted against average heights
resulted in a linear dependence. As illustrated in figure 3.3, fluctuation
amplitudes increase slightly with average heights.
Theory of membrane fluctuations near a wall predicts linear (limit of low
tension) or logarithmic (limit of high tension) scaling of amplitudes with
separation distance [24, 117][2]:

$$
\sqrt{\langle \delta h^2 \rangle} = \begin{cases} c \cdot \langle h \rangle & \sqrt{\langle \delta h^2 \rangle} < l_\sigma \\ l_\sigma \sqrt{\left(\frac{\langle h \rangle}{2l_\sigma} + \frac{1}{8} \ln\left(\frac{\langle h \rangle}{l_\sigma} \right) \right)} & \sqrt{\langle \delta h^2 \rangle} > l_\sigma \, , \end{cases} \tag{3.1}
$$

$l_\sigma = \sqrt{(k_B T / (2\pi\sigma))}$ is the crossover length between the two regimes and
c is a dimensionless prefactor. Inserting the average fluctuation amplitude
in $\sqrt{\langle \delta h^2 \rangle} < l_\sigma$ an upper tension limit is estimated below which linear
scaling holds. With $\sqrt{\langle \delta h^2 \rangle} = 12$ nm, σ amounted to 4.5 $\mu J / m^2$. In the
following it is shown, that typical vesicles featured a value just below this
tension, thus indicating linearity.

---

[2]In this work $\langle \delta h \rangle$ is identified with the vertical roughness amplitude, $\xi_\perp$, reported
therein.

Next, linear regression was applied and $c = 0.135$ determined. This is a factor $\times 3$ smaller than the theoretical scaling behaviour of two membranes separated by $\sqrt{\langle \delta h^2 \rangle}$ [117]. Precisely, in the limit of vanishing interaction potential $c = 0.45$, while for an attractive potential values of $c = 0.79$ were reported [117].

Similar deviations were detected in experiments by Rädler et al. [115]. Systematically smaller amplitudes found there were attributed to the limited spatial and temporal resolution of the camera. As their sampling rate of 25 Hz indicates prevalent camera performance[3], these findings underline the need for understanding the impact of finite resolution on the data.

3.3.1.3 Membrane-Substrate Interaction

Lipowsky et al. also derived an expression for the mean square amplitude $\langle \delta h^2 \rangle$ in presence of membrane-substrate interaction [24]. Again assuming small tensions, their expression reads:

$$\langle \delta h^2 \rangle = \frac{k_B T}{8\sqrt{\kappa \gamma}} \quad \sigma < \sigma^* \tag{3.2}$$

Here, γ is the second derivative of the interaction potential and $\sigma^* = \sqrt{4\kappa\gamma}$ a cross-over tension distinguishing between bending rigidity and tension dominated adhesion. Solving the equation for γ and substituting the upper equation of 3.1 for $\sqrt{\langle \delta h^2 \rangle}$, a $\propto 1/\langle h \rangle^4$ height dependence of γ is obtained:

$$\gamma = \frac{(k_B T)^2}{64\kappa(c \cdot \langle h \rangle)^4} \quad . \tag{3.3}$$

γ values calculated from fluctuation amplitude data are depicted in figure 3.3. With increasing height γ declines hyperbolically from $7.8 \cdot 10^8$ to $0.3 \cdot 10^8$ J/m^4. This trend is intuitive, as membrane fluctuations further away from the substrate are less confined and thus able to probe larger range of heights. As this graph was generated from the same data a $1/\langle h \rangle^4$ least square fit yielded a similar prefactor, $c = 0.130$. However, for small heights

---

[3]In the present system sampling rates were 20 Hz.

the hyperbolic decay in figure 3.3 appears to be stronger than suggested by equation 3.3. Here effects of stronger tension may already play a role. The average curvature of the potential, γ, is within the range of values reported for unspecific minima. With $\gamma \sim 10^8$ J/m^4, the curvature is a magnitude stronger as compared to measurements of weak adhesion by Rädler et al. [115]. On the other hand, Bruinsma et al. [116] estimated the curvature of the unspecific interaction to be on the order of 10^{12} J/m^4. Thus, γ values of this system also characterize a rather weak adhesion state.
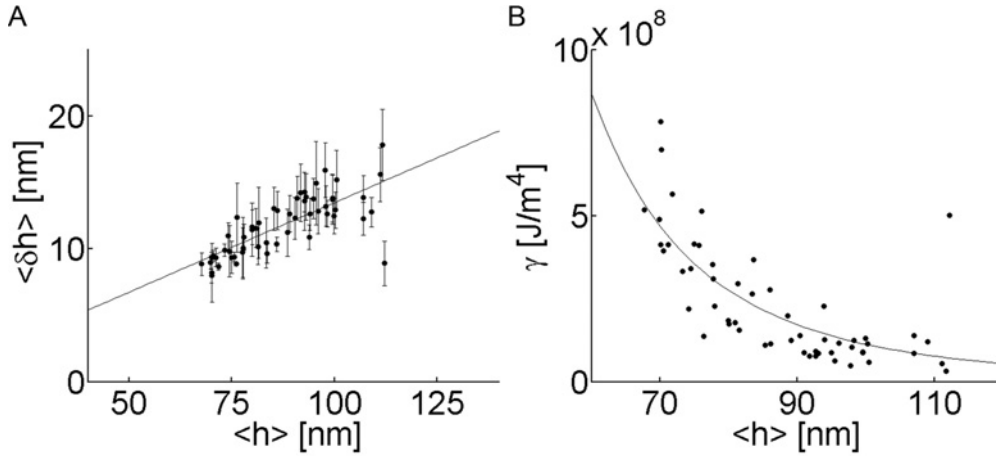
Figure 3.3: A: Average fluctuation amplitude $\sqrt{\langle \delta h^2 \rangle}$ vs. average height $\langle h \rangle$ measured at the centre of fluctuation areas. A linear increase is observed and a slope c = 0.135 determined from linear regression. B: Interaction potential curvature γ vs. $\langle h \rangle$. A $1/h^4$ hyperbolic decay is predicted from theory. The parameter c = 0.130 yielded best agreement between fit and data.

3.3.1.4 Theoretical Analysis

The experimental findings reported above agree well with numerical calculations by Daniel Schmidt, II. Institute for Theoretical Physics, Stuttgart University [118]. In his model, the membrane equilibrium profile is determined of the bending rigidity κ, the membrane tension σ, the interaction

potential curvature γ, equilibrium height $\langle h \rangle$ and square side length d of the pattern as variable parameters. Knowing κ, $\langle h \rangle$ and d, the system parameters σ and γ were obtained from the theoretical fluctuation amplitude expression of a free membrane residing in an interaction potential [118]:

$$\langle \delta h^2 \rangle = \frac{k_B T}{2 \cdot \pi} \int dq \, \frac{1}{\kappa q^3 + \sigma q + \gamma / q} \quad . \tag{3.4}$$

From experimentally determined $\langle \delta h^2 \rangle$ approximately 10 parameter combinations (σ, γ), were found to satisfy equation 3.4. In order to isolate the optimal parameter set, profiles of each case were calculated and compared to the experimental shape. From the smallest mean square deviation, the best theoretical representation was identified.

With this model nine 'typical' fluctuation areas, with average heights around 74 nm, and eight fluctuation areas at the 'low $\langle h \rangle$ limit', at 68 nm, were analyzed. Table 3.1 gives an overview of determined σ and γ values for the two cases. High agreement between theoretical and experimentally determined profiles was found, as mean square deviations were at most 2.6 nm^2.

Results of the 'typical' case are in well agreement with estimates from

case	$\sigma \, [\mu J / m^2]$	$\gamma \, 10^8 \, [J / m^4]$	#
typical	$3.7 \pm_p 0.7$	$2.3 \pm_p 0.2$	9
low $\langle h \rangle$ limit	$17.8 \pm_p 2.5$	$3.5 \pm_p 1.0$	8

Table 3.1: Theoretically determined membrane parameters for a 'typical' and 'low $\langle h \rangle$ limit' adhesion case. Calculations were done by D. Schmidt [118].

experimental data: σ is below the estimated upper tension limit $\sigma = 4.5$ $\mu J / m^2$, up to which weak adhesion holds. γ agrees well with the previously determined range of curvatures $\gamma = (2 - 5) \cdot 10^8 \, J / m^4$. In fact, 'typical' adhesion of vesicles to patterned substrates results in membrane parameters resembling weak adhesion to homogeneous substrates.

For the 'low $\sqrt{\langle \delta h^2 \rangle}$ limit' the situation is slightly different. Here fluctuation amplitudes $\sqrt{\langle \delta h^2 \rangle}$ were measured to be $\sim$ 8 nm (see figure 3.3).

Using $\sqrt{\langle \delta h^2 \rangle} < l_\sigma$, as before, a crossover tension $\sigma \sim 10\ \mu J/m^2$ is found. Thus, with $\sigma = 18\ \mu J/m^2$ (see table 3.1) theoretical analysis deduces a probable crossover of some vesicles to the tension dominated regime. While these seem to adhere more strongly to the substrate, the interaction potential curvature γ, which also depends on σ, increases only slightly (compare table 3.1) [118]. Apparently, γ is only moderately affected by tension changes. This finding indicates, that the tension dependent interaction term does not dominate the overall interaction.

In order to obtain further insight into the physical forces contributing to this interaction, these values are used in the following to construct a specific form of the interaction potential.

3.3.1.5 The Interaction Potential

Further understanding of the obtained membrane properties was anticipated from elucidating the individual forces acting on the membrane in the vicinity of the substrate. As for previous analysis, focus was on the centre of each fluctuation region, where the membrane was assumed to be freely fluctuating. Here, membrane-substrate interaction was assessed as superposition of mere unspecific interaction terms.

Attractive generic forces relevant for this system are van-der-Waals force and gravity. This attraction is counterbalanced mainly by entropic Helfrich repulsion, which arises from thermally induced membrane fluctuations. At very short distances steric repulsion due to the hydrated layer of polymer molecules arises. In the following, the specific form of each contributing interaction is shortly presented:

The van-der-Waals (vdW) interaction is of electrostatic nature, as it results from an attractive interaction between permanent and induced dipoles. For the system under study the best representation of this interaction is given by Lifshitz theory for a geometry of four planar layers: glass (g) - buffer (b) - membrane (m) - sucrose solution (s). Here, all interfaces ex-

hibiting large differences in dielectric properties are accounted for[4]. According to Parsegian the vdW - interaction for this situation reads [119]:

$$V_{vdW}(h_s) = -\frac{A_{gb|mb}}{12\pi h_s^2} - \frac{A_{gb|sm}}{12\pi(h_s + d)^2} \quad , \tag{3.5}$$

where d is the thickness of the bilayer and $h_s = h - R_{BSA} - R_{PEG}$ the glass-membrane distance, shifted by radii of gyration of BSA and PEG[5]. $A_{gb|mb}$ and $A_{gb|sm}$ are the Hamaker constants accounting for the dipole interaction across the buffer and buffer-membrane interface, respectively. In general, they depend on frequencies $\nu_n = k_B T\, n/\hbar$, $n \in \mathbb{N}$ and, with $\hbar$ the reduced Planck constant, for each fluctuation mode n as well as on layer spacing. Due to the small distances considered here, the latter dependence is neglected. Moreover, media exhibiting the same dielectric constants, such as (b) and (s), follow the relation $A_{gb|mb} = -A_{gb|sm}$ [119]. Thus, only $A_{gb|mb}$ had to be calculated. Moreover, interaction across an electrolyte solute results in screening effects from free polarized ions which drastically reduce the $\nu = 0$ frequency contribution. On the other hand, higher frequency terms remain unaffected [120]. Consequently, the screened non-retarded Hamaker constant subdivides into:

$$A_{gb|mb} = A_{\nu=0} \cdot 2k_D h\, e^{-2k_D h} + A_{\nu>0} \quad .$$

where, $k_D = 1/0.74\ nm^{-1}$ is the Debye length for PBS,

$$A_{\nu=0} = \frac{3}{4}k_B T \left(\frac{\epsilon_g - \epsilon_b}{\epsilon_g + \epsilon_b}\right)\left(\frac{\epsilon_m - \epsilon_b}{\epsilon_m + \epsilon_b}\right) \quad \text{and}$$

$$A_{\nu>0} = \frac{3\, h\, \nu_e}{8\sqrt{2}}\frac{(n_g^2 - n_b^2)(n_m^2 - n_b^2)}{(n_g^2 + n_b^2)^{1/2}(n_m^2 + n_b^2)^{1/2}\{(n_g^2 + n_b^2)^{1/2} + (n_m^2 + n_b^2)^{1/2}\}} \quad .$$

---

[4]The adsorbed BSA protein layer on the glass substrate does not exhibit as strong differences in dielectric properties as the membrane with its adjacent layers. Therefore, its influence on the Hamaker constant was not considered.

[5]Note that the origin of the height axis h is at the glass - buffer interface. However, in the experiment an additional protein layer R_{BSA} is on top of the glass as well as a polymer of radius R_{PEG} attached to the membrane. Both lead to a shift of the minimal possible height.

Inserting the dielectric permittivities $\epsilon_g = 4.5$, $\epsilon_b = 80$, $\epsilon_m = 2.1$, [119] and refractive indices $n_g = 1.523$, $n_b = 1.3347$, $n_m = 1.486$, the zero frequency, $A_{\nu=0} \sim 0$ vanishes. On the other hand, dispersion forces contribute to the Hamaker constant, such that $A_{gb|mb} = A_{\nu>0} = 7 \cdot 10^{-21}$ J $= 1.7\,k_B T$. This value is in accordance with measurements on biological material immersed in water, with typically $A_{gb|mb} = 0.75 - 4\,k_B T$ [11].

Gravitation plays a role, since vesicles are filled with sucrose solution of higher density than the surrounding buffer. For a deflated vesicle, forming a contact area $A = \pi R_A^2$ on the substrate, gravity is given by [115]:

$$V_{grav}(h_s) = \frac{V}{A} \cdot \Delta \rho \cdot g \cdot h_s \quad , \tag{3.6}$$

where $V = 4/3\pi R_V^3$ is the vesicle volume, $\Delta \rho$ the density difference between vesicle in- and exterior and g the acceleration due to gravity. On average, the vesicle equatorial radius R_V scaled with contact area radius R_A as $R_V \sim 1.5 \times R_A$.

The Helfrich interaction accounts for membrane out of plane fluctuations, which generate an entropic repulsion in the vicinity of a substrate. As the membrane approaches the substrate, it repeatedly bumps against the substrate whereby its fluctuations are attenuated. In 1978, Helfrich was the first to include this entropic term, V_H, in the interaction potential for the case of tensionless membranes [121]. Seifert extended Helfrich's work for tension [19] and proposed:

$$V_H(h_s) = \frac{1.5\,b\,k_B T \sigma}{\kappa\,\sinh^2\left(\frac{h_s}{2}\sqrt{\frac{\sigma}{b\,k_B T}}\right)} \quad , \tag{3.7}$$

where parameters are as before and b is a dimensionless prefactor. Its value was determined to 0.1 - 0.2 from Monte Carlo simulations [122] and renormalization group theory [24] for single free membranes.

Polymer steric repulsion contributes, once the membrane-substrate distance is minimized to the point where the polymer layer is squeezed together. From this, high energy cost arises, which results in a potential barrier at ~ 4 nm. This repulsive interaction was calculated according to Bruinsma et al. [116] for fixed concentration ensemble below overlap concentration:

$$V_{rep}(h_s) = \frac{\pi^2}{6} k_B T \sigma_0 \left(\frac{R_{PEG}}{h_s}\right)^2 e^{-\frac{3}{2}\left(\frac{h_s}{R_{PEG}}\right)^2} \quad .$$ (3.8)

Here, R_{PEG} is the radius of gyration of polyethylene glycol polymers and σ_0 their density.

With these considerations, the total interaction potential reads:

$$V_{tot} = V_H + V_{vdW} + V_{rep} + V_{grav} \quad .$$ (3.9)

Parameters appearing in equations 3.5 - 3.8 and the respective source are given in table 3.2. It has to be noted, that the Helfrich parameter $b = 0.67$ was chosen $\times 3$ larger, as it was originally determined by Helfrich and Safinya et al. [12, 123]. This is understood from recent studies by Lipowsky and Netz [24, 117], who accounted for tension effects as well as the influence of a potential. From their calculations the prefactor c was found to lie in the limit of zero potential (see section 3.3.1.1). In this limit b also changes to ~ 0.6 [117]. Figure 3.4 illustrates the shape of total interaction potentials for the range of tensions derived in section 3.3.1.1. The corresponding range of heights is indicated by dashed axial lines. In addition, the value for γ, the curvature of the interaction potential, was determined from a parabolic fit to 20 points around its minimum.

The simple superposition of interaction terms results in potential shapes, which are in good agreement with the range of tensions and heights derived in section 3.3.1.1. However, γ values presented there, exceed curvatures determined here by an order of magnitude. The same discrepancy between γ values was already observed by Bruinsma et al. in 2001 using
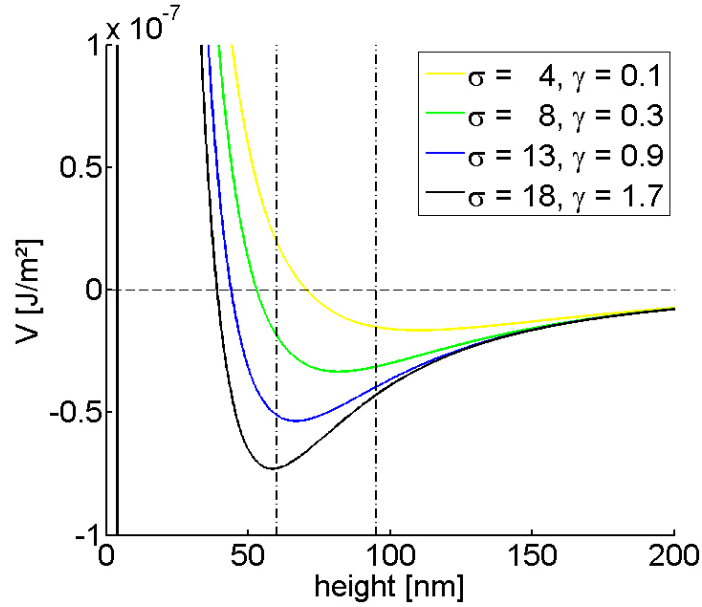
Figure 3.4: Total interaction potential shapes V_{tot}, with σ given in $\mu J/m^2$ and γ given in $10^8\ J/m^4$.

similar equations [124]. Up to date this problem appears to be unsolved. There are two possible explanations for this inconsistency. Either, an interaction is missing in equation 3.9 and e.g. 'enclosed' buffer below the membrane generates a hydrodynamic pressure which constrains membrane motion further. Or, finite resolution strongly diminishes fluctuation amplitudes presented in section 3.3.1.1. According to equation 3.2, an increase in amplitude by[6] $\times$ 3 would correspond to a curvature decrease by 81. Thus, γ would be on the order of $10^6\ J/m^4$, which is now smaller than curvatures given in figure 3.4.

Of course, this rough estimate only shows that resolution affects data in the right direction. A rigorous theory accounting for finite resolution is developed.

---

[6]this factor was estimated in section 3.3.1.2.

parameter	symbol	value	source
vesicle tension ('c')	σ	$4 - 18 \cdot 10^{-6}\ J/m^2$	[118]
density difference ('c')	ρ	$0.01 \cdot 10^3\ kg/m^3$	–
polymer density ('c')	σ_0	$10^{20}/2813\ 1/m^2$	–
Hamaker constant ('c')	$A_{gb|mb}$	$7 \cdot 10^{-21}\ J$	[119]
bending rigidity ('l')	κ	$20\ k_B T\ J$	[125]
membrane thickness ('l')	d	$4 \cdot 10^{-9}\ m$	[46]
PEG radius of gyration ('l')	R_{PEG}	$3.4 \cdot 10^{-9}\ m$	[126]
BSA radius of gyration ('l')	R_{BSA}	$4.5 \cdot 10^{-9}\ m$	[127]
Boltzmann constant ('l')	k_B	$1.38 \cdot 10^{-21}\ J/K$	–
Helfrich parameter ('l')	b	0.67	[117]
equatorial vesicle radius ('m')	R_{ves}	$35 \cdot 10^{-6}\ m$	–
temperature ('m')	T	$298\ K$	–

Table 3.2: Overview of literature ('l'), measured ('m') or theoretically calculated ('c') parameters appearing in the calculation of the total interaction potential of the present system. See equations 3.5 - 3.9.

3.3.2 Lipid Diffusivity

Up to this point, much has been clarified about microscopic membrane properties of the model system. However, the situation at nanoscopic lengthscales is still obscure.

In the following section analyses on lipid diffusion are presented. First, a novel variant of regular FCS measurements, the z-scan method, is applied to SLBs. Second, comparative studies of z-scan FCS and FRAP are discussed. These shed light on the lipid state within each characteristic membrane part of the model system: The vesicle top and the adhesion zone with bound and fluctuating regions.

Special consideration for the execution of FCS measurements and its key components is given in appendix A. Supplementary information provided there sums up the preparatory work undertaken to validate FCS measurements.

3.3.2.1   Z-scan FCS in Solid Supported Membrane

Z-scan FCS on SLBs were performed to determine the confocal volume waist ω_0 and to characterize lipid diffusion under standard experimental conditions.

For z-scan measurements, first, confocal images were acquired to roughly
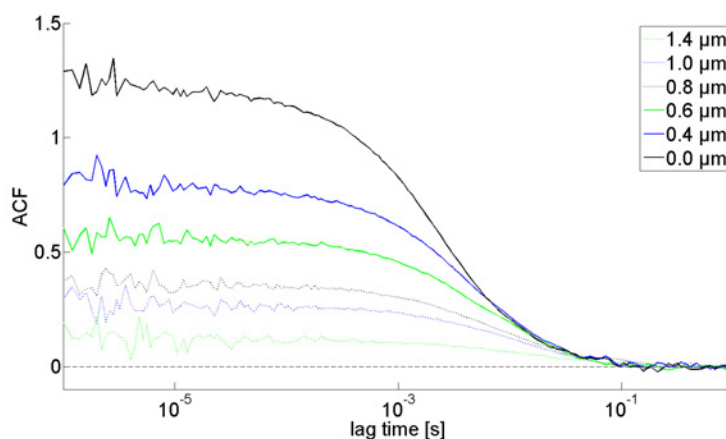
Figure 3.5: Example of z-scan FCS through SLB containing 0.01 mol% Bodipy-Fl DHPE tracer molecules. ACFs at different distances Δz from the centre. With increasing Δz, amplitudes decay, corresponding to increased particle number and diffusion times.

locate the membrane. Then a fast intensity scan in vertical direction determined the membrane position at the point of highest intensity (~ 20 kHz). The focus position was set $1.5\ \mu m$ below this point and one ACF was recorded. Subsequently, the axial focus position was increased in steps of $0.2\ \mu m$ $15\times$ and each time the measurement was repeated. Figure 3.5 shows the effect of a z-scan measurement on ACFs recorded in each plane. During measurement, SLBs were bleached for 3 s then, 6 - 10 traces of 5 s duration were recorded. The first ACF trace was discarded due to remaining recovery effects from bleaching. All other traces were averaged and the standard deviation of each lag time was calculated according to the method of Wohland et al. [86] (see section 2.3.3.2). Physically rele-

vant parameters diffusion time τ_D and particle number N were obtained from applying a Levenberg-Marquardt nonlinear-least squares fit to the data. Therefore, the 2D diffusion model including triplet formation was used (see equation 2.4). Figure 3.6 gives an example of an ACF of the cen-
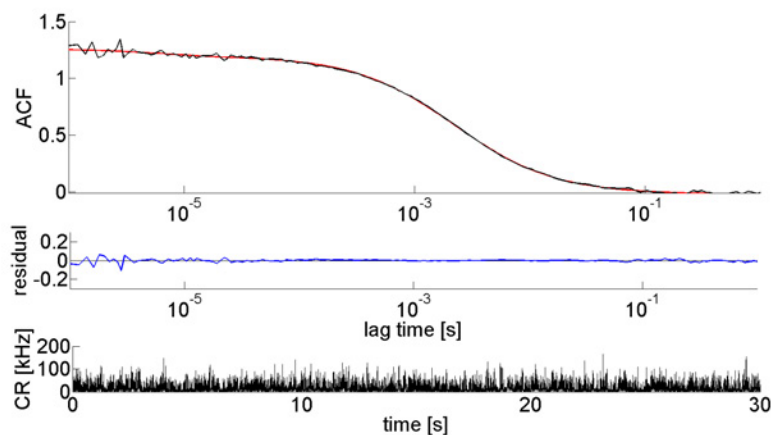
Figure 3.6: Example of z-scan FCS through SLB containing 0.01 mol% Bodipy-Fl DHPE tracer molecules. A: ACF, fit and residuals of central z-scan position. N =0.8 and $\tau_D = 2.2$ *ms* were derived.

tral position, the fit of a 2D diffusion model, residuals and intensity data. The corresponding set of autocorrelation curves at different z-positions is given below. Clearly, with relative distance from the centre, Δz, a decrease of the correlation amplitude and an increase in diffusion time is observed. This trend is expected as with increased Δz the confocal volume size enlarges. Hence, on average, more particles reside within the detection area and take longer times to diffuse across it.

For z-scan analysis N and τ_D of each fit were plotted against the relative z-position. Resulting parabola of both parameters were fitted with equations 2.6 and 2.5. Figures 3.7 - 3.8 illustrate this analysis exemplary for one SLB with 0.01 mol% TRITC-DHPE and for one SLB with 0.01 mol% Bodipy-Fl DHPE. From the fit ω_0, N_0 and D were obtained.

On average ω_0 amounted to $281 \pm_p 23$ *nm* (for $\lambda = 543$ nm) and $249 \pm_p 27$ *nm* (for $\lambda = 488$ nm). This is in high correspondence to results from ex-

Figure 3.7: Results of lipid diffusion in SLB with TRITC-DHPE tracer molecule. FCS z-scan data of particle number N (black dots) and diffusion time τ_D (green dots) are given. A parabolic fit to 9 central points of both curves (black lines and equations) yielded coefficients from which ω_0, N_0 and D were obtained (left). FCS z-scan diffusion law, i.e. τ_D vs. N/N_0 (black dots), allows to distinguish between free and hindered diffusion. The linear fit (black) line with ~ 0 intercept indicates free diffusion (right).

trinsic microsphere calibration, as deviations were only $\sim 1\%$. However, due to the larger error of ω_0 from parabolic fits, values from microsphere calibration were used for further analysis.

 Diffusion constants of lipids were $3.8 \pm_p 2.0\ \mu m^2/s$ (#11) for TRITC-DHPE and $5.7 \pm_p 0.8\ \mu m^2/s$ for Bodipy-FL DHPE (#9). Values for TRITC-DHPE are in well accordance with diffusion constants reported for lipid diffusion in SLBs [29, 87, 128]. The diffusion constant of Bodipy-FL DHPE is slightly higher than the largest diffusion constant found, which is 5 ± 1 $\mu m^2/s$ [128]. To some extend, this deviation may be explained by the reduced molecular weight of Bodipy-FL DHPE to TRITC-DHPE of 15% and
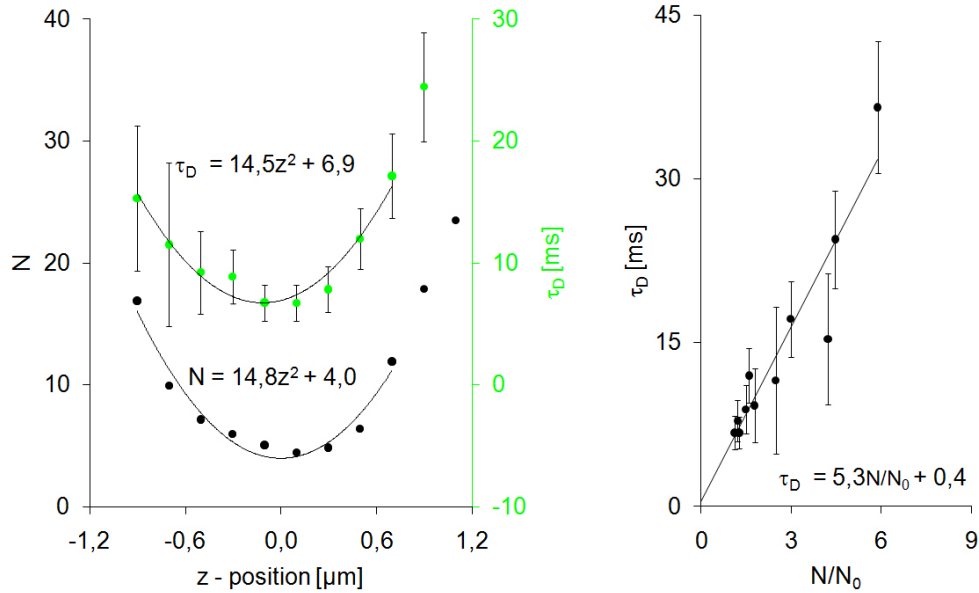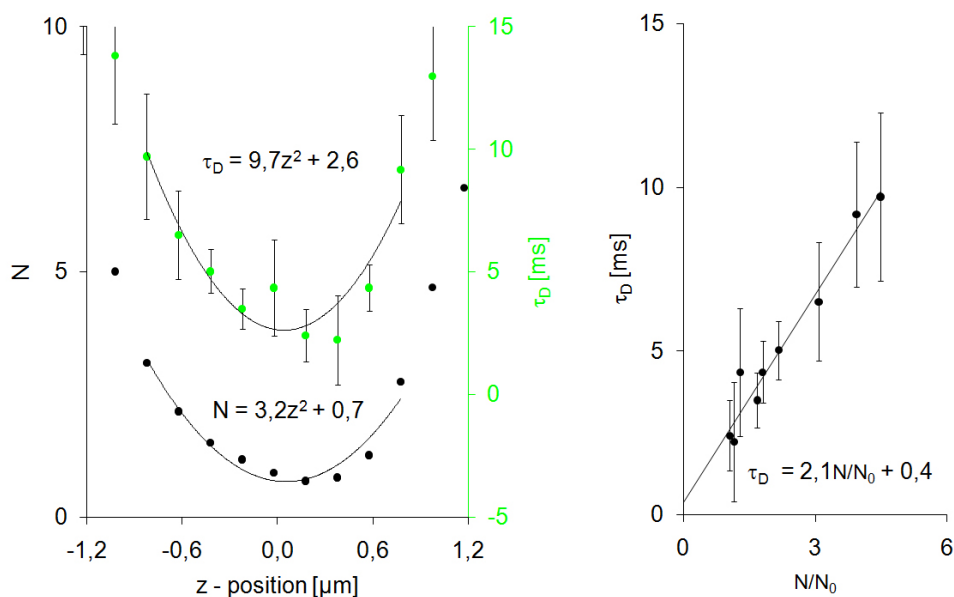
Figure 3.8: Results of lipid diffusion in SLB with Bodipy-FL DHPE tracer molecule. FCS z-scan data of particle number N (black dots) and diffusion time τ_D (blue dots) are given. A parabolic fit to 9 central points of both curves (black lines and equations) yielded coefficients from which ω_0, N_0 and D were obtained (left). FCS z-scan diffusion law, i.e. τ_D vs. N/N_0 (black dots), allows to distinguish between free and hindered diffusion. The linear fit (black) line with ~ 0 intercept indicates free diffusion (right).

temperature differences.

Furthermore, the normalized particle number N/N_0 was calculated for each z-position and plotted against τ_d. According to equation 2.7 the slope of this dependence is $\omega_0^2/(4D)$. Based on the work of Wawrezinieck et al. [81] a nonzero value for the intercept is indicative of hindered diffusion. Only for free diffusion a quadratic dependence of the diffusion time on the beam area holds. Since N/N_0 is essentially a measure of the illuminated area size an intercept 0 is anticipated for free diffusion. Other diffusion laws, on the other hand, are characterized by strictly positive of negative intercepts and absolute values > 10 [81, 128]. Analysis of SLBs data

showed that intercepts lay around 1 ± 2, thus confirming unconstrained diffusion.

Accordingly, the parabolic shapes of particle number and diffusion time are a robust means to determine correct z-positions and, in essence diffusion, constants. Several former studies who performed single FCS measurements with one particular waist, reported cases of anomalous diffusion. It was suggested that these may be re-examined with the z-scan method as it provides higher control of positioning and diffusion law determination [129, 130].

3.3.2.2 Diffusion in the Structured Adhered Vesicle Membrane

FCS and FRAP measurements on structured adhered vesicles were performed at the upper side of isolated sitting GUVs and at the lower vesicle site within the adhered part as well as within fluctuation areas. Vesicles of $> 30\,\mu m$ diameter were selected to ensure small curvature and sufficiently large areas to perform FRAP measurements at the vesicle top.

FCS z-scan experiments were conducted as described in 3.3.2.1. In addition, always the centre of vesicle top, fluctuation region and adhesion structure were chosen to ensure minimal membrane curvature and negligible boundary effects. Average diffusion constants at the vesicle top amounted to $12\,\mu m^2/s$. At the lower vesicle site diffusion constants were on average $10\,\mu m^2/s$ for the fluctuation region and $9\,\mu m^2/s$ for the adhered region. Thus, molecular binding appeared to induce obstacles within the adhesion zone which slowed down diffusion by $\sim 20\%$. Figure 3.9 shows a FCS z-scan result of lipid diffusion at the vesicle top.

For FRAP experiments two circular regions were chosen, of which one was bleached, while the other served as a reference area to monitor intensity decrease in the background. Usually for 0.5 s fluorescence intensity in both areas were recorded, before one region was bleached with high intensity. The duration of bleaching was 0.5 s. Subsequently, intensity recovery was monitored to the point, where no further intensity increase was detected. Figure 3.9 illustrates a typical FRAP measurement performed at the vesi-
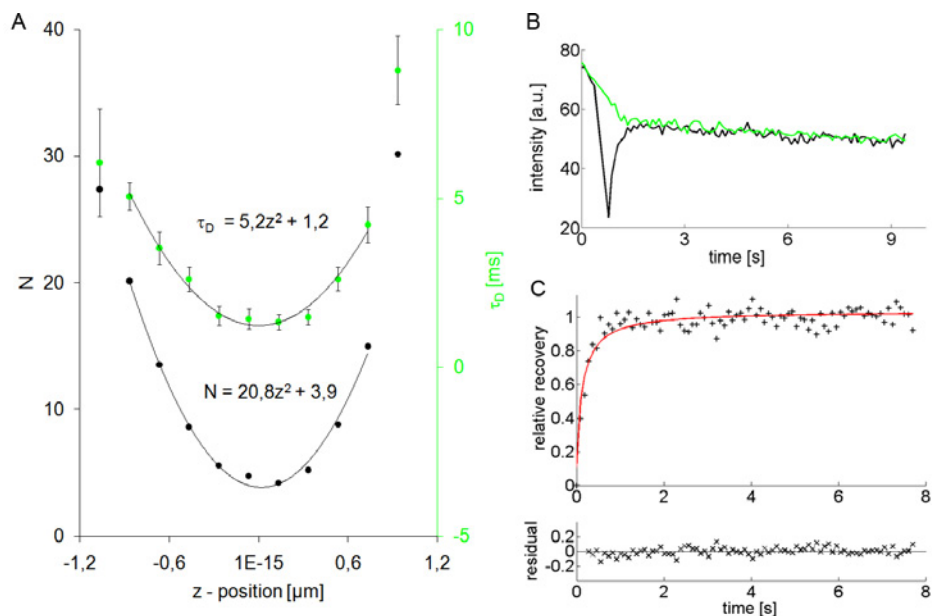
Figure 3.9: Results of lipid diffusion at the vesicle top. A: FCS z-scan data of particle number N (black dots) and diffusion time τ_D (blue dots). A parabolic fit to both curves (black lines and equations) yielded coefficients from which ω_0, N_0 and D were obtained. B: FRAP measurement. Intensity raw data of bleach (black) and reference area (blue) are shown at the top. Intensities were background corrected and normalized (black crosses), as shown at the bottom. A fit to the data (red) yielded D.

cle top. In addition, table 3.3 gives an overview of exact values, errors and number of measurements for both techniques.

With FRAP, diffusion at the upper vesicle site amounted to 11 $\mu m^2/s$. At the lower vesicle site diffusion decreased strongly. Here, diffusion constants were on average 2 $\mu m^2/s$ for the fluctuation region and 2 $\mu m^2/s$ for the adhered region (see table 3.3 for exact values and errors).

As a result, high correspondence between FCS and FRAP is found for the vesicle top. Moreover, a diffusion constant of $\sim$ 12 $\mu m^2/s$ and slightly smaller values (precisely, 12.5, 8.2 and 8 $\mu m^2/s$) were reported by Przybylo et al. [90] and Gielen et al. [131] for lipid diffusion in GUVs measured with FCS z-scan. Also, from a comparison to diffusion in SLBs the result

of Przybylo et al. [90] is confirmed, who found lipid diffusion in GUVs to be more than two times faster than in SLBs. For the present case, diffusion was faster by a factor $\times 3$.

However, results at the vesicle bottom showed poor agreement between FCS and FRAP. While FCS z-scans yielded a diffusion decrease by $\sim 20\%$ between vesicle top and bottom, FRAP measurements resulted in a $\sim 80\%$ decrease. This discrepancy can not be explained by differences in temperature or molecular structure. One possible explanation is, that fluorophores interact differently with the patterned substrate, such that any nonspecific interaction slowed down lipids even further. On the other hand, vesicle adhesion in these experiments may have been different. I.e. while vesicles adhered very weakly in one case, adhesion was strong in the other. This may correspond to the results of Daniel Schmidt (see section 3.3.1.4), who found a tension increase by ~ 5 for some vesicles. In fact, further experiments are needed to understand this discrepancy.

Despite the strong difference between vesicle top and adhesion zone, similar trends for diffusion reduction within the different regions was found: Diffusion in the vesicle top was fasted, in fluctuation areas it was partly reduced and decreased even further in the adhered area. Conclusively, vesicle adhesion to patterned substrates has an effect on lipid mobility. While no immobile fraction was detected, diffusion constants were reduced by $\sim 20\% - 80\%$.

	top	#	fluc. area	#	adh. area	#
FCS	$12.1 \pm_m 0.7$	8	$10.3 \pm_m 0.7$	14	$8.8 \pm_m 0.7$	10
FRAP	$11.4 \pm_m 1.2$	10	$2.3 \pm_m 0.3$	9	$1.6 \pm_m 0.5$	8

Table 3.3: Overview of diffusion constants in $[\mu m^2/s]$ at different locations of the structured adhered vesicle. # denotes the number of measurements.

3.4 Conclusion

In this chapter results on vesicle adhesion to large grid structures were presented. DW-RICM, FCS and FRAP were applied to characterize the adhesion state in membrane topography, diffusivity and fluctuation. To my knowledge, it is the first time that vesicle adhesion to a patterned substrate has been experimentally quantified.

Vesicles adhering to patterned substrates exhibited bound and fluctuating membrane regions in the adhesion zone according to the underlying pattern. While within adhesive regions, membrane was directly bound by receptors at average height $\langle h \rangle = 19 \, nm$, within fluctuating regions, membrane bent upward and reached a plateau at $\langle h \rangle = 79 \, nm$. Thus, substrate geometry allowed the formation of characteristic regions of specific and unspecific adhesion; repulsive forces within unbound membrane regions sufficed to generate strong and weakly adhered membrane regions.

Lipid mobility was verified by FCS z-scan and FRAP analysis at the vesicle top and within bound and fluctuating regions of the adhesion zone. While lipids diffused freely at the vesicle top with $\sim 12 \, \mu m^2/s$, diffusion within the adhesion zone was slowed. Here, diffusion constants decreased by $\sim$ 20-80 %. In addition, lipid mobility between bound and fluctuating membrane differed only slightly. From free to bound membrane regions diffusion constants decreased by 15-30 %. Accordingly, lipid mobility allowed for changes in membrane area within fluctuation regions ensured system equilibration. More importantly, within fluctuating regions the membrane was able to relax into the minimum of the unspecific membrane-substrate interaction potential. Frictional effects arose within bound regions of the membrane. This resulted in slowed but not stalled diffusion.

Analysis of membrane fluctuations and equilibrium shapes allowed for a determination of system parameters vesicle tension, σ, and interaction potential curvature at its minimum, γ. With fluctuation amplitudes of

$\delta h = 12$ nm, $\sigma = 4\mu J/m^2$ and $\gamma = 2 \cdot 10^8 J/m^4$, adhesion to large grid pattern was weak. Fluctuations were mostly bending rigidity dominated. For some cases slightly stronger adhesion was observed and a crossover from bending to tension dominated regime was identified. Note that due to our special substrate, adhesion here was weaker than those reported elsewhere. Those reported in literature were for δh on average a factor $\times$ 1.5-3 larger and for σ almost $\times$ 10 smaller [44, 115, 116].

In contrast to the references above DW-RICM instead of RICM was used, which provided absolute reliable height measurements. Combination of the present observation technique (DW-RICM) and model system (GUVs on patterned substrates) presented here represents an important tool for testing theoretical ideas on membrane physics.

Chapter 4

Constrained Membrane Fluctuations: Effects of Model System Variation

The model system characterized in chapter 3 is studied here with respect to variable adhesion conditions: On the one hand, the underlying adhesion structure is varied and its effects on the equilibrium state are studied. On the other hand external disturbances, in form of osmotic pressure changes, are applied. Here adhesion states in and out of equilibrium are observed. Consequences for the adhesion state are discussed.

4.1   Experimental Realization

Adhesion to patterned substrates was realized as described in section 3.2. Preparation and settings were identical to experiments of the previous chapter 3. Parameters of the adhesive structure and osmolarity were varied as described below:

4.1.1 Adhesive Structures

For variation of adhesion pattern, two structures in addition to the large
grid structure of the previous chapter were chosen. One featured squared
fluctuation areas and a lattice constant just half the size of the large grid
structure. This allowed to study the effect of bound membrane spacing.
The other consisted of lines, where in contrast to square structures the
buffer beneath the membrane was free to flow. Thus, effects of possibly
enclosed buffer within squares of other structures were elucidated. Pre-
cisely, small grid and line structure, as introduced in 2.2.2.1, served as
adhesive basis. Vesicles were added to the chamber and recorded after
adhesion was completed, as described before.

4.1.2 Osmotic Changes

For variation of membrane tension by means of osmotic pressure changes,
buffer solution of different osmotic strength was used. Two different sce-
narios were investigated:

- a sudden osmotic pressure change mimicked osmotic shock ;

- a variation of initial osmotic difference.

Precisely, in order to monitor dynamic changes, vesicles were prepared
as usual in 230 mOsm/l sucrose solution (see chapter 3). Vesicles were
added to the observation chamber filled with PBS, adhered to patterned
substrates and equilibrated. Subsequently, chambers were shortly uncov-
ered and 25 - 200 μl bulk solution of total was exchanged. In case of ex-
change for ultrapure water, the bulk solution was 400 mOsm/l PBS. In
case of exchange for 400 mOsm/l PBS buffer, the bulk solution was 300
mOsm/l PBS. This way, pressure changes across the membrane in both di-
rections were studied. System reactions to the disturbance were recorded
over time.

Adhesion statics, vesicles were swollen in sucrose solution of 230 $mOsm/l$

and suspended in PBS buffer of initially 250, 350 or 400 mOsm/l. Upon
addition to the chamber, vesicles were osmotically deflated to an extent
determined by the osmotic gradient. During equilibration vesicles sedi-
mented to the substrate and adhered. Employing standard settings de-
scribed in section 2.3.4.6 the adhered state was recorded.

For osmotic pressure changes, mainly the large grid structure served as
adhesive basis. Only in two experiments on membrane dynamics, large
grid was exchanged for SLB and small grid structure.

4.2 Results and Discussion

4.2.1 Variation of Adhesion Pattern

4.2.1.1 Elongation

Elongation of vesicle adhesion zone along the underlying pattern was
tested with line structures. Here, in contrast to structures large grid and
small grid, an axis of preferred direction is inherently given by the line
direction. Vesicle elongation was determined from fitting an ellipse to the
adhesion zone and identification of its major axis. Subsequently, the acute
angle between major axis and line orientation was calculated. Figure 4.1
shows typical results of this calculation.

 Angles of alignment varied highly between $0°$ and $90°$. Evaluation of #12
vesicles yielded an average angle of $44° \pm_p 32°$. In fact, as this value marks
the middle between full and perpendicular alignment and since the error
spans almost all possible values, no alignment of vesicles along line struc-
tures is found. Also, since for large and small grid structure elongation is
only detectable for acute angles below $45°$ between vesicle major axis and
one of the two main axis of the grid structure, the results on line structures
make analysis on grids senseless.

In addition, the aspect ratio of the vesicle adhesion zone was determined
for all structures used in this work. In general, vesicles adhering to ho-
mogeneous substrates adopt circular adhesion zones, as this represents
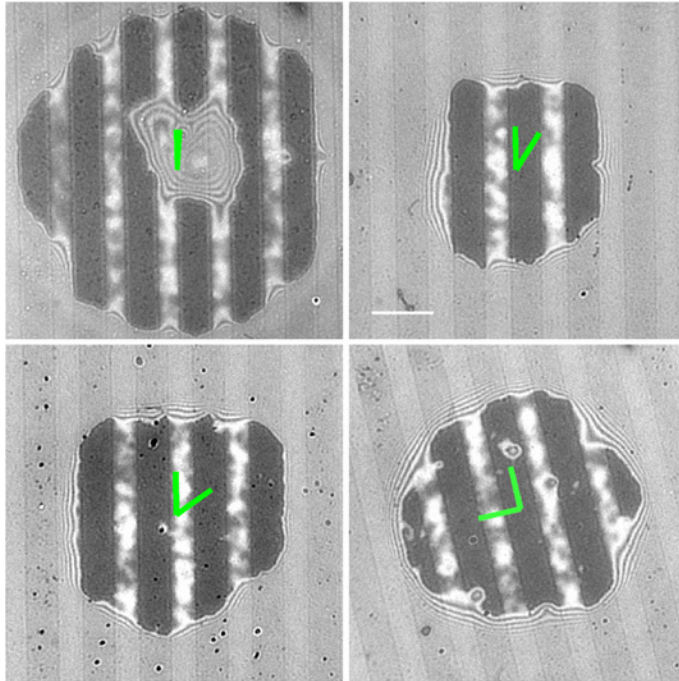
Figure 4.1: Results of vesicle adhesion and orientation along
line structures. The acute angle between vesicle major axis and
line direction is indicated (green). Scale bar: 7 μm (applies to
all).

the energetically most favourable shape. However, any distribution in re-
ceptor concentration induces deviations from the perfect circle and this
should apply to adhesion to patterned substrates as well.

Aspect ratios were determined again from an fitting an ellipse to the ad-
hesion zone. The ratio of minor to major axis of the ellipse yielded the
aspect ratio. Values obtained this way amounted to $0.91 \pm_p 0.04$, for line
structures, $0.89 \pm_p 0.08$, for large grid structures, and $0.90 \pm_p 0.07$, for small
grid structures. These results show that no differences between different
adhesion pattern arise. Absolute values deviated from a perfect circle by
10%. Here, small effects may originate in the patterned receptor distribu-
tion. However, imperfect circular shapes were also observed in studies
where substrates were prepared with initially homogeneous receptor dis-
tribution [33, 100]. Thus, measured deviations in aspect ratio from 1 may

be an indicator of heterogeneous receptor distribution in general, but not a particular result of the geometry studied here[1].

As a result, two explanations may account for the lack of orientation and elongation along adhesive sites: First, geometrical changes between the different structures may not be drastic enough to result in detectable changes of the adhesion state. Second and more likely, receptor concentrations are too low to allow for further spreading; i.e. the gain from binding enthalpy does not exceed the loss in translational entropy. Results of chapter 3 support the argument of low receptor density, as here adhesion to patterned substrates was found to be weak. Moreover, if this second aspect dominates adhesion, geometrical changes will become insignificant.

4.2.1.2 Adhesion Topography

Similar to previous analysis of adhesion topography on large grid structure (see section 3.3.1.1), membrane shapes on small grid and line structure were analyzed. Membrane topography was reconstructed with DW-RICM as described in section 2.3.4. Figure 4.2 gives typical examples of structured adhered vesicles and membrane topography for the three different structures. Between fluctuating and bound region, a frame of seven pixel width (= 0.7 μm) on line structure and of four pixel width (= 0.4 μm) on small grid structure were omitted, as here the membrane was not planar enough for correct DW-RICM analysis and since patterned substrate exhibited rough edges.

As before, membrane elevation from the edge toward the centre of fluctuation areas was observed. Due to the smaller size of fluctuation regions of small grid and line with respect to large grid structure the membrane exhibited a steeper rise and smaller plateau (Widths were 4 μm for large grid structure, 2.5 μm for line structure and 2 μm small grid structure.). This difference in membrane curvature can be explained from further analysis of average heights within the centre. Therefore, nine central points

---

[1]It has to be noted, that structures were chosen in a way to provide an almost equal ratio of adhesion/fluctuation area for all structures. This way, mere geometrical effects should play a role.
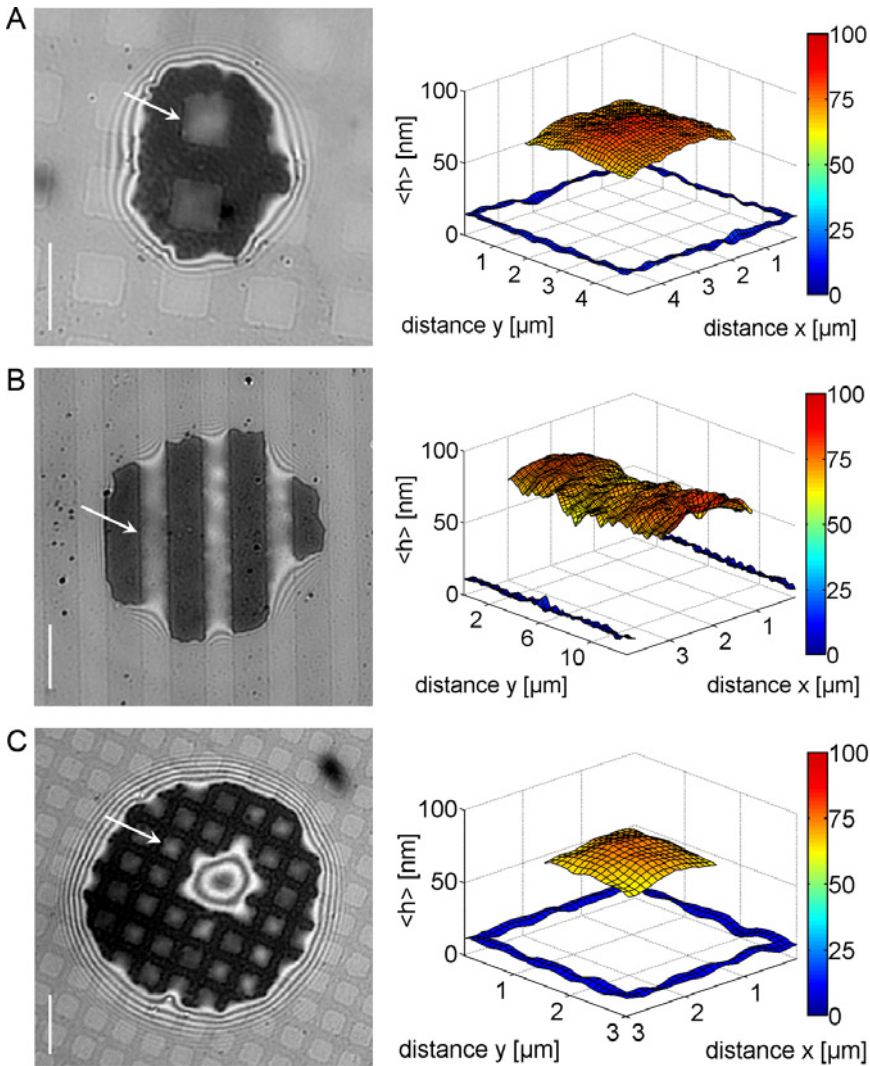
Figure 4.2: Topography reconstruction of structured adhered vesicles. A: Vesicle adhering to large grid structure, B: vesicle adhering to line structure and C: vesicle adhering to small grid structure. Average RICM images and reconstructed average height maps are shown. White arrows point to the fluctuation region depicted on the right. Scale bar 7 μm. The colour code indicates average heights in nm. Regions of steeply curved membrane had to be omitted. Note the scale difference between h and x, y axes as well as differences in x, y lengths of the line structure.

within fluctuation areas of small grid structure and two central lines within
fluctuation areas of line structure were chosen and height values extracted.
From their analysis average heights amounted to $81 \pm_p 9$ nm and $82 \pm_p$
8 nm for small grid and line structure, respectively. Table 4.1 gives an
overview of average heights and errors.

These findings are in well agreement with results obtained from large grid
structure (see section 3.3.1.1) and have two important consequences: First,
the bound membrane does not affect the average membrane height even
though spacings between adhesion sites are halved. As a consequence, the
previous assumption, to model membrane fluctuations within the centre
as free fluctuations (see section 3.3.1.4) is further supported by this ob-
servation. Second, average membrane heights are identical for vesicles
adhering to square regions and those adhering to lines. This finding to-
gether with results on lipid mobility within adhered membrane parts (see
section 3.3.2.2) support the hypothesis that the membrane reaches an equi-
librium state at the minimum of the unspecific interaction potential.

4.2.1.3 Fluctuations

Membrane fluctuations were calculated in order to estimate whether dif-
ferences in the nature of fluctuations arise from PBS being confined below
the membrane or being free to flow. Fluctuation amplitudes were calcu-
lated from the same points used for average height determination. As for
structure large grid (see section 3.3.1.2) squared deviations from the mean
height were averaged over time and subsequently the average of central
points was calculated. This way, fluctuation amplitudes for small grid
and line structure amounted to $9 \pm_p 3$ *nm* and $9 \pm_p 4$ *nm*, respectively. As
on large grid structures amplitudes were $12 \pm_p 2$ *nm*, the average value
is slightly smaller. Yet, the standard deviation indicates, that effectively
no significant change in absolute amplitudes between line, large grid and
small grid structure is found. Thus, free and possibly enclosed PBS buffer
appear to have no detectable effect on fluctuations. Table 4.1 gives an
overview of fluctuation values derived.

Figure 4.3 shows typical examples of fluctuation maps and average height

Structure	large grid	#	small grid	#	line	#
$\langle h \rangle \, [nm]$	76±8	88	81±9	80	82±8	27
$\sqrt{\langle (h - \langle h \rangle)^2 \rangle} \, [nm]$	12 ± 2	54	9 ± 3	80	9 ± 4	27

Table 4.1: Overview of average heights and fluctuation ampli-
tudes on different adhesion structures. Errors are standard de-
viations of the population. # denotes the number of evaluated
fluctuation areas.

maps of fluctuation areas for the three different structures. Most often it
was observed that areas of high average height exhibit strong fluctuations,
while low average heights featured weaker fluctuations. This confirms re-
sults on the large grid structure (see section 3.3.1.2) where a linear increase
of amplitudes with average height was found.

In addition, close observation of fluctuation regions revealed some dis-
tinct distribution of maximal fluctuations. For large grid structures maxi-
mal fluctuations appeared mostly toward the edge. Squares of small grid
structures, on the other hand, featured maximal fluctuations most often in
the middle of the square region. Fluctuation amplitudes along line struc-
tures exhibited some distinct distribution of strong and less fluctuating
regions (compare figure 4.3).

In order to quantify whether this is a significant feature, membrane fluc-
tuation spectra on the three different structures were determined. For this
analysis, it was checked first that sequences of 1500 images were suffi-
cient to have enough statistics of uncorrelated data[2]. If this was not the
case, measured equilibrium values, such as the average membrane height,
would still be influenced by fluctuations of long relaxation times. In order
to test this, average membrane profiles over an increasing number of im-
ages were calculated and these subtracted from each other. At sufficiently
long recording times hardly any detectable change between profiles ex-
isted. For data sets of more than 1500 images, the average deviation per
pixel was only ~ 0.5 nm (data not shown). Thus, the average height profile

---

[2]As mentioned in section 2.3.4.6 usually 2000 images were recorded.
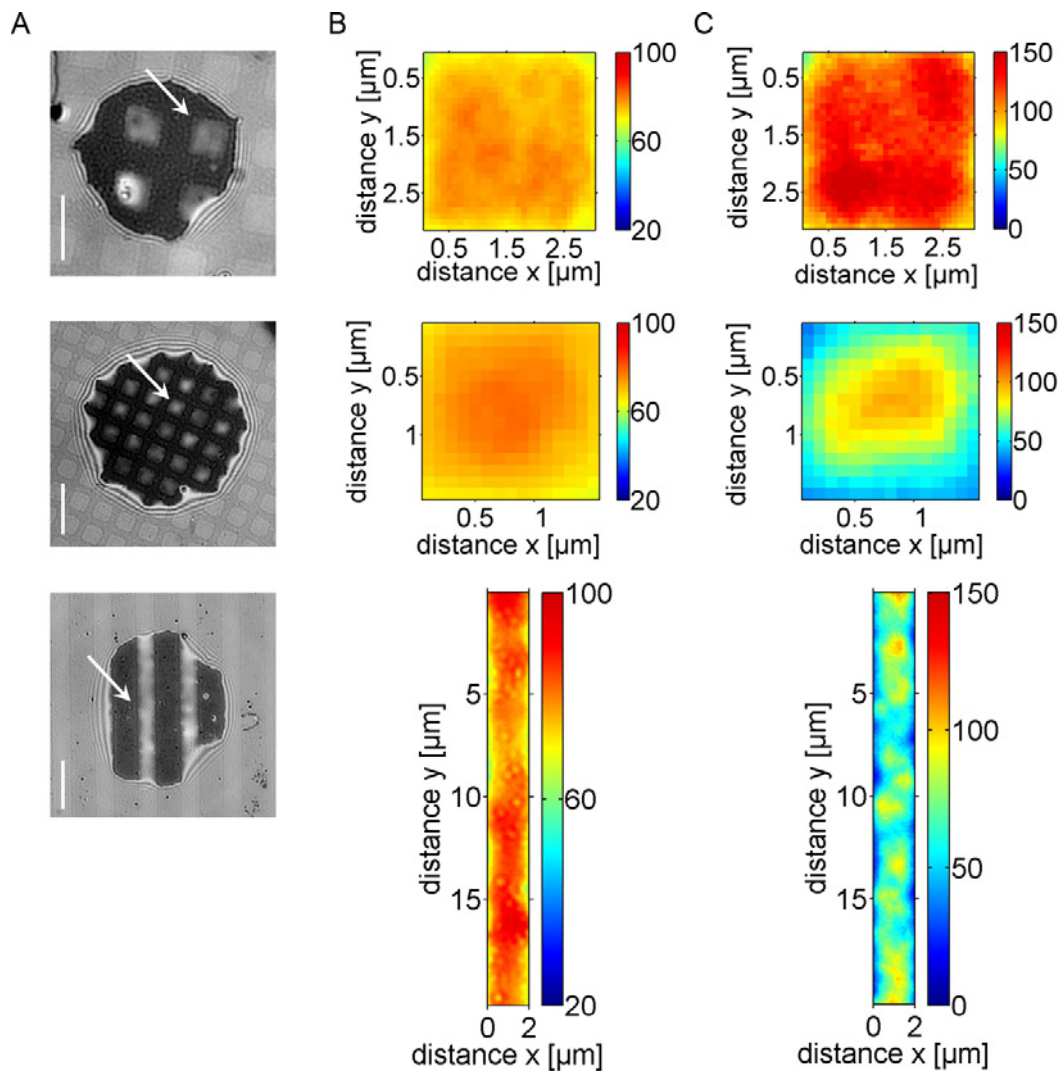
Figure 4.3: Comparison of average heights and fluctuation amplitudes of structured adhered vesicles. A: RICM images of vesicles adhering to different structures. White arrows point to the fluctuation region depicted on the right. Scale bars 7 μm. B: Average height maps of the central fluctuation region and colour code in nm. C: Mean square fluctuation amplitude maps and colour code in nm^2.

was not changing anymore. This finding implies, that relaxation times of the smallest contributing mode are shorter than recording times and thus, data was mostly uncorrelated. Moreover, it was estimated that sufficient

number of uncorrelated data sets were available, as this is an essential prerequisite of Fourier analysis (data not shown)[3]. Also, an extension of recording times to > 3000 images was not feasible, as focus drifts started to become visible. Thus, recording of 2000 images appeared to be a good compromise for robust Fast Fourier Transformation (FFT) analysis.

First, maps of amplitudes $A(m, n, t)$ for each time point were derived and its FFT was calculated according to:

$$A(k, l, t) \quad = \quad \frac{1}{N^2} \sum_{m=0}^{N-1} \sum_{n=0}^{N-1} A(m, n, t) e^{-i\frac{2\pi mk}{N}} e^{-i\frac{2\pi nl}{N}} \quad ,$$

where N × N are the number of pixel within the fluctuation region, indexed (m, n). Fourier amplitudes $A(k, l, t)$ were then averaged over the whole time sequence, T, according to

$$\langle A^2(k, l) \rangle = \frac{1}{T} \sum_{t=1}^{T} A^2(k, l, t)$$

This yielded maps of the mean square amplitude in Fourier space, as depicted in figure 4.4. Fourier maps exhibited radial (for large grid and small grid structure) and axial (for line structure) symmetrical regions of dominating wave vectors.

Due to the twofold symmetry of small grid and large grid structure and for better statistics the fluctuation spectrum was radially projected onto the wave vector

$$q = \sqrt{q_x^2 + q_y^2} = \sqrt{\left(\frac{n\pi}{L_x}\right)^2 + \left(\frac{m\pi}{L_y}\right)^2} \quad .$$

Here $q_{x,y}$ is the wave vector along one axis and $L_{x,y}$ the side length of the fluctuation area. In case of line structures only $q = q_y$ was evaluated (see figure 4.4).

---

[3]The relaxation time of the smallest contributing mode was found to be at most 5 s, which corresponds to 100 images. Thus, $\sim$ 20 sets of uncorrelated data were available.
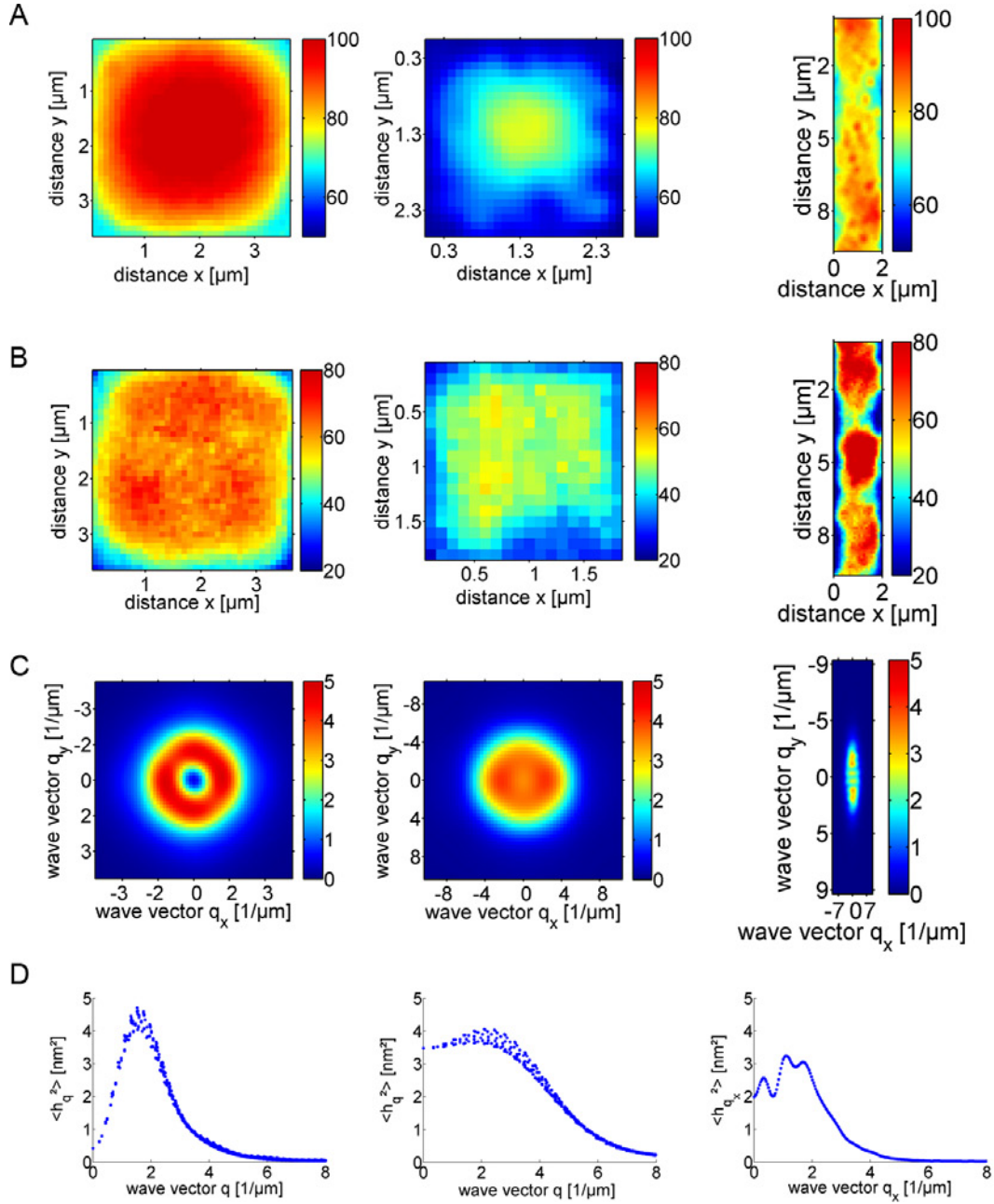
Figure 4.4: Results of FFT analysis on different adhesion structures. From left to right examples of large grid structure, small grid structure and line structure are given. A: Average height map *nm* B: Mean square amplitude map *nm²* C: Fourier map *nm²* D: Radial average of Fourier map (for large grid and small grid structure) and fluctuation spectrum along y-axis (line structure). Note the scale difference of x, y axes between different structures.

Plotting these projections for the large grid structure, one distinct wave vector at $q = 1.64 \pm_p 0.13 \ \mu m^{-1}$ and another less dominant wave vector at $q = 1.15 \pm_p 0.13 \ \mu m^{-1}$ were found. A comparison of these values to theoretically expected modes[4] for fluctuations on a grid of square area $L^2 = 4.2^2 \ \mu m^2$ resulted in good agreement with the (2,1), the so called 'swapping mode', for the predominant wave vector and the (1,1), the so called 'breathing mode', for the other contributing wave vector. For comparison between adhesion structures, specification of the corresponding wavelength is advantageous. Here, the 'swapping mode' corresponds to wavelengths of 4 μm and 8 μm for the two spatial directions and the 'breathing mode' denotes wavelengths of 8 μm. Results for small grid structure were slightly different. Here, only one dominant wave vector at $q = 2.4 \pm_p 0.2 \ \mu m^{-1}$ was found, a value corresponding to the 'breathing mode'. On this structure wavelengths of 4 μm primarily developed. Finally, analysis of line structures yielded contributions of several modes. Predominant was the first mode, with $q_y = 0.1 - 0.5 \ \mu m^{-1}$, and only slightly less contributing the sixth mode, with $q_y = 0.1 - 0.5 \ \mu m^{-1}$. Second and fourth mode, with $q_y = 0.6 - 1.2 \ \mu m^{-1}$ and $q_y = 0.6 - 1.1 \ \mu m^{-1}$, respectively, contributed as well. Since adhesion zones along lines were of highly variable length different wave vector values corresponded to one specific mode. Here calculation of corresponding wavelengths resulted in a value of $5.9 \pm_p 2.2 \ \mu m$ for the first mode, $5.7 \pm_p 1.8 \ \mu m$ for the sixth mode and wavelengths of $2.4 \pm_p 0.7 \ \mu m$ and $5.1 \pm_p 1.4 \ \mu m$ for the second and fourth mode respectively. Table 4.2 gives an overview of the statistics to these analyses.

Theoretically, fluctuations of a membrane pinned to a quadratic array were studied by Merath and Seifert [132]. They found maxima of shape fluctuation spectra to scale with the tethering distance. Qualitatively, this result is also seen in the present analysis, as with increasing structure

---

[4] For a membrane of area L^2 the wave vector is given by $q_{x,y} = \frac{2 \cdot \pi}{\lambda}(k,l)$ with $k,l = 0, \ldots, N-1$ and λ the fluctuation wavelength. As the membrane is bound to the substrate at distinct points, boundary conditions constrain the modes to multiples of half the wavelength $L_{x,y} = n \cdot \frac{\lambda}{2}$, $n \in \mathbb{N}$. Thus, wave vectors become: $q_{x,y} = n\frac{\pi}{L_{x,y}}$.

mode	SG: λ [μm]	#	LG: λ [μm]	#	mode	L: λ_y [μm]	#
(1,1)	4	43	8	6	1st	$5.9 \pm_p 2.2$	13
(1,2)			4	65	2nd	$2.4 \pm_p 0.7$	5
					4th	$5.1 \pm_p 1.4$	4
					6th	$5.7 \pm_p 1.8$	7

Table 4.2: Experimental results of FFT analysis for large grid (LG), small grid (SG) and line (L) structure. Predominant wave vectors $q_{(y)}$ are given. # denotes the number of evaluated regions where this mode was predominant. Other contributing modes of each spectrum were not considered in the statistic. Note that wave vectors $q_y = n \cdot \pi / l$, $n \in \mathbb{N}$ for line structure differ, since adhesion stripes exhibited variable length l.

modes corresponding to larger wavelengths contribute. Only, contributions from more than one mode were not considered there.

4.2.2 Variation of Membrane Tension - Dynamics

Systematic osmotic pressure changes were applied to test the system reaction to an external disturbance. First, results on sudden osmotic pressure changes to vesicles adhering to three different substrates are presented. Observed changes on large grid large grid and small grid small grid structure turned out to be equivalent. Therefore, examples shown in the following for these structures are representative of both. Vesicle adhesion to an SLB yielded complementary results as it served as example of adhesion to homogeneous substrates.

Figure 4.5 illustrates the reaction of structured adhered vesicles to osmotic deflation, corresponding to a tension decrease. Shortly after addition of PBS of increased osmotic strength the shock wave reaches the vesicle. This instantaneously ($\sim$ 5 s after addition) reacts by increasing the membrane - substrate distance within fluctuation regions. Often, several $\sim$ 100 nm height are reached within a few minutes. Moreover, observation over longer periods of time revealed in some cases a decrease in membrane velocity and a subsequent height decrease to $\sim$ 1/3 of the maximal

Figure 4.5: Time course of system reaction after osmotic pressure change: Vesicle adhering to small grid structure was disturbed by 100 μl of PBS 400 $mOsm/l$. RICM images (upper row) depict the system in s after disturbance. Scale bar 7 μm. Reconstructed height maps (lower row) show instantaneous lift of membrane upon osmotic deflation. Colour coded height is given in nm.

height (data not shown). Apparently, from the osmotic shock, local particle concentration differences arise, which cause the membrane to initially overshoot in height. Once particles are homogeneously distributed, the vesicle membrane slowly declines to reach an equilibrium state.

These observations have two important consequences: First, it appears energetically favourable to push excess membrane area into fluctuation regions and thus increase the membrane - substrate distance. Second, the membrane is fluid within the adhesion zone and lipid exchange between adhered and fluctuation region can take place. In addition to results on lipid diffusivity (see section 3.3.2.2) this experiment evidenced lipid mobility once more and without any fluorescence tracer.

Figure 4.6: Time course of system reaction after osmotic pressure change: Vesicle adhering to large grid structure was disturbed by 100 μl ultrapure water. Scale bar 7 μm. Sudden osmotic inflation causes a decrease in heights and freezing of membrane fluctuations. The initial strong and fast decrease, which arises from local concentration gradients, is followed by a slow increase in height and relaxation to equilibrium, as particles are homogeneously distributed.

In a second experiment the reverse disturbance, namely, osmotic infla-
tion and consequently a vesicle tension increase, was monitored. Figure
4.6 illustrates the time course of osmotic change effects on the adhesion
state of the system. Water was added to the chamber and, instantaneously,
membrane heights within fluctuation areas decreased. Within a minute,
membrane heights reached the substrate and membrane fluctuations were
not detected anymore. Also, vesicle tension appeared to increase as mon-
itored by the disappearance of interference fringes in figure 4.6. Often
osmotic shocks were strong enough to increase tension up to the point
where specific bond rupture occurred (see figure 4.6). Thus, a reduction
of the membrane adhesion zone was detected. Corresponding to osmotic
deflation experiments, partial recurrence of membrane fluctuations and
elevated membrane heights was observed. This can be explained by the
initial incomplete mixing of particles, which causes fast and strong varia-
tion in vesicle membrane height. This is then followed by the relaxation to
equilibrium, where particles are evenly distributed and where membrane
heights slowly adjust to the final particle concentration.

 As comparative experiment, osmotic shocks to vesicles adhering to SLBs
were applied. This way, examples of sudden tension decrease for homo-
geneously bound membranes were given. Figure 4.7 shows a 120 s time
course after PBS addition. Similarly to experiments on square structures,
almost instantaneously bright spots within the vesicle adhesion zone arise
indicating a lift from the substrate. Some of these blisters vanished, while
most of them remained stable for the time of observation ($\sim$ 15 min.). Pos-
sibly, the sudden osmotic gradient causes vast water flux out of the vesicle.
Simultaneously, membrane tension decreases and the interaction potential
minimum shifts to higher heights. This way, formation of blisters could be
promoted.

As a results, an increase of membrane - substrate distance as reaction to
sudden osmotic deflation was observed. Longer observations indicated
some relaxation processes to the original state, however, these were slow
and the original state was never reached. Surprisingly, principle observa-
tions were similar, independent of the underlying adhesion structure.
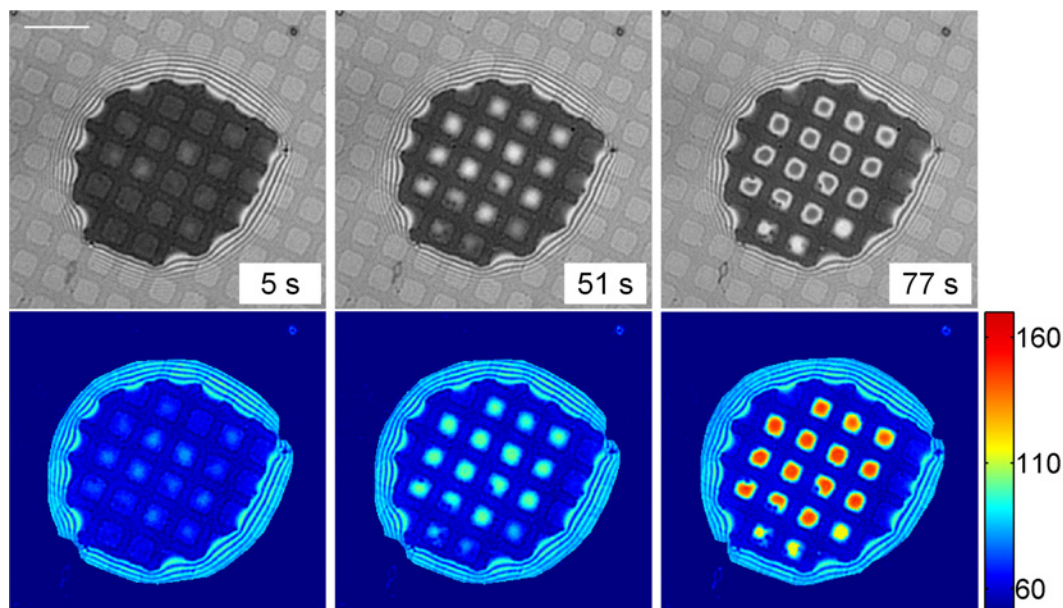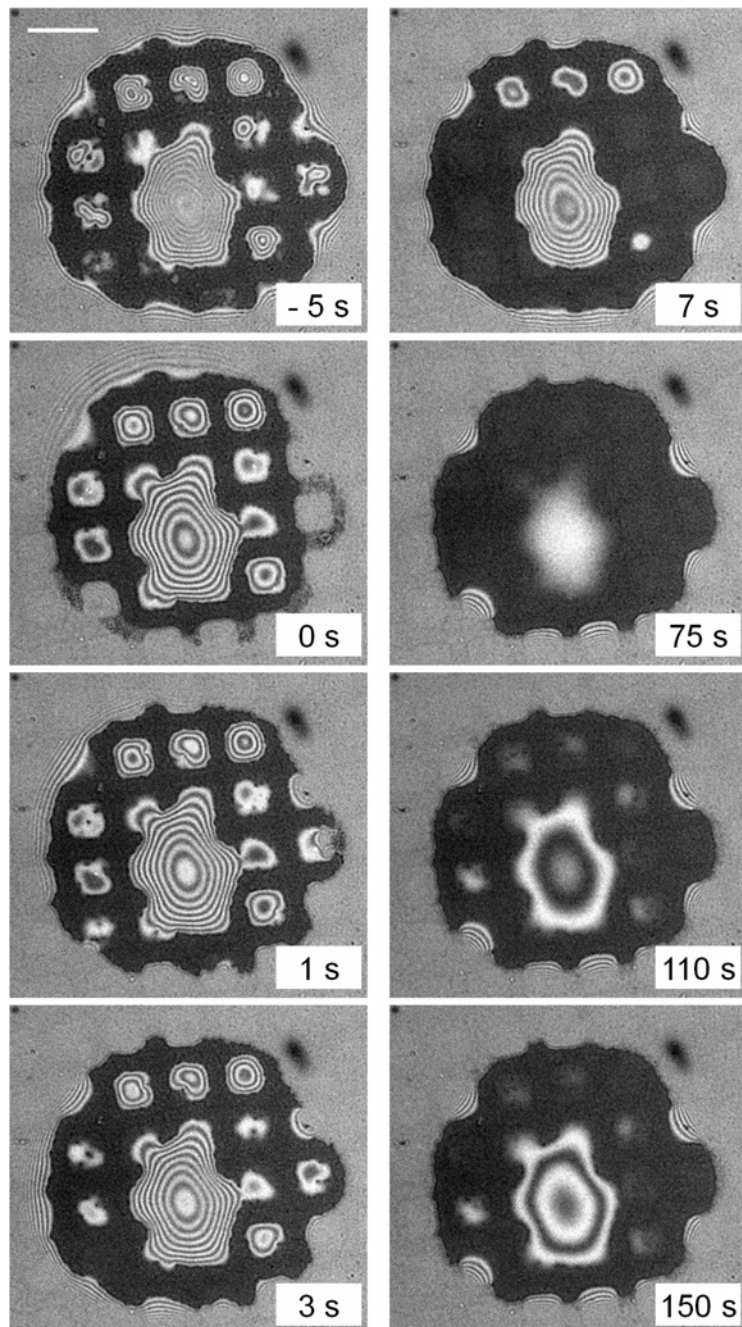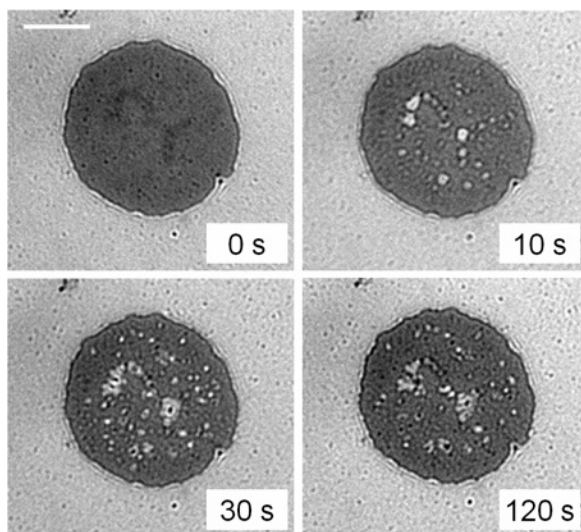
Figure 4.7: Time course of the system reaction after osmotic
pressure changes: Vesicle adhering to a SLB was disturbed by
200 μl of PBS 400 mOsm/l. Scale bar 7 μm. Osmotic deflation
results in formation of blisters.

No further quantitative analyses on membrane dynamical aspects were
undertaken, as micropipet application of solutes provided little control
over the extent of osmotic shocks and hence reaction strengths of the sys-
tem. Instead, initially varied osmolarity was applied and adhesion statics
were examined to obtain further understanding of the process.

4.2.3   Variation of Membrane Tension - Statics

Systematic variation of initial osmotic pressure demonstrated how system
parameters in equilibrium are affected. Vesicles exposed to osmotic gra-
dients $\Pi = 20, 70, 120, 145$ or 170 $mOsm/l$ were monitored after adhe-
sion. Due to the covered chamber osmolarities were highly controllable
and no additional perturbation occurred. Figure 4.8 gives an overview of
observed adhesion states.
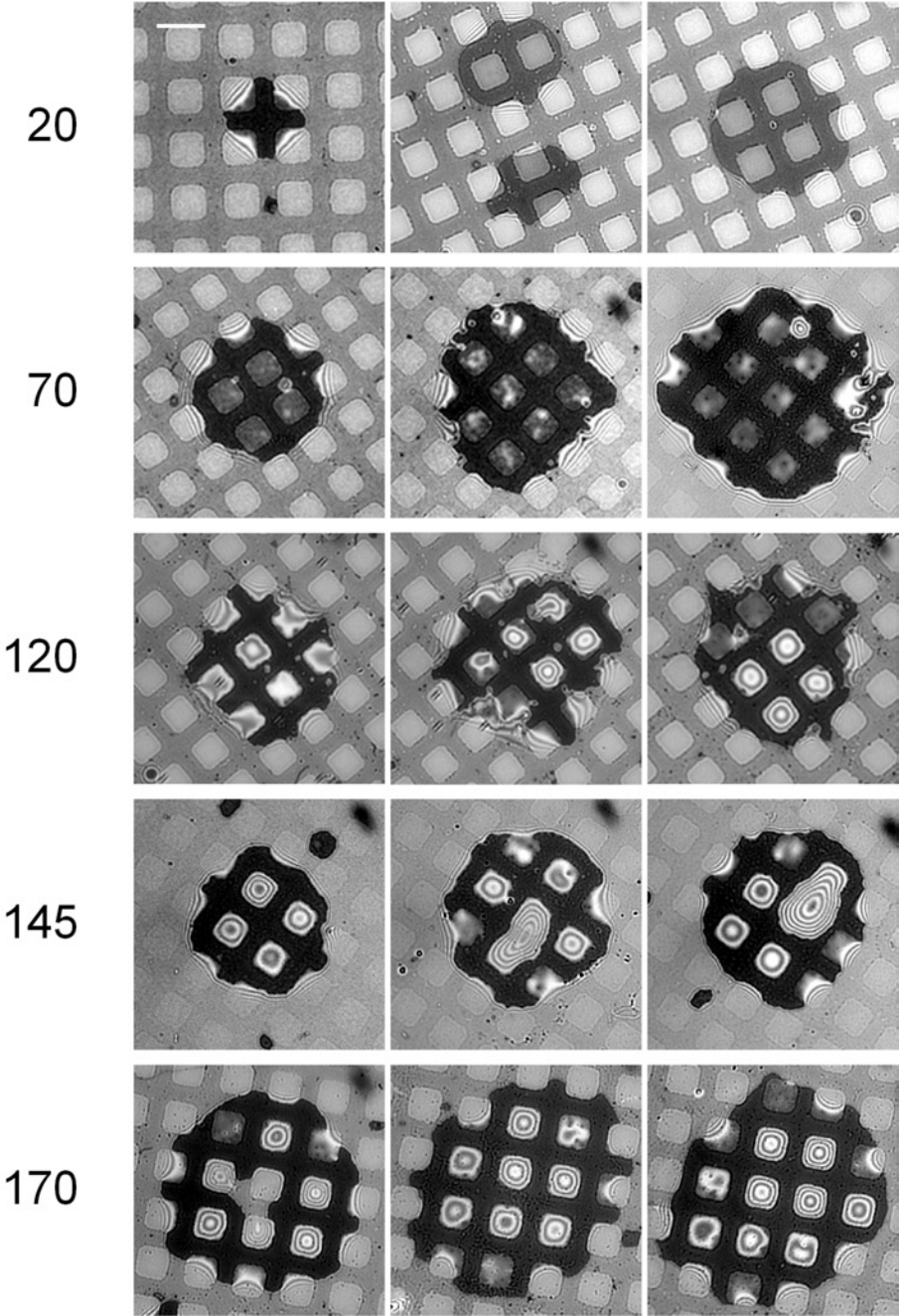
Figure 4.8: Results of initial osmotic pressure change. Vesicles encountered osmotic gradients upon addition to the chamber. During equilibration they sedimented to the substrate and adhered to large grid structure. Initial osmotic diffrences between vesicle in- and outside were $\Pi = 20, 70, 120, 145$ and 170 $mOsm/l$ (see numbers on the left). Scale bar: $7\ \mu m$ (applies to all). Increase in osmotic deflation results in elevated average membrane heights.

Obviously, average membrane heights within fluctuation regions rose
with increasing initial osmotic gradient. At $\Pi = 20\ mOsm/l$, fluctuations
were suppressed and unspecific adhesion was detected. With an increase
of Π to $70\ mOsm/l$, the membrane resided at average heights further away
from the substrate and fluctuations were clearly visible[5]. Increasing the
osmotic gradient even further, not only higher equilibrium heights and
stronger fluctuations were detected, but also a trend to larger adhesion
zones was observed. This effect is attributed to the increase in excess area,
which results from high osmotic deflation. In this case, a relatively large
membrane area probes the substrate and initial membrane tension is low.
This promotes bond formation and development of large adhesion areas.
For small osmotic gradients, vesicle tension is initially high. Here, a rel-
atively smaller membrane area is in contact with the substrate. In this
case, relatively fast is the loss in configurational entropy not exceed by
the gain from binding enthalpy anymore, and adhesion is stalled. Thus,
only small contact areas upon binding develop. At $\Pi = 120, 145$ and
$170\ mOsm/l$ bright interference rings within fluctuation areas appeared.
These evidenced strongly elevated heights as the distance between bright
rings corresponds to ~ 200 nm. Measurements at even higher osmotic
gradients were not feasible as vesicles featured low shape stability and
started to bud.

Quantitative results on vesicle adhesion at different osmotic gradients,
or, equivalently, membrane tensions, are given in figure 4.9. Depending
on the initial gradient, average membrane heights vary between 0 and
~ 500 nm. While between $\Pi = 70$ and $120\ mOsm/l$ a strong increase in
average heights is observed, the increase becomes less at higher osmotic
gradients. There are two possible reasons for these observations, which
may contribute at the same time: At high osmotic gradients vesicles are
unstable and loose access area already during sedimentation from bud-
ding. Thus, effects similar to lower osmotic gradients are observed. - This
may explain the observed saturation at high osmotic gradients. - Further-
more, the membrane - substrate interaction potential exhibits a minimum,

---

[5]This adhesion state was already characterized in chapter 3.
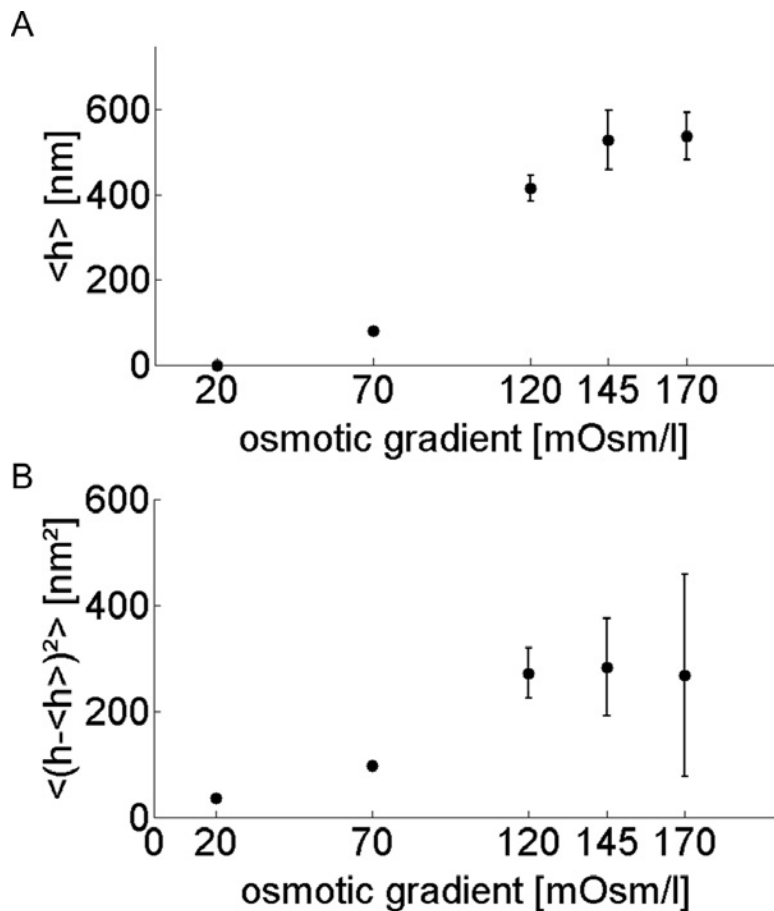
Figure 4.9: Results of initial osmotic pressure change of vesicles adhering to large grid structure. A: Average membrane heights $\langle h \rangle$ within fluctuation regions rise from 0 to ~ 550 nm. B: Mean square fluctuation amplitudes $\langle (h - \langle h \rangle)^2 \rangle$ increase from the noise background of $\sim 36 \; nm^2$ to $\sim 300 \; nm^2$.

which is shifted to higher heights at lower vesicle tensions. Effects of low tension are supported by the trend of mean square fluctuation amplitudes (see figure 4.9). An initially strong increase of 36 -300 nm^2 is followed by a leveling off at high osmotic gradients, which is in accordance with measured average heights.

It hast to be noted that the osmotic gradient also causes slight differences in vesicle gravity, which are opposite to vesicle tension variations: Dur-

ing osmotic deflation, density of sucrose solution inside the vesicle rises. Thus, gravity contributes slightly more to the membrane-substrate interaction and equilibrium heights would be shifted to lower values. During osmotic inflation, effects are opposite.

Even though, theoretically, this effect should contribute to the total membrane-substrate interaction, no obvious effect was detected here.

4.3   Conclusion

In this chapter, variations of the structured adhesion experiment were employed to test their influence on the adhesion state.

Small grid and line structure, as examples of altered spatial receptor distribution, allowed us to study effects of adhesive area spacing as well as differences arising from confinement and draining of the buffer trapped beneath the membrane. Analyses of orientation, topography and fluctuation demonstrated that mere geometrical changes in receptor distribution had negligible effect on the adhesion state. A lack of vesicle orientation along structures was attributed to weak adhesion of the system, as it was identified for the model system in the previous chapter 3. In contrast to reports on cell studies [110, 112], the vesicles did not exhibit any elongation along the line structures. This can be understood from basic thermodynamic considerations. When a vesicle is freshly sedimented on a substrate, its under surface flattens to form the so called contact zone. At this stage, the vesicle adheres weakly and the lower membrane resides in the weak minimum of the membrane-substrate interaction potential. If in addition there is a strong and steep minimum closer to the substrate, as is the case here over the patterned lines, the membrane, or parts of it, transits to this deeper minimum. At this stage, the contact zone (which now partially overlaps with the adhesion zone) may expand if the spreading pressure is high enough (see, for example, [23] for a discussion of spreading pressure). Here, as we have shown in the previous chapter, the adhesion is

weak. Thus the spreading pressure is expected to be weak also. Therefore, the contact zone remains unchanged by adhesion and elongation does not occur.

Moreover, identical average heights and fluctuation strengths demonstrated that adhesion is mostly influenced by membrane properties as well as generic interactions. Thus, evidence of vesicles equilibration was given and this is an essential prerequisite for the application of theoretical expressions to characterize the system.

Experiments of tension variation by means of osmotic pressure changes resulted in obvious effects on the adhesion state. Osmotic de- and inflation resulted in an increased and decreased membrane-substrate spacing within fluctuation areas. In addition, very similar effects of osmotic changes were found for different substrates and for static as well as dynamic changes. This demonstrated the generality of this effect. From these observations it was concluded, that with increasing tension, which corresponds to osmotic inflation, the minimum of the membrane-substrate interaction is shifted towards smaller heights. Decreasing vesicle tension causes the opposite effect. Another, not obvious effect, should arise from density differences between vesicle in- and exterior. As osmotic pressure directly influences gravity of vesicles, equilibrium heights should be shifted to slightly smaller values in case of osmotic deflation. For osmotic inflation, gravity should diminish and height shifted to slightly higher values. This effect is opposite to variation in tension. Thus, the nonspecific interaction depends on osmotic pressure in a non-trivial way. Also, since, in contrast to membrane tension effects, gravity effects are not obviously detectable, an indication of their contribution to the unspecific interaction potential is found. The position of the potential minimum appears to strongly dependent on the Helfrich term, while gravity has a significantly smaller effect.

In principle, observations of membrane dynamics after osmotic pressure changes, i.e. the change of membrane height observed over time, should

allow for further analysis of membrane permeability and mechanical aspects of a bound membrane. Theoretical and experimental studies of osmotically induced flux across membranes and membrane stability against hydraulic pressures have been published before [133,134]. The biomimetic system of this work is ideal to study osmotic pressure effects on adhesion.

Chapter 5

Free Membrane Fluctuations: Characterization of Fluctuation Correlation Spectroscopy (FluCS)

This chapter on fluctuation correlation spectroscopy first introduces theoretical aspects of membrane dynamics. In the main part, a modification of the standard FCS technique is described, which enables correlation analysis of membrane shape fluctuations. This new approach is henceforth called fluctuation correlation spectroscopy (FluCS). Theoretical considerations and its experimental realization are discussed in detail.

5.1   Introduction

The bending modulus of the vesicle membrane used in this study is very low ($20\,k_B T$). Therefore, vesicle configurational changes arising from thermal agitation were observed. The vesicle exhibits dynamical equilibrium fluctuations around the shape of lowest energy, whose static properties have been studied in detail in the previous chapters. In addition to elastic properties of the membrane presented before (see sections 3.3.1.1- 3.3.1.4, 4.2.1.2-4.2.1.3), membrane dynamics is also highly influenced by the surrounding liquid: Motion of the membrane induces motion of the liquid

which in turn exerts a hydrodynamic force on the membrane. During this process the membrane encounters viscous damping and energy is dissipated.

Dynamics of such membranes were first described by Brochard and Lennon in 1975 [135], who employed bending elasticity, first described by Helfrich [121] to quantify membrane fluctuation spectrum and amplitude and derived an expression for hydrodynamic damping. Later Seifert [136], Evans [137] and Miao [138] extended the work substantially accounting for membrane tension as well as intermonolayer friction, which both add to the relaxation of the system.

For the present work, analysis was restricted to the classical membrane model by Brochard and Lennon, where the membrane is a single fluid surface without any intrinsic dissipation mechanism. Considering in addition to bending elasticity, also membrane tension effects, dynamical equilibrium fluctuations of the system were described by Seifert [19]. The autocorrelation function of membrane height fluctuations in Fourier space are given by:

$$\langle h(q,t)h^*(q,t+\tau)\rangle = \frac{k_B T}{\kappa q^4 + \sigma q^2} e^{-\frac{\kappa q^3 + \sigma q}{4\eta}\tau} \quad . \tag{5.1}$$

The first factor is the well known static height-height correlation function for a membrane with bending rigidity κ and tension σ. The second factor describes the hydrodynamic relaxation, with a damping rate composed of dissipation $1/(4\eta q)$ and membrane energy $\kappa q^4 + \sigma q^2$. Here, q is the wavevector and η the bulk liquid viscosity.

In this study, dynamical equilibrium fluctuations were probed with a standard FCS setup (as described in section 2.3.3). In contrast to FCS, here the membrane is saturated with fluorescent dye molecules. Therefore, instead of detecting intensity fluctuations which arise from single molecule diffusion, the recorded intensity fluctuations originate from the spatial displacement of the membrane.

This new approach, called FluCS, does not require any changes in the hardware of a regular FCS setup: data recorded in the regular FCS mode is then analyzed to yield FluCS measurements. Thus, FluCS exploits the

high sensitivity and temporal resolution of FCS and gives access to fast dynamics of fluctuating objects. Unlike RICM (see e.g. section 3.3.1.1), objects close to a wall as well as further away from a substrate can be observed.

5.2 Theory of FluCS
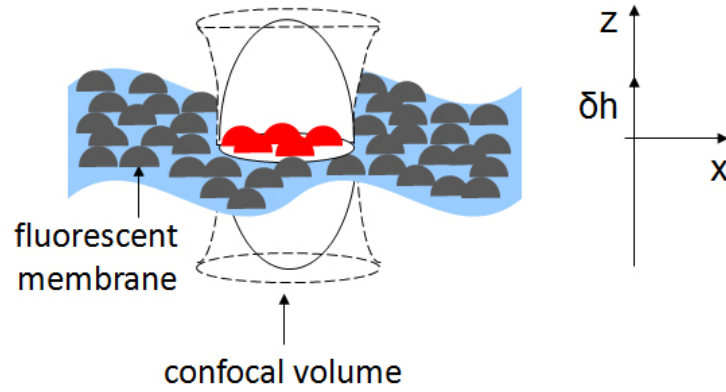
Figure 5.1: Sketch of the experiment. A membrane containing a relatively high amount of fluorophore is positioned in the confocal volume. The membrane fluctuates around its average position z and exhibits amplitudes δh.

A slightly modified theory of FCS was developed starting from the classical equation of detected intensity $I(h(t))$ from a homogeneous distribution of fluorescent molecules in a Gaussian illumination volume [139, 140]

$$
\begin{aligned}
I(h(t)) &= I_{max} \int dx \int dy\, e^{-2\left(\frac{x^2+y^2}{\omega_0^2}+\frac{z^2}{z_0^2}\right)} \cdot c_0 + I_B \\
&= I_{max}\frac{\pi c_0 \omega_0^2}{2} e^{-\frac{2z^2}{z_0^2}} + I_B \quad,
\end{aligned}
\tag{5.2}
$$

with I_{max} is the maximal intensity, c_0 the molecular concentration and ω_0

111

and z_0 the radial and axial size of the observation volume (see section A, 'confocal volume' for measured values of the latter two.).

For a theoretical description of membrane fluctuation correlation analysis, the following modifications to standard FCS theory are introduced:

- A soft membrane is considered, which exhibits fluctuations $\delta h(t)$ around its average position z (any drift in the position of the membrane is excluded). Thus, the membrane position $h(t)$ at time t is defined by:

$$h(t) = z + \delta h(t) \quad .$$

  Here, the membrane is horizontal and parallel to the x-axis. z denotes the average membrane position relative to the centre of the detection volume (see figure 5.1).

- The membrane contains a high percentage of fluorescently marked lipids. Therefore, any concentration variations within the detection volume are negligible with respect to the average concentration[1]:

$$c(h(t)) = c_0 \quad .$$

- The detected intensity I varies in the (x, y) plane according to a Gaussian illumination beam profile. In z direction, it is a Gaussian as detected through the variation of membrane position along the z axis. Furthermore, constant background intensity I_B, i.e. dark counts of the detector, is assumed. A sketch of the experimental setup and axes definitions is given in figure 5.1. Using equation 5.2, and replacing z

---

[1] A simple estimate demonstrates the reduction of number fluctuations. Assuming a standard deviation of number fluctuations $1/\sqrt{N}$ and $N = c\pi\omega_0^2/(100 \cdot A_{lipid})$ one obtains 51% fluctuations at $c = 0.001$ mol%, but only 16% fluctuations at $c = 1$ mol%. Here, ω_0 was 281 nm, as determined in section A, and $A_{lipid} = 8^2$ $Å^2$ the lipid diameter.

by $h(t)$ we get:

$$
\begin{aligned}
I(h(t)) &= I_{max} \int dx \int dy \, e^{-2\left(\frac{x^2+y^2}{\omega_0^2}+\frac{h(t)^2}{z_0^2}\right)} \cdot c_0 + I_B \qquad (5.3) \\
&= I_{max}\frac{\pi c_0 \omega_0^2}{2} e^{-\frac{2h(t)^2}{z_0^2}} + I_B
\end{aligned}
$$

As for regular FCS z-scan measurements (see 2.3.3.3 for an introduction or 3.3.2.1 for its application), the detected intensity, as given in equation 5.3, yields a Gaussian profile for measurements along the z-axis. This is an important consequence as it allows us to locate the membrane position within the confocal volume.

In the following, it is assumed that intensity fluctuations at each membrane position are sufficiently small to be approximated by a Taylor expansion of $I(h(t))$ around z up to second order:

$$
I(h(t)) \sim I(z) + \frac{\delta I}{\delta h}\Big|_z (h(t)-z) + \frac{1}{2}\frac{\delta^2 I}{\delta h^2}\Big|_z (h(t)-z)^2 \quad, \qquad (5.4)
$$

where from 5.3 the intensity $I(z)$ and the derivatives $\frac{\delta I}{\delta h}$ and $\frac{\delta^2 I}{\delta h^2}$ are given by

$$
I(z) = I\frac{\pi c_0 \omega_0^2}{2} e^{-\frac{2z^2}{z_0^2}} + I_B \quad, \quad \frac{\delta I}{\delta h}\Big|_z = I\frac{\pi c_0 \omega_0^2}{2}\left(-\frac{4z}{z_0^2}\right) e^{-\frac{2z^2}{z_0^2}}
$$

$$
\text{and} \quad \frac{\delta^2 I}{\delta h^2}\Big|_z = \frac{4}{z_0^2}\left(\frac{4z^2}{z_0^2}-1\right)(I(z)-I_B) \quad. \qquad (5.5)
$$

In appendix B, it is shown that this approximation yields sufficient spatial accuracy.

Of particular importance are membrane fluctuation measurements at the inflection point of the Gaussian intensity profile. Membrane fluctuations at the side of the excitation profile result in strong intensity variations, while with the membrane positioned at the centre of the profile, intensity variations are highly reduced. Thus, membrane motion at the inflection

point is converted most efficiently into intensity variations. At this point, the second derivative of the intensity vanishes and according to equation 5.4 displacements of the membrane scale approximately linearly with measured intensity:

$$\delta h(t) = (h(t) - z) \sim \frac{(I(h(t)) - I(z))}{\left.\frac{\delta I}{\delta h}\right|_z} = \frac{\delta I(h(t))}{\left.\frac{\delta I}{\delta h}\right|_z} , \qquad (5.6)$$

However, when analyzing membrane fluctuations rather then a time averaged height value, the relation is not so simple: Membrane roughness can not be considered to be a statistical contribution to an effective width of the membrane anymore. Instead, fluctuations at all scales have to be accounted for. For the present system their contribution depends on the form of the normalized point spread function $P(\vec{x})$, where

$$P(\vec{x}) = \frac{2}{\pi\omega^2} e^{-2\frac{\vec{x}^2}{\omega^2}}$$

This means that measured height fluctuations are in fact derived from a convolution of real fluctuations $h_r(x, y, t)$ with $P(\vec{x})$ in the $\vec{x} = (x, y)$ plane:[2]

$$
\begin{aligned}
\delta h(\vec{x}, t) &= \delta h_r(\vec{x}, t) * P(\vec{x}) \\
&= \int d\vec{x}' \, h_r(\vec{x}', t) \cdot P(\vec{x} - \vec{x}') \\
&= \frac{1}{(2\pi)^2} \frac{2}{\pi\omega^2} \int d\vec{x}' \int d\vec{q} \, \delta h_r(\vec{q}, t) e^{i\vec{q}\vec{x}'} e^{-2\frac{(\vec{x} - \vec{x}')^2}{\omega^2}} \qquad \text{, define } \vec{l} := \vec{x} - \vec{x}' \\
&= -\frac{1}{(2\pi)^2} \frac{2}{\pi\omega^2} \int d\vec{l} \int d\vec{q} \, \delta h_r(\vec{q}, t) e^{i\vec{q}(\vec{x} - \vec{l})} e^{-2\frac{\vec{l}^2}{\omega^2}}
\end{aligned}
$$

---

[2]The Fourier Transformation in general and for the Gaussian explicitly are of the form:

$$f(\vec{x}) = \frac{1}{(2\pi)^2} \int d\vec{q} \, f(\vec{q}) \, e^{i\vec{q}\vec{x}} \qquad , \qquad f(\vec{q}) = \int d\vec{x} \, f(\vec{x}) \, e^{-i\vec{q}\vec{x}}$$

$$f(\vec{x}) = e^{-a\vec{x}^2} \qquad , \qquad f(\vec{q}) = \frac{\pi}{a} e^{-\frac{\vec{q}^2}{4a}}$$

$$
\begin{aligned}
&= -\frac{1}{(2\pi)^4} \int d\vec{l} \int d\vec{q}\, \delta h_r(\vec{q},t) e^{i\vec{q}\vec{x}} e^{-i\vec{q}\vec{l}} \int d\vec{q}'\, e^{-\frac{q'^2\omega^2}{8}} e^{i\vec{q}'\vec{l}} \\
&= -\frac{1}{(2\pi)^4} \int d\vec{l} \int d\vec{q} \int d\vec{q}'\, \delta h_r(\vec{q},t) e^{i\vec{q}\vec{x}} e^{-i(\vec{q}-\vec{q}')\vec{l}} e^{-\frac{q'^2\omega^2}{8}} \\
&= -\frac{1}{(2\pi)^2} \int d\vec{q} \int d\vec{q}'\, \delta h_r(\vec{q},t) e^{i\vec{q}\vec{x}} e^{-\frac{q'^2\omega^2}{8}} \delta(\vec{q}-\vec{q}') \\
&= -\frac{1}{(2\pi)^2} \int d\vec{q}\, \delta h_r(\vec{q},t) e^{i\vec{q}\vec{x}} e^{-\frac{q^2\omega^2}{8}} \quad (5.7)
\end{aligned}
$$

It has to be noted, that due to the wide range of z positions probed, the confocal radius ω is not the confocal waist radius ω_0, but a measure which increases with respect to the membrane-confocal centre distance, as introduced in 2.3.3.3.

Based on these considerations, theoretical expressions for the height-height autocorrelation function and the correlation amplitude were derived as outlined in the following.

5.2.1 Height-height Correlation Function

The intensity autocorrelation function is calculated from equation 5.4 for measurements at the inflection point:

$$
\begin{aligned}
\frac{\langle I(h(t)) \cdot I(h(t+\tau)) \rangle}{\langle I(h(t)) \rangle^2} &= \frac{1}{\langle I(h(t)) \rangle^2} \left\{ \langle I(z)^2 \rangle + \left\langle \left[\left(\left.\frac{\delta I}{\delta h}\right|_z \right)^2 \delta h(t) \cdot \delta h(t+\tau) \right] \right\rangle \right. \\
&\quad + \left. \left\langle I(z) \cdot \left.\frac{\delta I}{\delta h}\right|_z \delta h(t) \right\rangle + \left\langle I(z) \cdot \left.\frac{\delta I}{\delta h}\right|_z \delta h(t+\tau) \right\rangle \right\} \\
&= \frac{1}{\langle I(h(t)) \rangle^2} \left\{ \langle I(z)^2 \rangle + \left(\left.\frac{\delta I}{\delta h}\right|_z \right)^2 \langle \delta h(t)\delta h(t+\tau) \rangle \right\} \quad (5.8)
\end{aligned}
$$

Here, time averages over $\delta h(t)$ vanish. According to the theory of membrane correlation analysis by Seifert et al. (see equation 5.1) and using the membrane equation of motion $h(\vec{q},t) = h(\vec{q},0) \cdot e^{-\frac{\kappa q^3}{4\eta}t}$ together with equation 5.7 as well as the equipartition theorem, the height-height correlation

115

function amounts to:

$$
\begin{aligned}
\langle \delta h(t) \delta h(t+\tau) \rangle &= \int d\vec{x}\, \langle \delta h(\vec{x},t) \delta h(\vec{x},t+\tau) \rangle \\
&= \frac{1}{(2\pi)^4} \int d\vec{x} \int d\vec{q} \int d\vec{q}'\, \langle \delta h_r(\vec{q},t) \delta h_r(\vec{q}',t+\tau) \rangle e^{-\frac{(\vec{q}^2+\vec{q}'^2)\omega^2}{8}} e^{i(\vec{q}+\vec{q}')\vec{x}} \\
&= \frac{1}{(2\pi)^2} \int d\vec{q} \int d\vec{q}'\, \delta(\vec{q}+\vec{q}') \langle \delta h_r(\vec{q},t) \delta h_r(\vec{q}',t+\tau) \rangle e^{-\frac{(\vec{q}^2+\vec{q}'^2)\omega^2}{8}} \\
&= \frac{1}{(2\pi)^2} \int d\vec{q}\, \langle \delta h_r(\vec{q},t) \delta h_r(-\vec{q},t+\tau) \rangle e^{-\frac{2\vec{q}^2\omega^2}{8}} \\
&= \frac{1}{(2\pi)^2} \int d\vec{q}\, \langle \delta h_r(\vec{q},t) \delta h_r^*(\vec{q},t+\tau) \rangle e^{-\frac{\vec{q}^2\omega^2}{4}} \quad \text{, using equation 5.1} \\
&= \frac{k_B T}{(2\pi)^2} \int dq \int d\phi\, \frac{q}{\kappa q^4 + \sigma q^2} e^{-\frac{(q\cos\phi)^2\omega^2}{4} + \frac{(q\sin\phi)^2\omega^2}{4}} e^{-\frac{\kappa q^3+\sigma q}{4\eta}\tau} \\
&= \frac{k_B T}{2\pi} \int dq\, \frac{1}{\kappa q^3 + \sigma q} e^{-\frac{q^2\omega^2}{4}} e^{-\frac{\kappa q^3+\sigma q}{4\eta}\tau} \quad .
\end{aligned}
\tag{5.9}
$$

And the mean square fluctuation amplitude reads:

$$
\langle \delta h(t)^2 \rangle = \frac{k_B T}{2\pi} \int dq\, \frac{1}{\kappa q^3 + \sigma q} e^{-\frac{q^2\omega^2}{4}} \quad .
\tag{5.10}
$$

The integral runs over all modes that can be excited on the membrane. It has a natural lower limit as determined by the vesicle size (radius R) and an effective upper limit through the size of the confocal volume. The smallest mode denotes the wavelength that extends around the vesicle circumference. The upper limit results from the fact that membrane undulations of wavelengths smaller than the detection volume will contribute a net intensity change of zero at all times. On the other hand, all modes larger than q_{max} contribute, if the membrane inside the detection volume moves as a whole. Limits corresponding to the present system were $q_{min} = \frac{1}{R} \sim 3.3 \cdot 10^4 m^{-1}$ and $q_{max} = \frac{\pi}{\omega_0} \sim 10^7 m^{-1}$. For typical membrane parameter values, $\kappa = 20\, k_B T$ and $\sigma = 1 - 10 \cdot 10^{-7} J/m^2$, the height-height correlation function was seen to dependent on both membrane parameters, as the calculated orders of magnitude for the two contributions overlap:

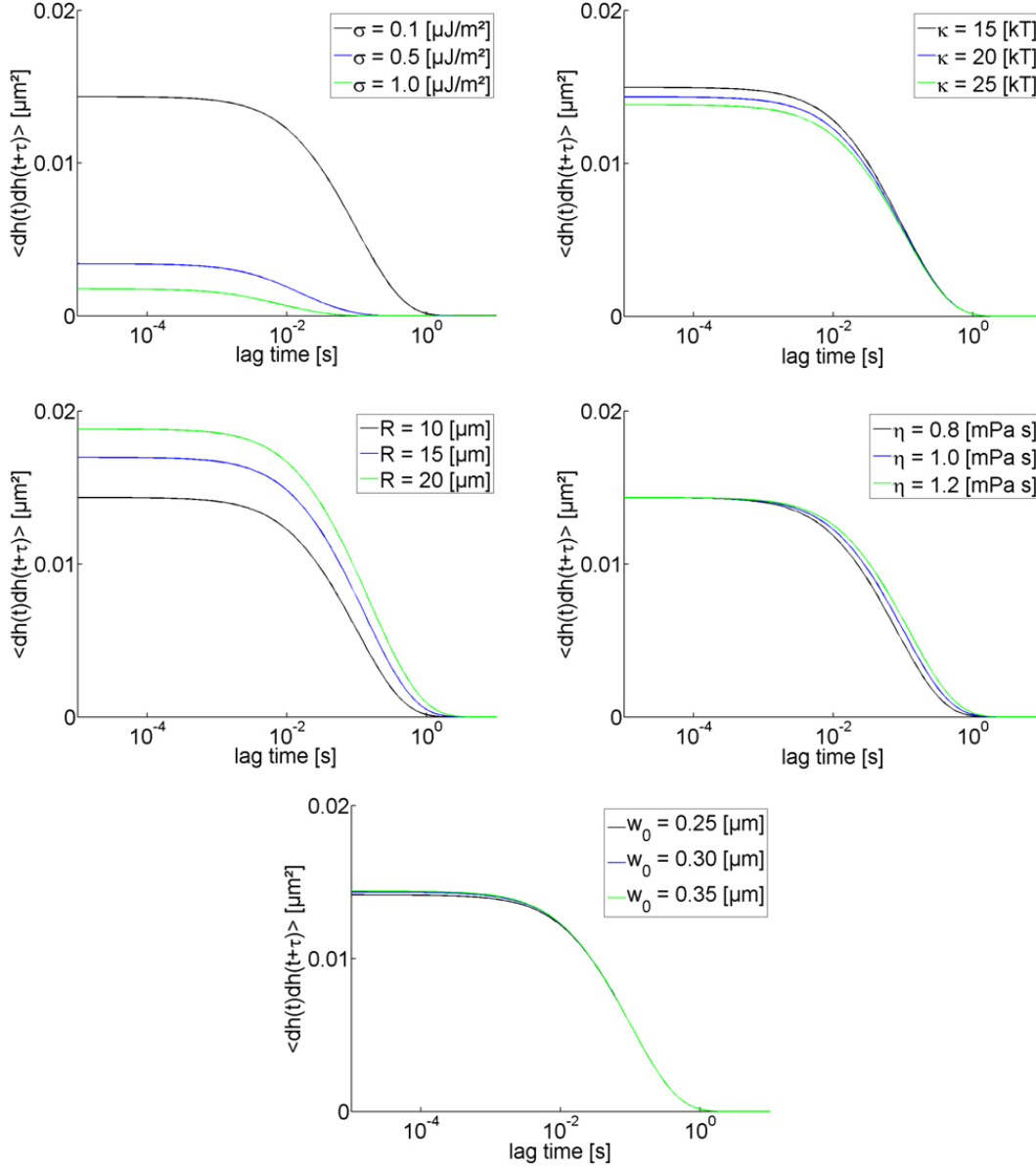Figure 5.2: Parameter variation of theoretical height-height correlation function (see equation 5.9). Values of unchanged parameters were: $\sigma = 0.1\ \mu J/m^2$, $\kappa = 20\ k_B T$, $R = 10\ \mu m$, $\eta = 0.001\ kg/(m \cdot s)$ and $\omega_0 = 0.3\ \mu m$.

$$\sigma \sim (1-10) \cdot 10^{-7} J/m^2 \sim \begin{cases} \kappa q_{max}^2 \sim 8 \cdot 10^{-6} J/m^2 \\ \kappa q_{min}^2 \sim 8 \cdot 10^{-11} J/m^2 \end{cases}$$

Thus, no approximation is feasible and the theoretical height-height correlation function depends on five parameters: Membrane tension σ, bending rigidity κ, vesicle radius R, effective friction η and the confocal waist radius ω_0. Figure 5.2 shows the influence of typical parameter values on the shape of the height-height correlation function. From vesicle parameters (σ, κ, R), σ vastly alters the function shape while κ has only minor influence on amplitude and decay. R affects the shape in a similar but stronger manner as bending rigidity. η determines the nature of damping in the system and shifts the decaying part of the function within a small range. Finally, ω_0 apparently has the smallest effect and alters only the correlation amplitude.

5.2.2 Correlation Amplitude

Is the investigated system stationary, i.e. it is translation invariant and ergodic, much information on membrane parameters is readily obtained from the analysis of the correlation amplitude. In the intensity approximation up to second order (see equations 5.4 - 5.5) it reads:

$$
\begin{aligned}
\frac{\langle I(h(t))^2 \rangle}{\langle I(h(t)) \rangle^2} &= \frac{I(z)^2 + (I(z) - I_B)^2 \frac{4}{z_0^4} \left(4z^2 \langle \delta h(t)^2 \rangle + \left(\frac{4z^2}{z_0^2} - 1 \right)^2 \langle \delta h(t)^4 \rangle \right)}{\left\{ (I(z) - I_B) e^{-\frac{2}{z_0^2} \langle \delta h(t)^2 \rangle} + I_B \right\}^2} \\
&\quad + \frac{\frac{4I(z)}{z_0^2} \left(\frac{4z^2}{z_0^2} - 1 \right) (I(z) - I_B) \langle \delta h(t)^2 \rangle}{\left\{ (I(z) - I_B) e^{-\frac{2}{z_0^2} \langle \delta h(t)^2 \rangle} + I_B \right\}^2} \\
&= \frac{1 + (1 - \frac{I_B}{I(z)})^2 \frac{4}{z_0^4} \left(4z^2 \langle \delta h(t)^2 \rangle + \left(\frac{4z^2}{z_0^2} - 1 \right)^2 \langle \delta h(t)^4 \rangle \right)}{\left\{ \left(1 - \frac{I_B}{I(z)} \right) e^{-\frac{2}{z_0^2} \langle \delta h(t)^2 \rangle} + \frac{I_B}{I(z)} \right\}^2} \\
&\quad + \frac{\frac{4}{z_0^2} \left(\frac{4z^2}{z_0^2} - 1 \right) \left(1 - \frac{I_B}{I(z)} \right) \langle \delta h(t)^2 \rangle}{\left\{ \left(1 - \frac{I_B}{I(z)} \right) e^{-\frac{2}{z_0^2} \langle \delta h(t)^2 \rangle} + \frac{I_B}{I(z)} \right\}^2} \quad . \qquad (5.11)
\end{aligned}
$$

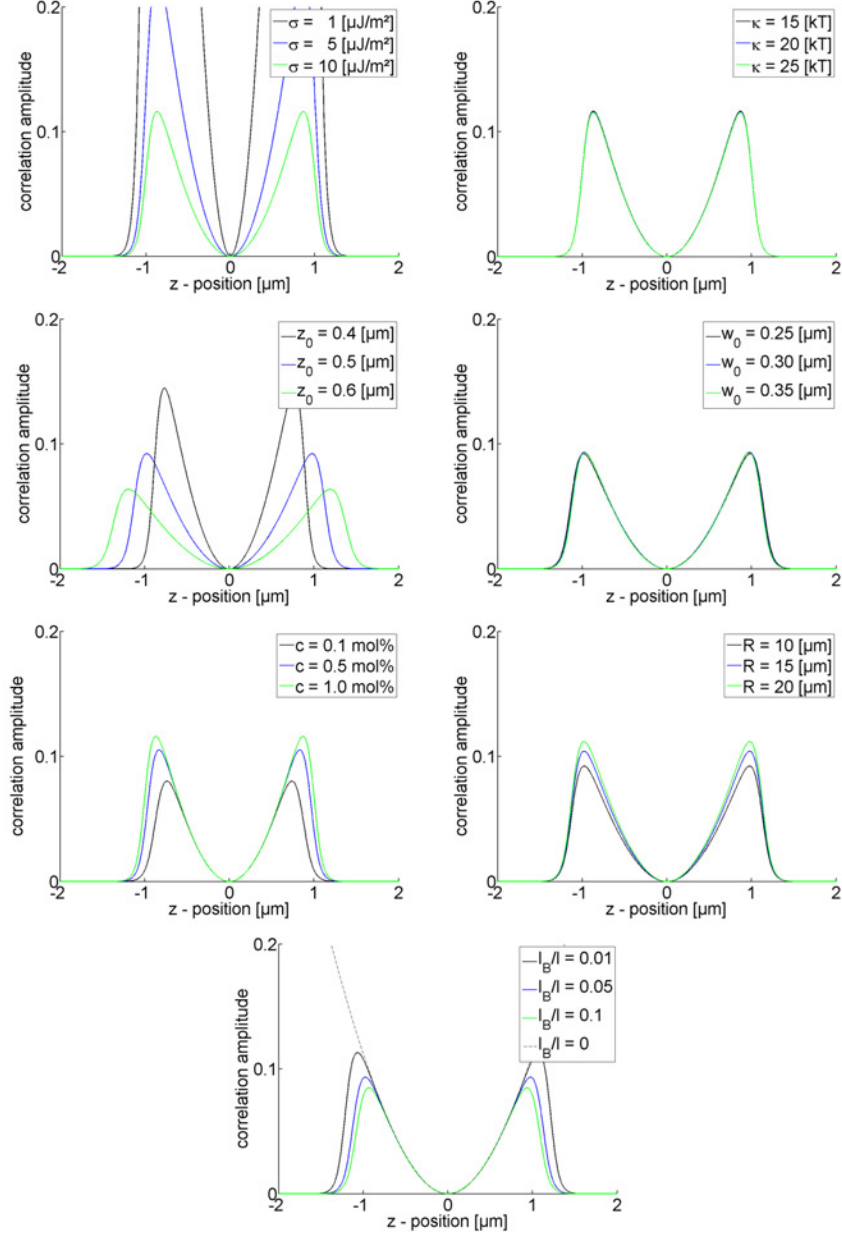Figure 5.3: Theoretical correlation amplitude (see equation 5.11) as a function of different z positions and the dependence of this function on the parameters σ, κ, z_0, ω_0, c, R and I_B. Values of unchanged parameters were: $\sigma = 10 \, \mu J/m^2$, $\kappa = 20 \, k_B T$, $z_0 = 0.5 \, \mu m$, $\omega_0 = 0.3 \, \mu m$, c = 1 mol%, R = 10 μm and $I_B = 0.01$ I.

At this point, the expression of the theoretical correlation amplitude depends on the parameters: Membrane tension σ, bending rigidity κ, vesicle radius R, fluorophore concentration c, background intensity I_B as well as confocal waist radii in radial and axial directions, ω_0 and z_0, respectively. Figure 5.3 gives examples of correlation amplitude dependence on typical system parameters.

As for height correlation, strong influence of σ is found, while κ hardly alters the shape. z_0 and ω_0 have strong and weak effect on the axial stretch of the function, respectively. R shifts the maxima of the correlation amplitude. Changes in background intensity I_B or concentration c induce equivalent and opposite changes, as both essentially vary the signal to noise ratio of the system. For a perfect system with $I_B \to 0$ the theoretical curve adopts a parabolic shape, as shown in figure 5.3.

More importantly, only the parameters σ, R and z_0 significantly alter the shape of the function close to $z = 0$. As a consequence, quantitative analysis is restricted to this parabolic part, where the number of parameters can be reduced. In addition, experimental uncertainties which arise in the axial extension of the confocal volume can be neglected. Thus, for quantitative studies, parameters I_B and c are eliminated from writing the theoretical correlation amplitude in the limit of $I_B \to 0$:

$$\frac{\langle I(h(t))^2 \rangle}{\langle I(h(t)) \rangle^2} = \frac{1 + \frac{4}{z_0^4} \left(4z^2 \langle \delta h(t)^2 \rangle + \left(\frac{4z^2}{z_0^2} - 1 \right)^2 \langle \delta h(t)^4 \rangle + z_0^2 \left(\frac{4z^2}{z_0^2} - 1 \right) \langle \delta h(t)^2 \rangle \right)}{e^{-\frac{4}{z_0^2} \langle \delta h(t)^2 \rangle}}$$

(5.12)

In the following analysis, this equation is used to interpret experimental data.

5.3   Experimental Realization

In the following a detailed description is given on how a standard Fluorescence Correlation Spectroscopy (FCS) setup is used for height measurements.
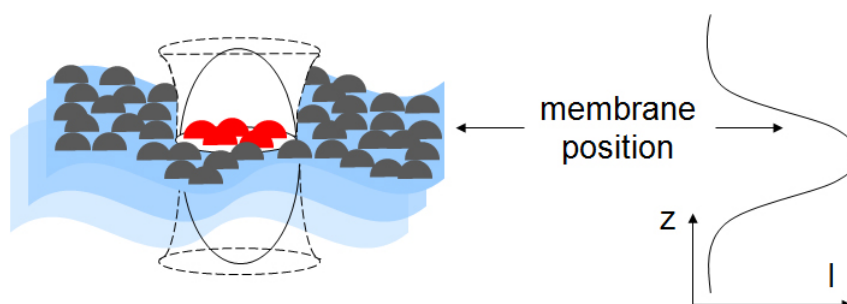
Figure 5.4: Measurement principle of FluCS: Autocorrelation curves are acquired from a fluctuating membrane saturated with fluorophore. The confocal volume is shifted through the membrane in a z-stack and ACFs recorded at each position. Recorded average intensities follow a Gaussian intensity profile, from which the membrane is located.

GUVs (see sections 2.2.1.1 for preparation details) served as test objects. The standard lipid mixture was used (see section 2.2.4) and different amount of lipids in the membrane were labeled with fluorescent molecules. Here, as for FCS the fluorophore stability is crucial to the measurement. Thus, excitation intensities of a 543 nm laser were damped with an AOTF to <0.2 μW intensity, to yield count rates between 60 - 100 kHz. Several repeats of the same measurement were employed to exclude any bleaching effects of the fluorophore. Unless stated otherwise, GUVs were observed in a hyperosmotic fluid environment which yielded large excess area and strong fluctuations. Prior to each experiment we waited 30 minutes for the GUVs to equilibrate. Autocorrelation curves were acquired in a z-stack, where the confocal volume position was shifted stepwise crossing the membrane position. First, a fast automated scan localized the membrane position. Second, z-stack measurements started -1 μm to -1.5 μm below the membrane centre. Third, after each measurement the axial position was increased in steps of 0.2 μm and this was repeated 15$\times$. On one hand, this yielded sufficient spatial accuracy and statistics for z-stack analyses. On the other hand, measurement time was not immoderately extended. As predicted by theory, detected intensities along the z-axis obeyed the Gaus-

sian intensity profile (see equation 5.3). Figure 5.4 depicts the measurement principle.

5.3.1 From FCS to FluCS
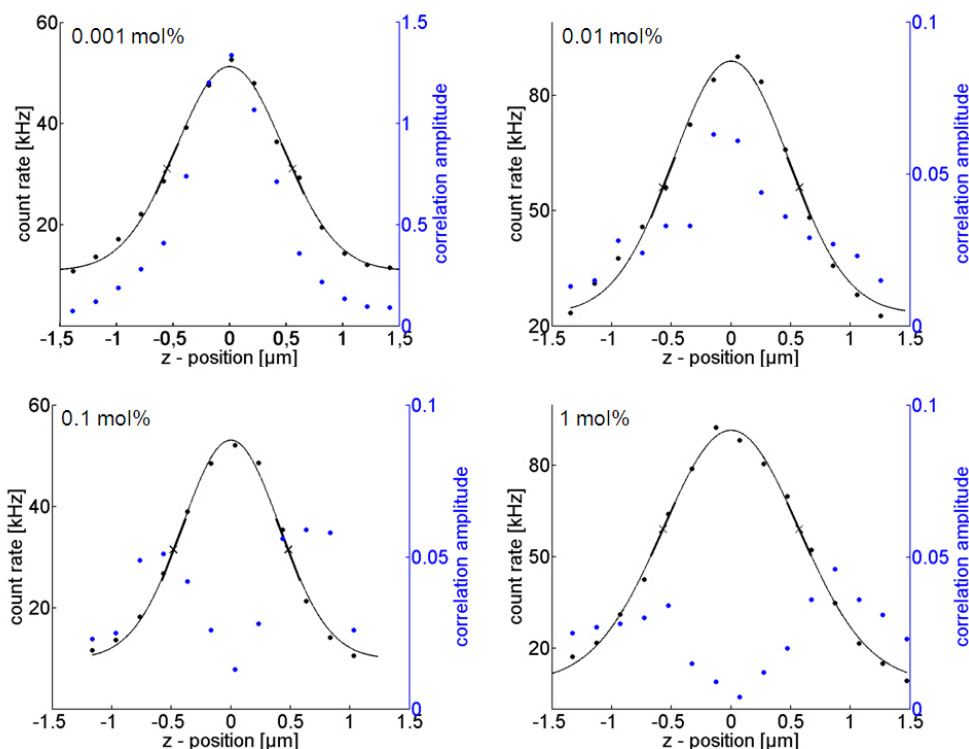
Figure 5.5: Effect of fluorophore concentration increase on z-stack measurements. The correlation amplitude (blue dots) changes from a Gaussian profile in the diffusion dominated case (0.001 mol%) to a characteristic double well shape in the fluctuation dominated case (1 mol%). Intensity profiles showed no significant change (black dots). In order to locate the central position and inflection points (black x's), intensity data was fitted with a 1D-Gaussian incl. an offset (black line).

We first considered the well-known diffusion dominated case. An increase in fluorophore concentration gave rise to a characteristic change

in the correlation amplitude as shown in figure 5.5. Concentrations of 0.001 mol% are generally employed for diffusion measurements. At this low concentration, the correlation amplitude represents the inverse of the number of particles and its Gaussian shape is understood from the following consideration. At the centre of the confocal volume, the detection area is smallest and so only a small number of molecules contributes to the signal. As the detection area increases with distance from its centre [88, 89], the number of detected particles therein rises as well and so, the correlation amplitude decays. Such behaviour arises purely due to diffusion and is also seen in a supported lipid bilayer. Next, fluorophore concentrations were raised in by an order of magnitude to 0.01 mol%. Here, a decay of the central amplitude peak was observed and the correlation amplitude deviated from a Gaussian. Further increase to 0.1 mol% shows the same trend. Finally, at 1 mol% fluorophore concentration, the correlation amplitude is significantly depressed and acquires a double well shape, with two maxima next to the inflection points of the intensity profile. At 1 mol% concentration the correlation amplitude does not represent the inverse particle number anymore, but is a measure of the membrane fluctuations. The shape is explained thus: When the membrane is at the centre of the confocal volume, its excursions which are small with respect to the beam size, give rise to small intensity variations. On the other hand, when the membrane is close to the edges of the beam, small excursions give rise to strong intensity variations, since the intensity is here a strongly decreasing function of z.

5.3.2 Control Experiments

Several control experiments were undertaken to verify that intensity fluctuations arise indeed from vesicle membrane fluctuations: First, a bilayer, consisting of a monolayer SOPC and an upper second layer of standard lipid mix with 1 mol% TRITC-DHPE was prepared as described before (see section 2.2.4 and 2.2.1.2). Z-stacks were recorded according to stan-

dard procedure (see 5.3.3). Seven SLB measurements were evaluated, a typical result is shown in figure 5.6. While the detected intensity exhibits the usual Gaussian intensity distribution, correlation amplitude values did not follow the characteristic double-well shape and absolute values were a magnitude lower then typical values of the correlation amplitude in membrane fluctuation experiments ($\sim$ 0.03). In a second experiment, vesicles of standard lipid mix with 1 mol% TRITC-DHPE were prepared in equiosmolar conditions to provide minimal excess area for fluctuations. Data was acquired similarly and five vesicles were evaluated, with a typical result given in figure 5.6. Intensity and correlation amplitude follow the same behaviour as in the case of SLBs. From these measurements a threshold to detect real vesicle fluctuations was derived, which has a correlation amplitude value of 0.003.
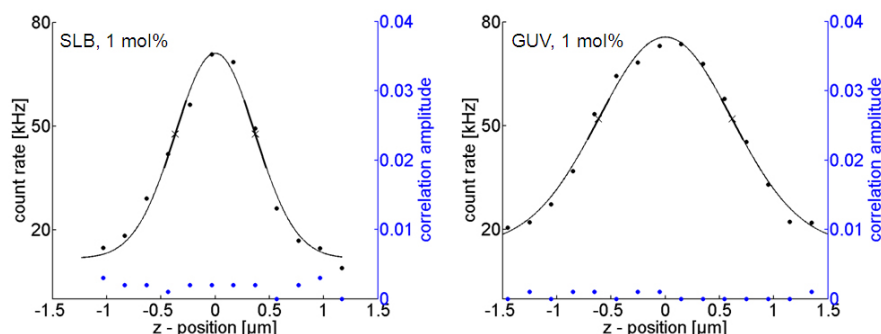
Figure 5.6: Control experiments on barely fluctuating systems: Z-stack of SLB with 1 mol% TRITC-DHPE in the upper layer (left) and z-stack of GUV immersed in equiosmolar conditions with 1 mol% TRITC-DHPE (right). Both systems exhibit no characteristic double well shape of the correlation amplitude. Instead it is flat and has maximal values of 0.003.

5.3.3   Optimization and Error Estimation

From the previous consideration follows: A typical FluCS measurement is realized using 1 mol% fluorophore (here the fluorophore coupled lipid

TRITC-DHPE was used) and observing GUVs in a hyperosmotic fluid environment, with an osmotic gradient of 170 $mOsm/l$ to provide sufficient excess area for fluctuations.

Stationarity of the signal and sufficient recording time are essential pre-
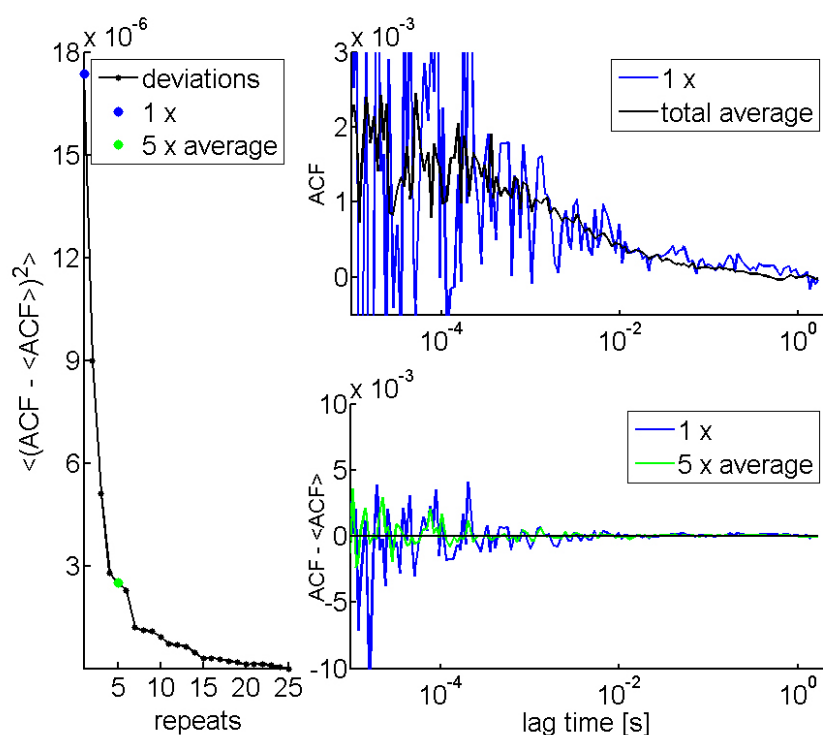
Figure 5.7: Check for signal stationarity and sufficient recording time. A long measurement of 125 s total duration was subdivided into 25 repeat measurements of 5 s duration. ACFs of the first repeat and the average over all repeats demonstrate the strong precision increase (upper right). Deviations from the total average indicate the stationarity of the signal (lower right). Mean square deviation from the total average is plotted for an increasing number of averaged repeats (left). A strong decline in deviations indicates increased precision. Minimal total measurement times were set to 5×5 s = 25 s.

requisites of FluCS. In order to test for these, several long measurements of 125 - 180 s total duration were acquired. Each measurement was sub-

divided into 25 - 36 short measurements, called repeats, of 5 s duration.
Averaging over ACFs obtained for each repeat yielded the optimal ACF
curve. An example of the first and the total average ACF is given in fig-
ure 5.7. Mean curves were calculated for an increasing number of repeats
and their deviation from the total average was plotted. Figure 5.7 shows
on the one hand the deviations of a $1\times$ and $5\times$ repeat average from the
optimal ACF. Here, a symmetric variation of the signal around 0 deviation
indicates stationarity of the signal. On the other hand, mean square devi-
ations of the signal from the optimal curve are plotted. A strong decrease
in values suggests a precision increase of the measurement. Again $1\times$ and
$5\times$ repeat averages are highlighted. Based on these results the minimal
total measurement time was set to $5\times5\,s = 25\,s$.[3]

The influence of the signal to noise ratio upon spatial resolution was es-
timated theoretically by calculating the error in height with variable fluo-
rescence and background intensity. It was assumed that intensities were
converted into heights at the inflection point of the Gaussian, where a lin-
ear dependence holds (see equation 5.6). For an increase in background
intensity, dI_B, the error in height, dh, is derived from the slope m which
has, in the inflection point where $z_0/2 = \pm(z - \mu)$, the analytical expres-
sion $m = \frac{2I_0}{z_0} \cdot 0.61$. z_0 is the axial waist of the confocal volume and I_0 the
central maximum, if there is no offset I_B, (as defined in equation 5.13):

$$dh = \frac{dI_B}{m} = \frac{dI_B \cdot \sigma_G}{I_0 \cdot 0.61}$$

Figure 5.8 shows the result of this estimation for typical fluorophore inten-
sity values $I_0 = 0 - 90\,kHz$. Background intensities were varied between
$I_B = 0 - 9\,kHz$. A lower limit of I_B arises from the dark current of the
APDs of $0.5\,kHz$. This is a common background intensity value for vesi-
cle experiments in PBS buffer. It has to be noted, however, that for other
systems[4] I_B values often reach higher values resulting in a corresponding
drastic increase in height error. To emphasize this, contour lines of 20 nm

---

[3]In most experiments, the total measurement time was 35 s.
[4]Depending on the medium used, cell experiments could have I_B values of $\sim 5\,kHz$.

and 100 nm error were added to the graph.
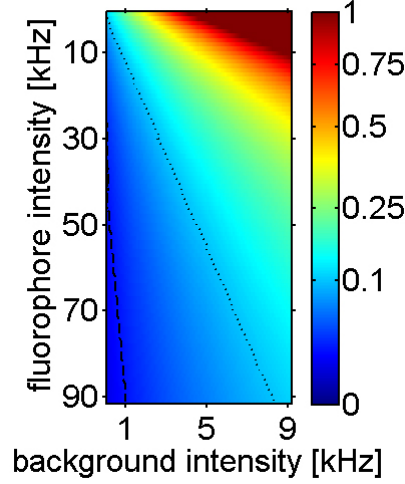
Figure 5.8: Dependence of error in height *dh* [*μm*] on signal to noise ratio. Contour lines denote 20 nm error (dashed black) and 100 nm error (dotted black), respectively.

5.4 Analysis Details

For data analyses, the average ACF and mean intensity $\langle I(h(t)) \rangle$ of all repeats was stored for each z-plane. A 1D Gaussian of the form

$$I(z) = I_0 \, e^{-2\frac{(z-\mu)^2}{z_0^2}} + I_B \quad , \tag{5.13}$$

was fitted to the intensity data. μ is the axial position of the intensity maximum and z_0 the confocal volume waist in axial direction. The inflection point (IP) and slope m at the IP for left and right side of the Gaussian were determined with the analytical expressions:

$$z_{IP} = \mu \mp \frac{z_0}{2} \qquad \text{and} \qquad m = \pm \frac{4(z_{IP} - \mu)}{z_0^2} \cdot (I(z) - I_B)$$

127

Data closest to the two inflection points were chosen. The height-height
autocorrelation function (HHACF), was derived from equation 5.8 apply-
ing the following steps: First normalized ACFs were multiplied by the
squared mean intensity $\langle I(h(t))\rangle^2$. Second, $\langle I(z)^2 \rangle$ was determined from
the average over five points of the HHACF at lag time 1 s, as this function
should decay to 0 at long correlation times τ. Finally, the result was di-
vided by the respective slope $m = \frac{\delta I}{\delta h}|_z$ and plotted.

Prior to fitting the experimental data with the theoretical model (see equa-
tion 5.9), its general applicability was tested. I.e. the best theoretical rep-
resentation of the data was determined and checked whether parameters
yield reasonable values. To do this, standard deviations of 6 - 10 ACF
repeats $\sigma_d(\tau)$ were calculated for each lag time τ. Then parameters of
the theoretical model were varied and for each parameter set the model
function was calculated. The absolute deviation between model and ex-
periment, called residual $\Delta(\tau)$, was identified at each point τ. A measure
of the best theoretical representation was deduced from the reduced χ^2-
value, which is defined as:

$$\chi^2_{red} = \frac{1}{N - p - 1} \sum_{i=1}^{N} \frac{\Delta(\tau_i)^2}{\sigma_d(\tau_i)^2} \quad ,$$

where N is the number of lag times and p the number of fitting parame-
ters. A χ^2_{red}-value close to 1 yields the best fit.

Of the five parameters of the theoretical model, the vesicle radius R and
the radial waist radius ω_0 were measured independently with high pre-
cision. Thus, three remaining variables (κ, σ, η) formed the parameter set
of the model function. Figure 5.9 shows a 3D parameter plot of reduced
χ^2-values for one HHACF curve. Parameters of the model function were
varied between $\kappa = 0 - 100 \, k_B T$, $\sigma = 0.1 - 1 \, \mu J/m^2$ and $\eta = 0.2 - 50 \cdot 10^{-3}$
$kg/(m \cdot s)$. The isosurface of $\chi^2_{red} \sim 1$ (black grid in figure 5.9) demon-
strates the sensitivity of HHACF to the parameters. While σ and η were
constrained to specific regions, κ extended over a wide range of physi-
cal values. Therefore, and since κ is a well known material constant, it
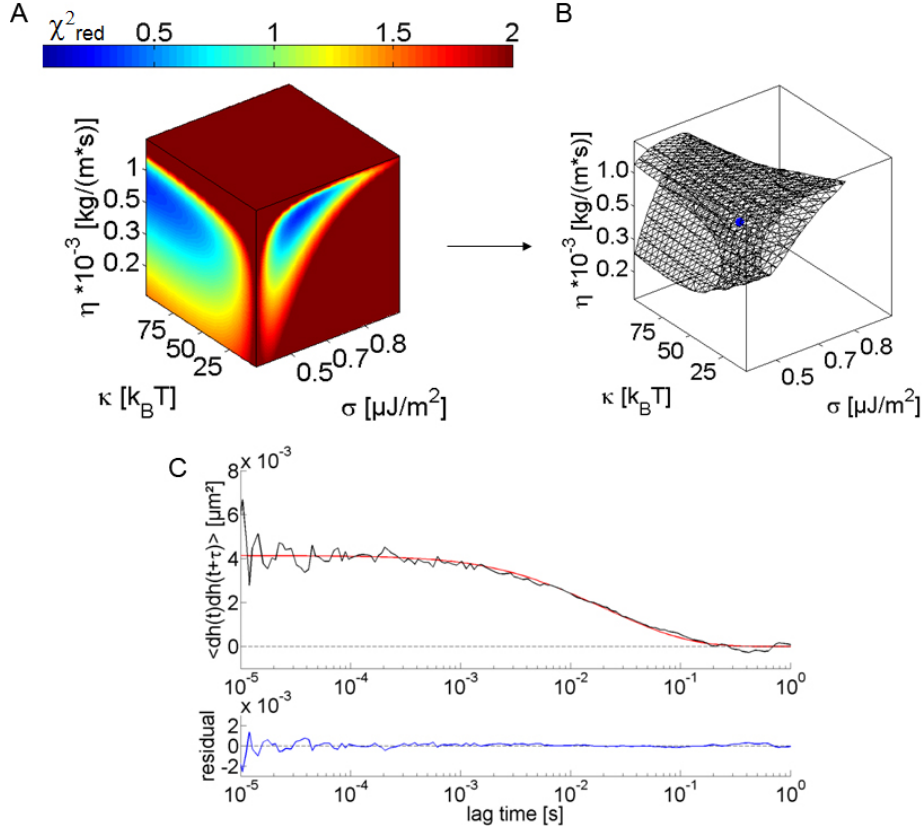
Figure 5.9: A: 3D parameter plot of χ^2_{red}-values for one HHACF curve. B: Isosurface of $\chi^2_{red} \in [0.95\ 1.05]$ (black grid). For fixed κ χ^2_{red} of 1.00 (blue dot) was found for the parameter set ($\kappa = 20$ $k_B T$, $\sigma = 0.48\ \mu J/m^2$, $\eta = 1.16 \cdot 10^{-3}\ kg/(m \cdot s)$). C: Measured HHACF (black), model function of the best parameter set (red) and residuals.

was decided to keep it fixed for analysis. κ was set to 20 $k_B T$ for the matrix lipid SOPC, as measured by Zhouy et al. and several other groups (see [125] and references therein). With this restriction, a χ^2_{red}-value of 1.00 was achieved for the parameter set ($\kappa = 20\ k_B T$, $\sigma = 0.48\ \mu J/m^2$, $\eta = 1.16 \cdot 10^{-3}\ kg/(m \cdot s)$). Thus, membrane tension σ and solvent viscosity η were close to the expected range, as adhered membranes exhibit membrane tensions on the order of $10^{-5} - 10^{-6}\ \mu J/m^2$ [104, 115] and a free membrane is expected to exhibit much smaller tension. Second, the

129

dynamic viscosity of water is $1.0 \cdot 10^{-3} \, kg/(m \cdot s)$ at 20 °C, which is also
expected for PBS buffer. In those cases where ACF repeat measurements
were available, a non-linear least square fit was applied to the data, using a
weighted Levenberg-Marquardt algorithm. Here, the χ^2 value, defined by
$\chi^2 = \sum_{i=1}^{N} \frac{\Delta(\tau_i)^2}{\sigma_d(\tau_i)^2}$ is minimized[5]. For the case of single ACF measurements
and no available standard deviation, a non-linear trust region method was
used. In this case, only the mean square deviation, defined by $\sum_{i=1}^{N} \Delta(\tau_i)^2$
is minimized. For the latter, parameters were constrained by upper and
lower bounds in such a way that sufficient variability was provided for:
$\sigma = [0.01, 1] \, \mu J/m^2$ and $\eta = [0.5, 5] \cdot 10^{-3} \, kg/(m \cdot s)$.
For the representation of height fluctuations over time, intensity fluctua-
tions $\delta I(h(t))$ were converted directly via the determined slope $m = \frac{\delta I}{\delta h}|_z$
into height fluctuations and plotted.

To obtain comparable results from correlation amplitude analyses, the
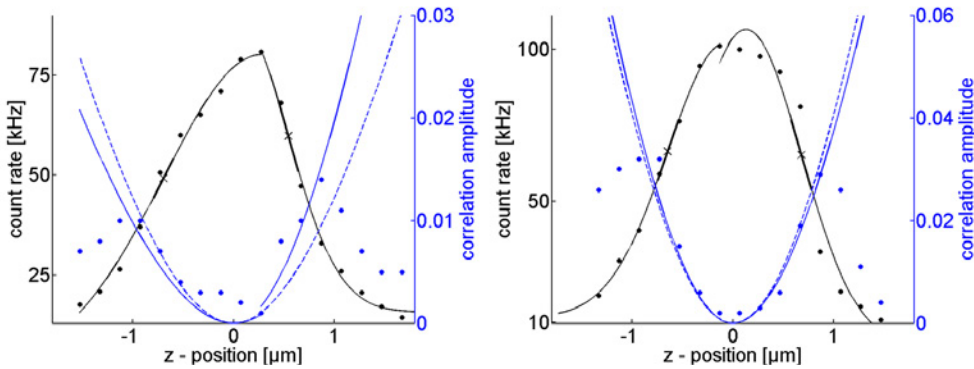
Figure 5.10: Results of one-sided fits to intensity and corre-
lation amplitude. Vesicles exhibiting strong (left) and weak
(right) axial asymmetry are plotted.

theoretical model was fitted to experimental data via the non-linear trust
region algorithm with upper and lower bounds as for HHACF analysis.
Here, the model function depended on the parameters membrane tension
σ, vesicle radius R as well as axial and radial waist radius z_0 and ω_0 (see

---

[5]$\Delta(\tau)$ is again the absolute deviation between model and experiment, called residual.
N is the number of lag times.

equation 5.12). Again, as the latter three are experimentally accessible with high precision, σ was the only parameter to be fitted. One source of error in this analysis is a possible asymmetric shape of the intensity and correlation amplitude values with respect to the origin. This may arise from the slightly differences between vesicle ex- and internal solution. To check for a possible influence, one sided model fits were undertaken. Figure 5.10 gives examples of vesicles exhibiting strong and weak asymmetry. From the theoretical fit to the data of 15 vesicles, a relative deviation of the slope m by 10% and of σ by 19% between both sides was found. However, since only half of the usual six central points were available for fitting, results are not very robust. In addition, the apparent asymmetry between both sides is rather small. In the following, fits of the complete data set were undertaken and relative deviations of the one sided fit interpreted as typical error.

5.5   Conclusion

The principle of how a standard Fluorescence Correlation Spectroscopy (FCS) set-up can be used for membrane fluctuation measurements was described. This method gives access to fast dynamics of fluctuating objects with high temporal resolution ($\sim$10 μs) and allows us to monitor object motion close to as well as further away from a substrate. A measurement time of 25 s, high fluorophore concentration (1 mol%) and photostability are necessary to suppress contributions arising from diffusion and to provide accurate data. Two independent analyses were presented, the height-height autocorrelation function and the correlation amplitude, which allow for a determination of membrane tension σ and dynamic viscosity η. Moreover, insight into membrane fluctuations over time can be obtained. A first comparison of experimental data to the theory show that the parameters deduced from experiments are within the expected range [25, 141–143].

131

Theoretical considerations showed, that for a z-stack in axial direction, the spatial resolution is limited to ~ 20 nm. In principle, spatial resolution can be improved by a stack measurement in radial direction. In this case the intensity profile decays over $\omega_0 \sim 0.3 \ \mu m$ instead of $z_0 \sim 1.2 \ \mu m$. The corresponding slope for height conversion would then increase by a factor ~ 4. However, whether the stronger asymmetries in the axial shape of the confocal volume (see e.g. images of the PSF in section A) are negligible for this measurement, has yet to be tested.

Chapter 6

Free Membrane Fluctuations: Application of FluCS

In this chapter the concept of FluCS is applied to biomimetic model systems as well as to living cells. Theoretical relations and analytic strategies presented in chapter 5 are tested and evaluated. Potentials and perspectives of FluCS for further application are discussed.

6.1 Vesicle Studies

Vesicles are ideal test objects to establish new measurement techniques in biological research. On the one hand they are simple enough to be sufficiently controllable and can be produced with diverse properties. On the other hand, they already feature several characteristics of living systems and thus allow to test the applicability of a method to this field of research. In the following, vesicle fluctuations close as well as far away from the substrate are investigated. Substrates are homogeneous passive coatings as well as patterned adhesive structures. This way, properties of a free membrane and of a membrane under constrains are examined. To the author's knowledge, for the first time, membrane fluctuations are analyzed with high temporal resolution in real space and static and dynamic properties of vesicles are derived. Moreover, comparative studies on free

and constrained membrane parts of the same vesicle are undertaken to estimate changes fluctuations are subject to.

6.1.1   Experimental Realization

Vesicles were prepared and recorded according to the optimal settings as described in 5.3.3. Prior to measurements standard FCS settings were checked as outlined before (see A and 2.3.3.4). Experiments presented in the following comprise vesicles sedimented to homogeneous substrates as well as vesicles adhering to patterned large grid substrates (see sections 2.2.2.2 and 2.2.2.1 for preparation). Vesicles were recorded at the top free side as well as at the lower side close to the substrate. Total measurement times varied between 25 - 45 s, i.e. 5 - 9 repeats of 5 s duration. Fluorescence and phase contrast images were acquired (as described in section 2.3.3.4) to measure the vesicle radius. All measurements were undertaken at room temperature. From recorded data, ACFs of each repeat, intensity vs. time curves and average intensities were stored for further analysis.

6.1.2   Results and Discussion

First, results of measurements at the vesicle top are presented. Figures 6.1 - 6.4 show characteristic examples of z-stack measurements and analyses. Count rate, correlation amplitude and HHACF were fitted with equations 5.13, 5.12 and 5.9, respectively. In addition, residuals of the latter fit are shown.

While the vesicle of figure 6.1 was obviously very 'soft', the vesicle of figure 6.4 exhibited apparently weaker fluctuations. Vesicles of figures 6.2 - 6.3 exhibited an intermediate state and were classified as obviously 'medium soft'. This tendency was also reflected in recorded data and analyses.

First, results of the fluctuation amplitude, indicated by a subscript CA, are given: Strong fluctuations yielded correlation amplitudes $\gg 0.003$, the noise threshold determined in section 5.3.2.
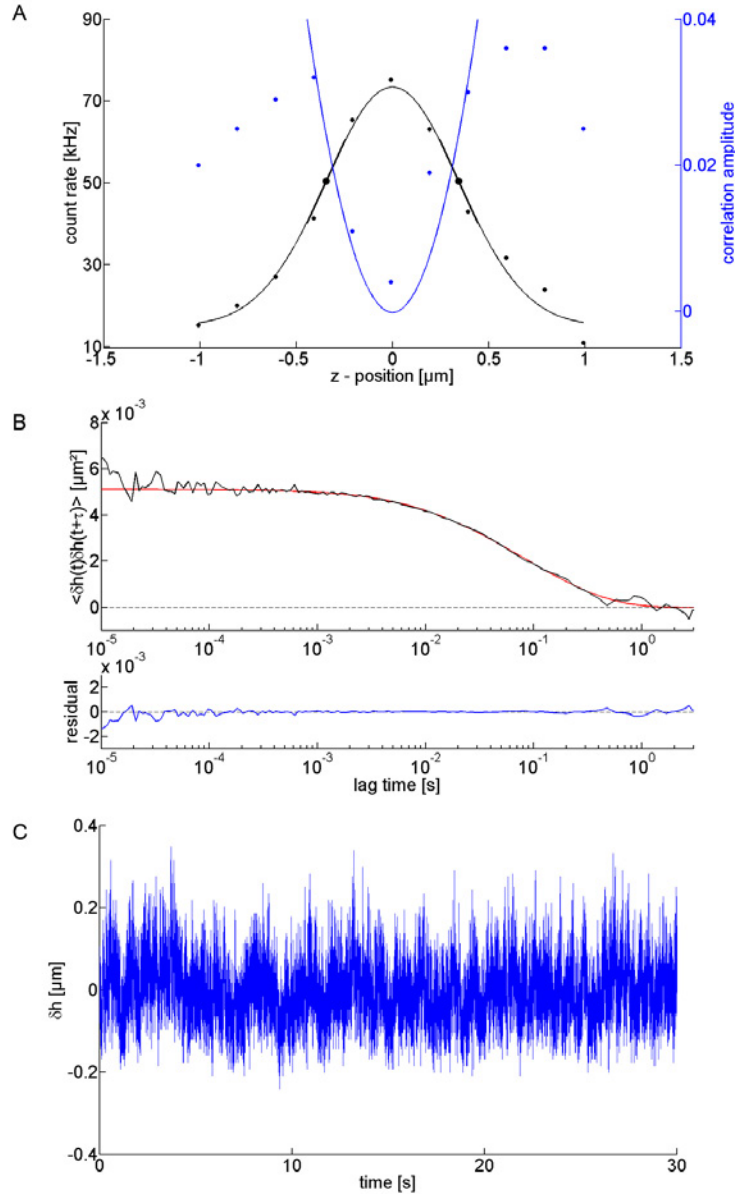
Figure 6.1: Result of strongly fluctuating vesicle, measured at the top. A: Z-stack measurement depicts count rate (black dots), correlation amplitude (blue dots) and corresponding fits (solid lines). Inflection points (large black dots) and slopes (thick black lines) are indicated. A parabolic fit to correlation amplitude data yields the membrane tension, σ_{CA} (eq. 5.12). B: HHACF (black), fit (red) and residuals below (blue). From a fit to the data (eq. 5.9) membrane tension, σ_{HH}, and hydrodynamic damping, η, are obtained. C: The height amplitude exhibits characteristic fluctuations over time (blue). Fit results were: $\sigma_{CA} = 0.36$ $[\mu J/m^2]$, $\sigma_{HH} = 0.41$ $[\mu J/m^2]$ and $\eta = 0.0036$ $[kg/(m \cdot s)]$. For the HHACF fit a trust-region algorithm was used.
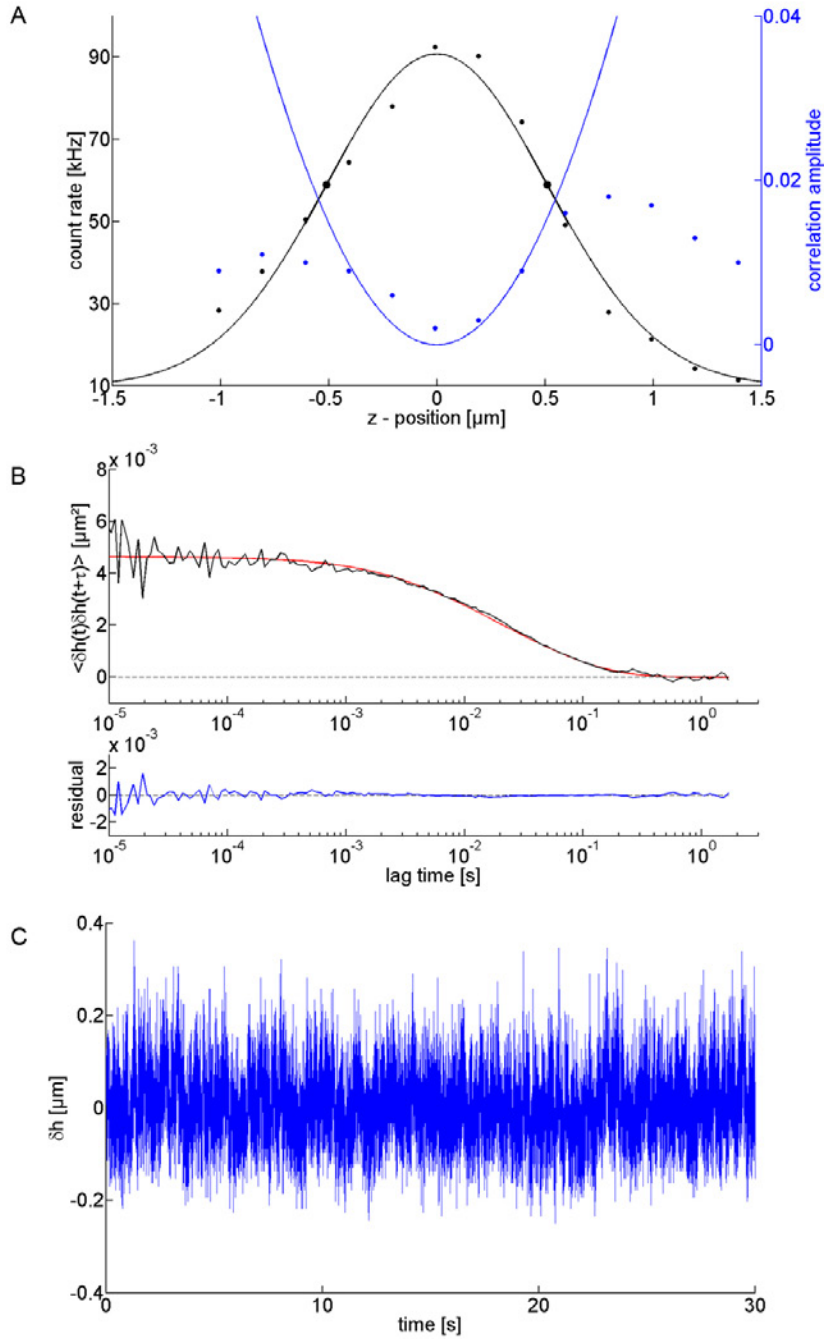
Figure 6.2: Result of medium fluctuating vesicle, measured at the top. See figure 6.1 for data description. Fit results were: $\sigma_{CA} = 0.46\ [\mu J/m^2]$, $\sigma_{HH} = 0.51\ [\mu J/m^2]$ and $\eta = 0.0010\ [kg/(m \cdot s)]$. For the HHACF fit a weighted Levenberg-Marquardt algorithm with 10 repeats was used.
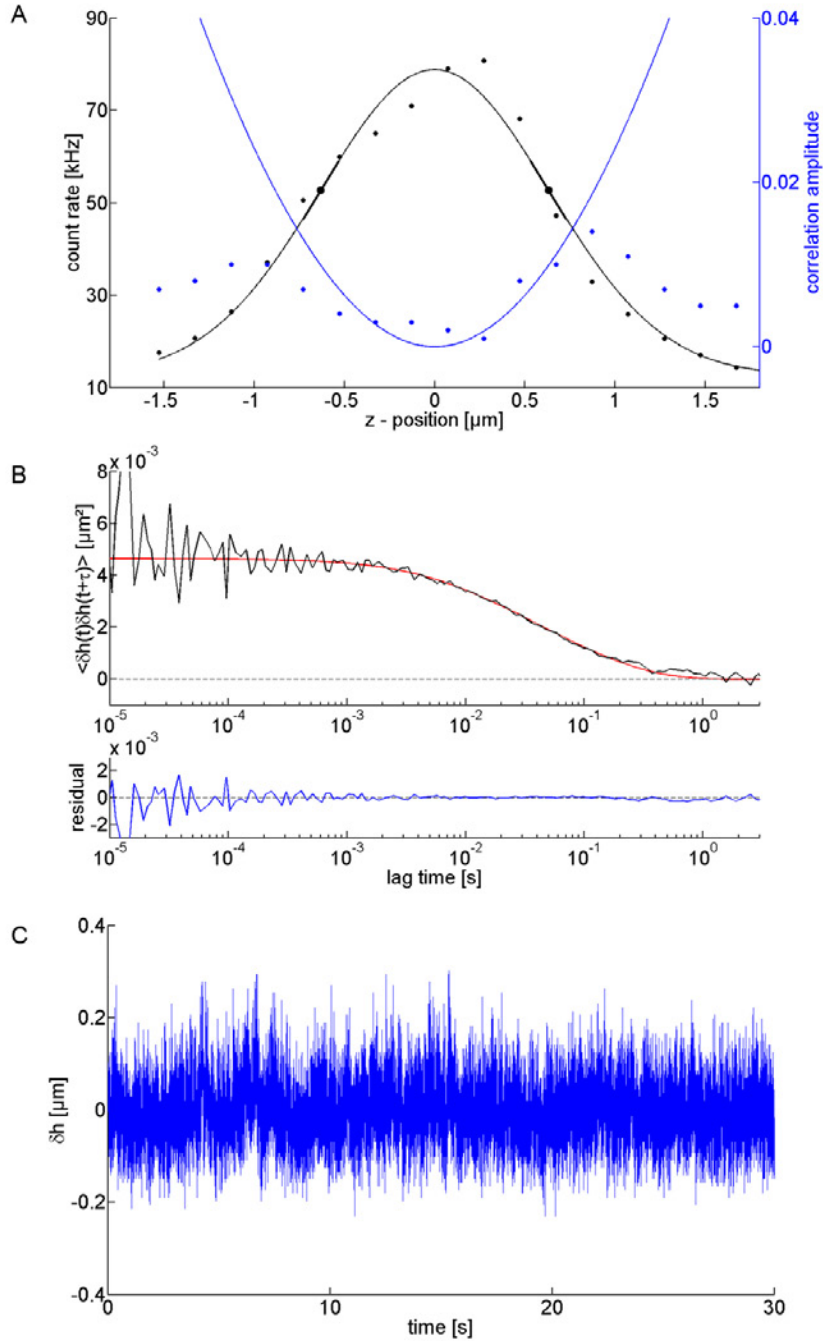
Figure 6.3: Result of medium fluctuating vesicle, measured at the top. See figure 6.1 for data description. Fit results were: $\sigma_{CA} = 0.52 \ [\mu J/m^2]$, $\sigma_{HH} = 0.53 \ [\mu J/m^2]$ and $\eta = 0.0018 \ [kg/(m \cdot s)]$. For the HHACF fit a trust-region algorithm was used.
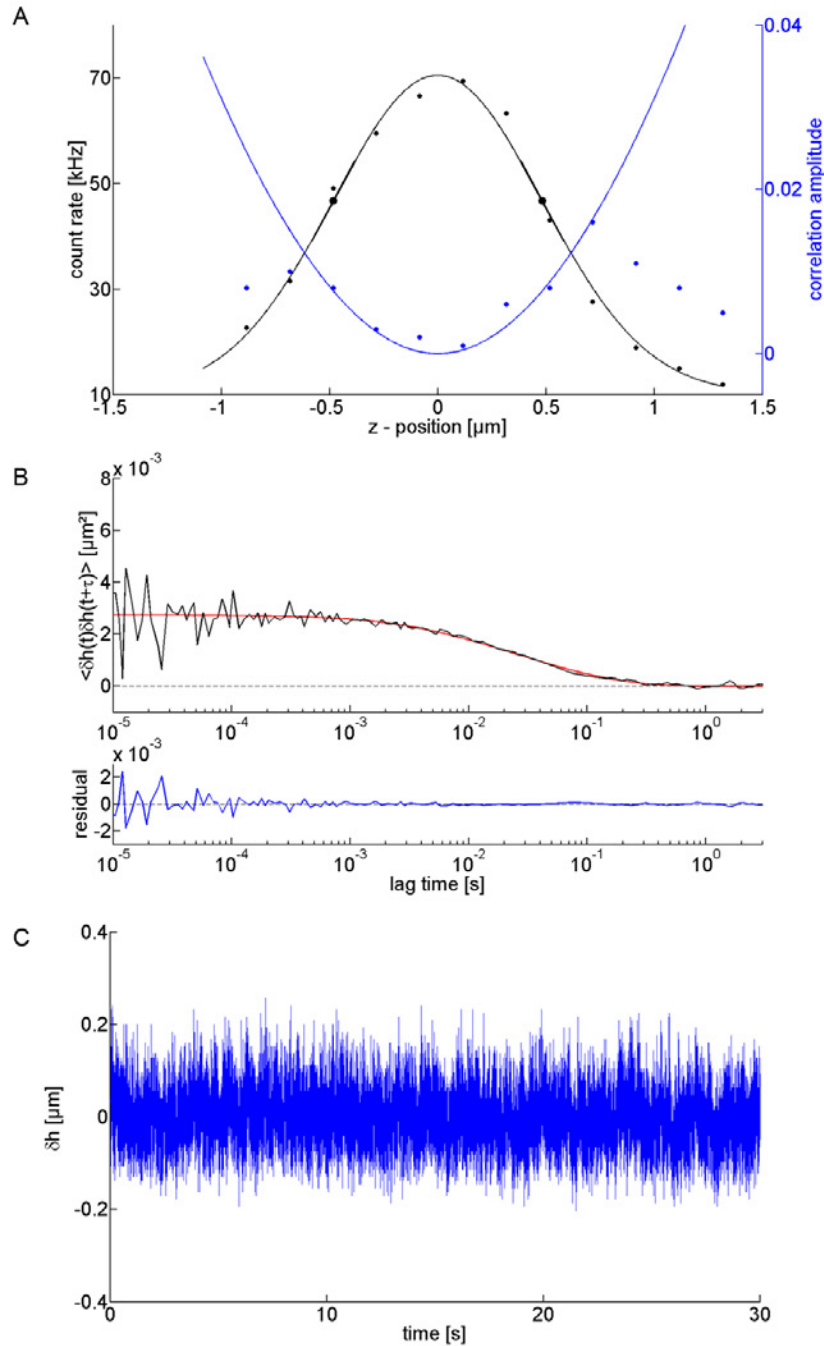
Figure 6.4: Result of weak fluctuating vesicle, measured at the top. See figure 6.1 for data description. Fit results were: $\sigma_{CA} = 1.09$ $[\mu J / m^2]$, $\sigma_{HH} = 0.89$ $[\mu J / m^2]$ and $\eta = 0.0023$ $[kg/(m \cdot s)]$. For a HHACF fit the trust-region algorithm was used.

Moreover, curvatures of the parabolic fit were high, resulting in small tension values of typically $\sigma_{CA} = 0.2 \ \mu J/m^2$. On the other hand, vesicles fluctuating weaker exhibited smaller correlation amplitudes and vertically compressed parabolas. Here, tensions were higher, typically $\sigma_{CA} = 1.0 \ \mu J/m^2$. Accordingly, 'medium soft' vesicles yielded average values between these limiting cases (See figure captions for exact values of depicted data).

Similar results were found from the examination of HHACFs, shown in the middle of figures 6.1 - 6.4. To distinguish between analyses, values of HHACF have a subscript HH. Here, a fit to the data resulted in tensions of typically $\sigma_{hh} = 0.4 - 0.9 \ \mu J/m^2$ for strong and weaker fluctuating vesicles, respectively. Tension values from HHACFs were to 35% in accordance with the corresponding result from correlation amplitude analysis. Considering both analyses minimal and maximal tensions were 0.01 $\mu J/m^2$ and 1.1 $\mu J/m^2$ respectively, while the average value amounted to $0.37 \pm_p 0.28 \ \mu J/m^2$. This value is a magnitude lower as determined in section 3.3.1.4, for structured adhered membranes prepared with smaller initial osmotic gradient. However, as tension increases during the process of adhesion [104], values found in section 3.3.1.4 only serve as an upper limit, which should and is not exceeded by the present results. Moreover, other groups investigated non - adhered vesicles with spectral-analysis methods and found tensions of the same magnitude [25, 141, 142]. Due to the comparable systems investigated there - often SOPC vesicles were suspended in hyperosmotic conditions and analyzed after sedimentation to the substrate - good verification of values presented here was found.

In addition, HHACF fits yielded a measure of the hydrodynamic damping in the system, the viscosity η. No significant differences of the function decay between strongly and weakly fluctuating vesicles was detected. On average, η amounted to $0.0013 \pm_m 0.0002 \ kg/(m \cdot s)$, a value slightly higher than expected for hydrodynamic damping in water ($0.0010 \ kg/(m \cdot s)$ at $20°C$). Even though at this point the origin of this observation is yet obscure, a possible explanation would be an effect of the 7% (w/w) sucrose solution within the vesicle. Only recently dynamic viscosities of sucrose

solutions were determined with FCS [144]. Here, 7% sucrose solution resulted in $\eta = 0.0011\ kg/(m \cdot s)$. As a consequence, this effect has to be accounted, but it may not be sufficient to explain the shift in total. Another possible effect may arise for bilayer internal friction. As theoretically predicted by Evans and Sackmann [145] and experimentally verified by Merkel et al. [27] the intermonolayer slippage provides an additional mode of curvature motion which dissipates through intermonolayer friction. In particular, this effect was evidenced to dominate at higher wavevectors [19, 136]. A first estimate on the relevant wavevector regimes showed, that in fact $q_{max} = \frac{\pi}{\omega_0}$ just reaches into the wavevector regime where intermonolayer friction plays a role.

Examples of membrane fluctuations over time are presented at the bottom of figures 6.1 - 6.4. For determination of average fluctuation amplitudes $\langle |\delta h(t)| \rangle$ and in order to rule out effects of noise, absolute amplitude values were binned over increasing time intervals and results averaged (data not shown). Mean fluctuation amplitudes derived this way varied between $0.052 - 0.132\ \mu$m. As a consequence, thermal excitation of free vesicles appear to result in much more pronounced fluctuations as compared to fluctuation amplitudes found for structured adhered membranes in similar osmotic conditions (see section 4.2.3). Precisely, with approximately $\sim 0.1\ \mu m$, free membrane fluctuations are enlarged by a factor $\times$ 5. This seems valid, as one expects fluctuations to decline once the vesicle adheres and loses conformation entropy [104]. Indeed, measurements on free vesicles reported amplitudes of same magnitude [142, 143].

In total 41 vesicles were analyzed, with average results for tension and hydrodynamic damping given in table 6.1. Accordingly, even though these parameters and amplitudes are in good agreement with literature values and expected physical limits, direct verification of vesicle fluctuation amplitudes via e.g. video microscopy would be beneficial.
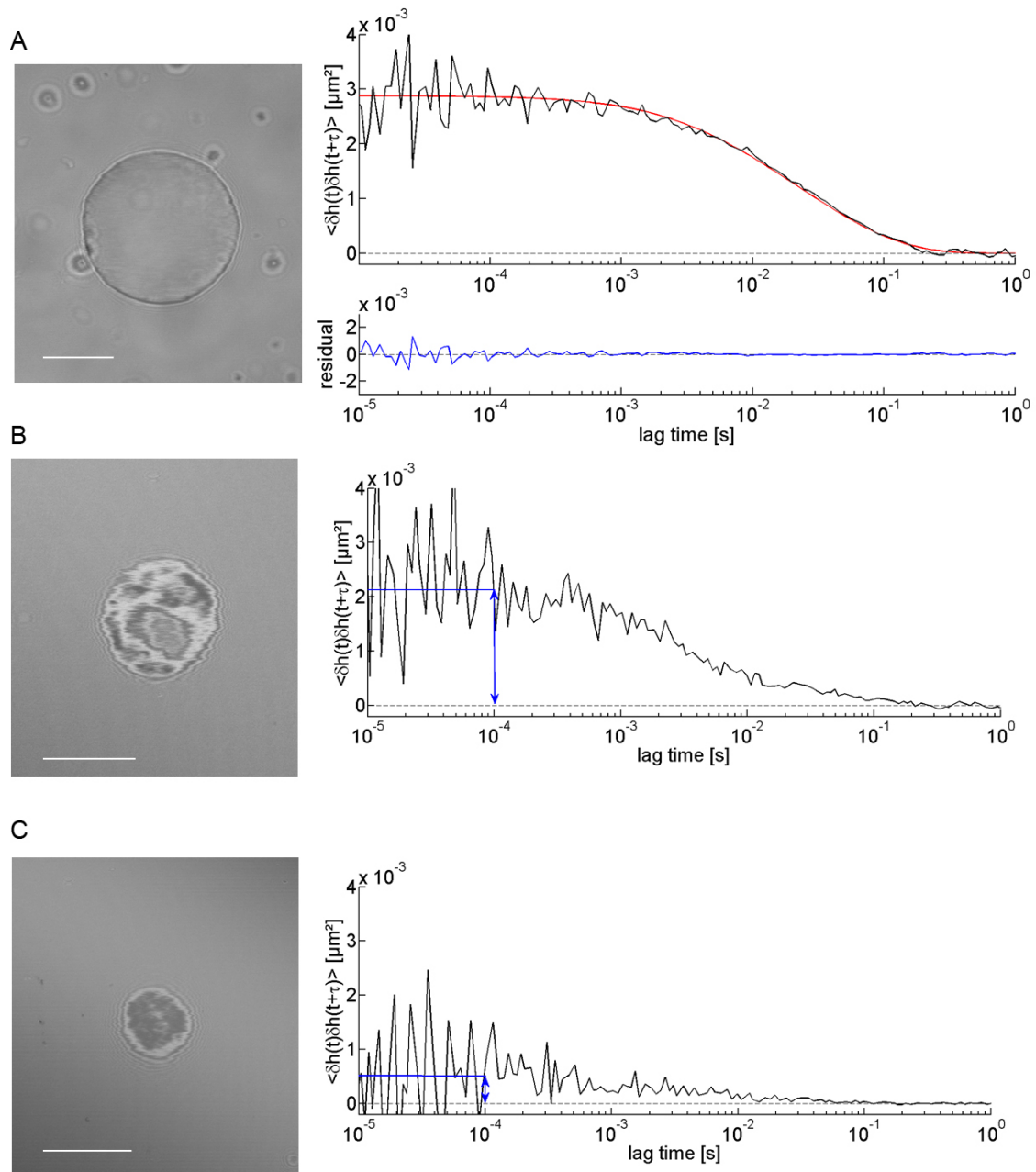
Figure 6.5: Result of vesicle fluctuations measured at the bottom (B and C right). For comparison, vesicle data of the top of vesicle C was added (A right). Phase contrast (A left) and reflection images (B and C left) show the vesicle i.e. its fluctuation state on the substrate. Scale bar: 10 μm. HHACF graphs show a decline in correlation function intercept with membrane - substrate proximity. Moreover, the decay of correlation functions from bottom data appears to be characteristically different as to data from the top.

In addition to measurements at the vesicle top, membrane in vicinity of the substrate was studied. Here, recording of real fluctuations was challenging as ACF values only seldomly exceeded the noise threshold. This was mostly due to small fluctuation amplitudes. However, presumably from the high amount of fluorophore in the membrane $\sim 30\%$ of vesicles adhered unspecifically. As a consequence, only four (out of 10) vesicles yielded reliable data. As for the free vesicle membrane, correlation amplitude and HHACF were analyzed. However, fitting of HHACF curves let to poor χ^2 values, and so analysis was restricted to the intercept of the correlation function. Its value was determined from averaging HHACF data in the time interval $10^{-5} - 10^{-4}$ s and subsequently membrane tension was calculated via equation 5.10.

Figure 6.5 gives two examples of vesicle data near the substrate: One exhibiting strong intensity variations in the image, which is regarded as being freely hovering above the substrate (figure middle). The second featuring a darker contact area, which is thus believed to be closer to the substrate (figure bottom). For the latter example also the corresponding measurement at the vesicle top is shown.

From the observation of HHACFs clearly a drop of fluctuation amplitude with substrate proximity is found. In addition, the decay of the correlation function appears to be characteristically different: After the initial decline between $10^{-3} - 10^{-2}$ s, a long flattened tail continues and reaches the baseline at ~ 1 s. However, due to the poor statistics care has to be taken to interpret these graphs a correct representations of HHACFs for free vesicle fluctuations near the substrate. Yet, eight measured curves[1] confirmed this qualitative trend and its average is depicted in figure 6.8. At a later point this result is discussed further.

Applying the same evaluation procedure as for the upper vesicle side, results of vesicle bottom data read: $\sigma_{CA} = 2.83 \pm_p 1.75\ \mu J/m^2$ and $\sigma_{HH} = 6.11 \pm_p 4.22\ \mu J/m^2$. Membrane fluctuations close to the substrate exhibited amplitudes of only $\delta h = 0.036 \pm_p 0.008\ \mu m$. Thus, in comparison to

---

[1]Since HHACF curves were obtained from both inflection points of the Gaussian function, eight curves and σ_{HH} values were derived for 4 vesicles.

fluctuations of a free membrane, membrane fluctuations in the vicinity of a wall are significantly diminished and on average a factor $\times 3$ smaller. At the same time, tensions are apparently a factor $\times 15$ larger than for a free membrane considering analyses of correlation amplitude and HHACF.

Since in general, a vesicle possesses only one universal membrane ten-
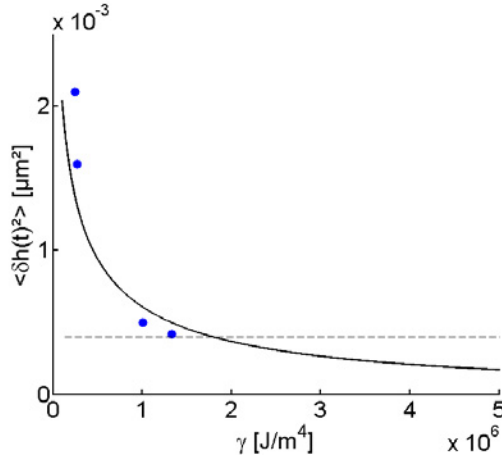
Figure 6.6: Theoretical accessible stiffness of the interaction potential γ. HHACF intercept values from vesicle bottom data and tension values, σ_{HH}, from the vesicle top data allow to calculate γ (blue dots). The continuous theoretical dependence for an average tension is indicated (black line). The dashed line marks the resolution limit of FluCS.

sion, this magnitude difference indicates that analysis via equations for the free membrane at the vesicle top may not be applicable to the situation at the vesicle bottom. It seems a factor is missing in the theoretical description for a membrane near a substrate, which adds to the finding of an altered HHACF shape. An obvious candidate for this missing factor is the interaction potential V, since any membrane-substrate interaction was neglected so far. As proposed in [146] and in a first attempt to assess the value of V, a harmonic potential was assumed and the second derivative of V, γ, included in the energy term of equation 5.10. This yielded:

$$\langle \delta h(t)^2 \rangle = \frac{k_B T}{2\pi} \int dq \, \frac{1}{\kappa q^3 + \sigma q + \gamma/q} e^{-\frac{q^2 \omega^2}{4}} \quad . \tag{6.1}$$

Subsequently, γ was calculated from equation 6.1 presuming a universal membrane tension. Therefore, $\langle \delta h(t)^2 \rangle$ from vesicle bottom data was used, κ was fixed at 20 $k_B T$ and σ_{HH} from the vesicle top was identified with the universal tension. Figure 6.6 shows the result of derived γ values and the theoretical trend for an average σ_{HH}. Minimal and maximal derived potential strengths were $0.2 \cdot 10^6$ and $1.3 \cdot 10^6$ J/m^4, respectively. As for higher γ the height correlation amplitude reaches the resolution limit, this graph indicates the range of potential strengths accessible with FluCS. In fact, since its values are usually in the range of $\sim 10^7$ J/m^4, only non- or partially adherent vesicles can be studied.

Finally, five vesicles adhering to patterned receptors were investigated (see chapter 3, for details of adhesion to large grid structure). Figure 6.7 gives an example of data obtained from the top and bottom of one vesicle. It has to be noted, that the initial osmotic gradient in this experiment is the usually applied difference in FluCS, which is, however, much higher as for the experiments in section 3. This was necessary, as otherwise, fluctuation amplitudes were again to small to be detectable.

Similar to previous analyses, correlation amplitudes were fitted for top and bottom data, while HHACF data was quantified in its temporal decay only for the vesicle top. From vesicle bottom data, σ_{HH} values were calculated from the function intercept for the same reasons and as described before.

Similar to measurements on free vesicles, a strong difference between fluctuation amplitudes between top and bottom was found. Here, amplitudes from vesicle top data were with 0.081 μm, only slightly smaller than previous results, while vesicle bottom data yielded on average $0.028 \pm_p 0.009$ μm amplitudes. The latter is slightly larger than findings of fluctuations at the same osmotic difference as described in section 4.2.3. This discrepancy may be attributed to the resolution limit of FluCS since lower fluctuation amplitudes are not observable. Thus, amplitude statistics need to be higher than 0.02 μm.
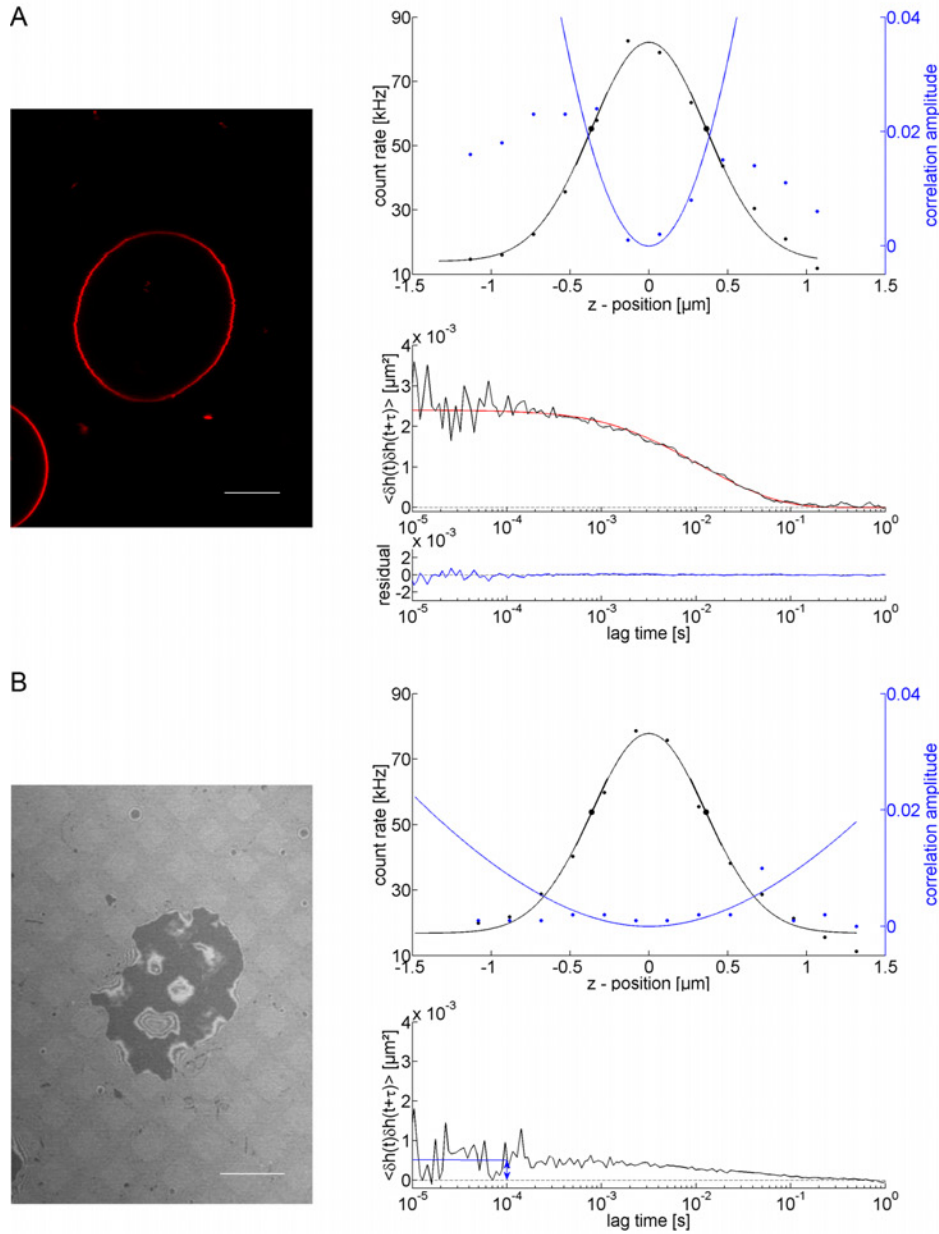
Figure 6.7: Result of vesicle fluctuations on patterned substrates. For comparison, vesicle data of top (A right) and bottom (B right) of the same vesicle are shown. Fluorescence (A left) and reflection images (B left) show the vesicle. Scale bars: 10 μm. See figure 6.1 for data description. Vertical compression of the parabola and decline of HHACF intercept suggest fluctuation damping and apparent tension increase. Fit values were: $\sigma_{CA,top} = 0.60$ [$\mu J/m^2$], $\sigma_{HH,top} = 0.58$ [$\mu J/m^2$], $\eta = 0.0013$ [$kg/(m \cdot s)$], $\sigma_{CA,bottom} = 5.48$ [$\mu J/m^2$] and $\sigma_{HH,bottom} = 4.90$ [$\mu J/m^2$].

145

Again, apparent vesicle tension between lower and upper vesicle site differed by a factor 14, emphasizing the need for an adjustment of theory. Thus, care should be taken to not misinterpret this higher tension value, since from the neglected membrane - substrate interaction it is in fact an apparent tension. Furthermore, data of the vesicle top resulted in tension and buffer viscosity of $\sigma_{CA} = 0.40 \pm_p 0.10 \; \mu J/m^2$, $\sigma_{HH} = 0.58 \pm_p 0.27 \; \mu J/m^2$ and $0.0013 \pm_m 0.0003 \; kg/(m \cdot s)$, respectively. As a consequence, while hydrodynamic damping on average did not change, vesicle tension increased by $0.13 \; \mu J/m^2$ for structured adhered vesicles in comparison to free vesicles. This tendency is expected. Nevertheless, for adherent vesicles tensions of $10^{-6} - 10^{-5} \; \mu J/m^2$ were reported in other studies [104,115] and in section 3 $10 \times$ larger tension values were determined for the same system, at smaller initial osmotic conditions.
Accordingly, changing from free to structured adhered vesicles yields the correct trends in parameters. Absolute values and the amount of increase are rather small as only osmotically deflated vesicles could be monitored. Again, due to the lacking statistics, further experiments and control measurements are necessary.

Moreover, membrane relaxation resulted again in a different characteristic decay of the HHACF. As can be seen from figures 6.7 and 6.8, the plateau region is followed by a stretched decay towards the baseline lacking a smooth leveling off. In order to distinguish the different observations for free and constrained membrane fluctuations near a substrate, averaged normalized HHACFs of all measured data were calculated for each case. Figure 6.8 depicts the result. Clearly significant differences in the shape are observed. Obviously structured adhere membrane systems encounter an increased hydrodynamic drag in comparison to free vesicle membranes near the substrate. The origin of this different behaviour is yet unclear. Only some studies examined the membrane hydrodynamics in substrate vicinity so far: Kaizuka and Groves [147] found increased damping for membrane stacks confined by intermembrane junctions. Moreover, Prost and Bruinsma proposed a change in relaxation behaviour once membrane permeability is taken into account [148] and Rodriguez-Garcia et al. [149]
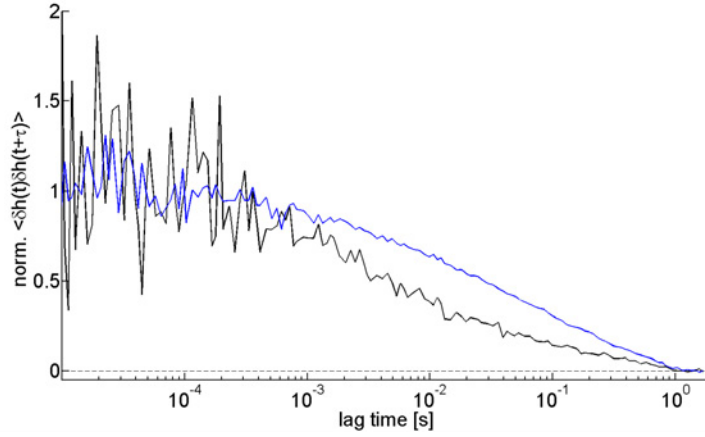
Figure 6.8: HHACFs of structured adhered (blue) and free vesicle bottom data (black). Curves are averages over 8 (black) or 9 (blue) measurements, which were normalized to an intercept of 1.

found a stretched - exponential decay for rigid polymer vesicles studied with ultrafast videomicroscopy. These and other results may play a role in obtaining further understanding of relaxation dynamics under constrains. Table 6.1 gives an overview of the obtained results for all systems.

position	σ_{CA} $[\mu J/m^2]$	σ_{HH} $[\mu J/m^2]$	$\eta \times 10^{-3}$ $[kg/(m \cdot s)]$	# vesicles
free top	$0.36\pm_p0.25$	$0.37\pm_p0.31$	$1.3\pm_m0.2$	41
free bottom	$2.83\pm_p1.75$	$6.11\pm_p4.22$	—	4
struc. adh. top	$0.40\pm_p0.25$	$0.58\pm_p0.61$	$1.3\pm_m0.3$	5
struc. adh. bottom	$4.37\pm_p3.27$	$2.44\pm_p1.99$	—	5

Table 6.1: Overview of results on fluctuation measurements. Errors marked by $\pm_p$ and $\pm_m$ refer to the standard deviation of the population and the mean, respectively.

6.2 Cell Studies

The applicability of FluCS to living organisms, i.e. the potential to measure membrane fluctuations of cells, was tested with two different cell types:

HEK293 cells and human macrophages.

6.2.1 Cell Culture

The HEK293 cell line was grown in an incubator at 37 °C, 5% CO_2 and saturated humid atmosphere, in Dulbeccos's modified eagle medium ($DMEM$, Sigma). The medium contained a pH indicator and was supplemented with 10% (v/v) foetal bovine serum (FBS, Sigma) and 1:100 penicillin/streptomycin (10000 U/ml, Sigma). This composition is henceforth called $DMEM^+$. Culture medium was changed every third day and confluency of cells did not exceed 80%.

Primary human macrophages (kindly provided by T. Urbansky, ICS-7, FZJ) were cultured under similar conditions in Roswell park memorial institute medium ($RPMI$1640, Gibco, Karlsruhe, Germany). Here, same supplements as for $DMEM$ were added, which is henceforth refered to as $RPMI^+$.

Prior to measurements cells were trypsinized, i.e. cells adhering to the culture flask were detached by cleaving adhesion proteins. For detachment, $DMEM^+$ medium was removed, and adherent cells washed with PBS to withdraw surplus organic compounds and remaining medium. Subsequently, cells were incubated in 3 ml trypsin-EDTA solution (consisting of 0.5% trypsin, 0.2% EDTA, Sigma) for 3 min at 37 °C. This yielded cells in suspension, which were transferred to a sterile 15 ml test tube (VWR, Darmstadt, Germany). After centrifugation (200 g, 3 min at room temperature, Eppendorf Centrifuge 5804R, Hamburg, Germany) cells were collected and resuspended in $DMEM^+$.

Cells were then transferred at desired density into specially fabricated cell culture dishes (3 cm diameter, Greiner, Solingen, Germany). Each cell culture dish featured a 1.5 cm diameter hole at the centre of its floor for microscopic observations. Prior to cell transfer, a thickness corrected glass coverslip (see section 2.1.5) was glued over this hole with silicone rubber (see section 2.1.5 for preparation details), which was cured at 60 °C for 2 h. Dishes were pre-coated with 10 $\mu g/ml$ human fibronectin (BD Bio-

sciences, Bedford, USA) in PBS for 30 min, at 37 °C. Then, directly after PBS removal, 10000 cells per dish were seeded in 1 ml $DMEM^+$. All cell specific steps were done under sterile conditions. Cell culture was mostly executed by C. Kleusch and N. Hersch, ICS-7, FZJ.

6.2.2 Fluorescent Labeling

Fluorescent labeling of a cell plasma membrane was faciliated by a method developed by Csiszár et al. [150]. Here, fusogenic liposomes, consisting of ternary lipid mixtures, enabled highly efficient incorporation of fluorescent molecules into mammalian cell membranes[2]. Liposomes were produced of 1,2-dioleoyl-sn-glycero-3-phosphoethanolamine (DOPE, Avanti) and 1,2-dioleoyl-3-trime- thylammonium-propane, chloride salt (DOTAP, Avanti) in a 1:1 weight ratio at a concentration of 1 mg/ml in chloroform. Furthermore, a fluorescently labeled lipid (1mg/ml in choloroform) was added to this lipid mixture in a weight ratio of 0.2. It has to be noted, that this concentration yielded high signal such that any correlation amplitude above the noise threshold was interpreted as real membrane fluctuation. Also, fluorescently labeled lipids applied in weight ratios of 0.5 had some toxic effect on HEK cells. Texas Red 1,2-dihexadecanoyl-sn-glycero-3-phosphoethanolamine, triethylammonium salt (Texas Red-DHPE, Invitrogen) was used for macrophages and N-(4,4-difluoro-5,7-dimethyl-4-bora-3a,4a-diaza-s-indacene-3-dodecanoyl)sphin- gosyl phosphocholine (BODIPY FL-SM, Invitrogen) was used for HEK cells. Putting the lipid chloroform solution in vacuum for 20 min all chloroform was removed. Lipids were resuspended in 20 mM 2-(4-(2-hydroxyethyl)-1-piperazinyl)-ethane-sulfonic acid (pH 7.5, HEPES, VWR) at 2.2 mg/ml final concentration. To produce multilamellar liposomes the suspension was stirred 1-2 min on a vortex-mixer. Further homogenization and size reduction was realized by 10 min ultrasound bath treatment and storage at 4 °C until usage.

---

[2]Details on the fusion mechanism are found in [150]

6.2.3 Experimental Realization

After seeding, cells were incubated for 15 min at 37 °C. During this time cells started to adhere to the substrate. Still, this period was short enough to yield only weak binding and to prevent formation of a distinct actin cortex. Therefore, the cell plasma membrane was conjectured to be in a state, where it was soft and exhibited high fluctuations.

For vesicle fusion, 5 μl liposomes were suspended in 500 μl preheated medium. Cells were incubated in this solution for 10 min at fully unchanged cell growth conditions. After incubation with liposomes the cell medium was carefully replaced by fresh preheated medium without serum ($DMEM$ without pH indicator (Gibco) but same supplements as for $DMEM^+$ [**?**]). This medium was used for experiments, as it features low background signal. This is an important prerequisite for FluCS as demonstrated in section 5.3.3. As this step is crucial for background signal reduction 1 ml medium was exchanged twice.

Measurement settings were as described in sections 5.3 and 5.3.3. However, as cells are out-of equilibrium objects, which generate movement actively, long measurement times were not feasible. Hence recording times were reduced to 10-15 s (2-3 repeats of 5 s each). The excitation laser was attenuated to the extent that maximum counts lay within 70 - 100 kHz (settings for 543 nm were: AOTF 1% and LI 3-7% and for 488 nm: AOTF 1% and LI 1-5%; see section 2.3.3.4 for abbreviations and an estimate on corresponding laser powers). For measurements a microscope with incubator at 37 °C and CO_2 supply was used.

6.2.4 Results and Discussion

Figure 6.9 shows two exemplary results of measurements with HEK cells and macrophages. Plasma membrane labeling via liposome fusion proved to be a reliable method to achieve intense staining. Shortly after fusion several fluorophore cluster were detected on the cell surface. In part, homogeneity of fluorophore distribution increased with time.
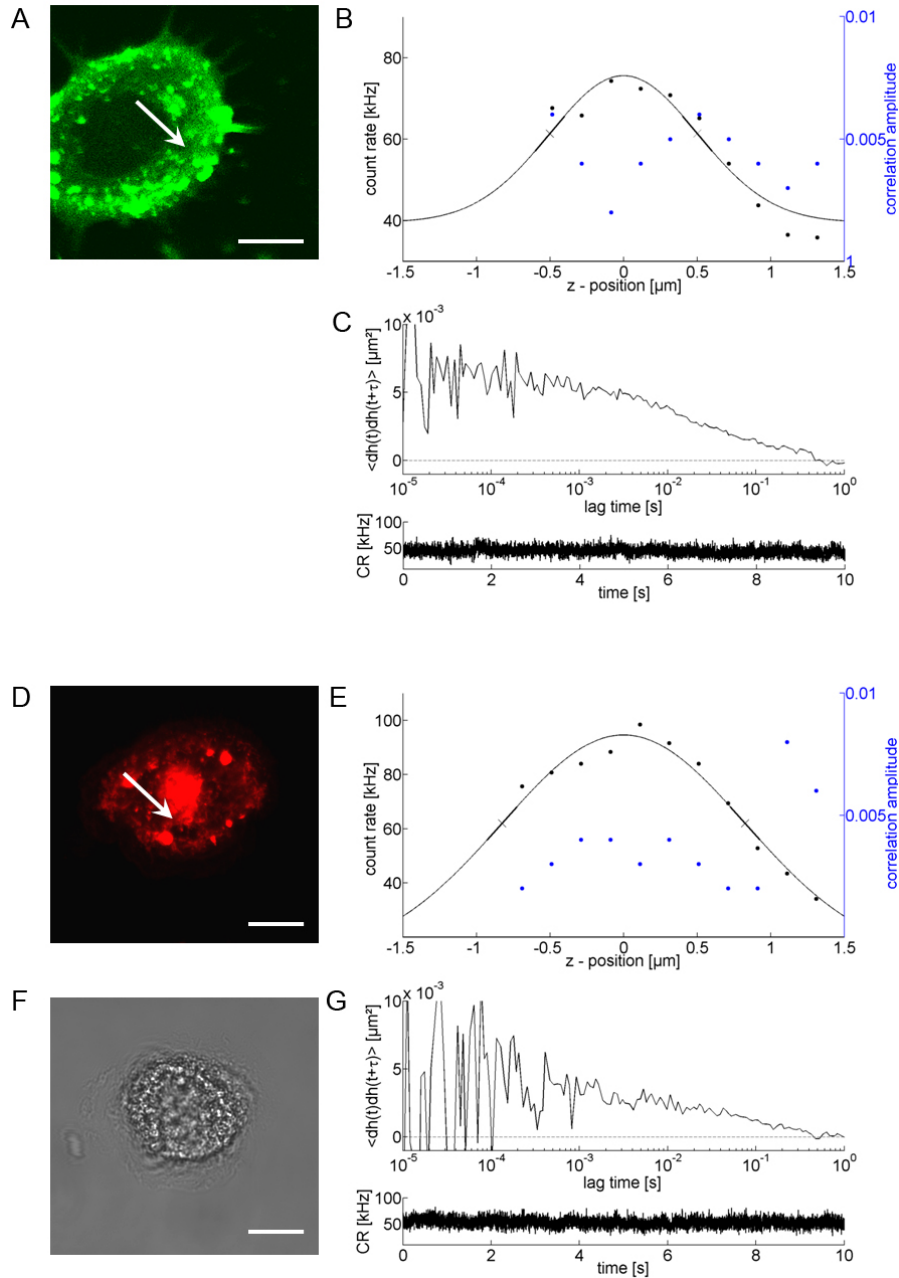
Figure 6.9: Results of FluCS measurements with cells. A: HEK293 cell with BODIPY FL-SM stained plasma membrane D,F: Fluorescence and phase contrast image of human macrophage. The white arrows indicate the points of measurement. Scale bar 10 μm. B,E: Results of z-stack measurements. The correlation amplitude clearly exceeds the noise threshold of 0.003. C,G: hhACFs results. While the relaxation differed from cell to cell, fluctuation amplitudes were on the order of $\sim 0.1 \mu m$.

151

But since experiments had to be recorded right after labeling, when cells were not fully adhered, the origin of clusters observed at this point was attributed to both: Misfunctional fusion as well as the lack of time for the lipids to distribute. Hence, care was taken to select regions of apparent homogeneous intensity, and z-stacks were recorded immediately. In figure 6.9 the selected points of measurement are marked.

Due to cellular movement, a full z-stack was hardly ever recorded. A
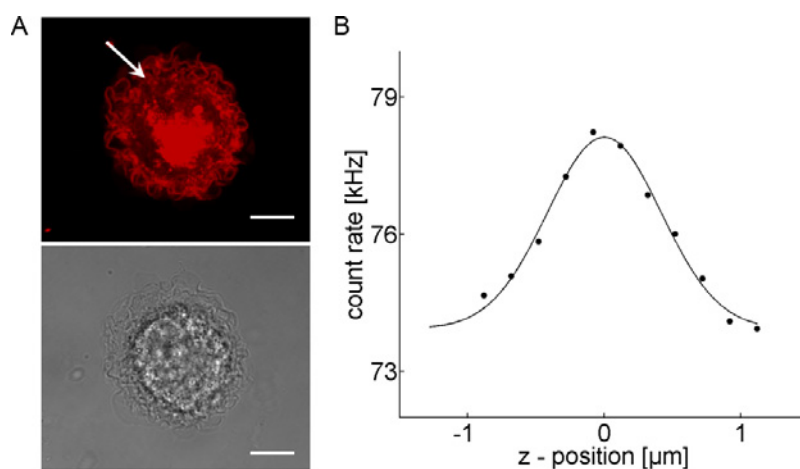
Figure 6.10: A: Fluorescence and phase contrast image of human macrophage. The cell membrane is stained with Texas Red-DHPE. The white arrow indicates the point of measurement. Scale bar 10 μm. Z-scan through the macrophage membrane. A Gaussian distribution is clearly detected.

fit of a Gaussian to the intensity distribution and determination of inflection points was feasible in most cases. Intensity distributions exhibited high variation in shape width, which was most likely caused by the long measurement time ($\sim$ 3 min for one z-stack) combined with cellular movement. In spite of this distribution, in most cases correlation amplitudes were above the threshold of noise (0.003) and interpreted as real membrane fluctuations. Conversion of intensity ACFs into hhACFs at the inflection point yielded relaxation behaviour of distinct different shapes. This is not surprising, considering the fact that a living object was monitored. Average fluctuation amplitudes of HEK cells amounted

to $0.12 \pm 0.06 \, \mu m$, while macrophages exhibited amplitudes of $0.06 \pm_p 0.05$ μm. More statistics is needed for conclusive results on the decay of fluctuations. The tests presented here have identified settings that are suitable for cell observations.

To avoid the time consuming z-stack and increase reliability of data, a slightly different procedure may be adapted: A fast scan over the position of the membrane can be used as a substitute for the z-stack, where ACFs are recorded at each stack position. From the Gaussian shape one can immediately infer the inflection points and record data only there. In addition, macrophages exhibited an apparent more homogeneous labeling than HEK cells, which may be an effect of the fluorophore used. Figure 6.10 gives an example of first improvements.

6.3   Conclusion

In this chapter, results of FluCS applied to biomimetic model systems were presented. Measurements at the top of free vesicles allowed for a determination of fluctuation amplitudes δh, on the order of $\sim 0.1 \, \mu m$, and membrane tensions of several $10^{-7} \, \mu J / m^2$. These are in accordance with results on similar systems reported by other groups. From membrane dynamics, a value of the system viscosity was derived, which amounted to $1.3 \cdot 10^{-3}$ $kg / (m \cdot s)$. This was 30% larger than expected from theory.

In addition, measurements on the upper site of free and structured adhered vesicles resulted in slightly higher tension for adhered vesicles. This yielded the correct trend, even though absolute values were almost a magnitude smaller than often reported in literature.

Experiments near substrates, showed a significant decrease in fluctuation amplitudes by a factor 3. This give values which are consistent with literature. Vesicle tension measured close to the substrate was greater than that measured elsewhere by a factor ~ 15. As in general, tension is a universal

vesicle property, this discrepancy indicated a missing contribution from e.g. the membrane-substrate interaction. In a first attempt accounting for this, potential curvatures of $10^6 J/m^4$ were found.

For vesicles adhered to structured as well as to homogeneous substrates, the observed hydrodynamic damping was different at the top and bottom of the vesicle. Height-height autocorrelation functions (HHACFs) of free membrane fluctuations near the substrate featured a discontinuous decay with an initial stronger decline followed by a slower decaying tail. The same analysis on structured adhered membranes led to a relaxation behaviour similar to a stretched exponential. These significant differences demonstrate a qualitatively different nature of membrane hydrodynamics in the vicinity of a substrate. A modified theory accounting for the membrane - substrate interaction as well as effects of water confinement (in the case of structured adhesion), is necessary for a more accurate analysis.

Chapter 7

General Conclusion

In this work fluctuations of model cell membranes, free or adhering to patterned receptors, were quantified by complementary light microscopic techniques.

Dual-Wavelength Reflection Interference Contrast Microscopy, which measures membrane-substrate distances with an accuracy of few nanometer and temporal resolution of 50 *ms*, was used to map instantaneous membrane configuration close to the substrate. Fluctuation Correlation Spectroscopy, a newly developed method that exploits the experimental setup of Fluorescence Correlation Spectroscopy, measures membrane fluctuations with 20 *nm* axial resolution and 10 *μs* temporal resolution. This gave access to faster dynamics and enabled membrane fluctuation measurements near as well as far away from the substrate.

From application of these methods to bio-mimetic model systems the following understanding of confined and free membrane fluctuations was achieved: Vesicles adhering to substrates that present receptors in the form of grid or line patterns exhibited regions of bound and fluctuating membrane, according to the underlying pattern. Within regions of fluctuating membrane, distinct membrane shapes developed, where the membrane rose from the from the edge bound at 19 *nm* toward the centre and reached

a plateau at a height of $\langle h \rangle = 79\ nm$. Variation of receptor patterned evidenced that this characteristic shape was independent of substrate geometry. This observation and further results outlined below supported the hypothesis that the equilibrium height within fluctuation regions is determined by the membrane-substrate interaction potential which in turn is influenced by membrane tension.

In absence of specific interaction (and in presence of short repulsive polymers), there is no deep minimum close to the substrate. Instead, a superposition of van der Waals force, gravity and Helfrich repulsion give rise to a relatively shallow minimum at around 80 nm from the substrate. A free membrane therefore remains at this height and fluctuates around it. Partially constrained membranes, as it is the case here, attain the typical shape described, in order to minimize the energy by placing the maximum possible area in the interaction potential minimum, at the same time adapting a shape that minimizes energy loss due to curvature.

Further support was provided by fluctuation analysis. At the centre of fluctuation regions amplitudes amounted to $\sqrt{\langle \delta h^2 \rangle} = 12$ nm. This value is characteristic of fluctuations, described in the bending rigidity dominated regime. As for equilibrium shape analysis, variation of pattern geometry at equal receptor concentration had no influence on the amplitude. Only membrane fluctuation spectra revealed differences with respect to pattern sizes. Contribution of the size dependent first mode was always present, while within square fluctuating regions an additional higher mode of about 4 μm wavelength developed and on line structures a higher mode of about 6 μm wavelength developed preferentially.

Theoretical analysis (collaboration with Daniel Schmidt, Universität Stuttgart/Prof. Udo Seifert, Universität Stuttgart/Prof. Ana Smith, Universität Erlangen-Nürnberg) of the shape and fluctuations confirms the above hypothesis that equilibrium height within fluctuation regions denote the minimum of the membrane-substrate interaction potential. Starting from

the experimentally determined values of $\langle h \rangle$ and $\sqrt{\langle \delta h^2 \rangle}$, and the unspecific interaction described they determined membrane tension, $\sigma = 4$ $\mu J/m^2$, and the second derivative of the interaction potential, $\gamma = 2 \cdot 10^8$ J/m^4. It is worth noting that both of these values are very difficult to measure directly, especially when the vesicles adheres. For example, the stiffness of the potential is only derived from membrane fluctuation analysis [115] and vesicle tensions are determined either indirectly by the Bruinsma model or from micropipette aspiration, both of which are applicable only to the case of higher tensions than probed here. Thus, exploiting the information from membrane shape and fluctuations to simultaneously determine σ and γ, our approach represents an important advancement in the field of vesicle studies. Moreover, derived absolute values of $\langle h \rangle$, $\sqrt{\langle \delta h^2 \rangle}$, σ and γ turned out to be in good agreement with results found in literature [115]. However, when trying to identify forces contributing to the membrane-substrate interaction, a discrepancy arose. Precisely, comparison of γ with a value calculated from simple superposition of interactions differed by an order of magnitude. In fact, such discrepancy was already identified 10 years ago [124], yet no solution to it exists. It turns out that finite space and time resolution of the data (collaboration with Daniel Schmidt/Prof. Udo Seifert/Prof. Ana Smith) may account for this discrepancy.

From these analyses and the current notion of vesicle adhesion, adhesion to patterned substrates was found to be weak. Moreover, in this limit of sparse molecular bond density, adhesion was independent of pattern geometry. Apart from the results presented in this thesis, little is known about the interplay of receptor concentration and their distribution in terms of adhesion. Systematic increase of receptor concentration may be of interest in future studies on patterning effects.

Lipid diffusion measurements within characteristic regions of the structured adhered vesicle provided insight into the situation at nanoscopic length scales. While the diffusion in the free membrane at the vesicle top

amounted to 12 $\mu m^2/s$, diffusion within the adhesion zone was slowed by more than 15%. In detail, within the adhesion zone lipid diffusion within fluctuating membrane regions where slowed by 15% while those in adhered regions where lowered further by an additional 15%. This significant reduction of diffusion constants was attributed to molecular friction effects of lipids within the adhesion zone. Clearly, the continued mobility of the lipids even in the adhered help the system to equilibrate.

In addition, a net flow of lipids resulting in membrane area changes within the adhesion zone was also made during osmotic pressure changes. Increasing osmotic gradients, effectively decreased vesicle tension and shifted the membrane height within fluctuation areas upward. The opposite effect was triggered by decreasing osmotic gradients. Evidently, any membrane area change required lipid mobility. While varying osmotic gradients between 20 and 170 $mOsm/l$ membrane substrate distances changed from 0 to 500 nm. Mean square amplitudes increased similarly, with absolute values varying from no detectable fluctuation to amplitudes of ~ 17 nm. From theoretical considerations shifts of average heights in the observed direction are expected. Thus, it was concluded that a decrease in tension leads to a shift of the interaction potential minimum towards higher membrane-substrate distances. Moreover, these experiments show that this is a promising model system to study effects on adhesion due to osmotic disturbances. While so far membrane permeability was probed with micropipette aspiration, the biologically relevant situation of adhered membranes had not been treated before.

Membrane fluctuation near as well as far away from a substrate were probed with FluCS. Measurements on non-adhered vesicles far from the substrate resulted in membrane tension and bulk solution viscosities of $0.4 \pm_p 0.2$ $\mu J/m^2$ and 0.0013 $kg/(m \cdot s)$, respectively. Vesicles adhering weakly to structured substrates featured slightly higher membrane tensions of $0.5 \pm_p 0.4$ $\mu J/m^2$ and the same viscosity. Deviations of viscosities from the expected value of (combined) water and sucrose solution were

attributed to, on the one hand, theoretical approximations in the hydro-dynamic damping expression and, on the other hand, to frictional effects from the bilayer leaflets. Thus, in order to isolate the origin of this effective hydrodynamic damping systematic changes of lipid composition or bulk solution will be necessary.

From measurements near the substrate an estimate of the stiffness of the interaction potential was calculated for the case of free vesicles, $\gamma = 7 \pm 3 \cdot 10^5 \; J/m^4$. Close to the substrate, hydrodynamic damping was very different. Measured height correlation functions deviated strongly from the theoretical form of the free fluctuating membrane. Damping near the substrate appeared to be higher than at the vesicle top. Moreover, damping on structured adhered substrates where higher than for free vesicles near the substrate. Since the current theory of simple hydrodynamic damping fails for the analysis, further theoretical expressions for hydrodynamic damping in the vicinity of a substrate and concomitant experiments need to be worked out. Here it may be noted that FluCS is uniquely suited for this kind of correlation analysis. Measurements with RICM are incapable of probing the damping effects because they are too slow. In the past, such analysis has been done using contour analysis in the bright field , but here we are able to probe not only the sides but any zone whatsoever. However, only strong fluctuations, typical of soft, weakly adhering vesicles are measurable with FluCS since the axial resolution is limited to 20 nm.

Finally, FluCS was applied to measure membrane fluctuations of living objects: HEK293 cells and human macrophages. Plasma membrane staining to saturate the membrane was facilitated from a novel liposome fusion method (developed by Agnes Csiszár), which is an essential prerequisite for FluCS. Adapted settings for cell measurement were defined and fluctuation amplitudes above the resolution threshold recorded. Analysis on substantial macrophage membrane fluctuations may allow for quantification of changes prior to and after their activation. Several ideas to improve FluCS in acquisition and treatment of data, e.g. time consuming z-stacks

159

are replaced by scans; lateral scans promise to increase spatial resolution by a factor 4, were proposed and should advance the applicability of FluCS further.

Appendix A

Validation of FCS

FCS is an ideal analytical tool for studying diffusion of molecules at nanomolar concentrations. Due to its high sensitivity, however, molecular properties and experimental settings have enormous influence on autocorrelation measurements. Numerous studies already dealt with effects which can bias the value of the derived diffusion coefficient [151–153]. In the following several optical and photophysical effects which influence the outcome of a FCS measurement are presented and solutions for the present set-up are given. First, several components of the set-up, the objective, the acousto-optic tunable filter, the software correlator and the confocal volume are examined. Second, several fluorophores are characterized in saturation, stability and experimental suitability.

Water immersion objective
Utilization of a water immersion objective for FCS measurements is important as it features high resolving power particularly for water mounted objects and is able to focus into the specimen some $\sim 200~\mu m$ with high clarity and accuracy. Oil objectives, on the other hand, decrease in their performance with any water layer between specimen and cover glass resulting in image degradation and severely lowered contrast. In addition, water immersion objectives are often equipped with a correction collar (CC) to adjust lens distance to coverslip thickness [154]. This way distortion of
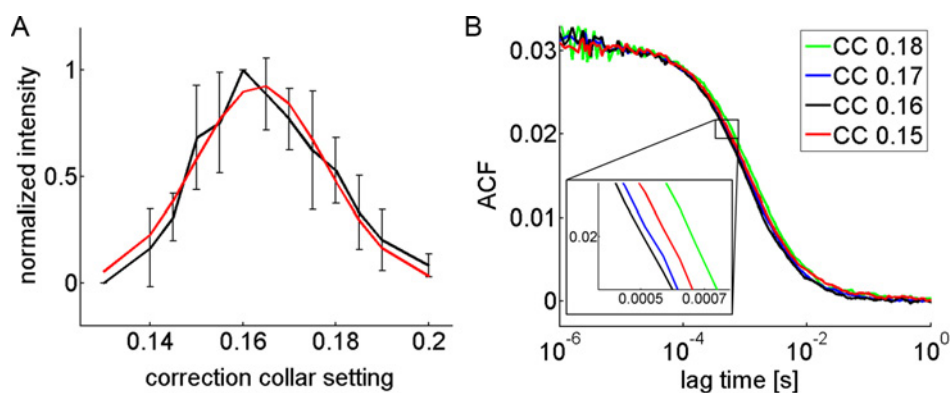
Figure A.1: Effects of correction collar settings. A: Detected intensities decline as the optical correction is set to a false coverslip thickness. Averaging over 5 measurements (black) and fitting with a Gaussian (red) yielded a value of 0.165 for best adjustment. B: ACFs for different correction collar (CC) settings. For larger deviations from 0.165 ACFs exhibit slightly slower temporal decay.

focus and chromatic abberations are diminished. The CC of the present objective was adjustable on a 0.14 - 0.2 scale. Maximizing the detected intensity signal let to a minimization of the above mentioned effects. For this calibration 10^{-6} M or 10^{-7} M TRITC-DHPE fluorophore in PBS buffer was recorded for 10 s employing standard FCS settings (see section 2.3.3.4). Care was taken to measure far away from the substrate to exclude effects from physisorbed fluorophore. Figure A.1 (left) shows the detected intensity change for different scale settings. In this measurement and for all following experiments a value of 0.165 was found optimal and intensity was highest. Corresponding effects on the ACF are illustrated in the same figure (right). Deviations from the optimal setting result in an increase of apparent diffusion times, and were found to be as high as 20% by Enderlein et al. [151].

Acousto-optic tunable filter

The acousto-optic tunable filter (AOTF) is the second important FCS component tested. It is an electro-optical device which functions as excitation
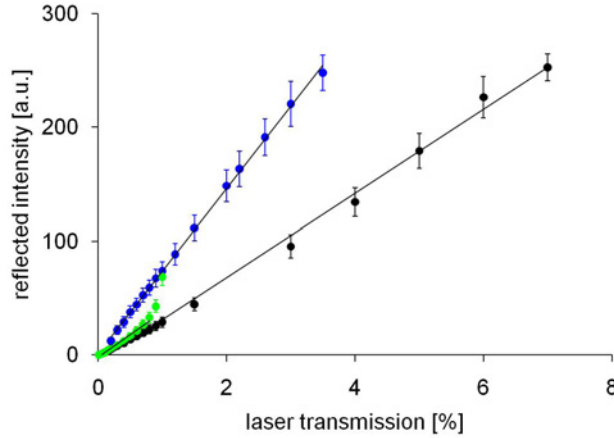
Figure A.2: AOTF attenuation behaviour. Reflected intensities of the 488 nm laser line for AOTF 100% (blue), 10% (black) and 1% (green). For each AOTF setting, the laser intensity (LI) was varied between 1% and 100%. AOTF and LI setting define the laser transmission, i.e. (AOTF = 1%, LI = 10%) = 0.1% laser transmission. Up to LIs of $\sim$ 70%, each curve is linear.

filter to simultaneously modulate the intensity of multiple laser lines. Typically AOTFs consist of an anisotropic quartz crystal coupled to a piezo-electric transducer. As the transducer generates a high-frequency vibrational wave that propagates into the crystal, its optical properties are changed. Nowadays, these devices are highly abundant in laser confocal microscopes and inevitable for all fast intensity switching applications [155]. Here, simply the AOTF's attenuation behaviour was checked, as any non-linear response from switching between different excitation intensities may cause unwanted bleaching or saturation effects. Intensities of a 488 nm laser were recorded with a PMT after reflection from a mirror fixed at the sample position and passage of a beam splitter (T80/R20, Zeiss). Data was acquired for 20 s and averaged over 512 pixels for each measurement. The initial laser intensity was stepwise attenuated by setting the AOTF to 100%, 10% and 1% transmission. For each attenuation step laser intensities (LI) were varied between 1% - 100%. AOTF transmission and LI together define the laser transmission plotted in figure A.2, i.e. (AOTF = 1%, LI

= 100%), (10%, 10%) and (100%, 1%) were plotted at 1% laser transmission. It has to be noted that AOTF settings 100% (blue), 10% (black) and 1% (green) would result in equal laser intensities, if AOTF attenuation was strictly linear. As seen in figure A.2 this is only partially fulfilled, as curves do not fall on top of each other. Nevertheless, for a specific AOTF setting, linearity holds for all LIs $\in$ [1% 70%]. Green data in figure A.2 exemplary shows how intensities increase nonlinearly from (1%, 70%) = 0.7% onwards[1].

As a result, care was taken to choose excitation intensities within the linear regime.

Software correlator

Another important part of the FCS set-up is the software correlator. It calculates the correlation function from photon pulses detected by the APDs. Real time calculation over a wide range of lag times τ is achieved from applying the multiple tau algorithm. This procedure was proposed by Schätzel et al. in 1985 [156] and is based on increasing the time window during which photons are counted with increasing sampling time. This provides a quasi-logarithmic time scale which enables fast calculation in comparison to linear algorithms which work with a constant time window. On the other hand, from averaging over a time window which increases with time, some information is lost. Nevertheless, the multiple tau algorithm is up to date the most elegant way to handle correlation data over large range of lag times with sufficient accuracy.

In this thesis autocorrelation curves were generated by the microscope software (ZEN, Zeiss) and fluorescence intensities were displayed as averages over ms. As the correlator is the central unit in correlation analysis to process photon information into meaningful data, its correct functioning had to be confirmed. Therefore, the software was used to store raw data from the measurement and a routine for data read out was used, which was kindly provided by S. Houben, ICS-7, FZJ. Raw data was further pro-

---

[1]Laser transmission > 7% = (10%, 70%) at AOTF 10% exhibited a similar nonlinear increase (data not shown).
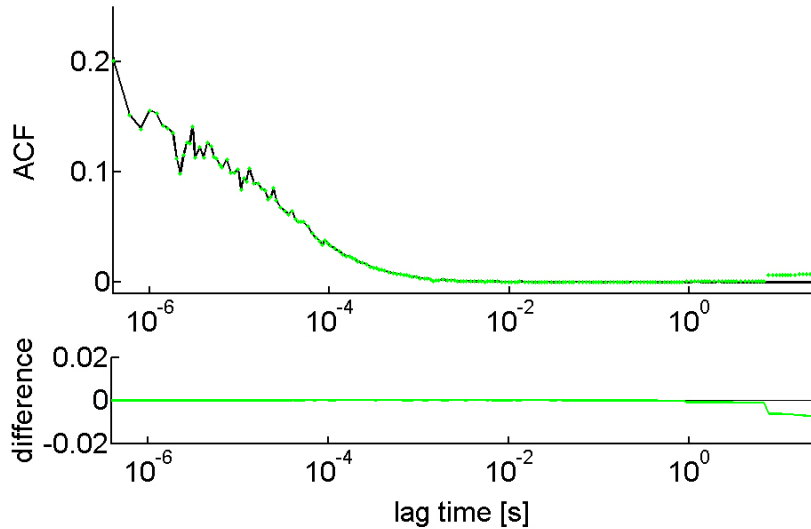
Figure A.3: Validation of software correlator functioning. ACF curves were obtained from the software ZEN (black) and from raw data processed by a self-written multiple tau algorithm (green dots). Correspondence between curves is achieved up to 1 s.

cessed by a self-written routine, containing the multiple-tau algorithm, as described in [86]. Calculated ACFs were compared to software generated ACFs and differences were plotted. Figure A.3 shows the result of this comparison. The autocorrelation function recorded from freely diffusing fluorophore in solution appears to coincide exactly up to a lag time of 1 s. From then onwards an erroneous stepwise increase of the output of the self-written programme is observed. Up to date this error is unsolved. Nevertheless, correct photon count processing for the relevant time interval was verified.

Confocal volume

The last and probably most important component of FCS is the confocal volume. Is is essentially a convolution of the excitation density of the focused laser beam and the detection efficiency of the light collecting optics.

165
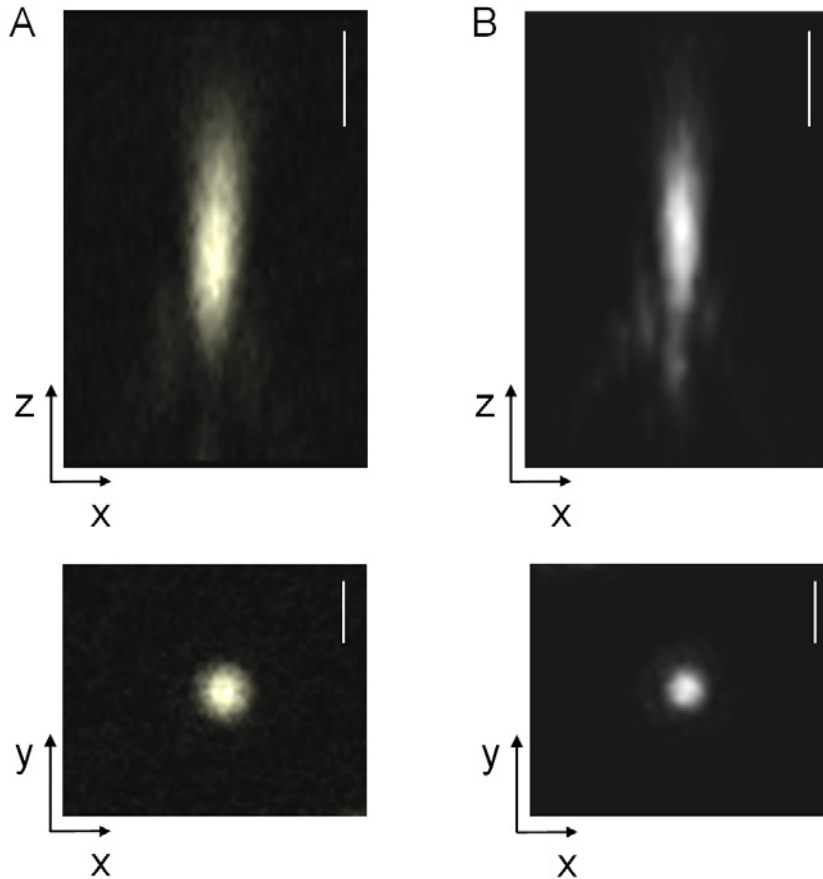
Figure A.4: Axial (XZ) and lateral (XY) view of subresolution beads excited with A: $\lambda = 543$ nm and B: $\lambda = 488$ nm laser lines. From the intensity distribution the size of the PSF is determined. Scale bar: 1 μm (XZ) and 0.5 μm (XY).

Its shape and size is the determining factor for quantitative FCS measurements, as theoretical expressions for autocorrelation functions are based on the assumption of a 3D Gaussian intensity distribution. In addition, the square of the beam waist radii ω_0 and z_0 are used to determine diffusion coefficients. For this reason, confocal volume size in axial and lateral direction have to be known with high accuracy. In this work ω_0 and z_0 were determined in two ways: On the one hand fluorescent beads of sub-resolution size were imaged and ω_0 and z_0 determined from a Gaussian fit

to the intensity profile. On the other hand, the FCS-zscan technique was applied to fluorescent lipids in a SLB, which allows to calculate ω_0 and z_0 as explained in section 2.3.3.3.

While results on SLBs are presented in section 3.3.2.1, bead measurements are outlined in the following: Multicolor fluorescent microspheres of 0.175 ± 0.005 μm size were suspended in PBS buffer at 1:10000 volume fraction and ultrasonicated for 5 min to prevent bead clustering. After addition to an observation chamber beads sedimented to the glass substrate. A waiting period of 15 min was sufficient to yield monodisperse single microspheres attached to the surface. Prior to recording, several fast scans were utilized to check for any remaining movement. Except for detection with PMTs the same optics as for FCS measurements (objective, pinhole and filters) were selected. Slow scan rates, small pixel sizes (0.1 μm) and an oversampling in axial direction (0.1 μm) resulted in improved signal to noise ratio and adequate resolution. Preparation and recording of samples was done by D. Kirchenbüchler, ICS-7, FZJ.

Figure A.4 shows typical examples of confocal images of beads excited to fluorescence with $\lambda = 543$ nm and $\lambda = 488$ nm laser lines: The cigar-like fluorescence intensity distribution in the axial (XZ) plane and the Airy disc of the central plane in lateral (XY) direction. Obvious deviations from the ideal 3D Gaussian shape are detected. Neither axial rotational symmetry nor symmetry with respect to the focal plane are exactly conserved (see (XZ) planes in figure A.4). Light reflexes at the side of the confocal volume facing the substrate (visible at the bottom part of the figure) reflect the presence of spherical abberations. This effect may be enhanced from the vicinity of the substrate, however, elaborated studies on this aspect verified its presence even within the bulk medium [70]. Yet, approximation of the confocal shape by a 3D Gaussian is a common and the only way, to facilitate quantitative analysis.

3D information of the recorded stacks was evaluated as follows: Central planes in XZ and XY direction were located via saving the coordinates of the intensity maximum. A 2D nonsymmetrical Gaussian fit to intensity distributions in these planes yielded standard deviation σ, full width at

167

half maximum (FWHM) and $1/e^2$ radii ω_0 and z_0 according to:

$$G(x,y) = A \cdot e^{-\frac{1}{2}\left(\frac{(x-x_0)^2}{\sigma_x^2} + \frac{(y-y_0)^2}{\sigma_y^2}\right)} + B \quad \& \quad \omega_0 = \sqrt{(x_i - x_0)^2 + (y_i - y_0)^2}$$

$$G(x,z) = A \cdot e^{-\frac{1}{2}\left(\frac{(x-x_0)^2}{\sigma_x^2} + \frac{z^2}{\sigma_z^2}\right)} + B \quad \& \quad z_0 = z_i \wedge x = 0 \quad,$$

$$\text{where} \quad x_i, y_i, z_i \in \left|\frac{A}{e^2} + B - G(x,y)\right| = min!$$

$$FWHM = 2\langle\sigma\rangle\sqrt{2\log 2} \quad \& \quad \langle\sigma\rangle = \frac{1}{2}(\sigma_x + \sigma_y) \quad.$$

Values for both coordinates in the XY plane, σ_x and σ_y, were averaged and differed by $\leq 7\%$ within one plane. z_0 values obtained from XZ and YZ planes were averaged as well. Table **??** gives an overview of the results. The $FWHM$ value $= 334 \pm 8$ for $\lambda = 543$ nm agreed up to 8% with measurements performed at a similar microscope in our group. Here it amounted to $FWHM = 358 \pm 12$ nm (M. Romanowska and I. Lauter, ICS-7, FZJ: Personal communication).

laser: $\lambda = 543$ nm			laser: $\lambda = 488$ nm		
radius		#	radius		#
$FWHM/2$	$= 165 \pm_p 4$ nm	10	$FWHM/2$	$= 147 \pm_p 3$ nm	13
ω_0	$= 281 \pm_p 7$ nm	10	ω_0	$= 251 \pm_p 9$ nm	13
z_0	$= 1284 \pm_p 11$ nm	10	z_0	$= 1219 \pm_p 14$ nm	13

Table A.1: Results of PSF determination for $1/e^2$ waist radii ω_0, z_0 and $FWHM/2$.

Fluorophore Saturation

The choice of fluorescent probes is the first decisive step in FCS. One may spent lots of time optimizing instrumentation, however, final experimental settings and analysis are determined by the spectral properties of the fluorophore. One largely underestimated fact e.g. is that the excitation probability of a fluorophore is not only dependent on the excitation-light distribution in the sample, but also on the molecule's saturation behaviour. Optical saturation occurs if laser intensities are sufficiently high to excite

more and more molecules to a higher state while there is too little time for them to decay back to the ground state. Thus, the ground state becomes depleted and higher states are occupied. As a consequence of this population depletion in the ground state, an increase in excitation light does not produce a corresponding increase in fluorescence emission.

In order to test this, fluorophore diluted to 10^{-8} M, 10^{-7} M or 10^{-6} M concentration was added to an observation chamber, which was covered with a glass slide. CC as well as pinhole size and alignment were checked and the confocal volume set to 200 μm above the glass substrate to prevent recording of adsorbed fluorophore. Intensities were averaged over 10 s and after each measurement laser intensities were stepwise increased. Precisely, the AOTF was set to a fixed % value, while LI was changed from 0.2% and 100%. Subsequently, the AOTF was increased by a factor 10 and laser intensities were varied again. In some cases, measurements were repeated in reverse direction to test for hysteresis effects, which effectively did not occur.

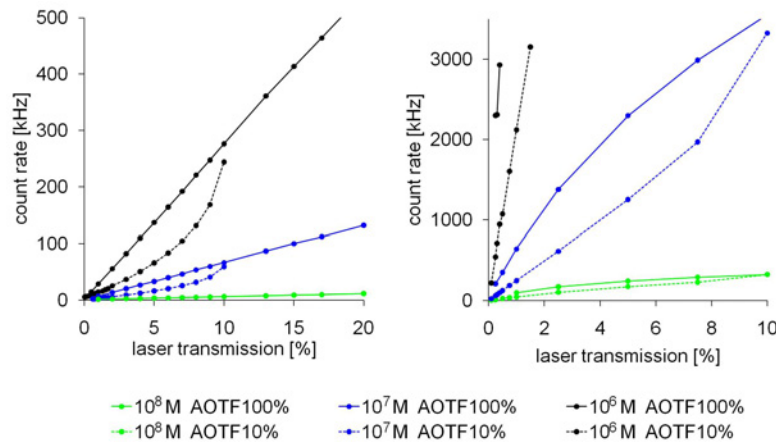Figure A.5 gives two examples of fluorophore response to illumination

Figure A.5: Fluorophore response to laser excitation. Apart from AOTF effects arising at LIs >70% in both cases, TRITC varies linearly over the probed excitation interval. Alexa488 is linear only for AOTF 10% transmission, while at AOTF 100% the fluorophore immediately saturates.

power (see 2.1.4 for fluorophore specification): TRITC, as example for the 543 nm laser line and Alexa488 for the 488 nm laser line. In both cases, curves show a non-linear increase between 7-10% laser transmission. This effect is opposite to fluorophore saturation and attributed to the AOTF non-linear behaviour as seen in figure A.2. Yet, saturation effects were detectable in some cases.

Except for AOTF effects TRITC fluorophore exhibited a linear response to all excitation intensities shown. Alexa488, on the other hand, showed direct saturation as the AOTF was set to 100% transmission. Switching the AOTF from 100% to 10% resulted in a drastically different behaviour. As in the case of TRITC, linearity was provided for over the whole excitation range, until AOTF effects were noticeable. Most probably, this drastic change is due to the strong difference in excitation power, as intensities for AOTF 10% and AOTF 100% vary by a factor $\sim$25 (488 nm, AOTF 10%, LI 1% = 1 μW; AOTF 100%, LI 1% = 25 μW). Similar properties were found for other fluorophores tested: Results of Atto550 corresponded to those found for TRITC. Here, non-linearity started at 15% laser transmission (AOTF 10%, LI 15%). Atto488 exhibited qualitative identical curves to Alexa488, however, the linear regime at AOTF 10% extended only up to 5% laser transmission (AOTF 10%, LI 50%). To exclude changes in fluorophore response from chemical coupling to another molecule, protein bound fluorophores were tested as well. No significant changes were detected.

Accordingly, TRITC and ATTO550 are only little prone to fluorophore saturation and linearity is given up to $\sim$34 μW (100%, 10%). Alexa488 and Atto488 should be recorded at excitation powers less than $\sim$4 μW (10%, 5%) to avoid fluorophore saturation.

 In terms of correlation analysis and high excitation intensities optical saturation effects are less often discussed than photobleaching effects. While from bleaching autocorrelation curves are shifted to shorter diffusion times, optical saturation, effects are opposite [157]. This is demonstrated in figure A.6 for Atto488 diffusing in solution. At 4% laser transmission the onset of saturation is visible, as recorded count rates deviate from linear-
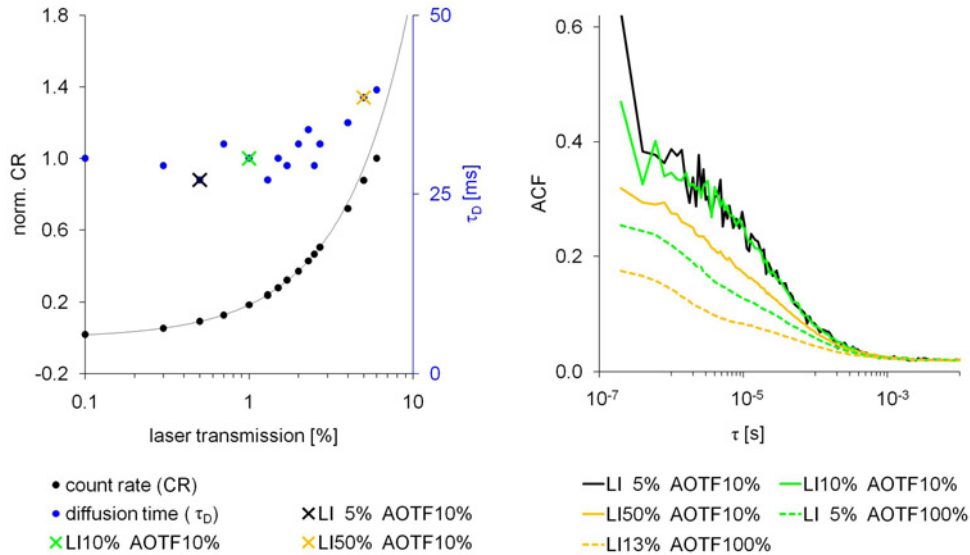
Figure A.6: Fluorophore saturation effects detected in FCS experiment of Atto488 diffusion. At the onset of saturation at 4% laser transmission, detected intensities deviate from linearity (black line) and diffusion times increase (left). ACF curves exhibit smaller amplitudes and apparently larger diffusion times as the fraction of molecules contributing to fluorescence decreases. Fraction of molecules excited to the triplet state rise, as suggested by the distinct shoulder at short correlation times (right).

ity. At the same time corresponding autocorrelation curves exhibit a decay in amplitude and an apparent diffusion time increase. This is due to the large number of molecules excited to the triplet state, as indicated by the distinct shoulder at short correlation times .

Fluorophore Stability

Photostability of fluorophores was tested by the following procedure: Molecules were physisorbed from a 10^{-7} M solution to the glass substrate. Excess water was removed and the fluorescent layer dried. Employing standard FCS settings, laser intensities were adjusted to achieve initial

171
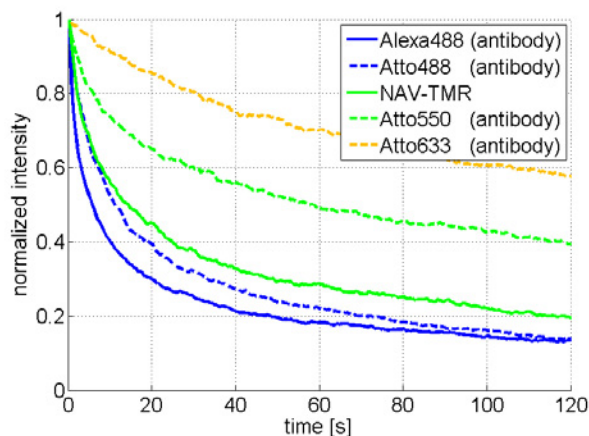
Figure A.7: Photostability of several fluorophores. Bleach curves of protein - bound fluorophore were normalized and averaged (Alexa488-antibody (#5), Atto488-antibody (#6), TMR-NAV (#5), Atto550-antibody (#9), Atto633-antibody (#6)).

count rates of ∼250 kHz in each experiment. Bleach curves were recorded for 120 s and normalized with respect to the first recorded intensity. Figure A.7 shows averaged results for five protein - coupled fluorophores (for molecular specification, see section 2.1.4). Fast exponential bleaching is observed. While intensities of Alexa488 and Atto488 show rapid decay, bleach curves of "red - shifted" fluorophores decay slower, thereby denoting higher stability. In addition, TMR appears to be less stable than Atto 550. A similar wavelength dependent stability, was found before [69]. However, fluorescent intensities observed there decrease much slower than in the present case. E.g. Alexa488 reduced to only 80% of its initial intensity after 60 s. Most likely this is due to the fluorophore - air interface in the present experiment, which appears to drastically reduce fluorescence stability. Thus, even though observed relative trends between fluorophores are in accordance with literature, it is speculative, whether differences would be as pronounced under physiological conditions.

Fluorophore Diffusion

In addition to tests on photophysical properties, diffusion constants of

Alexa488 and TRITC were measured. Therefore, 10^{-8} M fluorophore dissolved in PBS buffer was recorded for 300 s. A fit of the obtained ACF with equation 2.3 yielded diffusion times 37 ± 8 μs and 46 ± 6 μs for Alexa488 (# 20) and TRITC (# 29), respectively. Using the axial waist radius ω_0 from bead measurements, diffusion constants 423 $\mu m^2/s$ for Alexa488 and 427 $\mu m^2/s$ for TRITC were obtained. A comparison to literature values yields high agreement for Alexa488, as reported diffusion constants are 435 $\mu m^2/s$ [158] and 414 $\mu m^2/s$ [158]. As no literature values were found exactly for TRITC, results were compared to the most similar molecular structure. This was Rhodamine 6G, whose diffusion was studied extensively with FCS. As its diffusion constant was reported 389 $\mu m^2/s$ [159], 414 $\mu m^2/s$ [159] and 426 $\mu m^2/s$ [158], TRITC exhibited systematically higher diffusion. The deviation by ~ 10 %, may be explained by temperature differences and the slightly smaller molecular weight of TRITC (444 Da) in comparison to Rhodamine 6G (479 Da), which suggests slightly faster diffusion.

Choice of Fluorophore

A suitable fluorophore for FCS is characterized by high quantum efficiency, large absorption cross section, negligible saturation and high photostability [87, 139]. Several fluorophores which have been considered rather good in standard microscopy applications, e.g. fluorescein, photobleach already at very low excitation powers. Thus a series of dyes, e.g. Alexa as well as Atto, were specifically designed to meet the requirements of novel fluorescence techniques. Apart from their enhanced photostability, they often feature similar absorption and emission characteristics. Today they are highly popular in FCS application, next to the well established rhodamines, such as Rhodamine 6G and TRITC, who are highly stable but feature less quantum efficiency. Table **??** gives an overview of the fluorophores tested in this study. A comparison of these dyes confirms that tested Atto and Alexa dyes show the desired properties, while TRITC is slightly less optimal. However, a major common disadvantage of all synthetic dyes is that the molecule under study has to be labeled specif-

ically by the fluorophore. This is difficult and tedious, and most often novel engineered dyes attached to a functional molecule are commercially not available. As this is true for Atto and Alexa dyes and since TRITC was already used in several FCS studies [69, 87], this fluorophore was used most often in this work.

	Atto 633	Atto 550	TRITC	Atto 488	Alexa 488
λ_{abs} [nm]	629 [160]	554 [160]	544 [62]	501 [160]	495 [62]
λ_{em} [nm]	657 [160]	576 [160]	572 [62]	523 [160]	519 [62]
MW [Da]	749 [160]	791 [160]	444 [62]	981 [160]	643 [62]
ϕ	0.64 [160]	0.8 [160]	0.2 [161, 162]	0.8 [160]	0.92 [62]
ϵ [$10^4/(cm\,M)$]	13 [160]	12 [160]	8.4 [62]	9 [160]	7.3 [62]
I_{sat} [μW]*	–	$\sim$50	>34	$\sim$4	>9
$I(60)/I(0)$ [%]*	0.7	0.5	0.3	0.25	0.2
τ_{fl} [ns]	3.3 [160]	3.6 [160]	2.1 [161]	4.0 [160]	4.1 [62]
D [$\mu m^2/s$]*	–	–	427	–	423

Table A.2: Overview of tested fluorophores. λ_{abs} and λ_{em} are the maximum absorption and emission wavelengths, respectively, MW is the molecular weight, ϕ is the quantum efficiency, ϵ the molar absorption coefficient, I_{sat} is the intensity of saturation, $I(60)/I(0)$ the percent intensity remaining after 60 s illumination, τ_{fl} is the fluorescence lifetime and D the diffusion coefficient. Literature values are cited. Experimental details for values indicated by * are given in the text.

Appendix B

Error Estimate of Approximate Expressions

In the following an estimate of the error arising from developing the intensity function up to 2nd order is given. Therefore, higher orders of z in the intensity Fourier expansion are considered. The height trace as well as the autocorrelation function for each approximation are calculated and the differences in shape changes analyzed. Here, examples for an expansion of up to 4th order are presented:

$$I(h(t)) \sim I(z) + \frac{\delta I}{\delta h}\Big|_z \delta h(t) + \frac{1}{2!}\frac{\delta^2 I}{\delta h^2}\Big|_z \delta h(t)^2 + \frac{1}{3!}\frac{\delta^3 I}{\delta h^3}\Big|_z \delta h(t)^3 + \frac{1}{4!}\frac{\delta^4 I}{\delta h^4}\Big|_z \delta h(t)^4$$

First of all, intensity traces for expansions up to $\delta h(t)^2$ and $\delta h(t)^3$ were converted into the respective height traces via a look-up table (1 [nm] height accuracy). Amplitude values of intensity dI and height dh were calculated and plotted.

Figure B.1 depicts the result of intensity dI to height dh conversion for different expansion limits. Clearly, fluctuation amplitudes of up to 0.4 [μm] appear to be represented well with approximations up to 2nd order, while stronger fluctuations lead to erroneous conversions. Applying this to measured data a slight underestimation of fluctuation strengths from the first expansion term in comparison to higher orders in δh is found.
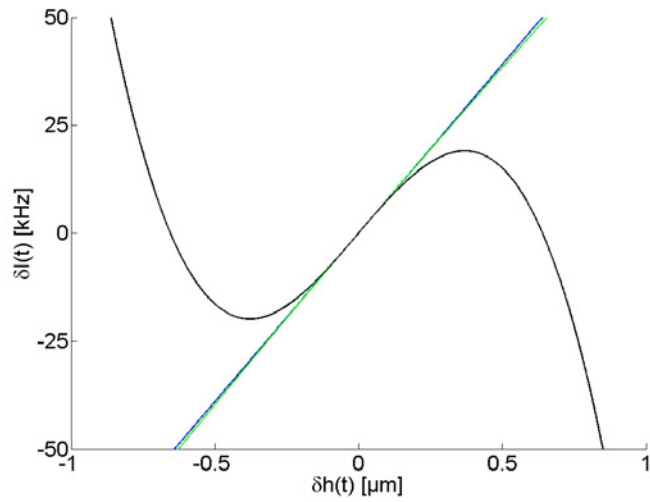
Figure B.1: Intensity amplitudes vs. height amplitudes for 1st (blue), 2nd (green) and 3rd (black) order.
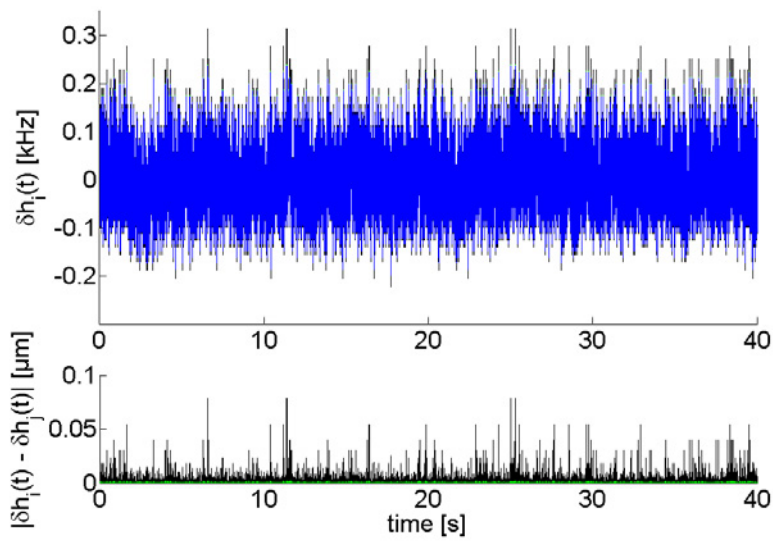

Figure B.2: Measured height amplitude traces, derived with different accuracies (top) and deviation of height amplitudes (bottom) calculated to first dh_1, up to second dh_2 and up to third order dh_3.

Figure B.2 gives an example of vesicle fluctuation amplitudes, with displacements of up to $\sim 0.3\,[\mu m]$. Comparison of absolute amplitude deviations between accuracies of 1st - 2nd and 1st - 3rd order, $abs(dh_2 - dh_1)$ and $abs(dh_3 - dh_1)$, respectively, yield an average deviation by 12 [nm]. Since this is well below the spatial resolution of FluCS, the present analysis is considered sufficiently accurate for fluctuations within the range of $0.4[\mu m]$.

The autocorrelation function was treated in a similar manner. From intensity traces expanded up to 4th order, the intensity autocorrelation function as well as the amplitude were calculated:

$$
\begin{aligned}
&\langle I(h(t)) \cdot I(h(t + \tau)) \rangle \\
=\ & I(z)^2 + \left(\left.\frac{\delta I}{\delta h}\right|_z \right)^2 \langle \delta h(t)\delta h(t+\tau) \rangle + \frac{1}{4} \left(\left.\frac{\delta^2 I}{\delta h^2}\right|_z \right)^2 \langle \delta h(t)^2 \delta h(t+\tau)^2 \rangle \\
+\ & I(z) \left\{ \left(\left.\frac{\delta I}{\delta h}\right|_z \right) \langle \delta h(t+\tau) \rangle + \frac{1}{2} \left(\left.\frac{\delta^2 I}{\delta h^2}\right|_z \right) \langle \delta h(t+\tau)^2 \rangle \right. \\
+\ & \frac{1}{6} \left(\left.\frac{\delta^3 I}{\delta h^3}\right|_z \right) \langle \delta h(t+\tau)^3 \rangle + \frac{1}{24} \left(\left.\frac{\delta^4 I}{\delta h^4}\right|_z \right) \langle \delta h(t+\tau)^4 \rangle \left. \right\} \\
+\ & \left(\left.\frac{\delta I}{\delta h}\right|_z \right) \langle \delta h(t) \rangle \left\{ I(z) + \frac{1}{2} \left(\left.\frac{\delta^2 I}{\delta h^2}\right|_z \right) \langle \delta h(t+\tau)^2 \rangle \right. \\
+\ & \frac{1}{6} \left(\left.\frac{\delta^3 I}{\delta h^3}\right|_z \right) \langle \delta h(t+\tau)^3 \rangle \left. \right\} + \frac{1}{24} \left(\left.\frac{\delta^4 I}{\delta^4 h}\right|_z \right) \langle \delta h(t)^4 \rangle I(z) \\
+\ & \frac{1}{2} \left(\left.\frac{\delta^2 I}{\delta^2 h}\right|_z \right) \langle \delta h(t)^2 \rangle \left\{ I(z) + \left(\left.\frac{\delta I}{\delta h}\right|_z \right) \langle \delta h(t+\tau) \rangle \right\} \\
+\ & \frac{1}{6} \left(\left.\frac{\delta^3 I}{\delta^3 h}\right|_z \right) \langle \delta h(t)^3 \rangle \left\{ I(z) + \left(\left.\frac{\delta I}{\delta h}\right|_z \right) \langle \delta h(t+\tau) \rangle \right\}
\end{aligned}
$$

Taking into account that all time averages over odd powers of $\delta h(t)$ cancel out and applying the following expressions for intensity derivatives

$$
\left.\frac{\delta I}{\delta h}\right|_z = -\left(\frac{4z}{z_0^2} \right) (I(z) - I_B)
$$

$$\frac{\delta^2 I}{\delta h^2}\bigg|_z = \frac{4}{z_0^2}\left(\frac{4z^2}{z_0^2} - 1\right)(I(z) - I_B)$$

$$\frac{\delta^3 I}{\delta h^3}\bigg|_z = \frac{16z}{z_0^4}\left(3 - \frac{4z^2}{z_0^2}\right)(I(z) - I_B)$$

$$\frac{\delta^4 I}{\delta h^4}\bigg|_z = \frac{16}{z_0^4}\left\{\left(\frac{4z^2}{z_0^2} - 3\right)^2 - 6\right\}(I(z) - I_B) \ ,$$

one obtains:

$$
\begin{aligned}
\langle I(h(0)) \cdot I(h(t)) \rangle &= I(z)^2 + \left(\frac{\delta I}{\delta h}\bigg|_z\right)^2 \langle \delta h(0)\delta h(t) \rangle + \frac{1}{4}\left(\frac{\delta^2 I}{\delta h^2}\bigg|_z\right)^2 \langle \delta h(0)^2 \delta h(t)^2 \rangle \\
&+ I(z)\left(\frac{\delta^2 I}{\delta h^2}\bigg|_z\right)\langle \delta h(t)^2 \rangle + \frac{I(z)}{12}\left(\frac{\delta^4 I}{\delta h^4}\bigg|_z\right)\langle \delta h(t)^4 \rangle \\
&+ \frac{1}{2}\left(\frac{\delta I}{\delta h}\bigg|_z\right)\left(\frac{\delta^2 I}{\delta^2 h}\bigg|_z\right)\left\{\langle \delta h(0)h(t)^2 \rangle + \delta h(0)^2 h(t) \rangle\right\} \\
&+ \frac{1}{6}\left(\frac{\delta I}{\delta h}\bigg|_z\right)\left(\frac{\delta^3 I}{\delta^3 h}\bigg|_z\right)\left\{\langle \delta h(0)h(t)^3 \rangle + \delta h(0)^3 h(t) \rangle\right\}.
\end{aligned}
$$

And for the correlation amplitude:

$$
\begin{aligned}
\frac{\langle I(h(t))^2 \rangle}{\langle I(h(t)) \rangle^2} &= -\frac{(I(z) - I_B)^2 \langle \delta h(t)^2 \rangle \frac{16z}{z_0^4}\left(\frac{4z^2}{z_0^2} - 1\right)\langle \delta h(t) \rangle}{\left\{(I(z) - I_B)\, e^{-\frac{2}{z_0^2}\langle \delta h(t)^2 \rangle} + I_B\right\}^2} \\
&+ \frac{I(z)^2 + (I(z) - I_B)\langle \delta h(t)^2 \rangle\left\{(I(z) - I_B)\frac{16z^2}{z_0^4} + I(z)\frac{4}{z_0^2}\left(\frac{4z^2}{z_0^2} - 1\right)\right\}}{\left\{(I(z) - I_B)\, e^{-\frac{2}{z_0^2}\langle \delta h(t)^2 \rangle} + I_B\right\}^2} \\
&+ \frac{(I(z) - I_B)^2 \langle \delta h(t)^4 \rangle\left\{\frac{4(I(z) - I_B)}{z_0^4}\left(\frac{4z^2}{z_0^2} - 1\right)^2 - \frac{64z}{3z_0^6}\left(3 - \frac{4z^2}{z_0^2}\right)\right\}}{\left\{(I(z) - I_B)\, e^{-\frac{2}{z_0^2}\langle \delta h(t)^2 \rangle} + I_B\right\}^2}
\end{aligned}
$$

$$+ \frac{(I(z) - I_B)\langle \delta h(t)^4 \rangle \left\{ \frac{4I(z)}{3z_0^4} \left\{ \left(\frac{4z^2}{z_0^2} - 3 \right)^2 - 6 \right\} \right\}}{\left\{ (I(z) - I_B) e^{-\frac{2}{z_0^2}\langle \delta h(t)^2 \rangle} + I_B \right\}^2}$$

Figure **??** gives an impression of the curve variation with different orders of accuracy. A good representation of the true correlation amplitude appears to be achieved from a 2nd order expansion or higher. Remaining deviations are highlighted in the inset of the graph. Experimentally, these are of the order of noise. In addition, there is high correspondence found for the central parabolic shape. Setting the background intensity I_B contribution to 0, the same parabolic trace is derived. A fit of the theoretical correlation amplitude with $I_B = 0$ hence allows to determine e.g. membrane tension σ as suggested by the strong influence on this central curvature. Table B.1 gives an overview of values for membrane tension σ,

κ [J]	σ [J/m^2]	$c[mol\%]$	R [μm]	w_0 [μm]	z_0 [μm]	I [Hz]	I_b
$20k_BT$	$10 \cdot 10^{-6}$	1	10	0.281	0.5	60000	$0.05 \cdot I$

Table B.1: Typical parameters used in calculations of the correlation amplitude.

bending rigidity κ, vesicle radius R, fluorophore concentration c, relative background intensity I_B to absolute intensity I as well as confocal waist radius in radial, ω_0, and axial, z_0, direction used to generate the graph.
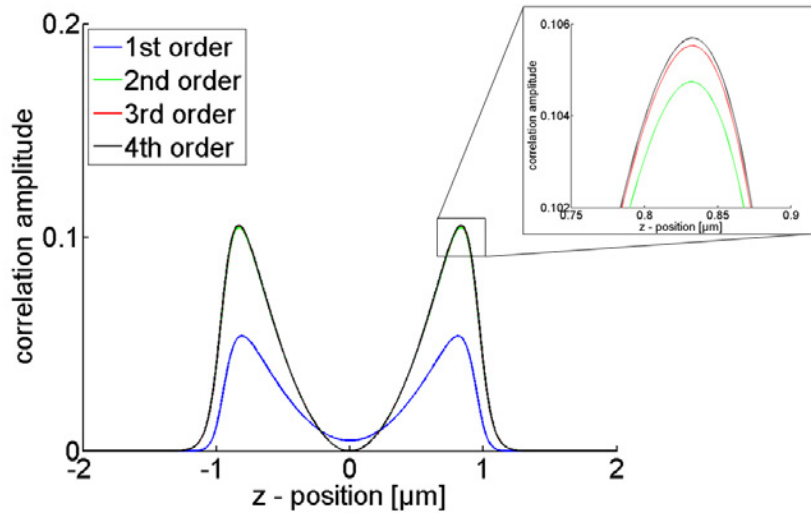
Figure B.3: Correlation amplitude changes with different orders of accuracy. A good representation of the true correlation amplitude is achieved already from a 2nd order expansion. Higher orders slightly increase maxima of the double-well shape.

Appendix C

Errata

In the following, errata in the originally submitted document are listed:

- frontmatter: Prof. Rudolf Merkel

- Page 1: This plasma membrane _ separates cytoplasm from cell exterior...

- Page 1: ... cause different diffusion processes within the membrane, which create_ lateral inhomogeneities.

- Page 3: ... which arise upon molecular interaction and <u>which</u> enhance <u>the</u> fidelity of molecular recognition, the term 'induced fit' <u>was</u> introduced.

- Page 3: ... which originate<u>s</u> from out of plane fluctuations...

- Page 82: ... within fluctuation regions <u>and</u> ensured system equilibration.

- Page 83: Those reported in literature were for δh on average a factor $\times$ 1.5-3 <u>smaller</u> and for σ almost $\times$ 10 <u>larger</u>.

- Page 100: Figure <u>4.7</u> shows a 120 s time course after PBS addition.

- Page 101: The first paragraph of 4.2.3 was moved one page up

- Page 121: The image was moved one page up

- Page 131: ... parameters deduced from experiments are within the expected range [25, 141–143].

- Page 139: This value is a magnitude lower as determined in section 3.3.1.4

- Page 140: ...hydrodynamic damping given in table 6.1.

- Page 153: This gave values ...

- Page 155: Fluctuation Correlation Spectroscopy, a newly developed method that exploits the experimental setup of Fluorescence Correlation Spectroscopy, measures membrane fluctuations...

- Page 156: ... supported the hypothesis that the equilibrium height within fluctuation regions is determined by the membrane-substrate interaction potential...

- Page 158: Clearly, the continued mobility of the lipids in the adhered region help the system to equilibrate.

Appendix D

List of Abbreviations

$\pm_m$	standard deviation of the mean
$\pm_p$	standard deviation of the population
ACF	autocorrelation function
AI^+	Argon ion
AOTF	acousto-optic tunable filter
APD	avalanche photodiode
Bodipy Fl- DHPE	1,2-dihexadecanoyl-sn-glycero-3-phosphoethanolamine-N-(4,4-difluoro-5,7-dimethyl-4-bora-3a,4a-diaza-s-indacene-3-propionyl)
BS	beam splitter
BSA (-biotin)	bovine serum albumin (-biotin)
CA	correlation amplitude
CC	correction collar
CCD	charge-coupled device
CLSM	confocal laser scanning microscope
CR	count rate
D	diffusion coefficient
DOPE-cap-biotin	1,2-dioleoyl-sn-glycero-3-phosphoethanolamine-N-cap biotinyl
DOPE-PEG2000	1,2-dioleoyl-sn-glycero-3-phosphoethanolamine-N-methoxy polyethylenglycol-2000
(DW-) RICM	(dual-wavelength) reflection interference contrast microscopy
FCS	fluorescence correlation spectroscopy
FFT	fast Fourier transformation
FluCS	fluctuation correlation spectroscopy
FRAP	fluorescence recovery after photobleaching

GUV	giant unilamellar vesicle
HeNe	Helium Neon
HHACF	height - height autocorrelation function
INA	illumination numerical aperture
IP	inflection point
ITO	indium tin oxide
LI	laser intensity
N	particle number
NA	numerical aperture
NAV (-TMR)	neutravidin (-tetramethylrhodamine)
NBD-PE	1,2-dioleoyl-sn-glycero-3-phosphoethanolamine-N-(7-nitro-2-1,3-benzoxadiazol-4-yl
PBS	phosphate buffered saline
PDMS	polydimethylsiloxane
PMT	photo multiplier tube
POP	polyolefin plastomer
PSF	point spread function
SLB	solid supported lipid bilayer
SOPC	1-stearoyl-2-oleoyl-sn-glycero-3-phosphocholine
TRITC-DHPE	N-(6-tetramethylrhodaminethiocarbamoyl)-1,2-dihexadecanoyl-sn-glycero-3-phosphoethanolamine
TRITC	tetramethylrhodamine-5-(and-6)-isothiocyanate

Appendix E

Curriculum Vitae

Bibliography

[1] N Campbell and J Reece. *Biology*. Benjamin Cummings, San Francisco, 8th edition, 2007.

[2] B Alberts, A Johnson, J Lewis, M Raff, K Roberts, and J D Watson. *Molecular Biology of the Cell*. Garland Science, New York, 4th edition, 2008.

[3] S J Singer and G L Nicolson. The fluid mosaic model of the structure of cell membranes. *Science*, 175:720–31, 1972.

[4] K Simons and E Ikonen. Functional rafts in cell membranes. *Nature*, 387:569–72, June 1997.

[5] L J Pike. The challenge of lipid rafts. *Journal of Lipid Research*, 50 Suppl(Supplement):S323–8, April 2009.

[6] D A Brown and E London. Structure and function of sphingolipid- and cholesterol-rich membrane rafts. *The Journal of Biological Chemistry*, 275:17221–4, June 2000.

[7] C Dietrich, L A Bagatolli, Z N Volovyk, N L Thompson, M Levi, K Jacobson, and E Gratton. Lipid rafts reconstited in model membranes. *Biophysical Journal*, 80:1417–1428, 2001.

[8] J Wyman and S J Gill. *Binding and Linkage: Functional Chemistry of Biological Macromolecules*. University Science Books, Herndon, 1990.

[9] E Fischer. Einfluss der Configuration auf die Wirkung der Enzyme. *Berichte der Deutschen Chemischen Gesellschaft*, 27:2985–2993, October 1894.

[10] D J Koshland. Application of a theory of enzyme specificity to protein synthesis. *Proceedings of the National Academy of Sciences*, 44:98–104, 1958.

[11] J N Israelachvili. *Intermolecular and Surface Forces, Third Edition*. Academic Press, Waltham, 3rd edition, 1991.

[12] W Helfrich. Steric interaction of fluid membranes in multilayer systems. *Zeitschrift Für Naturforschung, Section A*, 33:305–315, 1978.

[13] R J Pelham and Y l Wang. Cell locomotion and focal adhesions are regulated by substrate flexibility. *Proceedings of the National Academy of Sciences of the United States of America*, 94:13661–5, December 1997.

[14] A Harris. Behavior of cultured cells on substrata of variable adhesiveness. *Experimental Cell Research*, 77:285–297, March 1973.

[15] C Foa, M Soler, A-M Benoliel, and P Bongrand. Steric stabilization and cell adhesion. *Journal of Materials Science: Materials in Medicine*, 7:141–148, March 1996.

[16] E A Evans. Bending elastic modulus of red blood cell membrane derived from buckling instability in micropipet aspiration tests. *Biophysical Journal*, 43:27–30, July 1983.

[17] A Zidovska and E Sackmann. Brownian motion of nucleated cell envelopes impedes adhesion. *Physical Review Letters*, 96:048103, 2006.

[18] K Haldar, B U Samuel, N Mohandas, T Harrison, and N L Hiller. Transport mechanisms in Plasmodium-infected erythrocytes: lipid rafts and a tubovesicular network. *International Journal for Parasitology*, 31:1393–1401, October 2001.

[19] U Seifert. Configurations of fluid membranes and vesicles. *Advances in Physics*, 46:13–137, 1997.

[20] P Méléard, C Gerbeaud, P Bardusco, N Jeandaine, M D Mitov, and L Fernandez-Puente. Mechanical properties of model membranes studied from shape transformations of giant vesicles. *Biochimie*, 80:401–413, 1998.

[21] H G Döbereiner, E Evans, M Kraus, U Seifert, and M Wortis. Mapping vesicle shapes into the phase diagram: A comparison of experiment and theory. *Physical Review E*, 55:4458–4474, 1997.

[22] B Lorz. *Etablierung eines Modellsystems der Zelladhäsion über spezifische Bindungen geringer Affinität - eine mikrointerferometrische Studie*. PhD thesis, TU München, 2003.

[23] A-S Smith, K Sengupta, S Goennenwein, U Seifert, and E Sackmann. Force-induced growth of adhesion domains is controlled by receptor mobility. *Proceedings of the National Academy of Sciences of the United States of America*, 105:6906–6911, 2008.

[24] R Lipowsky and E Sackmann. *Structure and Dynamics of Membranes: I. From Cells to Vesicles / II. Generic and Specific Interactions*. North Holland, Amsterdam, 1995.

[25] J F Faucon, M D Mitov, P Méléard, I Bivas, and P Bothorel. Bending elasticity and thermal fluctuations of lipid membranes. Theoretical and experimental requirements. *Journal de Physique*, 50:2389–2414, 1989.

[26] S T Milner and S A Safran. Dynamical fluctuations of droplet microemulsions and vesicles. *Physical Review A*, 36:4371–4379, 1987.

[27] R Merkel, E Sackmann, and E Evans. Molecular friction and epitactic coupling between monolayers in supported bilayers. *Journal de Physique*, 1989.

[28] R M Servuss and W Helfrich. Mutual Adhesion of Lecithin Membranes at Ultralow Tensions. *Journal De Physique*, 50:809–827, 1989.

[29] S F Fenz, R Merkel, and K Sengupta. Diffusion and intermembrane distance: case study of avidin and E-cadherin mediated adhesion. *Langmuir*, 25:1074–85, January 2009.

[30] T R Weikl, M Asfaw, H Krobath, B Rozycki, and R Lipowsky. Adhesion of membranes via receptor-ligand complexes: Domain formation, binding cooperativity, and active processes. *Soft Matter*, 5:13, 2009.

[31] N Gov and S Safran. Pinning of fluid membranes by periodic harmonic potentials. *Physical Review E*, 69:1–10, 2004.

[32] C Dubus and J-B Fournier. A Gaussian model for the membrane of red blood cells with cytoskeletal defects. *Europhysics Letters Letters*, 75:181, 2006.

[33] S F Fenz. *Cell-cell adhesion mediated by mobile receptor-ligand pairs: a biomimetic study*. PhD thesis, Bonn University, 2008.

[34] C Tanford. *The hydrophobic effect: Formation of micelles and biologic membranes*. Wiley & Sons, Hoboken, 2nd edition, 1980.

[35] G Cevc. *Phospholipids handbook*. Marcel Dekker Inc., New York, 1993.

[36] S L Veatch and S L Keller. Separation of liquid phases in giant vesicles of ternary mixtures of phospholipids and cholesterol. *Biophysical Journal*, 85:3074–83, November 2003.

[37] F Quemeneur, A Rammal, M Rinaudo, and B Pépin-Donat. Large and giant vesicles "decorated" with chitosan: Effects of pH, salt or glucose stress, and surface adhesion. *Biomacromolecules*, 8:2512–2519, 2007.

[38] P Girard, J Pécréaux, G Lenoir, P Falson, J-L Rigaud, and P Bassereau. A new method for the reconstitution of membrane proteins into giant unilamellar vesicles. *Biophysical Journal*, 87:419–29, July 2004.

[39] R Langer. Drug delivery and targeting. *Nature*, 392:5–10, April 1998.

[40] D S Dimitrov and M I Angelova. Lipid swelling and liposome formation mediated by electric fields. *Bioelectrochemistry and Bioenergetics*, 19:323–336, 1988.

[41] L D Mayer, M J Hope, and P R Cullis. Vesicles of variable sizes produced by a rapid extrusion procedure. *Biochimica et Biophysica Acta*, 858:161–168, 1986.

[42] J C Stachowiak, D L Richmond, T H Li, A P Liu, S H Parekh, and D A Fletcher. Unilamellar vesicle formation and encapsulation by microfluidic jetting. *Proceedings of the National Academy of Sciences of the United States of America*, 105:4697–4702, 2008.

[43] J Senior and G Gregoriadis. Dehydration-rehydration vesicle methodology facilitates a novel approach to antibody binding to liposomes. *Biochimica et Biophysica Acta*, 1003:58–62, 1989.

[44] A Albersdörfer, T Feder, and E Sackmann. Adhesion-induced domain formation by interplay of long-range repulsion and short-range attraction force: A model membrane study. *Biophysical Journal*, 73:245–57, July 1997.

[45] M P Sheetz, J E Sable, and H-G Döbereiner. Continuous membrane-cytoskeleton adhesion requires continuous accommodation to lipid and cytoskeleton dynamics. *Annual Review of Biophysics and Biomolecular Structure*, 35:417–34, January 2006.

[46] W Rawicz, K C Olbrich, T McIntosh, D Needham, and E Evans. Effect of chain length and unsaturation on elasticity of lipid bilayers. *Biophysical Journal*, 79:328–39, July 2000.

[47] S Chiantia, N Kahya, J Ries, and P Schwille. Effects of ceramide on liquid-ordered domains investigated by simultaneous AFM and FCS. *Biophysical Journal*, 90:4500–8, June 2006.

[48] M Edidin. The state of lipid rafts: From model membranes to cells. *Annual Review of Biophysics and Biomolecular Structure*, 32:257–83, January 2003.

[49] C A Keller, K Glasmästar, V P Zhdanov, and B Kasemo. Formation of supported membranes from vesicles. *Physical Review Letters*, 84:5443–5446, 2000.

[50] L K Tamm and H M McConnell. Supported phospholipid bilayers. *Biophysical Journal*, 47:105–113, 1985.

[51] J Kim, G Kim, and P S Cremer. Investigations of water structure at the solid/liquid interface in the presence of supported lipid bilayers by vibrational sum frequency spectroscopy. *Langmuir*, 17:7255–7260, 2001.

[52] S P Massia and J A Hubbell. An RGD spacing of 440 nm is sufficient for integrin alpha V beta 3-mediated fibroblast spreading and 140 nm for focal contact and stress fiber formation. *The Journal of Cell Biology*, 114:1089–100, September 1991.

[53] C Monzel. *Thermische Fluktuationen zweidimensionaler, flexibler Objekte*. Diploma thesis, Bonn, 2008.

[54] L Limozin and K Sengupta. Quantitative reflection interference contrast microscopy (RICM) in soft matter and cell adhesion. *Chemphyschem*, 10:2752–2768, 2009.

[55] H Bakowsky, T Richter, C Kneuer, D Hoekstra, U Rothe, G Bendas, C Ehrhardt, and U Bakowsky. Adhesion characteristics and stability assessment of lectin-modified liposomes for site-specific drug delivery. *Biochimica et Biophysica Acta*, 1778:242–249, 2008.

[56] P G de Gennes. Conformations of polymers attached to an interface. *Macromolecules*, 13:1069–1075, 1980.

[57] K Hristova and D Needham. Phase Behavior of a Lipid/Polymer-Lipid Mixture in Aqueous Medium. *Macromolecules*, 28:991–1002, July 1995.

[58] Avanti Polar Lipids Inc. Product Catalogue, Revised: 07.2011.

[59] A Anastasiadis, C J Morton, G H Talbo, R E Koeppe, and F Separovic. Effect of Linker Length on Avidin Binding to Biotinylated Gramicidin A. *International Journal of Peptide Research and Therapeutics*, 12:243–252, 2006.

[60] E P Diamandis and T K Christopoulos. The biotin-(strept)avidin system: Principles and applications in biotechnology. *Clinical Chemistry*, 37:625–636, 1991.

[61] L Pugliese, M Malcovati, A Coda, and M Bolognesi. Crystal structure of apo-avidin from hen egg-white. *Journal of Molecular Biology*, 235:42–46, 1994.

[62] Molecular Probes Co. *The handbook: A guide to fluorescence probes and labeling technologies*. Molecular Probes, Eugene, 11th edition, 2010.

[63] O Livnah, E A Bayer, M Wilchek, and J L Sussman. Three-dimensional structures of avidin and the avidin-biotin complex. *Proceedings of the National Academy of Sciences of the United States of America*, 90:5076–80, 1993.

[64] G T Hermanson. *Bioconjugate techniques*. Academic Press, Waltham, MA, 2nd edition, 2008.

[65] F Zernike. Phase contrast, a new method for the microscopic observation of transparent objects. *Physica*, 9:686–698, 1942.

[66] D B Murphy. *Fundamentals of light microscopy and electronic imaging*, volume 18. Wiley & Sons, Hoboken, 2001.

[67] A Jablonski. Über den Mechanismus der Photolumineszenz von Farbstoffphosphoren. *Zeitschrift für Physik*, 94:38–46, January 1935.

[68] G G Stokes. On the Change of Refrangibility of Light. *Royal Society of London Philosophical Transactions Series I*, 142:463–562, 1852.

[69] J R Lakowicz. *Principles of fluorescence spectroscopy, Band 1*. Springer, Berlin, 2nd edition, 2006.

[70] J B Pawley. *Handbook of biological confocal microscopy*. Springer, Berlin, 3rd edition, 2006.

[71] M Minsky. Microscopy Apparatus, Patent, 1961.

[72] G J Brakenhoff, P Blom, and P Barends. Confocal scanning light microscopy with high aperture immersion lenses. *Journal of Microscopy*, 117:219–232, 1979.

[73] R Peters, J Peters, K H Tews, and W Bähr. A microfluorimetric study of translational diffusion in erythrocyte membranes. *Biochimica et Biophysica Acta*, 367:282–94, November 1974.

[74] D Axelrod, D E Koppel, J Schlessinger, E Elson, and W W Webb. Mobility measurement by analysis of fluorescence photobleaching recovery kinetics. *Biophysical Journal*, 16:1055–1069, 1976.

[75] D M Soumpasis. Theoretical analysis of fluorescence photobleaching recovery experiments. *Biophysical Journal*, 41:95–7, January 1983.

[76] D Magde, E Elson, and W Webb. Thermodynamic fluctuations in a reacting system - Measurement by fluorescence correlation spectroscopy. *Physical Review Letters*, 29:705–708, September 1972.

[77] K Schätzel, M Drewel, and S Stimac. Photon correlation measurements at large lag times: Improving statistical accuracy. *Journal of Modern Optics*, 35:711–718, 1988.

[78] P A Van Den Berg, J Widengren, M A Hink, R Rigler, and A J Visser. Fluorescence correlation spectroscopy of flavins and flavoenzymes: Photochemical and photophysical aspects. *Spectrochimica Acta Part A Molecular and Biomolecular Spectroscopy*, 57:2135–2144, 2001.

[79] S T Hess, S Huang, A A Heikal, and W W Webb. Biological and chemical applications of fluorescence correlation spectroscopy: A review. *Biochemistry*, 41:697–705, January 2002.

[80] S Weiss. Fluorescence spectroscopy of single biomolecules. *Science*, 283:1676–1683, March 1999.

[81] L Wawrezinieck, H Rigneault, D Marguet, and P-F Lenne. Fluorescence correlation spectroscopy diffusion laws to probe the submicron cell membrane organization. *Biophysical Journal*, 89:4029–42, December 2005.

[82] L Guo, J Y Har, J Sankaran, Y Hong, B Kannan, and T Wohland. Molecular diffusion measurement in lipid bilayers over wide concentration ranges: A comparative study. *Chemphyschem*, 9:721–8, April 2008.

[83] R Rigler, P Grasselli, and M Ehrenberg. Fluorescence correlation spectroscopy and application to the study of Brownian motion of biopolymers. *Physica Scripta*, 19:486–490, 1979.

[84] S A Kim, K G Heinze, and P Schwille. Fluorescence correlation spectroscopy in living cells. *Nature Methods*, 4:963–73, November 2007.

[85] O Krichevsky and G Bonnet. Fluorescence correlation spectroscopy: the technique and its applications. *Reports on Progress in Physics*, 65:251–297, 2002.

[86] T Wohland, R Rigler, and H Vogel. The Standard Deviation in Fluorescence Correlation Spectroscopy. *Biophysical Journal*, 80:2987–2999, 2001.

[87] A Benda, M Beneš, V Marecek, A Lhotský, W T Hermens, and M Hof. How to determine diffusion coefficients in planar phospholipid systems by confocal fluorescence correlation spectroscopy. *Langmuir*, 19:4120–4126, 2003.

[88] A G Palmer III and N L Thompson. Optical spatial intensity profiles for high order autocorrelation in fluorescence spectroscopy. *Applied Optics*, 28:1214, March 1989.

[89] S M Sorscher and M P Klein. Profile of a focussed collimated laser beam near the focal minimum characterized by fluorescence correlation spectroscopy. *Review of Scientific Instruments*, 51:98, July 1980.

[90] M Przybylo, J Sykora, J Humpolíckova, A Benda, A Zan, and M Hof. Lipid diffusion in giant unilamellar vesicles is more than 2 times faster than in supported phospholipid bilayers under identical conditions. *Langmuir*, 22:9096–9, 2006.

[91] P Schwille, U Haupts, S Maiti, and W W Webb. Molecular dynamics in living cells observed by fluorescence correlation spectroscopy with one- and two-photon excitation. *Biophysical Journal*, 77:2251–2265, 1999.

[92] A Vašíček. Theory of light reflection from a thin absorbing film deposited on a metal. *Optics and Spectroscopy*, 11:128, August 1961.

[93] M Abercrombie and E J Ambrose. Interference microscope studies of cell contacts in tissue culture. *Experimental Cell Research*, 15:332–345, 1958.

[94] A S G Curtis. The mechanisms of adhesion of cells to glass. A study by interference reflection microscopy. *The Journal of Cell Biology*, 20:199–215, 1964.

[95] G Wiegand, K R Neumaier, and E Sackmann. Microinterferometry: Three-dimensional reconstruction of surface microtopography

for thin-film and wetting studies by reflection interference contrast microscopy (RICM). *Applied Optics*, 37:6892–6905, 1998.

[96] H Verschueren. Interference reflection microscopy in cell biology: Methodology and applications. *Journal of Cell Science*, 75:279–301, April 1985.

[97] R Simson, E Wallraff, J Faix, J Niewöhner, G Gerisch, and E Sackmann. Membrane bending modulus and adhesion energy of wild-type and mutant cells of dictyostelium lacking talin or cortexillins. *Biophysical Journal*, 74:514–522, 1998.

[98] J Nardi, R Bruinsma, and E Sackmann. Adhesion-induced reorganization of charged fluid membranes. *Physical Review E*, 58:6340–6354, 1998.

[99] K Sengupta, H Aranda-Espinoza, L Smith, P Janmey, and D Hammer. Spreading of neutrophils: From activation to migration. *Biophysical Journal*, 91:4638–48, December 2006.

[100] L Limozin and K Sengupta. Modulation of vesicle adhesion and spreading kinetics by hyaluronan cushions. *Biophysical Journal*, 93:3300–13, November 2007.

[101] J Schilling, K Sengupta, S Goennenwein, A R Bausch, and E Sackmann. Absolute interfacial distance measurements by dual-wavelength reflection interference contrast microscopy. *Physical Review E*, 69:021901, 2004.

[102] K Spaeth, A Brecht, and G Gauglitz. Studies on the biotin-avidin adsorption by spectroscopic ellipsometry. *Journal of Colloid and Interface Science*, 196:128–135, 1997.

[103] J Rädler and E Sackmann. Imaging optical thicknesses and separation distances of phospholipid vesicles at solid surfaces. *Journal de Physique*, 3:727–748, 1993.

[104] K Sengupta and L Limozin. Adhesion of soft membranes controlled by tension and interfacial polymers. *Physical Review Letters*, 104:088101, 2010.

[105] J S Ploem. *Mononuclear phagocytes in immunity, infection and pathology*. Blackwell Scientific, Oxford, 1975.

[106] E Hecht. *Optics*. Addison - Wesley, Amsterdam, 2nd edition, 1987.

[107] Meschede D. *Gerthsen Physik*. Springer, Berlin, 22nd edition, 2004.

[108] C Monzel, S Fenz, R Merkel, and K Sengupta. Probing biomembrane dynamics by dual-wavelength reflection interference contrast microscopy. *Chemphyschem*, 10:2828–38, November 2009.

[109] M J Dalby, N Gadegaard, R Tare, A Andar, M O Riehle, P Herzyk, C D W Wilkinson, and R O C Oreffo. The control of human mesenchymal cell differentiation using nanoscale symmetry and disorder. *Nature Materials*, 6:997–1003, 2007.

[110] AI Teixeira, G A McKie, J D Foley, P J Bertics, P F Nealey, and C J Murphy. The effect of environmental factors on the response of human corneal epithelial cells to nanoscale substrate topography. *Biomaterials*, 27:3945–3954, 2006.

[111] D Cuvelier, M Théry, Y-S Chu, S Dufour, J-P Thiéry, M Bornens, P Nassoy, and L Mahadevan. The universal dynamics of cell spreading. *Current Biology*, 17:694–9, 2007.

[112] D Cuvelier, O Rossier, P Bassereau, and P Nassoy. Micropatterned "adherent/repellent" glass surfaces for studying the spreading kinetics of individual red blood cells onto protein-decorated substrates. *European Biophysics Journal*, 32:342–354, 2003.

[113] A Kusumi, Y Sako, and M Yamamoto. Confined lateral diffusion of membrane receptors as studied by single particle tracking (nanovid microscopy). Effects of calcium-induced differentiation in cultured epithelial cells. *Biophysical Journal*, 65:2021–40, November 1993.

[114] C Kleusch. *Analyse fluoreszenzmarkierter Lipide nach Einbau in Plasmamembranen von Myofibroblasten mittels fusogener Liposomen.* Diploma thesis, Universität Bonn, 2010.

[115] J O Rädler, T J Feder, H H Strey, and E Sackmann. Fluctuation analysis of tension-controlled undulation forces between giant vesicles and solid substrates. *Physical Review E*, 51:4526–4536, 1995.

[116] R Bruinsma, A Behrisch, and E Sackmann. Adhesive switching of membranes: experiment and theory. *Physical Review E*, 61:4253–4267, 2000.

[117] R R Netz and R Lipowsky. Stacks of fluid membranes under pressure and tension. *Europhysics Letters*, 29(4):345–350, 1995.

[118] D Schmidt. *Fluctuation effects for bound membranes.* Diploma thesis, Stuttgart, 2011.

[119] V A Parsegian. *Van der Waals forces: a handbook for biologists, chemists, engineers, and physicists.* Cambridge University Press, Cambridge, 2006.

[120] J Mahanty and B W Ninham. *Dispersion Forces*, volume 81. Academic Press, Waltham, MA, August 1976.

[121] W Helfrich. Elastic properties of lipid bilayers: theory and possible experiments. *Zeitschrift für Naturforschung, Teil C*, 28:693–703, 1973.

[122] R Lipowsky and B Zielinska. Binding and unbinding of lipid membranes: A Monte Carlo study. *Physical Review Letters*, 62:1572–1575, March 1989.

[123] C Safinya, D Roux, G S Smith, S K Sinha, P Dimon, N A Clark, and A M Bellocq. Steric interactions in a model multimembrane system: A synchrotron X - ray study. *Physical Review Letters*, 57:2718, 1986.

[124] R Bruinsma and E Sackmann. Bioadhesion and the dewetting transition. *Comptes Rendus de l'Academie des Sciences*, 2:803 – 815, 2001.

[125] Y Zhou and R M Raphael. Effect of salicylate on the elasticity, bending stiffness, and strength of SOPC membranes. *Biophysical Journal*, 89:1789–1801, 2005.

[126] J Majewski, T L Kuhl, M C Gerstenberg, J N Israelachvili, and G S J Smith. Structure of phospholipid monolayers containing poly(ethylene glycol) lipids at the air - water interface. *Physical Chemistry B*, 101:3122 – 3129, 1997.

[127] E M Slayter. An electron microscopy study of the conformational change in bovine serum albumin at low pH. *Journal of Molecular Biology*, 14:443 – 452, 1965.

[128] J Humpolíčková, E Gielen, A Benda, V Fagulova, J Vercammen, M VandeVen, M Hof, M Ameloot, and Y Engelborghs. Probing diffusion laws within cellular membranes by Z-scan fluorescence correlation spectroscopy. *Biophysical Journal*, 91:L23–L25, 2006.

[129] M Benes, D Billy, W T Hermens, and M Hof. Muscovite (mica) allows the characterisation of supported bilayers by ellipsometry and confocal fluorescence correlation spectroscopy. *Biological Chemistry*, 383:337–341, 2002.

[130] P Schwille, J Korlach, and W W Webb. Fluorescence correlation spectroscopy with single-molecule sensitivity on cell and model membranes. *Cytometry*, 36:176–182, 1999.

[131] E Gielen, M VandeVen, A Margineanu, P Dedecker, M Van der Auweraer, Y Engelborghs, J Hofkens, and M Ameloot. On the use of Z-scan fluorescence correlation experiments on giant unilamellar vesicles. *Chemical Physics Letters*, 469:110–114, February 2009.

[132] R-J Merath and U Seifert. Nonmonotonic fluctuation spectra of membranes pinned or tethered discretely to a substrate. *Physical Review E - Statistical, Nonlinear and Soft Matter Physics*, 73:010401, 2006.

[133] K Olbrich, W Rawicz, D Needham, and E Evans. Water permeability and mechanical strength of polyunsaturated lipid bilayers. *Biophysical Journal*, 79:321–327, July 2000.

[134] S Chiruvolu and J A N Zasadzinski. Membrane elasticity effects on permeability measurements in vesicles. *AIChE Journal*, 39:647–652, April 1993.

[135] F Brochard-Wyart and J-F Lennon. Frequency spectrum of the flicker phenomenon in erythrocyte. *Journal de Physique*, 36:1035–1047, 1975.

[136] U Seifert and S A Langer. Viscous modes of fluid bilayer membranes. *Europhysics Letters*, 23:71–76, 1993.

[137] E Evans, A Yeung, R Waugh, and Song J. The Structure and Conformation of Amphiphilic Membranes. *Springer Proceedings in Physics*, 66, 1992.

[138] L Miao, M A Lomholt, and J Kleis. Dynamics of shape fluctuations of quasi-spherical vesicles revisited. *European Physical Journal E*, 9, 1992.

[139] P Schwille and E Haustein. Fluorescence Correlation Spectroscopy: An Introduction to its Concepts and Applications. *Spectroscopy*, 94:1–33, 2009.

[140] C Fradin, A Abu-Arish, R Granek, and M Elbaum. Fluorescence Correlation Spectroscopy Close to a Fluctuating Membrane. *Biophysical Journal*, 84:2005–2020, 2003.

[141] W Haeckl, U Seifert, and E Sackmann. Effect of fully and partially solubilized amphiphiles on bilayer bending stiffness and temperature dependence of the effective tension of giant vesicles. *Journal De Physique Ii*, 7:1141–1157, 1997.

[142] J Pécréaux, H-G Döbereiner, J Prost, J-F Joanny, and P Bassereau. Refined contour analysis of giant unilamellar vesicles. *The European Physical Journal E*, 13:277–290, 2004.

[143] M B Schneider, J T Jenkins, and W W Webb. Thermal fluctuations of large quasi-spherical bimolecular phospholipid vesicles. *Journal de Physique*, 45:1457–1472, 1984.

[144] S Cha, S H Kim, and D Kim. Viscosity of Sucrose Aqueous Solutions Measured by Using Fluorescence Correlation Spectroscopy. *Journal of the Korean Physical Society*, 56:1315 – 1318, 2010.

[145] E Evans and E Sackmann. Translational and rotational drag coefficients for a disk moving in a liquid membrane associated with a rigid substrate. *Journal of Fluid Mechanics*, 194:553–561, September 1988.

[146] R Hirn, T M Bayerl, J O Rädler, and E Sackmann. Collective membrane motions of high and low amplitude, studied by dynamic light scattering and micro-interferometry. *Faraday Discussions*, 111:17–30, 1998.

[147] Y Kaizuka and J T Groves. Hydrodynamic damping of membrane thermal fluctuations near surfaces imaged by fluorescence interference microscopy. *Physical Review Letters*, 96:118101, March 2006.

[148] J Prost, J-B Manneville, and R Bruinsma. Fluctuation-magnification of non-equilibrium membranes near a wall. *The European Physical Journal B*, 1:465–480, March 1998.

[149] R Rodríguez-García, M Mell, I López-Montero, and F Monroy. Subdiffusive fluctuation dynamics of rigid membranes as resolved by ultrafast videomicroscopy. *Europhysics Letters*, 94:28009, April 2011.

[150] A Csiszar, N Hersch, S Dieluweit, R Biehl, R Merkel, and B Hoffmann. Novel Fusogenic Liposomes for Fluorescent Cell Labeling and Membrane Modification. *Bioconjugate Chemistry*, 21:537–543, February 2010.

[151] J Enderlein, I Gregor, D Patra, and J Fitter. Art and artefacts of fluorescence correlation spectroscopy. *Current Pharmaceutical Biotechnology*, 5:155–161, 2004.

[152] S T Hess and W W Webb. Focal volume optics and experimental artifacts in confocal fluorescence correlation spectroscopy. *Biophysical Journal*, 83:2300–2317, 2002.

[153] D E Koppel. Statistical accuracy in fluorescence correlation spectroscopy. *Physical Review A*, 10:1938–1945, 1974.

[154] R van Wezel. Advanced notes on water immersion lenses. Part 1: Introduction. *Micscape*, (114), 2005.

[155] P Wedekind, U Kubitscheck, and R Peters. Scanning microphotolysis: a new photobleaching technique based on fast intensity modulation of a scanned laser beam and confocal imaging. *Journal of Microscopy*, 176:23–33, October 1994.

[156] K Schätzel. New concepts in correlator design. *Institute of Physics Conference Series*, 77:175–184, 1985.

[157] I Gregor, D Patra, and J Enderlein. Optical saturation in fluorescence correlation spectroscopy under continuous-wave and pulsed excitation. *Chemphyschem*, 6:164–170, 2005.

[158] Z Petrásek and P Schwille. Precise measurement of diffusion coefficients using scanning fluorescence correlation spectroscopy. *Biophysical Journal*, 94:1437–48, February 2008.

[159] C B Müller, A Loman, V Pacheco, F Koberling, D Willbold, W Richtering, and J Enderlein. Precise measurement of diffusion by multicolor dual-focus fluorescence correlation spectroscopy. *Europhysics Letters*, 83:46001, August 2008.

[160] Atto-Tec GmbH. Product Information: ATTO 488, ATTO 550 and ATTO 633, Revised: 16.05.2011.

[161] S A Soper, H L Nutter, R A Keller, L M Davis, and E B Shera. the Photophysical Constants of Several Fluorescent Dyes Pertaining To Ultrasensitive Fluorescence Spectroscopy. *Photochemistry and Photobiology*, 57:972–977, 1993.

[162] D R Larson, H Ow, H D Vishwasrao, A A Heikal, U Wiesner, and W W Webb. Silica Nanoparticle Architecture Determines Radiative Properties of Encapsulated Fluorophores. *Chemistry of Materials*, 20:2677–2684, 2008.